Richtmyer–Meshkov Instability in Converging Geometries

Thesis by

Manuel Lombardini

In Partial Fulfillment of the Requirements

for the Degree of

Doctor of Philosophy

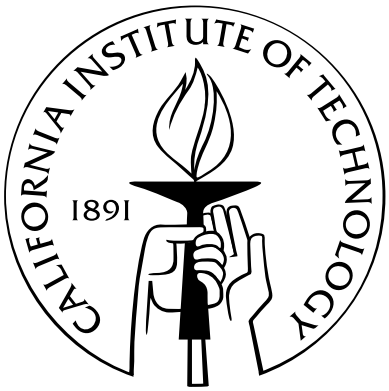

California Institute of Technology

Pasadena, California

2008

(Defended 2 May 2008)

A Lily, Fanny, et ma grand-mère Marie-Jeanne

Acknowledgements

First, I would like to thank my advisor, Prof. Dale Pullin, for his guidance, critique and enthusiasm over the years. Next, I would like to thank the other members of my thesis committee, Prof. Colonius, Prof. Meiron, and Prof. Shepherd, whose comments and suggestions have improved this work.

I am most grateful to Dr. Ralf Deiterding for his unlimited help and encouragement. I also thank Dr. David Hill for the many interesting research discussions we had together, for his patience, and for his laid-back personality. I wish to acknowledge Dr. Carlos Pantano for his help on the patch solver, among other things.

Much thanks to my friends Lily, Aaron, Rogier, Ivan, Laurent, Fanny...for making this PhD more than an academic experience. A special thanks to Nico, Jérôme, and Céline, who supported me despite the distance.

This effort was supported by the Academic Strategic Alliances Program (ASAP) of the Advanced Simulation and Computing (ASC) under subcontract no. B341492 of DoE contract W-7405-ENG-48.

Abstract

We investigate the Richtmyer-Meshkov instability (RMI) in converging geometries analytically and computationally. The linear, or small amplitude, regime is first covered as it is the onset to subsequent non-linear stages of the perturbation growth. While the plane interaction of a shock with a slightly perturbed density interface is classically viewed as a single interface evolving as baroclinic vorticity have been initially deposited on it, we propose a simple but more complete model characterizing the early interaction between the interface and the receding waves produced by the shock-interface interaction, in the case of a reflected shock. A universal time scale representing the time needed by the RMI to reach its asymptotic growth rate is found analytically and confirmed by ideal gas computations for various incident shock Mach numbers M_I and Atwood ratios A, and could be useful especially for experimentalists in non-dimensionalizing their data.

Considering again linear perturbations, we then obtain a general analytical model for the asymptotic growth rate reached by the instability during the concentric interaction of an imploding/exploding cylindrical shock with a cylindrical interface containing three-dimensional orthogonal perturbations, in the azimuthal and axial directions. Stable perturbations, typical of the converging geometry, are discovered. Comparisons are made with simulations where the effects of compressibility, wave reverberations, and flow convergence are isolated. Azimuthal and axial perturbation evolution are compared with results obtained for the plane RMI at comparable initial wavelengths.

A second interaction occurs when the transmitted shock, produced by the incident converging shock impacting the interface, converges to the axis and reflects to reshock the initially accelerated interface. This leads to highly non-linear perturbation growth. To isolate the complex wave interaction process, the interface is considered initially unperturbed so that the flow is radially symmetric. An accurate visualization procedure is performed to characterize the underlying physics behind the reshock event. We study extensively the cylindrical and spherical geometry, for various M_I and for the air$\rightarrow$ SF_6 ($A = 0.67$) and SF_6 $\rightarrow$air ($A = -0.67$) interactions, and draw important differences with the equivalent plane configuration.

A hybrid, low-numerical dissipation/shock-capturing method, embedded into an adaptive mesh refinement framework is optimized in order to achieve large-eddy simulations of the self-similar cylindrical converging shock-driven RMI and the turbulent mixing generated by the reshock. Com-

putations are produced for $M_I = 1.3$ and 2.0, and for air$\rightarrow$ SF_6 and SF_6 $\rightarrow$air interfaces. We develop statistics tools to study extensively the growth of the turbulent mixing zone using cylindrical averages as well as various measures such as probability density functions of the mixing and turbulent power spectra, with the objectives of understanding the turbulent mixing in this particular geometry.

Contents

Acknowledgements **iv**

Abstract **v**

Contents **vii**

List of Figures **xiii**

List of Tables **xxiii**

List of Symbols **xxv**

1 Introduction **1**

1.1 Motivation 3

1.2 Previous Related Work 4

1.2.1 Linear Regime in Plane and Curved Geometries 4

1.2.2 Converging Shocks 5

1.2.3 Mixing in Accelerated Inhomogeneous Flows 6

1.3 Outline of Present Work 8

2 Startup Process in the Richtmyer-Meshkov Instability **9**

2.1 Introduction 9

2.2 Analytical Model 10

2.2.1 General Formulation 10

2.2.2 Base Flow and Perturbations 12

2.2.3 Boundary Conditions at the Shocks 13

2.2.4 Kinematic and Dynamic Conditions at the Interface 15

2.3 Startup Period for Richtmyer-Meshkov Instability 16

2.3.1 Startup Time τ 16

2.3.2 Asymptotic Growth Rate 17

2.3.3 Initial Tangential Velocity at Interface 17

2.4 Numerical Simulations . . . 19
2.4.1 Numerical Method . . . 19
2.4.2 Parametric Study of the Amplitude and Growth Rate of the Interface Perturbation . . . 20
2.4.2.1 Amplitude and Growth Rate . . . 22
2.4.2.2 Influence of kh_0 . . . 22
2.4.2.3 Influence of M_I . . . 23
2.4.2.4 Influence of the Species . . . 23
2.5 On the Time-Scale τ . . . 23
2.5.1 Domain of Validity in the Case of a Reflected Shock . . . 24
2.5.2 Parametric Study of τ . . . 25
2.6 Summary . . . 26

3 Linear Perturbations in the Three-Dimensional Cylindrical Richtmyer-Meshkov Instability 32
3.1 Introduction . . . 32
3.2 Incompressible Linear Theory for Three-Dimensional Cylindrical Perturbations . . . 33
3.2.1 General Evolution Equations . . . 33
3.2.2 Richtmyer's Approach . . . 35
3.2.2.1 Limit Cases . . . 36
3.2.2.2 Critical Perturbations . . . 37
3.2.2.3 Assumption of Constant Interface Velocity . . . 38
3.2.2.4 Effect of the Interface Acceleration . . . 40
3.2.3 Effect of Shock Proximity . . . 40
3.3 Numerical Simulations of the Converging Cylindrical Linear RMI . . . 41
3.3.1 Numerical Method . . . 41
3.3.2 Parameters . . . 43
3.3.3 Converging Shock . . . 43
3.3.4 Axial Perturbations . . . 46
3.3.4.1 Influence of the Axial Wavenumber k . . . 46
3.3.4.2 Influence of the Incident Shock Mach Number M_I . . . 47
3.3.5 Azimuthal Perturbations . . . 51
3.3.5.1 Influence of the Azimuthal Wavenumber n . . . 51
3.3.5.2 Influence of the Incident Shock Mach Number M_I . . . 51
3.3.6 Comparison Between Plane and Cylindrical Geometries . . . 52

3.4 Summary . . . 52

4 Wave Diagrams for Shock- and Reshock-Contact Interactions 57

4.1 Introduction . . . 57
4.1.1 Previous Work . . . 57
4.1.2 Description of the Problem . . . 59
4.2 On the One-Dimensional Simulations . . . 59
4.2.1 Governing Equations . . . 59
4.2.2 Numerical Method . . . 61
4.2.3 Visualization . . . 62
4.3 Light-to-Heavy Interaction: Air $\rightarrow$ SF_6 . . . 65
4.3.1 Incident Mach Number $M_I = 1.2$ . . . 65
4.3.1.1 Plane Geometry . . . 65
4.3.1.2 Cylindrical Geometry . . . 65
4.3.1.3 Spherical Geometry . . . 66
4.3.2 Summary . . . 67
4.3.3 Incident Mach Number $M_I = 3.0$ . . . 72
4.3.3.1 Plane Geometry . . . 72
4.3.3.2 Cylindrical (Respectively Spherical) Geometry . . . 72
4.3.3.3 Summary . . . 73
4.4 Heavy-to-Light Interaction: SF_6 $\rightarrow$ Air . . . 77
4.4.1 Incident Mach Number $M_I = 1.2$ . . . 77
4.4.2 Incident Mach Number $M_I = 3.0$ . . . 81
4.5 Summary . . . 81

5 Large-Eddy Simulations of Shock-Generated Mixing in a Cylindrical Geometry 86

5.1 Introduction . . . 86
5.1.1 Flow Description . . . 86
5.1.2 Domain Geometry and Boundary Conditions . . . 86
5.1.3 Initial Conditions . . . 88
5.2 Governing Equations . . . 90
5.2.1 Two-Component Favre-Filtered Navier-Stokes Equations . . . 90
5.2.2 The Stretched-Vortex Subgrid Model . . . 92
5.3 Computational Approach . . . 93
5.3.1 AMROC Framework . . . 93
5.3.1.1 On the Use of SAMR Cartesian Grid for Converging Flows . . . 93

5.3.2 Hybrid Numerical Method . . . 94
5.3.2.1 TCD Stencil . . . 95
5.3.2.2 Stable TCD Formulation . . . 96
5.3.2.3 Flux-Based Formulation . . . 96
5.3.2.4 WENO-TCD Flux-Switching Technique . . . 97
5.3.3 Time-Marching Method for SAMR . . . 101
5.3.4 Description of the Large-Eddy Simulations . . . 101
5.4 Cylindrical-Shell Statistics: Definitions . . . 105
5.5 The Different Stages in the Growth of the Mixing Layer . . . 106
5.5.1 Visualization . . . 106
5.5.2 Mixing-Zone Growth . . . 106
5.5.3 Turbulence Statistics . . . 112
5.5.3.1 Shell-Averaged Statistics vs. Radius At Different Stages . . . 112
5.5.3.2 On the Decaying Turbulence . . . 115
5.6 Instantaneous Velocity, Density and Scalar Spectra . . . 123
5.6.1 Time Evolution . . . 123
5.6.2 Late-Time Spectra . . . 123
5.7 Kolmogorov and Taylor Statistics . . . 125
5.8 Mixing Statistics . . . 129
5.8.1 Local-Composition Evolution . . . 130
5.8.2 Joint Density-Mixture Fraction Probability Density Functions . . . 132
5.9 Summary . . . 133

6 Conclusion **135**
6.1 Summary . . . 135
6.2 Future Work . . . 136

A Interface Acceleration for Self-Similar Converging Shock-Contact Interactions **138**

B Shell-Averaged Equations **142**
B.1 Introduction . . . 142
B.2 Plane Richtmyer-Meshkov Instability . . . 142
B.2.1 Basic Quantities . . . 142
B.2.2 Un-Modeled Equations . . . 143
B.3 Cylindrical Richtmyer-Meshkov Instability . . . 144
B.4 Basic Quantities . . . 144
B.5 Un-Modeled Equations . . . 145

C Shell-Averaged Statistics: Methodology **146**

C.1 The Statistics Class Within AMROC 146

C.2 Output of Basic Quantities 147

C.3 One-Dimensional Statistics 150

C.3.1 Basic Shell-Averaged Quantities 150

C.3.2 Derived Quantities 154

C.3.2.1 Quantities Depending on (r, t) 154

C.3.2.2 Quantities Depending on t Only and Based on the Mass Fraction Y 157

C.3.2.3 Quantities Depending on t Only and Based on the Mol Fraction X . 159

C.4 Two-Dimensional Statistics For Spectrum, P.d.f., Subgrid Continuation... 161

Bibliography **163**

List of Figures

1.1 Two-dimensional simulations of the converging cylindrical Richtmyer-Meshkov instability in a 90° wedge, using adaptive mesh refinement. A cylindrical converging shock impacts at a Mach number 3.0 a cylindrical density interface separating air (outside) from sulfur hexafluoride (inside). Passive scalar contours (upper diagonal) show the distortion of the interface, while transmitted shock and reflected wave patterns appear on the pressure contours (lower diagonal). 3

1.2 Experiments of the Rayleigh-Taylor instability by Waddell et al. [111]. A sequence of planar laser-induced fluorescence images showing the development of an immiscible system with Atwood ratio 0.336 accelerated at 1.34 g: linear regime (a),(b); non-linear regime (c)–(g); chaotic appearance suggesting transition to turbulence (h)–(j). 4

2.1 Perturbed system. 11

2.2 Correction factor to Richtmyer's impulsive growth rate for varying incident shock strengths S (see Equation (2.28)) and various combinations of gases: air $\rightarrow CO_2$ (solid line), Ar $\rightarrow$ Xe (dashed-dotted line), air $\rightarrow SF_6$ (small dashed line), and He $\rightarrow$ air (long dashed line). 19

2.3 Early-time close-up: dimensionless amplitude and growth rate of the interface perturbation $h(t)/h_0$ and $\dot{h}/a_0$ vs. a_0kt; case air $\rightarrow SF_6$, $kh_0 = 0.1$, $M_I = 1.5$. Numerical simulations using AMROC are represented by crosses. The thin dashed and thick solid lines correspond to our model given by Equation (2.16) with two different choices for $\dot{h}_\infty$. The thin dashed line corresponds to our model using Richtmyer's asymptotic growth rate $\dot{h}_\infty = \dot{h}_{Rich.}$, while the thick solid line uses Yang's correction to Richtmyer's asymptotic growth rate $\dot{h}_\infty = \mathfrak{F}_{Yang}\,\dot{h}_{Rich.}$. $\dot{h}_{Rich.}$ is given by Equation (2.20) and $\mathfrak{F}_{Yang}$ is provided by Yang's linearized simulations [120]. We also recall that the model gives an explicit expression for the growth rate from Equation (2.16), but the amplitude of the interface perturbation is obtained by numerically integrating Equation (2.16) 21

2.4 Influence of M_I: dimensionless amplitude of the interface perturbation $h(t)/h_0$ vs. a_0kt; case air $\rightarrow SF_6$, $kh_0 = 0.1$. For key, see Figure 2.3. 28

2.5 Influence of the species: dimensionless amplitude of the interface perturbation $h(t)/h_0$ vs. a_0kt; case $kh_0 = 0.1$, $M_I = 1.5$. For key, see Figure 2.3. 29

2.6 Influence of the species: dimensionless growth rate of the interface perturbation $\dot{h}/a_0$ vs. a_0kt; case $kh_0 = 0.1$, $M_I = 1.5$. For key, see Figure 2.3. 30

2.7 Contour levels of $a_0k\tau$ in the (A, S) space; for each combination of specific heat ratios a dashed line drawn for small A represents the boundary of the domain of validity of τ as discussed in Subsection 2.5.1. 31

3.1 Iso-contours of the difference between the (dimensionless) cylindrical growth rate and the plane one $(1 + \kappa AF(n, \kappa, A)) - \sqrt{n^2 + \kappa^2}A$, in the wavenumber space (n, κ), with $\kappa \equiv kR_0$. 37

3.2 Contour levels of the Atwood ratio A_c corresponding to critical perturbations, in the wavenumber space (n, kR), for a given history $R(t)$. 39

3.3 Imploding and exploding shock front average radial positions r/R_0 vs. $(a_0/R_0)t$. Superposition of two-dimensional simulation results of cylindrical shock initialized by Chisnell's solution (crosses) and a power-law least-square fit for both imploding and exploding shocks (solid line). 44

3.4 Purely axial perturbations for a cylindrical interface. 47

3.5 Axial perturbations: Dimensionless amplitude (left) and growth rate (right) vs. a_0kt of the interface perturbation (top), spike front (middle), and bubble front (bottom), plotted for different axial wavenumbers k; case air $\rightarrow$ SF_6, $h_0/R_0 = 0.005$, $M_I = 1.2$. . 49

3.6 Axial perturbations: Dimensionless amplitude (left) and growth rate (right) vs. a_0kt of the interface perturbation (top), spike front (middle), and bubble front (bottom), plotted for three different incident Mach numbers M_I; case air $\rightarrow$ SF_6, $h_0/R_0 = 0.005$, $k = 4$. 50

3.7 Purely azimuthal perturbations for a cylindrical interface. 51

3.8 Azimuthal perturbations: Dimensionless amplitude (left) and growth rate (right) vs. $a_0(n/R_0)t$ of the interface perturbation (top), spike front (middle), and bubble front (bottom), plotted for different azimuthal wavenumbers n; case air $\rightarrow$ SF_6, $h_0/R_0 = 0.005$, $M_I = 1.2$. 54

3.9 Azimuthal perturbations: Dimensionless amplitude (left) and growth rate (right) vs. $a_0(n/R_0)t$ of the interface perturbation (top), spike front (middle), and bubble front (bottom), plotted for three different incident Mach numbers M_I; case air $\rightarrow$ SF_6, $h_0/R_0 = 0.005$, $n = 36$. 55

3.10 Dimensionless amplitude (left) and growth rate (right) vs. a_0Kt of the interface perturbation (top), spike front (middle), and bubble front (bottom), plotted for the azimuthal, axial, and plane perturbations; case air $\rightarrow$ SF_6, $M_I = 1.2$, $Kh_0 = 0.12$; for the azimuthal geometry $h_0/R_0 = 0.005$ and $K \equiv n/R_0 = 3$, for the axial geometry $h_0/R_0 = 0.005$ and $K \equiv k = 3$, for the plane geometry $K \equiv k = 3$. 56

4.1 $r - t$ wave diagram: example of the $M_I = 3.2$ cylindrical shock interaction with an air$\rightarrow SF_6$ interface. Density Schlieren levels (log scale) displayed. 63

4.2 Close-up on the first and second reverberations: example of the $M_I = 3.2$ cylindrical shock interaction with an air$\rightarrow SF_6$ interface. Density Schlieren levels (log scale) displayed on a wave diagram and superposed to the three different families of characteristics, $u - a$ (top), u (middle), and $u + a$ (bottom). 64

4.3 Density ρ/ρ_0 vs. position r/R_0 for the air$\rightarrow$ SF_6 plane (red solid line), cylindrical (green long-dashed line), and spherical (blue small-dashed line) shock interactions for a $M_I = 1.2$ incident shock. Density profiles initially (top), after the first reshock event (middle), and at a late time (bottom). After the first reshock, a shock will form behind the expansion tail in the cylindrical and spherical geometries, and another shock will form ahead of the expansion head in the spherical geometry. The interface is initially located at $r/R_0 = 1$; at $r/R_0 \simeq 0.4$ for the plane geometry and $r/R_0 \simeq 0.8$ for the cylindrical/spherical cases after the first reshock; at $r/R_0 \simeq 0.5$ for the plane geometry and $r/R_0 \simeq 0.7$ for the cylindrical/spherical cases at late times. 68

4.4 Density ρ/ρ_0 vs. radius r/R_0 for the air$\rightarrow$ SF_6 interactions at $M_I = 1.2$. Close-up at the center at different times between the first and second reshocks. (a) Plane case: the reflected expansion produced from the first reshock reflects off the wall as an expansion. (b) Cylindrical case: a shock forms behind the reflected expansion tail that was produced from the first reshock interaction, and reflects off the axis. (c) Spherical case: two shocks form behind the reflected expansion tail and ahead of its head; the inner shock reflects off the center and interacts with the outer one; the shock-shock interaction produces a weak shock traveling outwards to reshock the interface a second time, and a stronger and faster shock traveling inwards, reflecting off the center and reshocking the interface soon after the second reshock. 69

4.5 Wave diagrams for the air$\rightarrow$ SF_6 shock interaction for a $M_I = 1.2$ incident shock. Density Schlieren levels for the plane (top), cylindrical (middle), and spherical (bottom) shock interactions. 70

4.6 Wave diagrams for the air→ SF_6 shock interaction for a $M_I = 1.2$ incident shock. Close-up on the first and second reverberations, with characteristics $u-a$ superposed to density Schlieren levels for the plane (top), cylindrical (middle), and spherical (bottom) shock interactions. 71

4.7 Density ρ/ρ_0 vs. position r/R_0 for the air→ SF_6 plane (red solid line), cylindrical (green long-dashed line), and spherical (blue small-dashed line) shock interactions for a $M_I = 3.0$ incident shock. Density profiles initially (top), after the first reshock event (middle), and at a late time (bottom). Shocks form behind the reflected expansion tail (see lower Mach case), and will reflect to reshock the interface a second time. The interface is initially located at $r/R_0 = 1$; at $r/R_0 \simeq 0.1$ for the plane geometry, $r/R_0 \simeq 0.3$ for the cylindrical case, and $r/R_0 \simeq 0.4$ for the spherical case after the first reshock; at $r/R_0 \simeq 0.05$ for the plane geometry, $r/R_0 \simeq 0.1$ for the cylindrical case, and $r/R_0 \simeq 0.2$ for the spherical case at late times. 74

4.8 Wave diagrams for the air→ SF_6 shock interaction for a $M_I = 3.0$ incident shock. Density Schlieren levels for the plane (top), cylindrical (middle), and spherical (bottom) shock interactions. 75

4.9 Wave diagrams for the air→ SF_6 shock interaction for a $M_I = 3.0$ incident shock. Close-up on the first and second reverberations, with characteristics $u-a$ superposed to density Schlieren levels for the plane (top), cylindrical (middle), and spherical (bottom) shock interactions. 76

4.10 Density ρ/ρ_0 vs. position r/R_0 for the SF_6 →air plane (red solid line), cylindrical (green long-dashed line), and spherical (blue small-dashed line) shock interactions for a $M_I = 1.2$ incident shock. Density profiles initially (top), after the first reshock event (middle), and at a late time (bottom). The interface is initially located at $r/R_0 = 1$; at $r/R_0 \simeq 0.6$ for the plane geometry, $r/R_0 \simeq 0.7$ for the cylindrical case, and $r/R_0 \simeq 0.6$ for the spherical case after the first reshock; at $r/R_0 \simeq 0.6$ for the plane geometry, $r/R_0 \simeq 0.7$ for the cylindrical case, and $r/R_0 \simeq 0.6$ for the spherical case at late times. 78

4.11 Wave diagrams for the SF_6 →air shock interaction for a $M_I = 1.2$ incident shock. Density Schlieren levels for the plane (top), cylindrical (middle), and spherical (bottom) shock interactions. 79

4.12 Wave diagrams for the SF_6 →air shock interaction for a $M_I = 1.2$ incident shock. Close-up on the first and second reverberations, with characteristics $u-a$ superposed to density Schlieren levels for the plane (top), cylindrical (middle), and spherical (bottom) shock interactions. 80

4.13 Density ρ/ρ_0 vs. position r/R_0 for the SF_6 →air plane (red solid line), cylindrical (green long-dashed line), and spherical (blue small-dashed line) shock interactions for a $M_I = 3.0$ incident shock. Density profiles initially (top), after the first reshock event (middle), and at a late time (bottom). A strong shock resulting from the interactions of the transmitted shocks produced during the successive reshocks traveling outwards can be seen exiting the physical domain for late times. The interface is initially located at $r/R_0 = 1$; at $r/R_0 \simeq 0.05$ after the first reshock and at late times. 83

4.14 Wave diagrams for the SF_6 →air shock interaction for a $M_I = 3.0$ incident shock. Density Schlieren levels for the plane (top), cylindrical (middle), and spherical (bottom) shock interactions. 84

4.15 Wave diagrams for the SF_6 →air shock interaction for a $M_I = 3.0$ incident shock. Close-up on the first and second reverberations, with characteristics $u-a$ superposed to density Schlieren levels for the plane (top), cylindrical (middle), and spherical (bottom) shock interactions. 85

5.1 (a) Initial flow description. Time $t = 0$ actually corresponds to the incident shock standing just behind the interface with Mach number M_I. (b) Scalar isosurfaces representing the initial perturbed interface (data from run 11 and run 12). 87

5.2 Converging shock focusing in a wedge. Overlay of experimental results from VTF Phase 0 and two-dimensional simulation data from the WENO-TCD patch solver formulated on a Cartesian grid (a) and a shock-capturing method formulated on a body-fitted grid (b). Courtesy of C. L. Bond, D. J. Hill, and G. Matheou. 94

5.3 Conical shock-tube experiments and two-dimensional axisymmetric simulations. (a) Radial speed (normalized by initial shock speed) on the centerline vs. distance to the center; (b) isosurfaces of the three-dimensional magnitude of the density gradient (Schlieren) colored by the density. Speeds over Mach 18 at last measurement. Courtesy of D. J. Hill. 95

5.4 Comparison of decay of turbulence kinetic energy in a homogeneous decaying compressible LES computed on a grid of 32^3 points using standard WENO-5 vs. 5-point TCD scheme. DNS computed with a 256^3 grid and a Padé method, Case D9 of Samtaney et al. [98] with microscale Reynolds number of 175 and turbulent Mach number of 0.488. 96

5.5 Three-dimensional supersonic shear layer (periodic in the spanwise direction z). (x, y)-plane cut across the center of the jet of the density (top) and WENO-TCD flagging (bottom). WENO is turned on in the directions x and y (green) and x, y, and z (red) where shock waves are present. Courtesy of G. Matheou. 100

5.6 Three-dimensional supersonic inclined jet using SAMR (no periodicity in the z direction). (x, y)-plane cut of the WENO-TCD flagging. WENO is turned on in the directions x and y (green) and x, y, and z (red) where shock waves are present, in particular around the bow shock forming ahead of the jet. Courtesy of A. Ferrante. . 100

5.7 Differently colored iso-surfaces for mass fractions $\psi = 73.1\%$, 50%, and 26.9% visualize the evolution of the mixing zone: (a) the interface converges towards the axis; (b) the interface is reshocked a first time; (c) late-time turbulent mixing is observed. The gray levels on the background planes represent the domains of different mesh refinement. Case air→SF_6, $M_0 = 1.3$. 107

5.8 Differently colored iso-surfaces for mass fractions $\psi = 73.1\%$, 50%, and 26.9% visualize the evolution of the mixing zone: (a) the interface converges towards the axis; (b) the interface is reshocked a first time; (c) late-time turbulent mixing is observed. The gray levels on the background planes represent the domains of different mesh refinement. Case air→SF_6, $M_0 = 2.0$. 108

5.9 Evolution of the mixing-layer width δ (red solid line) and growth rate $d\delta/dt$ (blue small-dashed line). Case $M_I = 1.3$ (left) and 2.0 (right). 111

5.10 Evolution of the mixing-layer center r_c. Case $M_I = 1.3$ (left) and 2.0 (right). 111

5.11 Evolution of the mixing-layer width δ following the initial shock interaction. Simulation (red solid line), three-dimensional linear impulsive model $\dot{h}_\infty/a_0$ (blue small-dashed line), and $\beta\dot{h}_\infty/a_0$ (pink dotted line), with $\beta = 0.3$ for $M_I = 1.3$ and $\beta = 0.45$ for $M_I = 2.0$. $\dot{h}_\infty$ given by Equation (3.32). Case $M_I = 1.3$ (left) and 2.0 (right). 112

5.12 Evolution of the mixing-layer width δ following the first reshock. Simulation (red solid line) and $\beta_{rs} A^+_{rs} \Delta W_{rs}$ (blue small-dashed line), with A^+_{rs} and ΔW_{rs} determined at the reshock interaction and $\beta_{rs} = 0.75$ for $M_I = 1.3$ and $\beta_{rs} = 0.28$ for $M_I = 2.0$. Case $M_I = 1.3$ (left) and 2.0 (right). 112

5.13 Evolution of the bubble and spike shell-averaged radial velocities $\langle u_r \rangle_b$ (blue small-dashed line) and $\langle u_r \rangle_s$ (pink dotted line). Case $M_I = 1.3$ (left) and 2.0 (right). 113

5.14 Evolution of the mixing-layer volume per unit $z-$length V. Case $M_I = 1.3$ (left) and 2.0 (right). 113

5.15 Shell-averaged scalar $\langle Y \rangle$ centered on the mixing-layer center r_c vs. r, at different stages of the mixing-layer evolution. Case $M_I = 1.3$ (left) and 2.0 (right). 114

5.16 Shell-averaged scalar $\langle Y \rangle$ (red solid line) and scalar variance $\mathrm{Var}_\rho(Y)$ (blue small-dashed line) vs. r, after the incident shock interaction (top), right after the first reshock (middle), and at late time (bottom). Case $M_I = 1.3$ (left) and 2.0 (right). . . 116

5.17 Shell-averaged density $\langle\rho\rangle$ (red solid line) and density variance Var(ρ) (blue small-dashed line) vs. r, after the incident shock interaction (top), right after the first reshock (middle), and at late time (bottom). Case $M_I = 1.3$ (left) and 2.0 (right). . . 117

5.18 Shell-averaged resolved scale turbulent kinetic energy $\langle K\rangle$ (red solid line) and subgrid turbulent kinetic energy $\langle k\rangle$ (blue small-dashed line) vs. r, after the incident shock interaction (top), right after the first reshock (middle), and at late time (bottom). Note the order of magnitude difference in the scale of the plots: $\langle K\rangle \sim 10\langle k\rangle$ for the case $M_I = 1.3$ and $\langle K\rangle \sim 20\langle k\rangle$ for the case $M_I = 2.0$. Case $M_I = 1.3$ (left) and 2.0 (right). 118

5.19 Shell-averaged resolved scale dissipation rate $\langle\varepsilon_{res}\rangle$ (red solid line) and subgrid dissipation $\langle\varepsilon_{sgs}\rangle$ (blue small-dashed line) vs. r, after the incident shock interaction (top), right after the first reshock (middle), and at late time (bottom). Note the order of magnitude difference in the scale of the plots: for the case $M_I = 1.3$ (respectively 2.0) $\langle\varepsilon_{sgs}\rangle \sim 30\langle\varepsilon_{res}\rangle$ (respectively 100) prior to the first reshock, $\langle\varepsilon_{sgs}\rangle \sim 200\langle\varepsilon_{res}\rangle$ (respectively 1000) after the first reshock, and $\langle\varepsilon_{sgs}\rangle \sim 100\langle\varepsilon_{res}\rangle$ (respectively 100) at late time. Case $M_I = 1.3$ (left) and 2.0 (right). 119

5.20 Shell-averaged Mach number $\langle M\rangle$ (red solid line) and turbulent Mach number M_t (blue small-dashed line) vs. r, after the incident shock interaction (top), right after the first reshock (middle), and at late time (bottom). Note the order of magnitude difference in the scale of the plots. Case $M_I = 1.3$ (left) and 2.0 (right). 120

5.21 Shell-averaged radial velocity component $\langle u_r\rangle$ (red solid line), azimuthal velocity component $\langle u_\theta\rangle$ (blue small-dashed line) and axial velocity component $\langle u_z\rangle$ vs. r, after the incident shock interaction (top), right after the first reshock (middle), and at late time (bottom). Note the order of magnitude difference in the scale of the plots. Case $M_I = 1.3$ (left) and 2.0 (right). 121

5.22 Volume-averaged total turbulent kinetic energy TKE_{vol} as a function of time. Case $M_I = 1.3$ (left) and 2.0 (right). 122

5.23 Shell-averaged integral length scale ℓ computed in the center of the mixing zone $r = r_c$ as a function of time, during the decay of turbulent kinetic energy. Case $M_I = 1.3$ (left) and 2.0 (right). 122

5.24 Shell-averaged turbulent Reynolds number Re_ℓ computed in the center of the mixing zone $r = r_c$ as a function of time, during the decay of turbulent kinetic energy. Case $M_I = 1.3$ (left) and 2.0 (right). 122

5.25 k_z-power spectra of velocity $E_{u_r}(k_z)$ computed in the center shell of the mixing zone at four different times: For $M_I = 1.3$ (left), $(a_0/R_0)t = 2.69$ (dashed-dot line), $(a_0/R_0)t = 5.52$ (long dashed-line), $(a_0/R_0)t = 6.44$ (small-dashed line), and $(a_0/R_0)t = 8.16$ (solid line). For $M_I = 2.0$ (right), $(a_0/R_0)t = 1.21$ (dashed-dot line), $(a_0/R_0)t = 2.43$ (long-dashed line), $(a_0/R_0)t = 3.09$ (small-dashed line), and $(a_0/R_0)t = 5.07$ (solid line). All computed wavenumbers shown and $k_{max} = 256$. 124

5.26 k_z-power spectra of velocity components $E_{u_r}(k_z)$ (solid line), $E_{u_\theta}(k_z)$ (small-dashed line), and $E_{u_z}(k_z)$ (long-dashed line) computed in the center shell of the mixing zone at late time $(a_0/R_0)t = 8.16$ for $M_I = 1.3$ (left) and $(a_0/R_0)t = 5.07$ for $M_I = 2.0$ (right). All computed wavenumbers shown and $k_{max} = 256$. 125

5.27 k_z-power spectra of density $E_\rho(k_z)$ (solid line) and $E_\psi(k_z)$ (dashed line) computed in the center shell of the mixing zone at late time $(a_0/R_0)t = 8.16$ for $M_I = 1.3$ (left) and $(a_0/R_0)t = 5.07$ for $M_I = 2.0$ (right). All computed wavenumbers shown and $k_{max} = 256$. 125

5.28 Measure of anisotropy displayed on the k_z-power spectra $E_{u_r}(k_z)/(E_{u_r}(k_z)+E_{u_\theta}(k_z)+E_{u_z}(k_z))-1/3$ computed in the center shell of the mixing zone at late time $(a_0/R_0)t = 8.16$ for $M_I = 1.3$ (left) and $(a_0/R_0)t = 5.07$ for $M_I = 2.0$ (right). All computed wavenumbers shown and $k_{max} = 256$. 126

5.29 Shell-averaged Kolmogorov microscales η (red solid line), η_r (blue small-dashed line), and $\eta_{\theta z}$ (pink dotted line) computed in the center of the mixing $r = r_c$ zone as a function of time. Case $M_I = 1.3$ (left) and 2.0 (right). 127

5.30 Shell-averaged Taylor microscales λ_T (red solid line), λ_r (blue small-dashed line), and $\lambda_{\theta z}$ (pink dotted line) computed in the center of the mixing zone $r = r_c$ as a function of time. Note the order of magnitude difference in the scale of the plots. Case $M_I = 1.3$ (left) and 2.0 (right). 129

5.31 Shell-averaged Taylor Reynolds numbers Re_{λ_T} (red solid line), Re_{λ_r} (blue small-dashed line), and $Re_{\lambda_{\theta z}}$ (pink dotted line) computed in the center of the mixing zone $r = r_c$ as a function of time. Note the order of magnitude difference in the scale of the plots. Case $M_I = 1.3$ (left) and 2.0 (right). 130

5.32 Shell-averaged scalar Taylor microscales λ_{Y_r} (blue small-dashed line) and $\lambda_{Y_{\theta z}}$ (pink dotted line) computed in the center of the mixing zone $r = r_c$ as a function of time. Case $M_I = 1.3$ (left) and 2.0 (right). 131

5.33 Evolution of the entrainment length P_m (red solid line) and the mixing length P_t (blue small-dashed line). Case $M_I = 1.3$ (left) and 2.0 (right). 132

5.34 Evolution of the mixing parameter Ξ. Case $M_I = 1.3$ (left) and 2.0 (right). 132

5.35 Probability density function $\tilde{\mathrm{P}}(\psi)$ of the mixture fraction at different times calculated from the resolved scales, across three shells of the mixing zone: $r_b \equiv r_c - \delta/4$ (small-dashed line), r_c (solid line), and $r_s \equiv r_c + \delta/4$ (dashed line), at late time $(a_0/R_0)t = 8.16$ for $M_I = 1.3$ (left) and $(a_0/R_0)t = 5.07$ for $M_I = 2.0$ (right). 134

List of Tables

2.1 Various shock-contact interactions for different species and varying incident Mach number, with $kh_0 = 0.1$. For each gas combination and incident Mach number M_I, the shock strength S, post-shock Atwood ratio A^+, dimensionless characteristic startup time $a_0 k\tau$, and dimensionless Richtmyer's asymptotic growth rate $kh(0^+)A^+\Delta W/a_0$ (see Equation (2.20)) are evaluated by solving the one-dimensional shock-interface interaction problem. $\mathfrak{F}_{Yang}$ is given by Yang's linearized simulations [120] and represents the exact asymptotic growth rate for the RMI in the linear regime. The models for $\mathfrak{F}_{Rich.Circ.}$ (given by Equation (2.23a)) and $\mathfrak{F}_{Samt.Circ.}$ (given by Equation (2.24a)) must be compared to the reference value $\mathfrak{F}_{Yang}$. 22

2.2 Conditions, in the (A, S) space, for the reflected wave to be a shock wave. 25

3.1 3-parameter least-square fit for imploding and exploding shocks. 46

5.1 Gas properties of air and SF_6 at 25°C and 1 atm. 87

5.2 Parameters used in the lower-resolution air→ SF_6 three-dimensional simulations of shock-driven mixing in a converging cylindrical geometry. MKS units. Note that $0.785 \simeq \pi/4$. 102

5.3 Parameters used in the higher-resolution air→ SF_6 three-dimensional simulations of shock-driven mixing in a converging cylindrical geometry. MKS units. Note that $1.000 \simeq 7\pi/22$. 103

5.4 Parameters used in the currently running higher-resolution SF_6 →air three-dimensional simulations of shock-driven mixing in a converging cylindrical geometry. MKS units. Note that $1.000 \simeq 7\pi/22$. 104

5.5 Basic characteristic quantities for dimensionless data representation. The index 0 denotes the fluid standing initially on the side where the incident shock comes from. . . 106

5.6 Key approximate dimensionless times $(a_0/R_0)t$, growth rates $(1/a_0)d\delta/dt$, interface velocity differences $\Delta W/a_0$ created by the shock acceleration, post-shock perturbation amplitudes $h(0^+)/R_0$ and Atwood ratios A^+, characterizing the important stages of a cylindrical air→SF_6 interface accelerated by a cylindrical converging shock of incident Mach number $M_I = 1.3$ and 2.0. Comparisons with Vetter and Sturtevant's plane experiments at $M_I = 1.24$ and $M_I = 1.98$ [109, 43]. In these experiments, the sound speed is $a_0 \simeq 339$ m.s^{-1} for the case $M_I = 1.24$ and $a_0 \simeq 347$ m.s^{-1} for $M_I = 1.98$. . . 110

List of Symbols

Greek Characters

α	TCD stencil parameter, page 95
$\alpha(\gamma)$	Guderley's exponent for a converging shock traveling in a gas of specific heat ratio γ, page 43
$\alpha_2(\gamma_2)$	Guderley's exponent for a converging shock traveling in in region $j = 2$ (between the accelerated interface and the transmitted shock), page 40
α^E	Guderley's exponent for the exploding shock after apex refection of an imploding shock, page 45
α_{Lax}	threshold for Lax entropy conditions, page 98
α_{Map}	threshold for geometric-mapping condition, page 98
β_r	factor of radial extent of the computational domain in Chapter 5, page 86
β_z	factor of axial extent of the computational domain in Chapter 5, page 86
Δ_c	LES cutoff length scale or convolution kernel spatial width, page 90
$\delta^C(t)$	intrinsic thickness of the contact between the two fluids at time t, page 19
δ_0^C	initial intrinsic thickness of the contact between the two fluids, page 19
$\dot{\delta}(t)$	growth rate of the mixing layer, page 109
δ_{ij}	Kronecker delta function, page 60
$\delta(t)$	width of the mixing layer, page 106
Δ	spherical surface radius in the structure function averaging, page 92
$\delta\tilde{u}_i^{\pm}(\boldsymbol{e}_j, \boldsymbol{x}_o)$	local resolved-scale velocity component difference in the unitary direction $\boldsymbol{e}_j$ at the location $\boldsymbol{x}_o$, page 93

ΔW	speed of the accelerated interface in the frame of the laboratory, page 7
ΔW	jump in radial velocity of the interface accelerated at $t = 0$ in the frame of the laboratory, corresponding to $-\dot{R}(0^+)$, page 34
Δx	finest grid size, page 45
$\delta_D(t)$	Dirac delta function of time t, page 11
$(\Delta_x, \Delta_y, \Delta_z)$	finest grid resolution, page 102
ε_0	characteristic dissipation defined ahead of the incident shock, page 106
ε	local cell-averaged dissipation, page 92
ε_j	small parameter for linearizing the perturbed flow on each side of the accelerated interface $j = 1, 2$ in Chapter 2, page 11
$\langle\varepsilon_{res}\rangle(r,t)$	shell-averaged resolved-scale dissipation, page 112
$(\langle\varepsilon_r\rangle, \langle\varepsilon_\theta\rangle, \langle\varepsilon_z\rangle)(r,t)$	total dissipation rates in the r-, θ-, and z-direction, page 126
$\langle\varepsilon_{sgs}\rangle(r,t)$	shell-averaged subgrid energy transfer, page 112
$\langle\varepsilon\rangle(r,t)$	shell-averaged total dissipation, page 113
$\eta(s,\gamma)$	Chisnell's constant, page 44
$\eta(t)$	instantaneous isotropic Kolmogorov microscale evaluated at the center of the mixing layer, page 125
$(\eta_r, \eta_\theta, \eta_z)(t)$	instantaneous Kolmogorov microscales in the r-, θ-, and z-direction evaluated at the center of the mixing layer, page 126
$\eta_{\theta z}(t)$	instantaneous in-shell Kolmogorov microscale evaluated at the center of the mixing layer, page 127
γ	specific heat ratio for a pure fluid, page 43
$\Gamma_1'(A, S, \gamma_R, \gamma_L)$	circulation deposited by the passage of a shock on a planar interface, see [99], page 18
γ_j	ratio of specific heats on each side of the interface $j = 1, 2$ or L, R, page 20
$\gamma(\boldsymbol{x}, t)$	specific heat ratio of the mixture, page 60
κ	dimensionless axial wavenumber, page 35

$\overline{\kappa}(\boldsymbol{x},t)$ Temperature-dependent filtered heat conduction of the mixture, page 90

$(\lambda_r,\lambda_\theta,\lambda_z)(t)$ instantaneous Taylor microscales in the r-, θ-, and z-direction evaluated at the center of the mixing layer, page 128

$(\lambda_{Y_r},\lambda_{Y_\theta},\lambda_{Y_z})(t)$ instantaneous Taylor-like microscales related to variances in the scalar field in the r-, θ-, and z-direction evaluated at the center of the mixing layer, page 129

$\lambda_T(t)$ instantaneous isotropic Taylor microscale evaluated at the center of the mixing layer, page 127

$\lambda_\theta(t)$ azimuthal wavelength at time t when the interface base position is $r = R(t)$, page 37

λ_{θ_0} azimuthal wavelength at time $t = 0$ when the interface base position is $r = R_0$, page 89

$\lambda_{\theta z}(t)$ instantaneous in-shell Taylor microscale evaluated at the center of the mixing layer, page 128

$\lambda_{Y_{\theta z}}(t)$ instantaneous in-shell Taylor-like scalar microscale evaluated at the center of the mixing layer, page 129

λ_z axial wavelength, page 37

$\mu(t)$ strength of sink/source potential at time t, page 33

μ_0 base dynamic viscosity ahead of the incident shock, page 106

$\overline{\mu}(\boldsymbol{x},t)$ Temperature-dependent filtered viscosity of the mixture, page 91

$\nu(\boldsymbol{x},t)$ kinematic viscosity, page 115

$\boldsymbol{\omega}(\boldsymbol{x},t)$ vorticity field, page 1

$\phi(\boldsymbol{x},t)$ potential field on each side of the accelerated interface $j = 1, 2$ in Chapter 2, page 13

$\phi'_j(r,\theta,z,t)$ perturbed potential in region j for three-dimensional cylindrical perturbations in Chapter 3, page 33

$\varphi(\vartheta)$ mapping function for the WENO-TCD switching, page 98

$\psi(\boldsymbol{x},t)$ mixture fraction field (mass fraction) materializing the interface, asymptotic to 0 on the side where the incident shock comes from and to 1 on the other side, page 19

ψ_m fraction of mixed fluid, page 130

ψ_s mixture fraction for a stoichiometric mixture, page 131

$\rho(\boldsymbol{x}, t)$ density field, page 1

ρ_0 base density ahead of the incident shock, page 20

$\varrho_j(\boldsymbol{x}, t)$ density field on each side of the accelerated interface $j = 1, 2$ in Chapter 2, page 11

ρ_j post-shock base densities on each side of the accelerated interface $j = 1, 2$ in Chapter 2, page 11

ρ_S density just behind the converging shock, page 44

$\sigma_{ij}(\boldsymbol{x}, t)$ total (resolved plus subgrid) stress tensor, page 113

$\tau_{ij}(\boldsymbol{x}, t)$ subgrid stress tensor, page 90

θ azimuthal angle in cylindrical coordinates, page 33

$(\theta_{min}, \theta_{max})$ azimuthal window in which the shell statistics are performed, page 105

ϑ_i normalized pressure gradient at the cell face i, page 98

$\xi(r, t)$ similarity variable, page 43

$\Xi(t)$ mixing parameter, page 131

$\zeta(\theta, z, t)$ position of the cylindrically perturbed interface assuming single modes in (θ, z) in Chapter 3, page 33

$\zeta(x, t)$ position of the perturbed plane interface assuming normal mode in x in Chapter 2, page 10

Roman Characters

A constant related to the structure function matching, page 92

a_0 base sound speed ahead of the incident shock, page 20

$A_c(n, kR(t))$ critical Atwood ratio corresponding to stable perturbations, page 38

$a(\boldsymbol{x}, t)$ sound speed field, depending on (r, t) for the radially symmetric one-dimensional problem and on (x, t) for the plane one, page 62

a_j	post-shock base sound speed on each side of the accelerated interface $j = 1, 2$ in Chapter 2, page 11
$\mathcal{A}_r$	surface area of the two-dimensional cylindrical shell of radius r, page 105
A	Atwood ratio, > 0 (respectively < 0) for light-to-heavy (respectively heavy-to-light) interaction, see Subsection 2.5.1 for exact denomination, page 7
A_{rs}^{+}	post-reshock Atwood ratio, page 110
A^{+}	post-shock Atwood ratio based on post-shock densities, page 11
$A_{*}^{+}(A, \gamma_R, \gamma_L)$	post-shock Atwood ratio strong shock limit $S \to 1^{-}$, page 25
$\tilde{a}$	axial strain along the subgrid vortex axis, page 92
$\mathcal{C}_i$	cells i satisfying Alg. 1, page 99
$\mathcal{C}_i^m$	set of cells in the neighborhood of cell i satisfying Alg. 1, page 99
$\overline{\mathcal{C}_i^m}$	complement of $\mathcal{C}_i^m$, page 99
$c_{p,\mathrm{air}}$	heat capacity at constant pressure of air, assumed temperature-independent and evaluated at 25°C and 1 atm, page 91
$\widetilde{c}_p(\boldsymbol{x}, t)$	Favre-filtered heat capacity at constant pressure of the mixture, assumed temperature-independent, page 91
$c_{p,\mathrm{SF_6}}$	heat capacity at constant pressure of SF_6, assumed temperature-independent and evaluated at 25°C and 1 atm, page 91
$\mathfrak{Cr}$	compression ratio defined as the ratio of the final position of the (unperturbed) interface to its initial position and representing the degree of compression of the inner fluid, page 65
$\mathrm{D}(s, \gamma)$	Chisnell's constant, page 44
ΔW_{rs}	post-reshock interface velocity difference, page 110
$\widetilde{D}(\boldsymbol{x}, t)$	Temperature-dependent Favre-filtered diffusivity of the mixture, page 90
$\overline{d}_{ij}(\boldsymbol{x}, t)$	Favre-filtered deviatoric Newtonian stress tensor, page 90
e_i^v	direction cosines of the subgrid vortex axis, page 92
$\boldsymbol{e}_j$	unitary direction, page 93
$e(\boldsymbol{x}, t)$	internal energy per unit mass, page 60

$E(\boldsymbol{x},t)$ total energy, page 60

$E(k)$ energy spectrum of the subgrid motion, page 92

$E_f(k_z)(r,t)$ instantaneous θ-averaged power spectrum in the z-direction evaluated at the shell of radius r, page 123

$\mathcal{F}_2(\boldsymbol{r})$ second-order velocity structure function, page 92

$\overline{\mathcal{F}_2}(r)$ second-order velocity structure function spherical average, page 92

$\mathfrak{F}_{Rich.Circ.}$ ratio of the asymptotic growth rate derived using a model based on Richtmyer's circulation, to Richtmyer's asymptotic growth rate [94], page 18

$\mathfrak{F}_{Samt.Circ.}$ ratio of the asymptotic growth rate derived using Samtaney's circulation [99] to Richtmyer's asymptotic growth rate [94], page 18

$\mathfrak{F}_{Yang}$ ratio of the asymptotic growth rate given by Yang's simulations [120] to Richtmyer's asymptotic growth rate [94], page 18

$\mathrm{F}(s,\gamma)$ Chisnell's constant, page 44

$f_j(r), g_j(t)$ functions defining the perturbed potential $\phi'_j(r,\theta,z,t)$ assuming separation of variables in r and t and single modes in (θ,z) in Chapter 3, page 33

$F_{i+1/2}$ flux corresponding to the derivative of a function at the cell wall $i+1/2$ (cell center i), page 97

$\boldsymbol{F}(\boldsymbol{x},t)$ directional flux vector, page 60

$\boldsymbol{F}_r(r,t)$ directional flux vector for the radially symmetric one-dimensional problem, page 61

$\boldsymbol{F}_x(x,t)$ directional flux vector for the plane one-dimensional problem, page 60

$F^{skew}_{i+1/2}$ flux corresponding to the derivative of a product of functions in a skew-symmetric form at the cell wall $i+1/2$ (cell center i), page 97

$F(n,\kappa,A)$ function taking place in the modeled asymptotic growth rate describing the dependency on axial and azimuthal wavenumbers, page 36

$f(\theta,z)$ symmetry-breaking perturbation component, page 89

$g(t)$ impulsive acceleration due to the initial shock interaction, page 11

$G_{\Delta_c}(\boldsymbol{x})$ convolution kernel with spatial width Δ_c, page 90

$h(t)$	perturbation amplitude, page 10
h_0	pre-shock perturbation amplitude, page 7
$h(0^+)$	post-shock perturbation amplitude, page 15
$h(0^+)_{rs}$	post-reshock mixing-layer width, page 110
h_1	initial amplitude of the small symmetry-breaking perturbation component $f(\theta, z)$ in Chapter 5, page 89
$h_B(t)$	bubble amplitude, page 42
$\mathrm{H}(s, \gamma)$	Chisnell's constant, page 44
$\dot{h}(t)$	perturbation growth rate, page 15
$\dot{h}_B(t)$	bubble growth rate, page 42
$\dot{h}_\infty$	asymptotic growth rate, page 15
$\dot{h}_{Rich.}$	asymptotic growth rate modeled by Richtmyer [94], page 17
$\dot{h}_S(t)$	spike growth rate, page 42
$H(t)$	Heaviside function of t, page 15
$H(z)$	Heaviside function of z, page 13
$H(\boldsymbol{x}, t)$	enthalpy field, page 98
$h_{S_j}(t)$	transmitted (respectively reflected) shock perturbation amplitude for $j = 1$ (respectively $j = 2$) in Chapter 2, page 14
$h_S(t)$	spike amplitude, page 42
$\imath$	imaginary unit, $\imath^2 = -1$, page 10
$I_m(x)$	modified Bessel function of the first kind of the variable x and integer order m, page 35
K	formal perturbation wavenumber, such that $K \equiv n/R_0$ for purely azimuthal modes and $K \equiv k$ for purely axial modes, page 39
k	perturbation wavenumber in the x-direction for plane perturbation in Chapter 2, page 10
K_0	Kolmogorov pre-factor, page 92

K_0	wavenumber parameter of the symmetry-breaking perturbation spectrum, page 89
k	axial wavenumber for three-dimensional cylindrical perturbations, page 33
$K_m(x)$	modified Bessel function of the second kind of the variable x and integer order m, page 35
k	wavenumber varying from π/Δ_c to ∞ in Equation (5.12), page 92
K	wavenumber of the symmetry-breaking perturbation spectrum, page 89
$\tilde{k}$	subgrid kinetic energy, page 92
k_z	axial wavenumber referring to one-dimensional power spectra taken in the z-direction, page 123
$\ell(r,t)$	integral length scale, page 115
(L_x, L_y, L_z)	dimensions of the computational domain, page 102
$M(\boldsymbol{x},t)$	local Mach number, page 115
$M_{R_*}(A,\gamma_R,\gamma_L)$	reflected shock Mach number strong shock limit $S \to 1^-$, page 25
$M_T(A,S,\gamma_R,\gamma_L)$	transmitted shock Mach number, page 26
$M_{T_{**}}(S,\gamma_R,\gamma_L)$	transmitted shock Mach number in the limit $A \to 1^-$, page 26
$M_t(r,t)$	turbulent Mach number, page 114
m_{air}	molecular weight of air, page 91
M_I	incident shock Mach number as the incident shock impacts the interface, page 11
$m(\boldsymbol{x},t)$	molecular weight of the mixture, page 60
M_S	incident converging shock Mach number at $t = 0$ in Subsection 3.3.3, also noted M_I, page 43
m_{SF_6}	molecular weight of SF_6, page 91
n	azimuthal wavenumber for three-dimensional cylindrical perturbations, page 33
$\boldsymbol{n}$	local normal to the interface, page 34
(N_x, N_y, N_z)	base resolution, page 102

p_0	base pressure ahead of the incident shock, page 20
$p_{0''}$	base pressure behind the incident shock, page 20
$\mathrm{P}(\rho, \psi; \boldsymbol{x}, t)$	instantaneous two-dimensional p.d.f. of density and mixture fraction interpolated over a shell of given radius, page 133
$\tilde{\mathrm{P}}(\psi; \boldsymbol{x}, t)$	instantaneous Reynolds joint density-mixture fraction p.d.f. over a shell of given radius, page 133
$\Phi(r, t)$	potential model of the base flow describing a cylindrical implosion/explosion in Chapter 3, page 33
$p_j(\boldsymbol{x}, t)$	pressure field on each side of the accelerated interface $j = 1, 2$ in Chapter 2, page 11
$P_m(t)$	maximum chemical product thickness (or entrainment length), page 131
$p(\boldsymbol{x}, t)$	pressure field, page 1
p_S	pressure just behind the converging shock, page 44
$P_t(t)$	total chemical product thickness (or mixing length), page 131
$\mathrm{q}(s, \gamma)$	Chisnell's constant, page 44
$q_j^{\psi}(\boldsymbol{x}, t)$	subgrid scalar transport flux, page 90
$q_j^{T}(\boldsymbol{x}, t)$	subgrid heat transport flux, page 90
$\boldsymbol{q}(\boldsymbol{x}, t)$	vector of state, page 59
r	radial distance to the z-axis in cylindrical coordinates, page 33
r	radial distance to the axis/origin for the cylindrically/spherically symmetric flow in Chapter 4, page 60
R_0	initial position of the unperturbed interface (before shock interaction), page 7
$r_c(t)$	center of the mixing layer in Chapter 5, page 109
$r_c(\theta, t)$	centerline position of the density interface for the purely azimuthal RMI in Chapter 3, page 42
$r_{c_{bubble}}(t)$	position of the bubbles for the purely azimuthal RMI in Chapter 3, page 42
$r_{c_{spike}}(t)$	position of the spikes for the purely azimuthal RMI in Chapter 3, page 42

$\ddot{R}(0^+)$	post-shock acceleration of the interface in curved geometries, page 40
$(Re_{\lambda_r}, Re_{\lambda_\theta}, Re_{\lambda_z})(t)$	instantaneous Taylor Reynolds numbers in the r-, θ-, and z-direction evaluated at the center of the mixing layer, page 128
$Re_{\lambda_T}(t)$	instantaneous isotropic Taylor Reynolds number evaluated at the center of the mixing layer, page 128
$Re_{\lambda_{\theta z}}(t)$	instantaneous in-shell Taylor Reynolds number evaluated at the center of the mixing layer, page 128
$Re_\ell(r,t)$	turbulent Reynolds number, page 115
R	ideal gas constant, page 60
$r_m(\boldsymbol{x},t)$	specific gas constant of the mixture, page 98
$r_I(\theta,z)$	centerline position of the perturbed interface at (θ,z) in Chapter 5, page 88
r_{in}	inner cylindrical or spherical reflective boundary, page 62
r_{out}	outer cylindrical radius, page 106
$R_S(t)$	incident converging shock position at time t, page 43
R_{S_0}	incident converging shock position at time $t=0$, page 43
$r_{s,p}(t)$	spike, bubble radial position, page 133
R_S^E	exploding shock position at time $t=2t_S$ after apex refection of an imploding shock at $t=t_S$, page 45
$R(t)$	position of the accelerated unperturbed interface at time t, page 7
$S_1(t)$	position of the transmitted shock in the frame of the accelerated interface, page 10
$S_2(t)$	position of the reflected shock in the frame of the accelerated interface, page 10
S	incident shock strength, page 20
$S^\star(A)$	critical incident shock strength beyond which the reflected wave type changes, page 24
$\tilde{S}_{ij}$	locally resolved rate-of-strain tensor, page 92
$\boldsymbol{S}(\boldsymbol{x},t)$	geometric source vector, page 61

s	space index, $s = 2$ for cylindrically symmetric flows and 3 for spherically symmetric flows, page 40
τ	characteristic time of the early linear growth, page 16
$T(\boldsymbol{x}, t)$	temperature field, page 60
t	time, page 7
$\langle K \rangle(r, t)$	shell-averaged resolved-scale TKE, page 112
$\langle k \rangle(r, t)$	shell-averaged subgrid-scale TKE, page 112
$TKE_{vol}(t)$	volume-averaged total TKE, page 115
t_S	implosion time in Subsection 3.3.3, also noted t_I, page 43
$\boldsymbol{U}(r, t)$	velocity field derived from the potential model of the base flow describing cylindrical implosion/explosion in Chapter 3, page 33
$\boldsymbol{u}_j(\boldsymbol{x}, t)$	velocity field on each side of the accelerated interface $j = 1, 2$ in Chapter 2, page 11
$u'(r, t)$	turbulent intensity, page 114
u_S	radial velocity just behind the converging shock, page 44
U_{S_1}	transmitted shock velocity in the frame of the accelerated interface, page 10
U_{S_2}	reflected shock velocity in the frame of the accelerated interface, page 10
$\boldsymbol{u}(\boldsymbol{x}, t)$	velocity field, page 1
u	velocity field $u_x(x, t)$ (respectively $u_r(r, t)$) for the plane (respectively radially symmetric) one-dimensional problem, page 62
$u_r(r, t)$	velocity field for cylindrically symmetric flow in Chapter 3, page 44
$u_r(r, t)$	velocity field for the radially symmetric one-dimensional problem, page 61
$u_x(x, t)$	velocity field for the plane one-dimensional problem, page 60
$V_0(\gamma)$	Chisnell's coefficient, see Equation (3.10) of [15], page 45
$V_{0_2}(\gamma_2)$	Chisnell's coefficient in region $j = 2$ (between the accelerated interface and the transmitted shock), see Equation (3.10) of [15], page 40
$\mathrm{V}(\xi)$	Chisnell's function, page 44

$\langle u_r \rangle_{s,b}(r,t)$	spike, bubble shell-averaged radial velocity, page 111
$V(t)$	volume of the mixing zone, page 111
$\mathrm{V}_S(s,\gamma)$	Chisnell's constant, page 44
x	direction transverse to the base flow in Chapter 2, page 10
x	distance to the wall for the plane flow in Chapter 4, page 60
$\boldsymbol{x}_o$	cell location, page 93
$\boldsymbol{x}$	point in space $\boldsymbol{x} = (x_1, ..., x_d)^{\mathrm{T}} \in \mathbb{R}^d$, page 11
$Y(\boldsymbol{x},t)$	scalar function, page 111
z	direction of propagation of the base flow in Chapter 2, page 10
z	height coordinate in cylindrical coordinates, page 33
$z_c(x,t)$	centerline position of the density interface for the plane RMI in Chapter 2, page 20
$z_{c_{bubble}}(t)$	position of the bubbles for the plane RMI in Chapter 2, page 20
$z_{c_{spike}}(t)$	position of the spikes for the plane RMI in Chapter 2, page 20

Operators

$\langle Q \rangle(r,t)$	instantaneous average of a quantity $Q(\boldsymbol{x},t)$ over a cylindrical shell of radius r, page 105
$\overline{f}$	dimensionless variable in Section 2.2, page 11
$\overline{f}(\boldsymbol{x},t)$	LES filtering operation in Section 5.2, page 90
$f * g(\boldsymbol{x})$	spatial convolution of the functions f and g of the variable $\boldsymbol{x}$, page 90
$\boldsymbol{a} \times \boldsymbol{b}$	cross of a vector $\boldsymbol{a}$ with a vector $\boldsymbol{b}$, page 1
$\nabla \times \boldsymbol{a}(\boldsymbol{x})$	curl of a vector field $\boldsymbol{a}$, page 1
$\mathcal{D}_x f$	one-dimensional discrete derivative operator of the function f in the x-direction, page 95
$\dot{f}(t)$	time derivative of the function f of the only variable t, page 14
$\widehat{F}(r,\theta,k_z,t)$	Fourier transform in the z-direction of the function f of the variables (r,θ,z,t), page 123

$Df/Dt(\boldsymbol{x},t)$	material derivative of the function f of the variables $(\boldsymbol{x},t)$, page 34
$\nabla f(\boldsymbol{x})$	gradient of a function f of the variable $\boldsymbol{x}$, page 1
$\nabla \cdot \boldsymbol{a}(\boldsymbol{x})$	divergence of a vector field $\boldsymbol{a}$ of the variable $\boldsymbol{x}$, page 1
$f'(x)$	derivative of the function f with respect to its variable x, page 34
$Q''(r,\theta,z,t)$	instantaneous departure from the Favre-like, shell-average $\widetilde{Q}(r,t)$, page 105
$Q'(r,\theta,z,t)$	instantaneous departure from the shell-average $\langle Q\rangle(r,t)$, page 105
$\widetilde{f}$	dimensionless variable in Section 3.2, page 35
$\widetilde{Q}(r,t)$	instantaneous Favre-like, shell-average of a quantity $Q(\boldsymbol{x},t)$ over a cylindrical shell of radius r, page 105
$\widetilde{f}(\boldsymbol{x},t)$	LES Favre-filtering operation in Section 5.2, page 90
$\mathrm{Var}(Q)(r,t)$	instantaneous shell-variance of $Q(\boldsymbol{x},t)$, page 105
$\mathrm{Var}_\rho(Q)(r,t)$	instantaneous Favre-like, shell-variance of $Q(\boldsymbol{x},t)$, page 105

Subscripts

0	index denoting the un-shocked region from where the incident shock is coming, page 12
i	cell index in Subsections 5.3.2.1, 5.3.2.3, and 5.3.2.4, page 95
i,j,k	index for vector or tensor Euclidian coordinates in Chapters 4 and 5, page 59
j	post-shock region index in Chapter 2, $j=1$ on the transmitted-shock side and $j=2$ on the reflected-shock side, page 10
j	region index, $j=1$ corresponds to the side of the interface where the incident shock comes from and $j=2$ to the other side, page 33
L	index for the region to the left of the interface in Chapter 2, page 22
L	index for the left state of the Riemann problem in Paragraph 5.3.2.4, page 98
R	index for the region to the right of the interface in Chapter 2, page 20
R	index for the right state of the Riemann problem in Paragraph 5.3.2.4, page 98
$\star$	index for the Roe-averaged solution of the Riemann problem in Paragraph 5.3.2.4, page 98

Superscripts

(0)	zeroth-order flow solution or base flow solution in Chapter 2, page 12
(1)	first-order flow solution or perturbed flow solution in Chapter 2, page 12
m	index denoting the neighboring cells, page 99
T	transpose, page 11
WENO,TCD	WENO or TCD flux index, page 99

Acronyms and Chemical Element Symbols

AMROC	Adaptive Mesh Refinement in Object-oriented C++, page 3
SAMR	Structured Adaptive Mesh Refinement, page 19
Ar	Argon, page 18
CACR	Center for Advanced Computing Research, page 101
CCW	Chester-Chisnell-Whitham, page 58
CO_2	Carbon dioxyde, page 18
CPU	Central Processing Unit, page 102
DNS	Direct Numerical Simulation, page 6
D-T	Deuterium-Tritium, page 2
GFM	Ghost Fluid Method, page 94
HDF	Hierarchical Data Format, page 147
He	Helium, page 18
ICF	Inertial Confinement Fusion, page 2
Kr	Kripton, page 58
LES	Large-Eddy Simulation, page 3
LLNL	Lawrence Livermore National Laboratory, page 41
ODE	Ordinary Differential Equation, page 16
p.d.f.	probability density function, page 106

RANS	Reynolds-Averaged Navier-Stokes, page 91
RK	Runge-Kutta, page 101
RMI	Richtmyer-Meshkov Instability, page 1
RM	Richtmyer-Meshkov, page 57
RTI	Rayleigh-Taylor Instability, page 1
RT	Rayleigh-Taylor, page 82
SF_6	Sulfur hexafluoride, page 11
SGS	SubGrid-Scale, page 92
SHC	Shared Heterogeneous Cluster, page 101
SSP	Strong-Stability Preserving, page 101
SN	SuperNova, page 3
TCD	Tuned Center-Difference, page 19
TKE	Turbulent Kinetic Energy, page 94
TMZ	Turbulent Mixing Zone, page 57
uP	unclassified Purple, page 41
VTF	Virtual Test Facility, page 3
WENO	Weighted Essentially Non-Oscillatory, page 19
Xe	Xenon, page 18

Chapter 1

Introduction

The interactions of shock waves with perturbed interfaces separating fluids of different properties are of crucial importance in compressible turbulence, as they occur in a myriad of applications, both natural and man-made. This class of problems is generally referred to as the Richtmyer-Meshkov instability (RMI), after Richtmyer, who first rigorously analyzed the growth rate of a perturbation at a plane density inhomogeneity following an impulsive acceleration modeling the passage of a shock parallel to the interface [94], and Meshkov, who confirmed, at least qualitatively, Richtmyer's predictions using shock-tube experiments [77]. In [94] Richtmyer also compared his analytical results with numerical simulations of the linearized compressible Euler equations. The RMI is sometimes thought of as an impulsive, or shock-induced, version of the Rayleigh-Taylor instability (RTI), where the density interface is submitted to a finite sustained acceleration (e.g., gravitational field) [107, 92].

The dominant fluid dynamics process responsible for the amplification of the interface perturbation is local vorticity generation by means of baroclinic torque, due to the misalignment of the pressure gradient across the shock and the local density gradient at the interface during shock passage. Consider the evolution equation of the vorticity field $\boldsymbol{\omega} = \nabla \times \boldsymbol{u}$, with $\boldsymbol{u}$ velocity field. In the absence of dissipation terms,

$$\left(\frac{\partial}{\partial t} + \boldsymbol{u} \cdot \nabla\right) \boldsymbol{\omega} = \frac{\nabla\rho \times \nabla p}{\rho^2} + (\boldsymbol{\omega} \cdot \nabla)\boldsymbol{u} - \boldsymbol{\omega}\nabla \cdot \boldsymbol{u}, \tag{1.1}$$

where ρ is the density field and p the pressure field. The first term of the right-hand side represents the production of baroclinic vorticity and constitutes the main mechanism for vorticity generation in the RMI. The second term, called vortex stretching, only appears in three-dimensional flows where the vorticity field is a priori not perpendicular to the velocity field. The last term is the vortex compression and is related to compressibility effects. For moderate incident shocks, this term is expected to remain small [43]. However, it might not be the case in converging geometries where the flow can be accelerated to very high velocities. After the shock passage, the distribution of vorticity deposited during the shock refraction drives the evolution of the instability (other effects

are discussed in Chapter 2). Samtaney and Zabusky produced a detailed analysis of the circulation deposition for general incident shock strengths and fluid combinations [99]. As the interface becomes more distorted, the heavy fluid penetrates into the light fluid causing the formation of spikes, while the lighter fluid raises into the heavy fluid causing the formation of bubbles. The instability exhibits characteristic mushroom-like structures (e.g., see Figure 1.1) due to the rolling up of the spikes. Additional baroclinic vorticity is produced during the roll-up in a mechanism called vortex-accelerated-vorticity-deposition [85]. Secondary instabilities such as the shearing Kelvin-Helmholtz instability develop, and vortex pairing can be observed between the structures already generated by the RMI, resulting in a wide range of physical scales and ultimately turbulent mixing between the two fluids. The intensity of the turbulent motions can be further increased when the interface is processed by additional pressure waves, such as reshocks. During a reshock, baroclinic vorticity is deposited with opposite sign to the initially deposited vorticity, transforming spikes into bubbles and vice versa in a process called phase inversion. Note that other types of baroclinic instability, besides the RMI, include the RTI previously cited and shown in figure 1.2, and the Landau-Darrieus instability driven by mass transfer across the interface [60].

The RMI arises in the context of various shock-accelerated flows. In combustion systems, the instability resulting from the interaction of a shock wave with a flame has an important role in the transition from deflagration to detonation [57]. There has also been considerable interest in exploiting shock-induced fuel/oxidizer mixing properties of the instability for supersonic and hypersonic air-breathing combustors (scramjets) [119]. Vapor explosions that result from the intense heat transfer following contact between a hot liquid and a cold, more volatile one, have been widely studied as well, as they can occur in severe accidents when the core of a nuclear reactor is molten [5]. Other inhomogeneous reacting flows can involve converging shocks, e.g., concave detonation-driven flows [45], inertial confinement fusion (ICF), etc. Unlike magnetic fusion designs, which holds fuel in a magnetic field, ICF relies on isentropic compression of fusion fuel. In an ICF capsule implosion, a laser drives a shock that compresses deuterium-tritium (D-T) gas causing ignition and fusion. In such technology, the effect of gravity is negligible but the fluid is accelerated. As a consequence, RTI forms at the D-T interface, inhibits thermonuclear reactions, and limits final compression required to achieve fusion [70, 69]. RMI is also important in ICF because it can produce seeds, which are later amplified by the more violent RTI. The RMI has been used to explain the rapid collapse of gas bubbles in liquids [86, 32]. Other examples of multi-phase flows involving converging shocks, such as sonoluminescence [90, 29] and shock-wave lithotripsy [51], have drawn increasing scientific interest. Aeronautical engineers need accurate prediction of the sonic-boom focusing, called “superboom” [72]. The superboom develops when an aircraft changes its speed, turns, or maneuvers. The ground noise of superboom is magnified up to 2–3 times the original sonic-boom noise, which could propagate to the ground and severely harm human ears, as well as structures. The RMI in curved geometries also

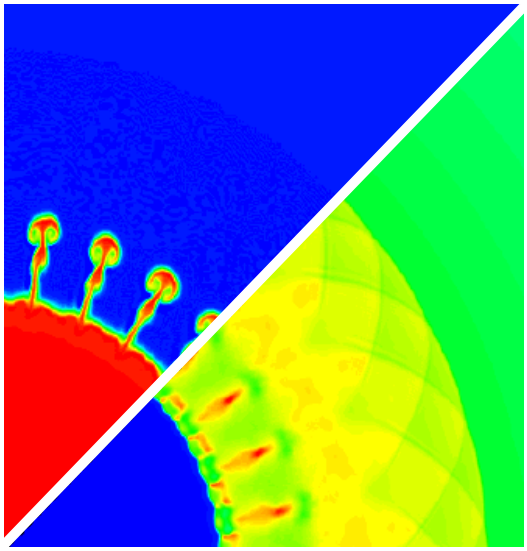

Figure 1.1: Two-dimensional simulations of the converging cylindrical Richtmyer-Meshkov instability in a 90° wedge, using adaptive mesh refinement. A cylindrical converging shock impacts at a Mach number 3.0 a cylindrical density interface separating air (outside) from sulfur hexafluoride (inside). Passive scalar contours (upper diagonal) show the distortion of the interface, while transmitted shock and reflected wave patterns appear on the pressure contours (lower diagonal).

manifests itself in natural phenomena such as supernova (SN) collapse. The RMI has been observed in remnants of the explosion of SN 1987A [1, 33, 73] and is used to explain the overturn of the outer portion of collapsing cores of supernovas and the unexpected mixing in the outer regions of supernovas [103, 105, 56].

These examples have recently raised considerable interest in understanding the physical processes behind this instability, and have motivated reviews by Zabusky [121], Berthoud [5], and Brouillette [10], among others.

1.1 Motivation

This research project was initiated to investigate the RMI in curved geometries, in particular when driven by converging shocks. The objectives were to: (i) model the linear regime of the converging RMI, (ii) set up a canonical large-eddy simulation (LES) of the shock-driven turbulent mixing in a converging geometry, and (iii) identify the differences with the mixing observed in the plane geometry in [109, 43]. The computations were performed within the adaptive mesh refinement framework AMROC [21] as part of the Virtual Test Facility (VTF) [22]. A long-term goal is to compare these large-scale LES against validation experiments of converging shocks in a wedge (VTF phase 2) currently being conducted by the group of Prof. Dimotakis at GALCIT [24].

The most important accomplishment of the present work has been the comparison, in various

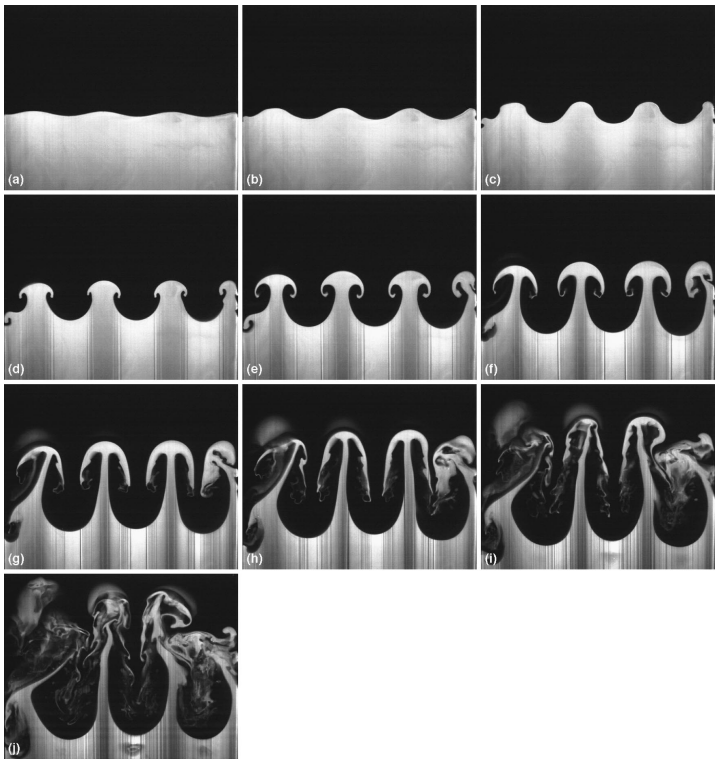

Figure 1.2: Experiments of the Rayleigh-Taylor instability by Waddell et al. [111]. A sequence of planar laser-induced fluorescence images showing the development of an immiscible system with Atwood ratio 0.336 accelerated at 1.34 g: linear regime (a),(b); non-linear regime (c)–(g); chaotic appearance suggesting transition to turbulence (h)–(j).

conditions (e.g., incident shock strength, density ratio), of the plane and converging geometries for (i) the early stages of the RMI, (ii) the reshock events with a visual study of wave diagrams, and (iii) the long-term turbulent mixing following the reshocks with new techniques developed to study statistics of the turbulent flow. Both analytical and numerical approaches have been undertaken. In particular, this project has motivated improvements of the patch solver and new developments of the statistics class within AMROC.

1.2 Previous Related Work

1.2.1 Linear Regime in Plane and Curved Geometries

The linear regime of the RMI has been principally studied in the plane geometry and been focused on modeling the asymptotic growth rate reached by the instability as commonly observed during the small amplitude perturbation growth [94, 31, 118, 108, 116, 117, 39]. There are two reasons for possible discrepancies between experiments and analytical models. First, most of these formulations

work well for weak incident shocks but fail to model the exact asymptotic growth rate when the incident shock is strong, the density ratio across the interface high, or the difference between specific heat ratios important [120]. Complex models (e.g., see [116]) are needed to cover the wide range of initial parameters. Second, early experimental results, obtained in the nonlinear regime because small amplitude could not be measured accurately (e.g., see [77]), could only confirm qualitatively the impulsive model predictions. However, better agreement is achieved in recent low [55] and high [46] Mach-number experiments. Although impulsive models are approximate, they provide insight and simple estimates of the growth rate.

On the other hand, the approach of Wouchuk (e.g., [116]) has the potential to take into account all physical phenomena involved (initial vorticity deposition, bulk vorticity deposition by relaxation of deformed shock fronts, baroclinic generation by reverberation of acoustic waves emitted by the deformed shock front, etc.). Wouchuk's analysis contains the following features: (i) The flow between the perturbed interface and moving deformed reflected and transmitted waves is linearized (wave equations); (ii) a change of coordinate suggested in [7, 75] is used; (iii) the Laplace transform of one of the new coordinates is applied; (iv) after considerable algebra a functional equation is found and approximately solved by iteration in order to determine the quantities F_a and F_b needed in Equation (3) of [116]. The method works well for different gas combinations and various incident shock strengths. Although only three iterations are needed to get good agreement with estimates of the asymptotic growth rate from the reference simulations of Yang for plane linear perturbation growth [120], this approach is best viewed as semi-analytical. For example, no scaling law can be deduced from this analysis.

Less analytical work has been achieved in curved geometries. The contributions basically reduce to Mikaelian's impulsive model for the spherical geometry [80] and for the cylindrical geometry only for azimuthal perturbations [81]. Tests of this incompressible model are limited to comparisons against gelatin-ring computational experiments, and no simulations of highly compressible materials are performed. However, Mikaelian's work considers both RMI and RTI for spherical and two-dimensional cylindrical stratified shells, discusses "freeze-out" phenomenon in plane, cylindrical and spherical geometries, and provides a model of turbulent mix.

1.2.2 Converging Shocks

There are underlying challenges in studying imploding geometries, analytically, numerically, and above all, experimentally. No exact solutions exist for converging shocks. However, Guderley produced asymptotic similarity solutions in the strong-shock limit for converging cylindrical and spherical shocks whose strength increases as a power-law [40]. Whitham's shock dynamics theory provides accurate solutions to the converging shock valid below the strong shock limit [113]. A solution in the form of a series expansion, whose leading order corresponds to Guderley's power-law solution, is

described in [87]. In this problem, the flow admits a general solution where an infinitesimally weak shock from infinity strengthens as it converges towards the origin. The importance of this type of self-similar solutions in the study of shock waves compares to that of the Taylor-Sedov solution for point explosion. Chisnell gave an analytical approximation to the flow behind Guderley's converging shocks in [15]. In the present thesis, we use this solution to generate imploding flows.

The first numerical investigation of these solutions was carried out by Payne, who adapted the so-called Lax scheme to appropriately compute the pressure term in the momentum equations [84] (see [8] for the explosion problem). The converging shock originates due to the sudden rupture of a cylindrical diaphragm, separating two uniform regions of gas at rest with a higher pressure in the outside region. By a suitable choice of initial conditions, Payne obtained a flow with a shock wave, an expansion wave, but no contact discontinuity that could affect the shock and lead to numerical inaccuracy in the flow. As the shock converges and becomes stronger, agreement with Guderley's power-law can be achieved. Other than the difficulty of initializing numerical simulations properly, converging shocks simulations raise other questions, such as the treatment of the flow singularity at the center, or the need of robust methods not only able to capture strong shocks but also to compute correctly the turbulent mixing dissipation in the area of the fluid inhomogeneities [44].

Experimentalists can face difficulties in focusing shock while keeping reasonably stable axisymmetry. Imperfect focusing can, for example, reduce the pressure at the center of the converging shock, and has therefore motivated research on converging shock stability. Experiments of converging shocks usually generate unstable converging polygonal structures (development of triple points) [112] similar to those studied in stability theories of axisymmetric converging shocks [113, 101]. These observations led to investigation of polygonal shock waves (e.g., see [27]), and confirm the importance of creating converging shocks with minimal imperfections in their symmetry. Hosseini and Takayama have succeeded in producing converging cylindrical shock waves with minimum disturbances using an annular coaxial diaphragm-less shock-tube [50]. The shock interacts with a cylindrical soap bubble filled up with various gases and the RMI appears on the bubble front. Dimotakis and Samtaney have theoretically designed a gas lensing technique (referred to as VTF phase 1) that can smoothly focus a planar shock into a segment of a circular cylinder in a two-dimensional wedge geometry [24].

1.2.3 Mixing in Accelerated Inhomogeneous Flows

A number of experiments have been carried out with the objective of capturing convergence effects on the RMI: electron-beam targets [106], cylindrical metal shells [66], laser targets [52, 61], and gelatin rings [78, 79].

As far as we know, there have been no three-dimensional direct numerical simulations (DNS) of turbulence in cylindrical or spherical geometries for RTI and RMI-type flows, the reason being that the Reynolds numbers involved are too high for these accelerating flows, resulting in viscous

dissipation scales impossible to capture with current computers. LES is probably the best approach, but only LES for the RTI [18, 12, 11] and the RMI with reshock [43] in plane geometries have been performed. For the RMI, the difficulty lies on the conception of a numerical method that can capture shocks of various strengths (shock waves cannot be fully resolved since the shock thickness is of the order of the mean free path), as well as the turbulent activity in some regions of the flow. A more detailed discussion on computation of compressible turbulence is provided in Chapter 5.

Two-dimensional simulations of the instability for imploding and exploding cylindrical shocks using front tracking of the interface and a shock-capturing scheme have also been performed by Saltz et al. [97] and most importantly by Zhang et al. [123]. Saltz reports numerical solutions obtained from two different codes, *FronTier*, a front-tracking method using a directionally split second-order Godunov scheme, and RAGE, embedding a similar numerical method into a continuous adaptive mesh refinement framework. Zhang's work completes a scaling analysis for RMI driven by strong shocks (e.g., converging shocks) [122]. It considers various reshock configurations. Indeed, the occurrence of re-acceleration of the material interface caused by the waves reflecting from the origin is unavoidable in curved geometry. In plane geometry, we only need to distinguish between light-to-heavy and heavy-to-light interactions, while in curved geometry, we further need to distinguish exploding and imploding shock interactions. Nevertheless, no study of the resulting long-term turbulent mixing was done. Note that front tracking is in general not adapted to compute the complex turbulent mixing occurring in three dimensions.

Elaborate models for the turbulent mixing zone growth, including, e.g., dissipation effects, are available [91]. We focus on Mikaelian's minimal model [80, 81], where the evolution of the mixing thickness in planar, cylindrical, or spherical geometry, has a non-trivial dependence on convergence, i.e., on $R(t)/R_0$, with R_0 initial position of the unperturbed interface (before shock interaction) and $R(t)$ position of the accelerated unperturbed interface at time t, and is proportional to a constant, c (e.g., see Equations (32–36) in [81] for the cylindrical case). There is no dependence on initial conditions other than a simple additive constant h_0 representing the initial perturbation amplitude. The DNS of the RTI in plane geometry of Cook and Dimotakis [19] suggests that c, also noted c_{plane} in this geometry, may depend on initial perturbation wavelengths and amplitudes. Plane RMI shock-tube experiments [109, 28] and simulations [43] are consistent with $h = c_{\text{plane}}\, A\Delta W t$ with $c_{\text{plane}} \approx 0.10 - 0.14$. In this expression, A is the Atwood ratio and ΔW being the speed of the accelerated interface) . For the curved RMI, more research is needed to compare with Mikaelian's model the results on the mixing obtained in the very few shock-tube experiments in cylindrical [50] and spherical [59] geometries.

1.3 Outline of Present Work

Chapter 2 presents a theoretical model describing the early growth of the plane RMI and its validation against numerical simulations. Chapter 3 summarizes an analytical model for the asymptotic growth rate of the RMI for three-dimensional cylindrical linear perturbations. The model is combined with the theory of the previous chapter. Plane, pure axial and pure azimuthal linear perturbations are compared to each other in various computations. Chapter 4 investigates the reshock phenomenon occurring after radially symmetric converging waves reflect off the center of the geometry. Wave diagrams are constructed from highly resolved computations for different geometries (plane, cylindrical, and spherical), various gas combinations, and incident shock strengths. The LES performed to study the post-reshock mixing are described in Chapter 5. All the simulations of the converging RMI are initialized using self-similar converging shocks. Finally, conclusions and implications of this research are presented in Chapter 6. Appendices B and C report the detailed statistics employed to post-process the extensive data from the LES.

Chapter 2

Startup Process in the Richtmyer-Meshkov Instability

2.1 Introduction

Here and hereinafter, we consider only the case of a reflected shock corresponding in general to a light-to-heavy shock-contact refraction.

The RMI generally combines different phenomena such as, but not limited to, shock refraction, hydrodynamic stability, and both linear and non-linear growth periods. There are two important contributions to the early-time, or small-amplitude linear growth of the instability, before nonlinear development of the perturbation appears. First, the baroclinic deposition of vorticity due to the direct interaction of the incident shock with the interface, where the pressure gradient at the shock is misaligned with the local density gradient at the interface. If the initial interface is sharp, it can therefore be viewed as a vortex sheet that leads to its own self-induced distortion. The second contribution concerns the influence of the transmitted and reflected shocks as they leave density and vorticity perturbations behind them. Relaxation of these shock fronts both deposits bulk vorticity and also emits acoustic waves that, by reverberation, modify the vorticity on the interface. In the weak shock limit, the linear growth reduces essentially to the first contribution, while for strong incident shocks, the produced transmitted shock takes a longer time to separate from the interface.

Richtmyer first derived the compressible perturbed equations and obtained a simple analytical expression for the asymptotic linear growth rate [94], assuming that transmitted and reflected shocks have traveled sufficiently far, compared to the wavelength of the perturbation, that the second contribution is subdominant. Other methods concentrating also on the first contribution have attempted to correct the impulsive growth rate to better model the behavior for strong incident shocks or high Atwood ratio without loss of simplicity [108]. At the same time numericists and experimentalists have addressed the effect of shock proximity by using empirical corrections to the impulsive growth rate of [46, 53, 36]. More complex, semi-analytical studies have taken into account all relevant

phenomena [31, 116], and showed good agreement with numerical results obtained by linearizing the Euler equations between the perturbed interface and transmitted/reflected waves [120], and with the linear interaction analysis at low Atwood numbers of Griffond [39].

In what follows, by modeling the proximity of the receding transmitted and reflected shocks, the analysis of Section 2.2 establishes a simple analytical expression for the growth rate that captures some of the early features of the perturbation evolution before it has reached the asymptotic growth linear in time. Figure 2.3 best describes how the model compares to the reality. As analyzed in Section 2.3, the solution addresses the early-time physics of the linear growth, with a characteristic time τ, while allowing for the determination of the asymptotic, or later-time, growth rate by additional physics. Section 2.4 compares results to computations obtained from two-dimensional, highly resolved numerical simulations of the RMI under various initial conditions. Different realistic combinations of Atwood ratio and specific heat ratio are tested, as well as incident shock strength, initial perturbation amplitude, and wavenumber. A more thorough parametric study of the characteristic time τ is presented in Section 2.5.

2.2 Analytical Model

2.2.1 General Formulation

At $t = 0$, in Cartesian axes (x-z), a plane shock traveling to the left (negative z direction) impacts a plane unperturbed density interface, $z = 0$, separating two fluids of different density, producing a transmitted shock and a reflected shock. We work in a frame of reference in which the undisturbed interface is always at $z = 0$ and in which the transmitted shock velocity is $U_{S_1} < 0$ and the reflected shock velocity is $U_{S_2} > 0$. We define more generally $S_j(t)$, $j = 1, 2$ as the average position of these shocks at time t. In the laboratory reference frame, the interface is impulsively accelerated to velocity $-\Delta W \mathbf{e}_z$, $\Delta W > 0$, at $t = 0$. For given fluids and given incident shock strength, $U_{S_1}, U_{S_2}, \Delta W$, and the post-shock densities and Atwood number A^+ can be determined by solution of the one-dimensional Riemann problem. We will focus on regions directly in contact with the interface and denote these by the subscript j, where $j = 1$ for the region to the left, $z < 0$, of the interface and $j = 2$ for the region to the right, $z > 0$, of the interface. The interface is slightly perturbed (Figure 2.1), with a perturbation amplitude small compared to its fundamental wavelength. Its position is

$$z = \zeta(x, t) = h(t)e^{\imath\, kx}. \tag{2.1}$$

The purpose of this analytical work is to determine a simple approximation for the growth $h(t)$ for small t, within the linear approximation.

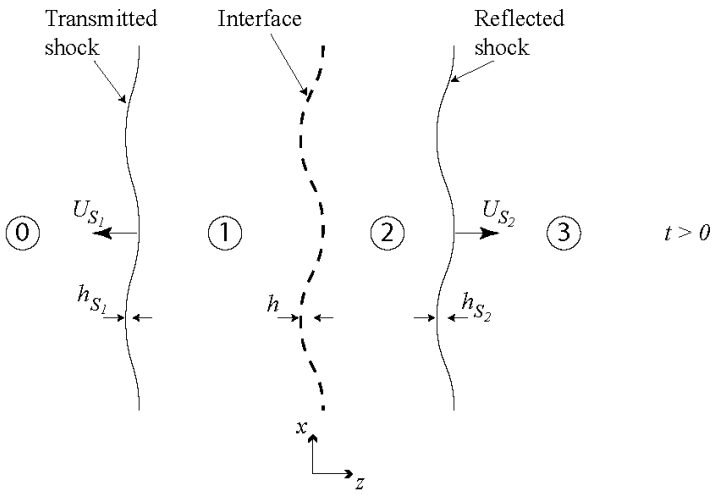

Figure 2.1: Perturbed system.

The fundamental length scale in this problem is the wavelength of the perturbation $2\pi/k$. We choose $1/k$ as our characteristic length scale. The characteristic velocity scale is chosen to be $kh(0)/(2\pi)A^+\Delta W$ since Richtmyer's impulsive model of the asymptotic growth rate for the linear RMI is $kh(0)A^+\Delta W$ [94], with $A^+ = (\rho_1 - \rho_2)/(\rho_1 + \rho_2)$ the post-shock Atwood ratio based on post-shock densities and $h(0)$ amplitude of the perturbation at $t = 0$. An appropriate time scale characteristic of the linear growth of the instability is thus $2\pi/(k^2h(0)A^+\Delta W)$ (> 0 as long as $A^+ > 0$). The density scales like the constant post-shock densities ρ_1 to the left of the interface, or ρ_2 to the right. Similarly, the pressure scales like $\rho_j(kh(0)/(2\pi)A^+\Delta W)^2$, $j = (1, 2)$. The impulsive acceleration $g = \Delta W\delta_D(t)$ of the interface is made dimensionless by the characteristic acceleration $k(kh(0)/(2\pi)A^+\Delta W)^2$. Define a_j as the post-shock speed of sound to the left or right of the interface. To summarize, for each region $j = (1, 2)$, original quantities are related to dimensionless quantities, denoted with a bar, as follows:

$$\boldsymbol{x} = \frac{1}{k}\,\overline{\boldsymbol{x}},\ t = \frac{1}{k\varepsilon_j a_j}\,\bar{t}_j,\ \varrho_j = \rho_j\,\overline{\varrho}_j,\ \boldsymbol{u}_j = \varepsilon_j a_j\,\overline{\boldsymbol{u}}_j,\ p_j = \rho_j(\varepsilon_j a_j)^2\,\overline{p}_j,\ g = k(\varepsilon_j a_j)^2\,\overline{g}_j, \tag{2.2}$$

where the following dimensionless parameter is defined:

$$\varepsilon_j = \frac{kh(0)}{2\pi}A^+\frac{\Delta W}{a_j}. \tag{2.3}$$

The parameter ε_j defined in (2.3) is in general small since $kh(0)/(2\pi) \ll 1$, $A^+ \leq 1$, and $\Delta W/a_j$ is of the order of unity. This latter ratio can be greater than unity in the heavy region 1 when the incident shock Mach number M_I is very high, but remains less than ten as long as A^+ is not too close to unity and the incident shock is not too strong. For example, in the case of a 'light air →

heavy SF_6' shock interaction at $M_I = 8.0$, whose Atwood number $A^+ \simeq 0.7$ is quite high (1:5 density ratio), in the heavy region $\Delta W/a_1 \simeq 4.2$.

The Euler equations in the frame of the accelerated interface are now written in terms of dimensionless quantities on each side of the interface:

$$\frac{\partial \overline{\varrho}_j}{\partial \overline{t}_j} + \frac{\partial}{\partial \overline{x}}(\overline{\varrho}_j \overline{u}_j) + \frac{\partial}{\partial \overline{z}}(\overline{\varrho}_j \overline{w}_j) = 0, \tag{2.4a}$$

$$\overline{\varrho}_j \left(\frac{\partial \overline{u}_j}{\partial \overline{t}_j} + \overline{u}_j \frac{\partial \overline{u}_j}{\partial \overline{x}} + \overline{w}_j \frac{\partial \overline{u}_j}{\partial \overline{z}} \right) = -\frac{\partial \overline{p}_j}{\partial \overline{x}}, \tag{2.4b}$$

$$\overline{\varrho}_j \left(\frac{\partial \overline{w}_j}{\partial \overline{t}_j} + \overline{u}_j \frac{\partial \overline{w}_j}{\partial \overline{x}} + \overline{w}_j \frac{\partial \overline{w}_j}{\partial \overline{z}} \right) = -\frac{\partial \overline{p}_j}{\partial \overline{z}} + \overline{\varrho}_j \overline{g}_j(\overline{t}_j), \tag{2.4c}$$

$$\left(\frac{\partial \overline{p}_j}{\partial \overline{t}_j} + \overline{u}_j \frac{\partial \overline{p}_j}{\partial \overline{x}} + \overline{w}_j \frac{\partial \overline{p}_j}{\partial \overline{z}} \right) = -\frac{1}{\varepsilon_j^2} \overline{\varrho}_j \left(\frac{\partial \overline{u}_j}{\partial \overline{x}} + \frac{\partial \overline{w}_j}{\partial \overline{z}} \right), \tag{2.4d}$$

where it has been assumed that the sound speed is uniform and constant equal to a_j. The acceleration of the frame in which the Euler equations are written is contained in the last term of Equation (2.4c).

2.2.2 Base Flow and Perturbations

The flow is decomposed as a base part uniform in the transverse direction x, and a small perturbation sinusoidal in x. For any dimensionless flow quantity $\overline{q}_j$ in each region:

$$\overline{q}_j(\overline{x}, \overline{z}, \overline{t}_j) = \overline{q}_j^{(0)}(\overline{z}, \overline{t}_j) + \varepsilon_j \overline{q}_j^{(1)}(\overline{z}, \overline{t}_j) e^{\imath \overline{x}} + ... \tag{2.5}$$

At leading order in ε_j, an admissible base flow in the regions 1 and 2 is expressed as

$$\overline{\varrho}_j^{(0)} = 1, \quad \overline{u}_j^{(0)} = 0, \quad \overline{w}_j^{(0)} = 0, \quad \overline{p}_j^{(0)} = \overline{P}_0 + \overline{g}_j(\overline{t}_j)\overline{z}, \tag{2.6}$$

where $\overline{P}_0$ is an arbitrary background pressure. The base flow is simply the incompressible response to an impulse that instantaneously accelerates the flow to the speed ΔW in the negative z-direction. Expressed in dimensional variables, the base quantities can be determined by solving the one-dimensional Riemann problem of the shock interaction at $t = 0$. Linearizing the Euler equations in each region with small parameter ε_j in region j , the leading-order perturbed equations

are

$$\frac{\partial \overline{\varrho}_j^{(1)}}{\partial \overline{t}_j} + \imath\, \overline{u}_j^{(1)} + \frac{\partial \overline{w}_j^{(1)}}{\partial \overline{z}} = 0, \tag{2.7a}$$

$$\frac{\partial \overline{u}_j^{(1)}}{\partial \overline{t}_j} = -\imath\, \overline{p}_j^{(1)}, \tag{2.7b}$$

$$\frac{\partial \overline{w}_j^{(1)}}{\partial \overline{t}_j} = -\frac{\partial \overline{p}_j^{(1)}}{\partial \overline{z}} + \left(\frac{\rho_2 - \rho_1}{\rho_j}\right) \overline{g}_j(\overline{t}_j)\left[H(\overline{z}) - H(\overline{z} - kh)\right], \tag{2.7c}$$

$$\imath\, \overline{u}_j^{(1)} + \frac{\partial \overline{w}_j^{(1)}}{\partial \overline{z}} = 0, \tag{2.7d}$$

where $H(z)$ is the Heaviside function. Equation (2.7c) is obtained by subtracting Equation (2.4c) to its equivalent equation for the base field, at every location (x, z). The right-hand side source term of the equation obtained for the perturbation $\overline{w}_j^{(1)} e^{\imath \overline{x}}$ contains the window function $H(\overline{z}) - H(\overline{z} - \overline{\zeta})$, which is rewritten as $\left[H(\overline{z}) - H(\overline{z} - kh)\right] e^{\imath \overline{x}}$. Equation (2.7d) shows that the leading-order perturbed flow is incompressible and, from Equation (2.7a), the perturbed density is independent of time. From Equations (2.7b) and (2.7c), the post-shock perturbed flow is irrotational on each side of the interface except in a small window between $z = 0$ and the interface $z = \zeta$. Therefore a perturbed potential $\overline{\phi}_j^{(1)}$ can be introduced such that $\overline{\boldsymbol{u}}_j^{(1)} = \overline{\nabla \phi}_j^{(1)}$. Outside of the forced region, the perturbed potential is a solution of the Laplace equation and can be written in terms of dimensional variables as

$$\phi_j^{(1)}(z, t) = A_j(t) \sinh(kz) + B_j(t) \cosh(kz), \tag{2.8}$$

where A_j and B_j are complex coefficients. The assumption of potential incompressible flow on each side of the interface was initially used by Layzer to describe the single-mode nonlinear growth [65]. Most recently, based on Layzer's model at an infinite density ratio ($A = 1$) (see also [42]), Srebro et al. found a general buoyancy-drag model at every A describing the stages of the RMI and RTI [104]. These models allows to compute the bubble velocities, assuming that the flow is governed by the behavior near the bubble tips, supposed parabolic in shape.

2.2.3 Boundary Conditions at the Shocks

Boundary conditions at the transmitted and reflected shocks are now investigated. From the shock refraction process occurring when the incident shock impacts a perturbed interface with wavenumber k, the transmitted and reflected shock waves produced are similarly perturbed with the same wavenumber but are expected to evolve with a different growth than that of the interface perturbation. The initial shock perturbation $h_{S_j}(t = 0^+)$ is expected *a priori* of the same order of the amplitude of the interface perturbation $h(t = 0^+)$. Our simulations (see Section 2.4) confirm the

well-known results on planar shock stability: small perturbations at the shock front decay, while interface perturbations grow for $t > 0$. Landau determined that the stability criterion for small disturbances traveling in the direction perpendicular to the shock was simply a consequence of the requirement of the second law of thermodynamics [60]. Considering a corrugation in the transverse direction, Dýakov's criterion expresses that, in the case of a perfect gas, a discontinuous shock front is unconditionally stable [26]. To complete the discussion, we note that Yang found, in the case (not considered presently) of a reflected rarefaction wave, the trailing edge of the fan is always unstable (Section C of [120]).

Linearizing the Rankine-Hugoniot jump conditions with respect to small shock perturbation amplitude $h_{S_j}(t)$, i.e., corresponding to small interface perturbation $h(t)$, the axial velocity perturbation behind the shock can be related to $h_{S_j}(t)$ as

$$w_j^{(1)}(S_j(t) + h_{S_j}(t)e^{\imath kx}, t) \simeq w_j^{(1)}(S_j(t), t) \simeq C_j \dot{h}_{S_j}, \tag{2.9}$$

where C_j is a constant function of the unperturbed densities upstream and downstream of each shock. As the shock perturbation decays, the growth $\dot{h}_{S_j}$ tends to zero. We therefore assume the following approximate boundary condition: for $t > 0$, the growth of the shock perturbation is zero at leading order in ε_j and, therefore, the perturbed axial velocity must be zero at the shock. This assumption is consistent with incompressible, irrotational motion for the perturbed flow at leading order: the shocks then physically behave like moving plane boundaries along which there exists a uniform distribution of sources of just sufficient strength to produce the post-shock, incompressible flow. At higher order these 'walls' essentially confine the reach of reverberating waves to the flow regions between the interface and the receding shocks. It is this effect that presently modifies Richtmyer's theory [94].

With this ansatz, Equation (2.8) simplifies and we can express the perturbed velocity field in each region as

$$u_j^{(1)}(z,t) = \imath\, kE_j(t)\cosh(k(z - S_j(t))), \tag{2.10a}$$

$$w_j^{(1)}(z,t) = kE_j(t)\sinh(k(z - S_j(t))), \tag{2.10b}$$

where $E_j(t)$ are functions to be determined. This solution allows for shear at the 'wall-shocks' where the perturbed transverse velocity is non zero. From the momentum equation in the x-direction, the pressure perturbation is

$$p_j^{(1)}(z,t) = -\rho_j \frac{\partial}{\partial t}\left(E_j(t)\cosh(k(z - S_j(t)))\right). \tag{2.11}$$

2.2.4 Kinematic and Dynamic Conditions at the Interface

At the contact $z = \zeta(x,t) = h(t)e^{\imath\, kx}$, the perturbed z-velocity must be continuous, and, after linearization

$$w_1^{(1)}(0,t) \simeq w_2^{(1)}(0,t) \simeq \dot{h}. \tag{2.12}$$

Using the simplified form of $w_j^{(1)}(z,t)$ in each region 1 and 2 found in the previous paragraph at dominant order, the linearized kinematic condition becomes

$$-kE_1(t)\sinh(kS_1(t)) = -kE_2(t)\sinh(kS_2(t)) = \dot{h}. \tag{2.13}$$

We observe that the coefficients E_j are real. A dynamic boundary condition is obtained by integrating the perturbed momentum equation (2.7c) in z from $z = 0$ to $z = h(t)$. The linearized dynamic condition to order ε_j requires that at $z = h$ (in dimensional variables)

$$p_1^{(1)}(x,z,t) - \rho_1 \Delta W \delta_D(t) z = p_2^{(1)}(x,z,t) - \rho_2 \Delta W \delta_D(t) z. \tag{2.14}$$

Using Equation (2.11), the linearized dynamic condition becomes

$$-\rho_2 \frac{\partial}{\partial t}\left(E_2(t)\cosh(kS_2(t))\right) + \rho_1 \frac{\partial}{\partial t}\left(E_1(t)\cosh(kS_1(t))\right) \simeq (\rho_2 - \rho_1)\Delta W \delta_D(t) h(t). \tag{2.15}$$

The functions $E_j(t)$ are fully determined (up to the initial condition $E_j(0)$) by integrating Equation (2.15) from $t = 0$ to t. From Equation (2.13), an expression for the growth rate is found as

$$\dot{h}(t) = \frac{2\,\dot{h}_\infty}{(1-A^+)\coth(kS_2(t)) + (1+A^+)\coth(k(-S_1(t)))}, \tag{2.16a}$$

$$\dot{h}_\infty = kh(0)A^+\Delta W H(t) + \frac{k}{2}\left((1-A^+)E_2(0) - (1+A^+)E_1(0)\right), \tag{2.16b}$$

where $H(t)$ is the Heaviside function. We recovered the asymptotic growth rate predicted by Richtmyer in the first term of the right-hand side of Equation (2.16b). In this formula, A^+ comes from the use of post-shock densities ρ_j. Moreover, $h(0)$ is the perturbation amplitude at $t = 0$ right when the shock passes the interface and has not been clearly defined at this point. E.g., $h(0)$ could be modeled as the arithmetic average of the pre-shock and post-shock amplitudes $h(0^-) \equiv h_0$ and $h(0^+)$.

2.3 Startup Period for Richtmyer-Meshkov Instability

2.3.1 Startup Time τ

We observe that, within the linearized approximation, the large t asymptotic growth rate $\dot{h}_\infty$ is not determined presently. Eliminating the functions E_j from Equation (2.15) by using Equation (2.13), a second-order ordinary differential equation (ODE) is straightforwardly obtained for $h(t)$. The ODE has a regular singular point at $t = 0$, which admits a family of solutions, regular at $t = 0$, with a free parameter $\ddot{h}(t = 0^+)$ that is equivalent to the free asymptotic growth rate $\dot{h}_\infty$. Once $\dot{h}_\infty$ is determined, the amplitude of the interface perturbation can be obtained by numerically integrating Equation (2.16), given $h(0)$. Second, both terms in the denominator of (2.16b) are positive since $-1 < A^+ < 1$, and $S_1(t) < 0$ and $S_2(t) > 0$. Third, the actual form of $S_1(t)$ and $S_2(t)$ has not been used, and the instantaneous growth rate is a function only of the relative locations of the shocks and the interface, not the history of these locations. Since the leading order perturbed equations are incompressible this suggests that our results are dependent on the equation of state of the fluids via the solution of the one-dimensional Riemann problem.

The shock locations can now be modeled with

$$S_j(t) = U_{S_j} t H(t). \tag{2.17}$$

As $t \to 0^+$, the growth rate simplifies to

$$\dot{h} = \dot{h}_\infty \frac{t}{\tau} + \mathcal{O}(t^2), \tag{2.18}$$

where

$$\tau = \frac{1}{2k}\left(\frac{1 - A^+}{U_{S_2}} + \frac{1 + A^+}{(-U_{S_1})}\right). \tag{2.19}$$

The time τ obtained from our new model represents the characteristic time during which the presence of the shocks influences the growth of the interface and is fully determined by solving the one-dimensional Riemann problem described as the base flow. For $t \gg \tau$, the asymptotic growth $\dot{h}_\infty$ is recovered. Equation (2.18) shows that the growth rate immediately following the shock interaction, $\dot{h}(0^+)$, is zero. The kinematic condition (2.12) taken at $t \to 0^+$ implies that $w_j^{(1)}(z = 0, t = 0^+)$ is zero, which is consistent with the boundary condition assuming zero axial velocity perturbation at the shocks, the shocks being concentrated at $z = 0$ as $t \to 0^+$. Numerical two-dimensional simulations shown later, as well as the linear compressible simulations of Yang [120], corroborate that the growth rate is zero just following the shock interaction. The model gives a non-zero positive initial acceleration as $\ddot{h}(0^+) \sim \dot{h}_\infty/\tau$.

2.3.2 Asymptotic Growth Rate

The growth rate, initially zero, increases to an asymptotic limit $\dot{h}_\infty$ as the shocks recede. Richtmyer [94] initially proposed the impulsive model in an unbounded domain that gives the asymptotic growth as

$$\dot{h}_{Rich.} = kh(0)A^+\Delta W. \tag{2.20}$$

For any time, the transmitted and reflected waves are already at infinity. It has been shown, however (Yang [120]), and confirmed by Wouchuk's semi-analytical model [116] that the impulsive model generally fails to represent the correct terminal linear growth rate. Solving the linearized Euler equations numerically, Yang concludes that his linear theory and the impulsive model agree when the incident shock strength decreases, but that large discrepancies appear for high incident shock strengths. Indeed, the simple observation that, for strong shocks, both shocked interface and transmitted shock remain close to each other for small t is sufficient to contradict the assumption of shocks at infinity during the initial growth phase. Yang also observed that the agreement with Richtmyer's model improves as the adiabatic exponents increase while remaining very close. Figure 16 of [120] (reflected shock case) shows that, for the air $\rightarrow SF_6$ case, which we chose to study in Section 2.4, the disagreement with Richtmyer's mode grows as the incident shock strength increases. A heuristic correction to the impulsive model has been proposed by Vandeboomgaerde [108] using the average of the pre- and post-shock properties. But, as other impulsive formulations, the discrepancy with the exact solution can be very large as the incident shock becomes stronger. The true asymptotic growth rate will now be written as a correction to Richtmyer's asymptotic growth under the following form:

$$\dot{h}_\infty = \mathfrak{F}\,\dot{h}_{Rich.}. \tag{2.21}$$

In the limit of weak incident shock, $\mathfrak{F}$ is expected to tend to 1. Figure 16 of [120] represents the quantity $1/\mathfrak{F}_{Yang} - 1$ computed from numerical computations.

2.3.3 Initial Tangential Velocity at Interface

We now discuss a framework for modeling the terminal or long-time linear growth rate. From Equation (2.16b), the terminal growth rate is determined up to the knowledge of the $E_j(0)$, in other words the initial transverse velocities. According to Equation (2.10a), in the case of zero initial transverse velocity on each side of the interface, Richtmyer's asymptotic solution is recovered. To improve the asymptotic model, a relationship is required between the asymptotic growth rate $\dot{h}_\infty$ and the initial jump in transverse velocity, or circulation distribution, across the interface. From

Equation (2.16a) substituted into Equation (2.13) and then Equation (2.10a), it can be shown that

$$\dot{h}_\infty = - \frac{\imath}{2} \frac{(1-A^+)U_{S_2} - (1+A^+)U_{S_1}}{U_{S_2} - U_{S_1}} \Delta[u^{(1)}], \tag{2.22a}$$

$$\Delta[u^{(1)}] \equiv \left(u_1^{(1)} - u_2^{(1)} \right)_{t=0}. \tag{2.22b}$$

$\Delta[u^{(1)}]$ is the tangential velocity jump across the interface as $t \to 0^+$. In our notation it is purely imaginary, owing to a one-quarter wavelength phase difference between the interface shape perturbation and the tangential velocity jump. Hence finding the long-time linear growth rate is equivalent to determining the initial circulation-line density, or vortex-sheet strength, across the interface. As a last remark, it can be shown after some algebra that, within the model presented here, the jump in transverse velocity $u_1^{(1)} - u_2^{(1)}$ across the interface is not constant with time unless the base flow is symmetric, that is $-U_{S_1} = U_{S_2}$. However, the momentum slip $\rho_1 u_1^{(1)} - \rho_2 u_2^{(1)}$ across the interface is conserved with time.

If the (constant) circulation related to Richtmyer's asymptotic model is taken to be the initial circulation in the present model, Equation (2.22) lead to

$$\dot{h}_\infty = \mathfrak{F}_{Rich.Circ.} \dot{h}_{Rich.} = \frac{(1-A^+)U_{S_2} - (1+A^+)U_{S_1}}{U_{S_2} - U_{S_1}} \dot{h}_{Rich.}, \tag{2.23a}$$

$$\Delta[u^{(1)}] = 2\imath k h(0) A^+ \Delta W. \tag{2.23b}$$

Using the leading order (small angles of incidence α) Γ_1' of the circulation deposited by the passage of a shock on a planar interface, given the long expression (2.14) in Samtaney and Zabusky [99], Equation (2.22) becomes

$$\dot{h}_\infty = \mathfrak{F}_{Samt.Circ.} \dot{h}_{Rich.} = \frac{(1-A^+)U_{S_2} - (1+A^+)U_{S_1}}{U_{S_2} - U_{S_1}} \frac{\Gamma_1'}{2A^+\Delta W} \dot{h}_{Rich.}, \tag{2.24a}$$

$$\Delta[u^{(1)}] = \imath k h(0) \Gamma_1'. \tag{2.24b}$$

Subsection 4.4 of [99] suggests a scaling analysis for Γ_1' in terms of incident Mach number, density ratio (and therefore Atwood ratio), and ratio of specific heats.

Referring to the form (2.21), we display in Figure 2.2 (and later on Table 2.1) the correction factor $\mathfrak{F}$ determined from Richtmyer's circulation modeling summarized in (2.23a), noted $\mathfrak{F}_{Rich.Circ.}$, and from Samtaney's circulation analysis expressed in (2.24a), noted $\mathfrak{F}_{Samt.Circ.}$. In Figure 2.2, various common gas are used, such as air, Ar, CO_2, He, SF_6, and Xe. A discussion is provided in Subsection 2.4.2. For the comparison against numerical simulations in the following section, the terminal growth rate given by Richtmyer's asymptotic model $\dot{h}_{Rich.}$ and Yang's correction $\mathfrak{F}_{Yang} \dot{h}_{Rich.}$ will be used. To determine $\dot{h}_{Rich.}$ (Equation (2.20)) we assume that $h(0)$ in Equation (2.20) is the post-shock perturbation amplitude $h(0^+)$ (which is different from the amplitude before the shock

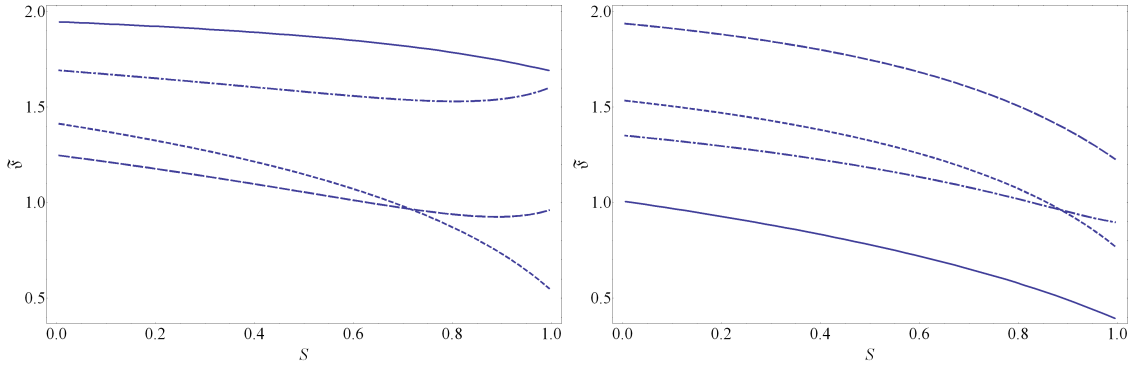

(a) $\mathfrak{F}_{Rich.Circ.}$ based on Richtmyer's circulation

(b) $\mathfrak{F}_{Samt.Circ.}$ based on Samtaney's circulation

Figure 2.2: Correction factor to Richtmyer's impulsive growth rate for varying incident shock strengths S (see Equation (2.28)) and various combinations of gases: air $\rightarrow CO_2$ (solid line), Ar $\rightarrow$ Xe (dashed-dotted line), air $\rightarrow SF_6$ (small dashed line), and He $\rightarrow$ air (long dashed line).

interaction).

2.4 Numerical Simulations

2.4.1 Numerical Method

Two-dimensional simulations were conducted within the AMROC framework developed by Deiterding [21], based on the structured adaptive mesh refinement (SAMR) algorithm by Berger and Oliger [4]. The numerical method, applied to each subgrid of the mesh hierarchy, consists of a hybrid method written for the multi-component Euler equations of gas dynamics assuming calorically perfect gas: A weighted, essentially non-oscillatory (WENO) scheme is used to capture discontinuities (such as shock waves, contact wave, or fine/coarse mesh interfaces) but switches to a low-numerical dissipation, explicit, tuned center-difference scheme (TCD) in the smooth regions [44, 83].

The density interface is nominally defined by the mixture fraction field $\psi(x, z, t)$. This scalar field is asymptotic to $\psi(x, z, t) = 0$ on the very right side, $\psi(x, z, t) = 1$ on the very left side, and is initially setup using a tanh profile with intrinsic thickness δ_0^C (taken as about one fifth of the pre-shock perturbation amplitude h_0). When the shock impacts the smeared interface, it is compressed down to a thickness $\delta^C(t)$ until the end of the shock refraction where both reflected and transmitted shock travels away from the interface. It is important to ensure that during the whole simulation, in particular during the shock interaction, δ^C is fully resolved. The resolution, controlled by the number of refinement levels, is chosen such that at least 10 points are used to resolved the interface thickness.

At $t > 0$, we define the centerline of the smeared density interface by

$$z_c(x,t) \equiv \frac{\int_{-\infty}^{\infty} z(1-\psi)\psi \mathrm{d}z}{\int_{-\infty}^{\infty}(1-\psi)\psi \mathrm{d}z}. \tag{2.25}$$

At a given time t, for a fixed x, the scalar profile is well approximated by a tanh centered at $z_c(x,t)$ and with thickness $\delta^C(t)$:

$$\psi(x,z,t) = \frac{1}{2}\left[1 + \tanh\left(\frac{2(z - z_c(x,t))}{\delta^C(t)}\right)\right]. \tag{2.26}$$

It is easily verified that $z_c(x,t)$ is recovered when (2.26) is used in (2.25). The spike and the bubble positions and the flow velocity at these locations allow a measurement of perturbation amplitude and growth rate:

$$h(t) = |\frac{z_{c_{spike}} - z_{c_{bubble}}}{2}|, \tag{2.27a}$$

$$\dot{h}(t) = |\frac{w|_{z_{c_{spike}}} - w|_{z_{c_{bubble}}}}{2}|. \tag{2.27b}$$

2.4.2 Parametric Study of the Amplitude and Growth Rate of the Interface Perturbation

The parameters involved are the pre-shock Atwood ratio A, the ratio of specific heats γ_j for each specie, the incident shock Mach number M_I (or its strength S), the perturbation wavenumber k, and the pre-shock perturbation amplitude h_0. The Atwood ratio is chosen such that the temperature is continuous across the initial interface (which is consistent with experimental conditions), and as a result A is a function only of the molecular weights of both species. To a given combination of parameters corresponds a numerical simulation from which amplitude and growth rate of the interface are obtained. Simulation data are compared to the theoretical model presented in the previous section on (2.16).

First recall that the incident shock strength is given by the ratio of the pressures ahead and behind the incident shock p_0 and $p_{0''}$, or in terms of the incident Mach number:

$$S = 1 - \frac{p_0}{p_{0''}} = \frac{1}{1 + \frac{\gamma_R+1}{2\gamma_R(M_I^2-1)}}. \tag{2.28}$$

In the region on the right of the interface before the shock interaction, the speed of sound

$$a_0 \equiv \sqrt{\frac{\gamma_R p_0}{\rho_0}} \tag{2.29}$$

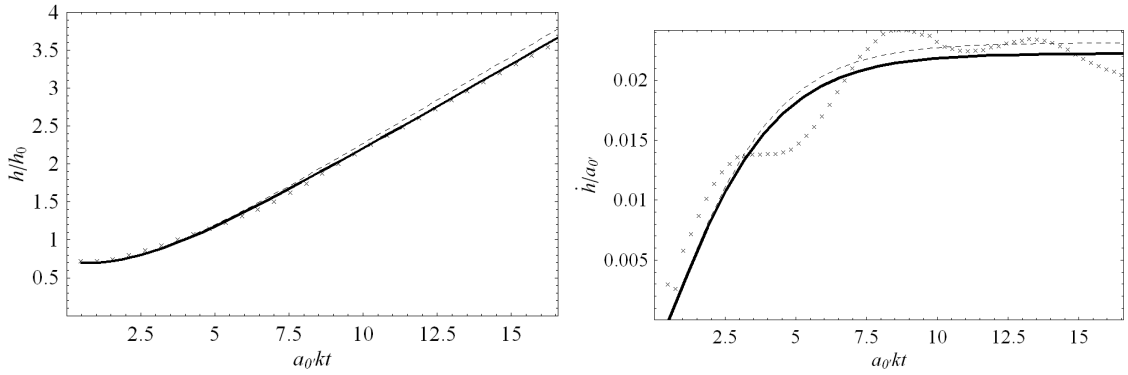

(a) $h(t)/h_0$ (b) $\dot{h}/a_0$

Figure 2.3: Early-time close-up: dimensionless amplitude and growth rate of the interface perturbation $h(t)/h_0$ and $\dot{h}/a_0$ vs. a_0kt; case air $\rightarrow$ SF_6, $kh_0 = 0.1$, $M_I = 1.5$. Numerical simulations using AMROC are represented by crosses. The thin dashed and thick solid lines correspond to our model given by Equation (2.16) with two different choices for $\dot{h}_\infty$. The thin dashed line corresponds to our model using Richtmyer's asymptotic growth rate $\dot{h}_\infty = \dot{h}_{Rich.}$, while the thick solid line uses Yang's correction to Richtmyer's asymptotic growth rate $\dot{h}_\infty = \mathfrak{F}_{Yang}\,\dot{h}_{Rich.}$. $\dot{h}_{Rich.}$ is given by Equation (2.20) and $\mathfrak{F}_{Yang}$ is provided by Yang's linearized simulations [120]. We also recall that the model gives an explicit expression for the growth rate from Equation (2.16), but the amplitude of the interface perturbation is obtained by numerically integrating Equation (2.16)

is the reference velocity scale in the data representation. $1/(a_0k)$ is the reference time scale. Table 2.1 shows different types of shock-contact interaction (at a fixed kh_0). For each combination of species, at a given Mach number, we compute the post-shock Atwood ratio A^+, the dimensionless time $a_0k\tau$, the dimensionless impulsive growth rate $kh(0^+)A^+\Delta W/a_0$, and the correction factor $\mathfrak{F}$ to Richtmyer's impulsive growth rate using Yang's numerical computations (see Figure 16 of [120]), or a model based on Richtmyer's circulation or Samtaney's initial circulation deposited during the shock interaction. Comparing to the reference computations of Yang, the model based on Samtaney's circulation appears satisfactory for low Atwood ratios, but overestimates the asymptotic growth rate for high Atwood ratios. This is because we used Samtaney's circulation derived for low-density contrasts (see domain of validity in figure 15 of [99]). The model based on Richtmyer's circulation overestimates the growth rate for low Atwood ratios, but performs very well for higher Atwood ratios and a wide range of Mach numbers as shown in the example of air$\rightarrow$ SF_6. Some further effort on modeling could be justified, in particular because the factor $((1-A^+)U_{S_2}-(1+A^+)U_{S_1})/(U_{S_2}-U_{S_1})$ does not tend to unity in the limit of weak incident shocks. We note that the simulations were used to evaluate $h(0^+)$. The post-shock amplitudes proved to be almost independent on k over the chosen range of k and Table 2.1 presents results obtained with a fixed k.

	M_I	S	A^+	$a_0 k\tau$	$kh(0^+)A^+\frac{\Delta W}{a_0}$	$\mathfrak{F}_{Yang}$	$\mathfrak{F}_{Rich.Circ.}$	$\mathfrak{F}_{Samt.Circ.}$
air $\rightarrow$ CO_2	1.2	0.339	0.222	0.735	0.0048	1.07	1.90	0.86
$\gamma_R = 1.40 \quad \gamma_L = 1.29$	1.5	0.593	0.237	1.095	0.0092	1.14	1.85	0.72
$A = 0.21$	2.0	0.778	0.253	1.368	0.0128	1.12	1.79	0.60
Ar $\rightarrow$ Xe	1.2	0.355	0.533	1.053	0.0087	1.06	1.61	1.24
$\gamma_R = 1.67 \quad \gamma_L = 1.65$	1.5	0.610	0.527	1.393	0.0175	1.11	1.55	1.13
$A = 0.53$	2.0	0.789	0.507	1.455	0.0251	1.16	1.53	1.03
	1.2	0.339	0.700	1.914	0.0114	1.02	1.24	1.41
air $\rightarrow$ SF_6	1.5	0.593	0.732	3.153	0.0231	0.96	1.07	1.26
$\gamma_R = 1.40 \quad \gamma_L = 1.09$	2.0	0.778	0.766	4.492	0.0390	0.85	0.89	1.09
$A = 0.67$	3.0	0.903	0.801	5.586	0.0669	0.71	0.72	0.92
	5.0	0.966	0.825	5.203	0.1144	0.61	0.61	0.83
	8.0	0.987	0.835	3.908	0.2103	0.56	0.57	0.78
He $\rightarrow$ air	1.2	0.355	0.770	2.024	0.0100	1.01	1.11	1.81
$\gamma_R = 1.67 \quad \gamma_L = 1.40$	1.5	0.610	0.779	2.837	0.0222	1.00	1.00	1.67
$A = 0.76$	2.0	0.789	0.780	3.122	0.0401	0.56	0.57	0.78

Table 2.1: Various shock-contact interactions for different species and varying incident Mach number, with $kh_0 = 0.1$. For each gas combination and incident Mach number M_I, the shock strength S, post-shock Atwood ratio A^+, dimensionless characteristic startup time $a_0 k\tau$, and dimensionless Richtmyer's asymptotic growth rate $kh(0^+)A^+\Delta W/a_0$ (see Equation (2.20)) are evaluated by solving the one-dimensional shock-interface interaction problem. $\mathfrak{F}_{Yang}$ is given by Yang's linearized simulations [120] and represents the exact asymptotic growth rate for the RMI in the linear regime. The models for $\mathfrak{F}_{Rich.Circ.}$ (given by Equation (2.23a)) and $\mathfrak{F}_{Samt.Circ.}$ (given by Equation (2.24a)) must be compared to the reference value $\mathfrak{F}_{Yang}$.

2.4.2.1 Amplitude and Growth Rate

Figure 2.3 shows the early-time evolution of amplitude and growth rate of the perturbation for a set of parameters indicated in the caption. The model captures well the time-scale of the growth. In order to capture the higher-frequency features in details, which are purely compressible effects due to reverberation of waves between the interface and shocks, a higher-order solution in ε_j would be needed as well as higher-order boundary conditions at shocks.

2.4.2.2 Influence of kh_0

We now discuss and summarize the influence of the dimensionless parameter kh_0 without showing relevant figures of the growth amplitude and rate vs. time. Consider for example the shock inter-

action air $\rightarrow$ SF_6, as an incident shock of Mach number $M_I = 1.2$ travels from air to SF_6. The initial dimensionless amplitude of the perturbation kh_0 was varied from 0.03 to 0.3 (varying both k and h_0 independently). Additional levels of refinement were used in the simulations such that sufficient resolution was provided to capture smaller wavelengths as well as smaller amplitudes of the perturbation. As long as $kh(t)$ remained small compared to 2π, the growth was observed to be predominantly linear and good comparisons were obtained between theory and simulation. As kh_0 increased (typically $kh_0 \sim 0.2$ in the present case), the linear growth was found to become faster and to compete earlier with non-linear growth.

2.4.2.3 Influence of M_I

We consider further the case of the air $\rightarrow$ SF_6 interaction. The perturbation shape is fixed in amplitude h_0 and wavenumber k, with $kh_0 = 0.1$. The effect of incident shock strength is now studied (see Table 2.1). Figure 2.4 shows good agreement between the simulated amplitude and that obtained from the model using Yang's correction for different shock strengths. We recall that the combination air $\rightarrow$ SF_6 is the most critical test for very strong incident shocks where the discrepancy between the model of Richtmyer significantly overestimates the actual asymptotic growth rate. For very high incident shock strengths, non-linear slowdown appears earlier and the asymptotic linear growth at late times tends to overestimate the terminal growth obtained in the simulations. It is surprising that the model works rather well even in the strong incident shock case where the interface is accelerated enough that it remains close to the transmitted shock, yet the incompressible model does not include the direct coupling between interface and shock perturbations.

2.4.2.4 Influence of the Species

An incident shock of moderate Mach number $M_I = 1.5$ impacts a density interface of characteristics h_0 and k fixed such that $kh_0 = 0.1$. The main characteristics of these interactions are reported in Table 2.1. Perturbation amplitude vs. time is represented on Figure 2.5. As shown in Figure 2.6, the growth rate of the instability computed from the simulations exhibits a different structure depending on the combination of species chosen, but the model summarizes well the simulated growth rate, in particular for low density ratios. Here, the captured growth rate He $\rightarrow$ air appears noisier than the other gas-pair combinations.

2.5 On the Time-Scale τ

In this section we investigate the dependence of τ, given by (2.19), on the flow parameters sufficient to describe the RMI. The timescale τ represents the characteristic time for the growth rate to attain the constant asymptotic growth rate predicted by the present linearized model. This asymptotic

growth generally persists for a further time period, which may be long compared with τ, and is then followed by the onset of the non-linear regime, when the amplitude of the perturbation has increased and the growth-rate begins to slow. Non-linear effects are expected for high k, A, or M_I (thus ΔW), as appearing, for example, in Figure 2.4c.

In the present theory, the dimensionless time $a_0 k\tau$ depends on the post-shock Atwood number A^+ and the reflected shock speeds U_{S_1} and U_{S_2}. These quantities in turn are functions of the pre-shock Atwood number A ($-1 < A < 1$), the incident shock Mach number M_I or equivalently its shock strength S ($0 < S < 1$), and the specific heat ratios γ_R (for the fluid on the right of the interface) and γ_L (on the left). They can be computed by solving the one-dimensional Riemann problem at $t = 0$ for the range of parameters that admit a reflected-shock solution. Presently we consider $a_0 k\tau$ as a function of (A, S) for given γ_L, γ_R. If it is assumed that for $t < 0$ the interface is both temperature and pressure matched, then A is determined uniquely by the ratio of molecular weights of the species separated by the interface: see Table 2.1.

2.5.1 Domain of Validity in the Case of a Reflected Shock

Because we presently restrict attention to the reflected-shock case, it is useful to consider the domain of validity for this case in terms of the parameters that determine $a_0 k\tau$. A (p-w)-diagram analysis enables determination of the reflected wave type produced when a plane shock impacts a plane interface, depending on the parameters A, S, γ_R, and γ_L. Generally, a reflected shock is produced if the acoustic impedance on the right of the interface $\rho_R a_R$ is less than the left one $\rho_L a_L$, that is

$$A > \frac{\gamma_R - \gamma_L}{\gamma_R + \gamma_L}. \tag{2.30}$$

If $\gamma_R = \gamma_L$, this is simply $A > 0$; a reflected shock is produced for a light-to-heavy shock-contact interaction. Anomalous reflection can actually occur in the case $\gamma_R \neq \gamma_L$ for particular incident shock strengths. Omitting the detailed analysis of the shock-contact interaction problem, we summarize the conditions for reflected shock in Table 2.2. The critical incident shock strength $S^\star$ beyond which the reflected wave type changes depends on A as

$$S^\star(A) = 2\frac{\gamma_R - \gamma_L - (\gamma_R + \gamma_L)A}{\gamma_R - \gamma_L - (\gamma_R + \gamma_L - 2)A}. \tag{2.31}$$

For real gases, γ_R and γ_L are sufficiently close that the change in the structure of the reflected wave occurs at relatively small Atwood ratios.

$\gamma_R = \gamma_L$:		$\forall A \in]0,1[$,	
$\gamma_R < \gamma_L$:		$\forall A \in]\frac{\gamma_R-\gamma_L}{\gamma_R+\gamma_L+2}, 1[$,	
	or	$\forall A \in]\frac{\gamma_R-\gamma_L}{\gamma_R+\gamma_L}, \frac{\gamma_R-\gamma_L}{\gamma_R+\gamma_L+2}[$,	$S \in]0, S^\star(A)[$
$\gamma_R > \gamma_L$:		$\forall A \in]\frac{\gamma_R-\gamma_L}{\gamma_R+\gamma_L}, 1[$,	
	or	$\forall A \in]\frac{\gamma_R-\gamma_L}{\gamma_R+\gamma_L+2}, \frac{\gamma_R-\gamma_L}{\gamma_R+\gamma_L}[$,	$S \in]S^\star(A), 1[$

Table 2.2: Conditions, in the (A, S) space, for the reflected wave to be a shock wave.

2.5.2 Parametric Study of τ

For the case of a reflected shock, the dimensionless startup time $a_0 k\tau$ was computed numerically as a function of (A, S) for several sets of γ_L, γ_R. Results are shown in Figure 2.7 where it can be seen that τ reaches its highest values for A close to unity, and for high incident shock strengths S. These conditions correspond to the situation where the accelerated interface follows closely the transmitted shock. Pressure waves actively move back and forth between the interface and the shock, and τ, that was determined from an incompressible analysis, can be understood as the result of an averaging of these reverberating waves adding or removing baroclinic vorticity at their passage through the interface, and therefore affecting the growth of the perturbation. This idea is validated by the various successful comparisons against numerical simulations as shown in the precedent section.

We investigate the weak incident shock limit $S \to 0^+$. On performing analysis of the one-dimensional shock-contact interaction in this limit (omitted presently), it is found that both reflected and transmitted shocks are weak. The post-shock Atwood ratio A^+ tends to the pre-shock Atwood ratio A, and the shock speeds in the frame of the moving interface tend to the pre-shock sound speeds on each respective side of the interface. This leads to

$$a_0 k\tau = \frac{(1-A)^{3/2} + \sqrt{\frac{\gamma_R}{\gamma_L}}(1+A)^{3/2}}{2\sqrt{1-A}} \; + \; \mathcal{O}(S) \;\; \text{as} \;\; S \to 0^+. \tag{2.32}$$

The dominant term of τ is independent of S. In particular, in this limit, as $A \to 0^+$ and if $\gamma_R = \gamma_L$, $a_0 k\tau \to 1$. As $A \to 1^-$, τ becomes infinite.

The strong shock limit $S \to 1^-$ is now analyzed. As the incident shock becomes stronger, the transmitted shock strength increases accordingly while the Mach number of the reflected shock converges to a finite number M_{R_*}. The post-shock Atwood ratio tends to a finite value A_*^+. Finally

τ is given by

$$\begin{aligned} a_0 k\tau &= \frac{1}{2}\sqrt{\frac{\gamma_R+1}{\gamma_R-1}}\left[\frac{1-A_*^+}{M_{R_*}-\frac{2}{\gamma_R+1}\frac{M_{R_*}^2-1}{M_{R_*}}}+\frac{1+A_*^+}{(\gamma_L-1)\left((2\gamma_R(\gamma_R-1))^{-1/2}-\frac{1}{\gamma_R+1}\frac{M_{R_*}^2-1}{M_{R_*}}\right)}\right] \\ &\quad \times\sqrt{1-S}+\mathcal{O}((1-S)^n) \quad \text{as} \quad S\to 1^-, \end{aligned} \tag{2.33}$$

with $n > 1/2$ *a priori* and where A_*^+ is a function of M_{R_*} of the form

$$A_*^+ = \frac{1-\left(\frac{1-A}{1+A}\right)\left(\frac{\gamma_R+1}{\gamma_R-1}\right)\left(\frac{\gamma_L-1}{\gamma_L+1}\right)M_{R_*}^2\left(1+\frac{\gamma_R-1}{\gamma_R+1}(M_{R_*}^2-1)\right)^{-1}}{1+\left(\frac{1-A}{1+A}\right)\left(\frac{\gamma_R+1}{\gamma_R-1}\right)\left(\frac{\gamma_L-1}{\gamma_L+1}\right)M_{R_*}^2\left(1+\frac{\gamma_R-1}{\gamma_R+1}(M_{R_*}^2-1)\right)^{-1}}, \tag{2.34}$$

and M_{R_*} is itself a function of (γ_R, γ_L, A) obtained from solving the following polynomial equation:

$$\left(1+\frac{2\gamma_R}{\gamma_R+1}(M_{R_*}^2-1)\right)-\left(\frac{1+A}{1-A}\right)\left(\frac{\gamma_L+1}{\gamma_R+1}\right)\left(1-\frac{\sqrt{2\gamma_R(\gamma_R-1)}}{\gamma_R+1}\frac{M_{R_*}^2-1}{M_{R_*}}\right)^2=0. \tag{2.35}$$

Finally, we consider the limiting case $A \to 1^-$, or $\rho_L \gg \rho_R$ (e.g., gas-to-liquid RMI). The shock interaction compressing the heavy fluid, the post-shock Atwood ratio also tends to 1^-. Moreover, the shock speed naturally becomes smaller and smaller on the heavy side, such that in Equation (2.19), the second term is dominant, and $\tau \sim 1/(k(-U_{S_1}))$. Since $-U_{S_1}$ is the following function of the transmitted shock Mach number M_T

$$-U_{S_1} = a_0\sqrt{\frac{\gamma_L}{\gamma_R}}\sqrt{\frac{1-A}{1+A}}\left(M_T-\frac{2}{\gamma_L}\frac{M_T^2-1}{M_T}\right), \tag{2.36}$$

where M_T converges to a finite value $M_{T_{**}}$ as $A \to 1^-$ ($M_{T_{**}}$ is obtained by solving numerically the one-dimensional Riemann problem for a given shock strength S), we then have

$$a_0 k\tau = \frac{\sqrt{2\frac{\gamma_R}{\gamma_L}}}{M_{T_{**}}-\frac{2}{\gamma_L+1}\frac{M_{T_{**}}^2-1}{M_{T_{**}}}}\frac{1}{\sqrt{1-A}} \;+\; \mathcal{O}\left(\frac{1}{(1-A)^m}\right) \quad \text{as} \quad A\to 1^-, \tag{2.37}$$

with $m < 1/2$.

The analysis of τ for small A is more difficult to investigate since the nature of the reflected wave can change in this region, as discussed earlier.

2.6 Summary

A simple analytical model for the initial growth rate of the planar RMI has been presented for the case of a reflected shock, which corresponds in general to a light-to-heavy shock interaction. The

model captures the main features of the interfacial perturbation growth before the regime with linear growth in time is attained. The analysis provides a characteristic dimensionless time scale $a_0 k\,\tau$ for the startup phase of the RMI, where k is the perturbation wavenumber and a_0 the pre-shock sound speed on the 'light' side of the interface, and provides an explicit expression for τ as a function of k, the algebraic transmitted and reflected shock speeds $U_{S_1} < 0$ and $U_{S_2} > 0$ and the post-shock Atwood number A^+:

$$\tau \quad = \quad \frac{1}{2k}\left(\frac{1-A^+}{U_{S_2}} + \frac{1+A^+}{(-U_{S_1})}\right). \tag{2.38}$$

Results have been compared with computations obtained from two-dimensional, highly resolved numerical simulations of the RMI. The RMI-startup model has been found to perform well over a wide range of incident shock strength S and pre-shock Atwood ratio A. A degree-of-freedom appearing in the analysis allows for additional modeling of the baroclinic vorticity deposition produced by the shock-interface impact physics. Several scenarios for corrections to the asymptotic growth rate of Richtmyer have been investigated, with emphasis on the case of very strong incident shocks. Extensions to the present analysis could lead to improved understanding of the linear RMI in more complex applications, such as imploding waves propagating into a stratified medium (see Chapter 3).

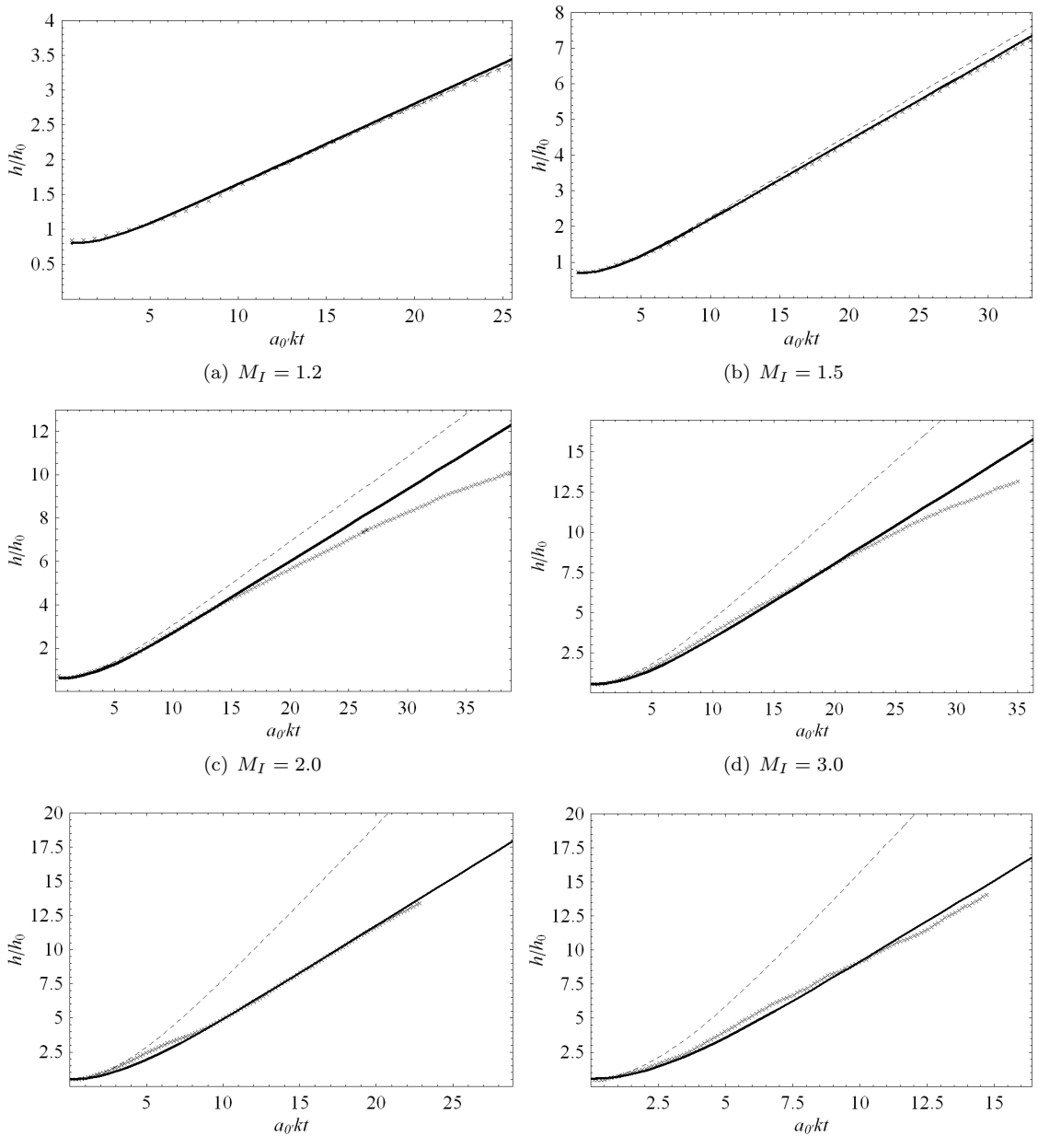

(a) $M_I = 1.2$ (b) $M_I = 1.5$

(c) $M_I = 2.0$ (d) $M_I = 3.0$

(e) $M_I = 5.0$ (f) $M_I = 8.0$

Figure 2.4: Influence of M_I: dimensionless amplitude of the interface perturbation $h(t)/h_0$ vs. a_0kt; case air $\rightarrow$ SF_6, $kh_0 = 0.1$. For key, see Figure 2.3.

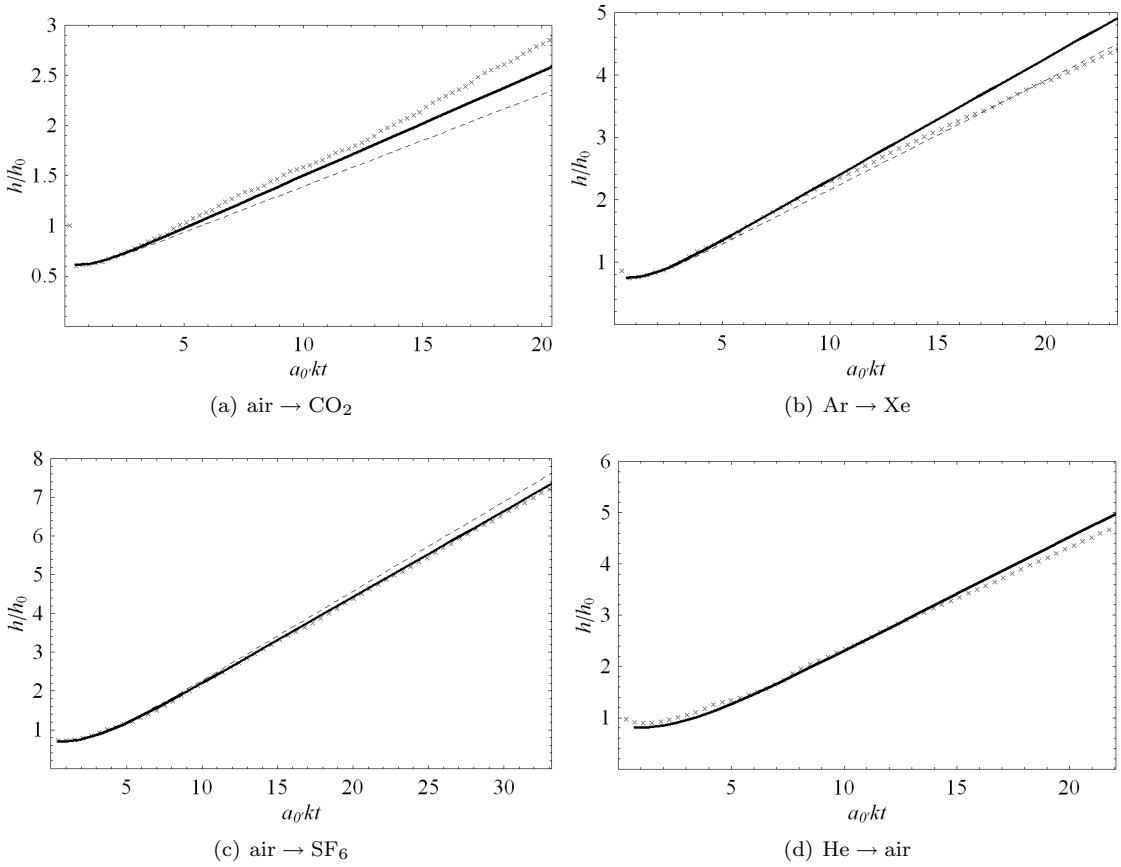

(a) air → CO_2 (b) Ar → Xe

(c) air → SF_6 (d) He → air

Figure 2.5: Influence of the species: dimensionless amplitude of the interface perturbation $h(t)/h_0$ vs. a_0kt; case $kh_0 = 0.1$, $M_I = 1.5$. For key, see Figure 2.3.

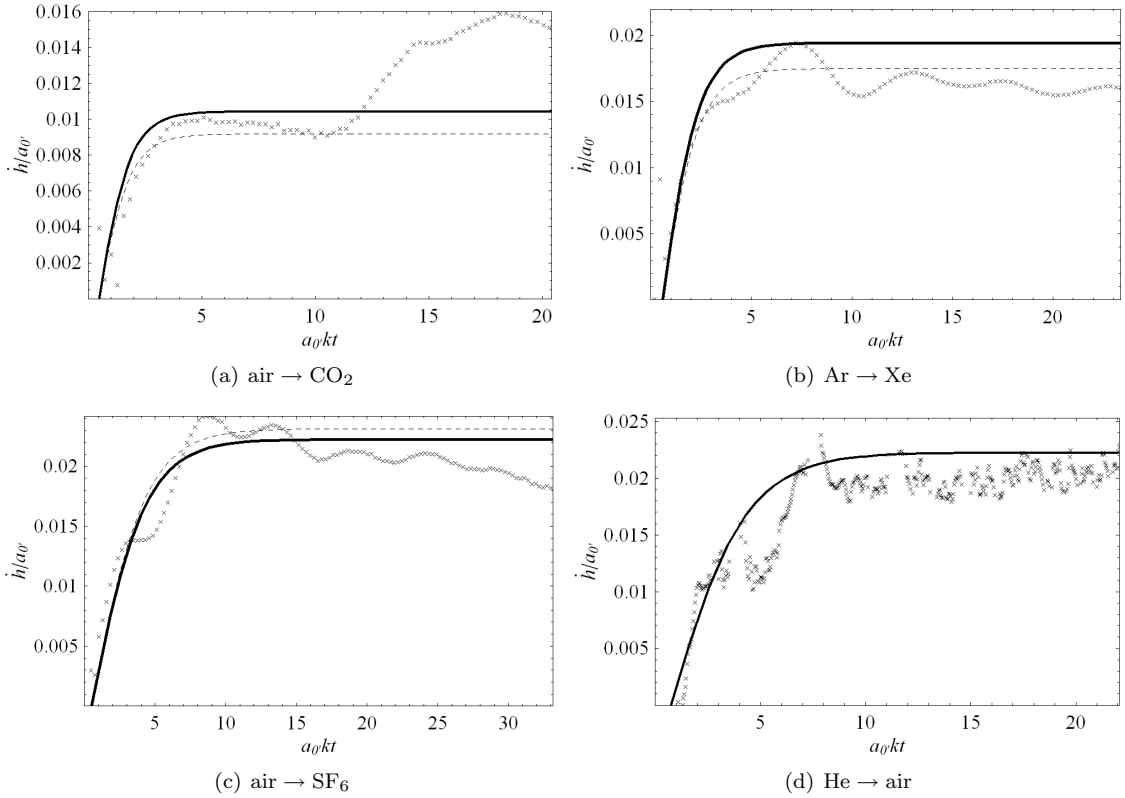

(a) air $\rightarrow CO_2$ (b) Ar $\rightarrow$ Xe

(c) air $\rightarrow SF_6$ (d) He $\rightarrow$ air

Figure 2.6: Influence of the species: dimensionless growth rate of the interface perturbation $\dot{h}/a_0$ vs. $a_0 kt$; case $kh_0 = 0.1$, $M_I = 1.5$. For key, see Figure 2.3.

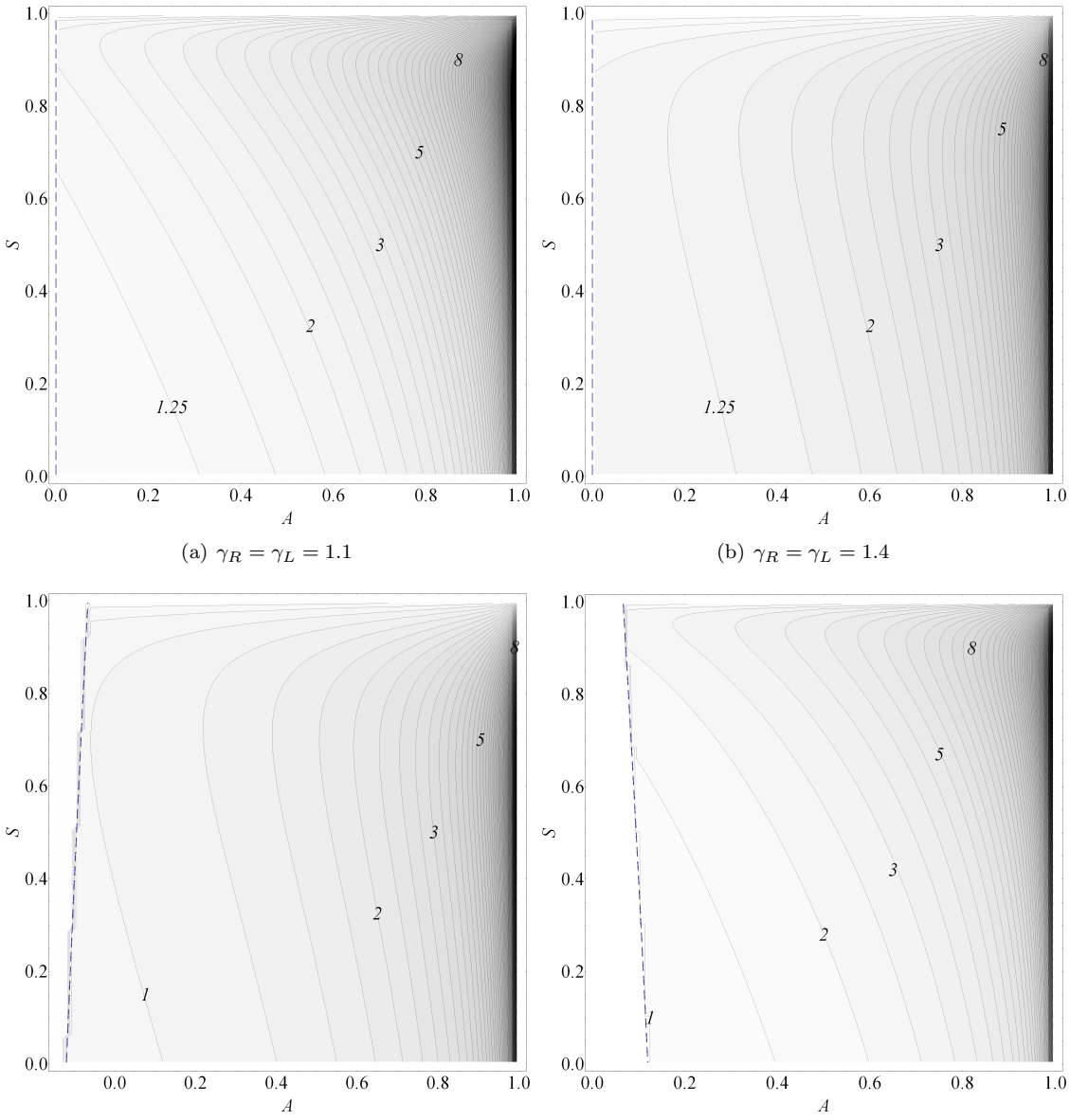

Figure 2.7: Contour levels of $a_0 k\tau$ in the (A, S) space; for each combination of specific heat ratios a dashed line drawn for small A represents the boundary of the domain of validity of τ as discussed in Subsection 2.5.1.

Chapter 3

Linear Perturbations in the Three-Dimensional Cylindrical Richtmyer-Meshkov Instability

3.1 Introduction

The research cited previously in Chapter 1 concerns mainly the non-linear and/or multi-mode regime of the RMI initialized with large interface perturbation amplitudes, as well as the reshock process and the subsequent turbulent mixing. Recent analytical work has also been reported on the effects of convergence on the linear, or small-amplitude regime of RMI occurring in spherical [80] and cylindrical [81] stratified shells. For simplicity, compressible effects often observed in the RMI of gases (such as shock refraction, shock proximity effects, etc. [116]) were omitted. Moreover, in the cylindrical case, Mikaelian only considered purely azimuthal perturbations.

Presently we study several features of the three-dimensional cylindrical RMI in the linear regime, using both simple analysis and numerical, Euler-based simulations. The analysis of Section 3.2 first extends, to three-dimensional azimuthal and axial perturbations, the results of Mikaelian (in the case of one shell). An explicit expression for the asymptotic growth rate of the cylindrical linear RMI is obtained. The effect of proximity of the transmitted and reflected shocks produced by the initial shock refraction is also modeled following the methodology described in Chapter 2. Section 3.3 compares results from the linearized analysis to numerical simulations of the RMI under various initial conditions. The effects of azimuthal and axial wavenumbers for different incident shock strengths and a comparison with the plane RMI are exposed.

3.2 Incompressible Linear Theory for Three-Dimensional Cylindrical Perturbations

3.2.1 General Evolution Equations

The interaction of a shock with a perturbed density interface is an atypical hydrodynamics stability problem. The shock refraction process produces distorted transmitted and reflected waves in the vicinity of the interface. The related perturbed pressure field induces perturbations in the tangential component of the velocity field to the interface, producing circulation that can be directly related to the initial baroclinic vorticity deposited at the interface. In what follows, $t = 0$ refers to the time right when the shock impacts the interface, in the zeroth-order, or unperturbed flow. We denote by the subscript $j = 1$ the region on the outer side of the interface where the incident shock originates, and by $j = 2$, the region on the inner side of the interface. This includes the axis.

The stability of density interfaces in converging geometries was studied by Plesset [86] in the particular case of spherical bubbles. For imploding flows, a sink-like motion with center $r = 0$ was used to produce flow/interface contraction while maintaining constant density. Following Plesset and Mikaelian [81], we model our base flow as an incompressible impulse sink of strength to be determined of the form $m(t) = \mu(t)H(t)$ with velocity potential

$$\Phi(r,t) = m(t)\ln\left(\frac{r}{R(t)}\right), \tag{3.1}$$

$R(t)$ being the base radial position of the interface and $H(t)$ the Heaviside function at time t. For an imploding, accelerated flow, $\mu(t) < 0$ for $t \geq 0$. Impulsively accelerated flow requires $m(0) < 0$. At this point, $\mu(t)$ and $R(t)$ remain to be specified. The base velocity field is given by

$$\boldsymbol{U}(r,t) = \frac{m(t)}{r}\boldsymbol{e}_r. \tag{3.2}$$

We consider three-dimensional azimuthal and axial infinitesimal perturbations about the time-dependent state $R(t)$ of the form

$$\phi_j'(r,\theta,z,t) = f_j(r)g_j(t)e^{i(n\theta+kz)} \tag{3.3a}$$

$$\zeta(\theta,z,t) = R(t) + h(t)e^{i(n\theta+kz)}. \tag{3.3b}$$

The perturbed potential $\phi_j'(r,\theta,z,t)$ for the gas j $(j = 1,2)$ is assumed to be separable in r and t, $\zeta(\theta,z,t)$ is the perturbed position of the interface after it has been impulsively accelerated by the passage of the shock and n and k are integers representing respectively the azimuthal and axial wavenumbers and are assumed to not be functions of time.

When the interface is strictly cylindrical, a kinematic condition that the radial velocity is continuous at the interface, and equal to an interfacial particle velocity gives that

$$\dot{R} = \left(\frac{\partial \Phi}{\partial r}\right)_{r=R}, \tag{3.4}$$

which leads to

$$\mu = R\dot{R}. \tag{3.5}$$

Full knowledge of the base flow therefore requires specification of the implosion/explosion history $R(t)$, at least for times such that the perturbation growth remains linear. We insist on the simple constraint that R is at least piecewise continuous at $t = 0$, and we define $R_0 \equiv \lim_{t\to 0} R(t)$. The interface speed $\dot{R}$ and the potential strength μ may be discontinuous at $t = 0$. The jump in $\dot{R}$ around $t = 0$ simply represents the impulsive change in the interface velocity ΔW. This presently models the impulsive acceleration produced by the shock interaction. Defining $\Delta W > 0$ for an implosion (respectively explosion) the jump in radial velocity is $-\Delta W$ (respectively ΔW) since the motion is inwards (respectively outwards). ΔW can be computed by solving the locally plane interaction of the incident shock with the unperturbed interface. Requiring that the base pressure field be continuous at the interface, and using Bernoulli's theorem shows that

$$\rho_1 \left[\frac{\partial \Phi}{\partial t} + \frac{1}{2}\left(\frac{\partial \Phi}{\partial r}\right)^2 - C_1(t)\right] = \rho_2 \left[\frac{\partial \Phi}{\partial t} + \frac{1}{2}\left(\frac{\partial \Phi}{\partial r}\right)^2 - C_2(t)\right]_{r=R}. \tag{3.6}$$

Consider now the distorted interface. The kinematic condition $D\zeta/Dt = (\boldsymbol{u}.\boldsymbol{n})_{r=\zeta}$, where $\boldsymbol{u}$ is the velocity field and $\boldsymbol{n}$ is the local normal to the interface, can be linearized and simplified as follows using the base kinematic condition (3.4)

$$\dot{h} + \frac{\dot{R}H}{R}h = g_j f_j'(R), \quad \text{for } j = 1, 2. \tag{3.7}$$

Similarly, a dynamic condition is obtained by linearizing the continuity of pressure at the perturbed interface and, using Equation (3.6) to give

$$R\dot{R}H\dot{h} + [(\dot{R}^2 + R\ddot{R})H + R\dot{R}\delta_D]h = \frac{R}{2}\left[\left(\frac{1}{A} - 1\right) f_1(R)\dot{g}_1 - \left(\frac{1}{A} + 1\right) f_2(R)\dot{g}_2\right]. \tag{3.8}$$

where $\delta_D(t)$ is the Dirac delta function and $A = (\rho_2 - \rho_1)/(\rho_2 + \rho_1)$ represents the Atwood number based on the densities on each side of the interface. To be precise, A should also depend on t in the radially imploding base flow, but in what follows, for simplicity, A will be assumed constant. Its value could be identified with the post-shock Atwood number A^+ given by the densities of

the two post-shocked regions found in the plane shock interaction analysis leading to ΔW. The unknown functions of time (h, g_1, g_2) can be found by solving numerically the set of three first-order ODE (3.7,3.8) given the history of the unperturbed interface position $R(t)$ and specific initial conditions.

3.2.2 Richtmyer's Approach

Richtmyer first modeled interfacial instability produced by a plane shock impact on a perturbed density interface using incompressible fluids. This essentially assumes that the transmitted and reflected waves have already traveled sufficiently far from the interface. He also replaced the constant gravitational acceleration of Taylor's [107] linear theory by an impulse that modeled the initial shock interaction as a brief event; this ignores the compressible effects of the initial shock refraction phase. Without loss of generality, we consider the case of an imploding shock interaction. Ignoring for now the transmitted and reflected waves, and assuming also that no re-shock has yet occurred following shock reflection off the axis, the relevant post-shock regions on each side of the interface to be considered are $\zeta < r < \infty$ for region $j = 1$, and $0 < r < \zeta$ for region $j = 2$.

The functions $f_j(r)$, $j = 1, 2$, are fully determined by solving the Laplace equation for the perturbed potential $\Delta\phi'_j = 0$ on each side of the interface. The $f_j(r)$ are then generally a linear combination of the modified Bessel functions of the first and second kinds, $I_n(kr)$ and $K_n(kr)$. For the fluid $j = 1$ (region $r > \zeta$), the boundary condition $\nabla\phi'_1 \to 0$ as $r \to +\infty$ is prescribed. For the fluid $j = 2$ (region $0 < r < \zeta$), ϕ'_2 should remain non-singular as $r \to 0$. We then obtain

$$f_1(r) = \begin{cases} K_n(kr) & ; \ k > 0 \\ \left(\frac{R_0}{r}\right)^n & ; \ k = 0 \end{cases}, \tag{3.9a}$$

$$f_2(r) = \begin{cases} I_n(kr) & ; \ k > 0 \\ \left(\frac{r}{R_0}\right)^n & ; \ k = 0 \end{cases}. \tag{3.9b}$$

We require h continuous at $t = 0$ and $h(0) \equiv \lim_{t\to 0} h(t)$ but for an impulsively accelerated flow modeling the shock refraction process, the g_j as well as $\dot{h}$ are *a priori* discontinuous at $t = 0$. Next, a set of dimensionless variables is prescribed as

$$\widetilde{h} = \frac{h}{h(0)}; \ \widetilde{r} = \frac{r}{R_0}; \ \widetilde{t} = \frac{t}{R_0/\Delta W}; \ \widetilde{g}_j = \frac{g_j}{h(0)\Delta W}. \tag{3.10}$$

together with an axial wavenumber $\kappa = kR_0$. Integrating the linearized dynamic condition (3.8) between $t = 0^-$ and 0^+ and using Equation (3.7), the growth rate of the three-dimensional pertur-

bation, as well as the perturbed potential functions g_j, at $t = 0^+$ are

$$\widetilde{\dot{h}}(0^+) = 1 + \kappa A F(n, \kappa, A), \tag{3.11a}$$

$$\widetilde{g}_1(0^+) = A\frac{F(n, \kappa, A)}{K_n'(\kappa)}, \tag{3.11b}$$

$$\widetilde{g}_2(0^+) = A\frac{F(n, \kappa, A)}{I_n'(\kappa)}, \tag{3.11c}$$

where $F(n, \kappa, A)$ is given by

$$F(n, \kappa, A) = 2\Big/\left((1 + A)\frac{I_n(\kappa)}{I_n'(\kappa)} - (1 - A)\frac{K_n(\kappa)}{K_n'(\kappa)}\right)^{-1}. \tag{3.12}$$

The result obtained for the growth rate assumes that transmitted and reflected waves are at large distances from the interface at $t = 0$. In that sense, the time $t = 0^+$ after the passage of the incident shock could refer to an asymptotic state, and Equation (3.11a) would represent the asymptotic growth rate of the instability in the sense of Richtmyer. Note that, as the linear growth rate in the plane RMI, the dimensional initial growth rate is proportional to the amplitude $h(0)$ at $t = 0$ (see next section), as well as ΔW, in other terms $-\dot{R}(0^+)$. The interface initial acceleration $\ddot{R}(0^+)$ does not appear in the initial growth rate. The initial growth rates for the plane and curved RMI are similar in that sense.

In order to compare the growth rate obtained in cylindrical geometry with its plane counterpart for a given A, we plot in Figure 3.1 the difference between the dimensionless growth rate given by (3.11a) with Richtmyer's asymptotic growth rate for a two-dimensional plane perturbation with equivalent wavenumbers k and n/R_0. The plane growth rate is $\sqrt{n^2 + \kappa^2}A$.

3.2.2.1 Limit Cases

Several limiting cases in A are of interest. In particular

$$\widetilde{\dot{h}}(0^+) \sim 1 \text{ if } A \to 0 \text{ , i.e., } \rho_1 \sim \rho_2, \tag{3.13a}$$

$$\widetilde{\dot{h}}(0^+) \sim 1 + \kappa\frac{I_n'(\kappa)}{I_n(\kappa)} \text{ if } A \to 1 \text{ , i.e., } \rho_1 \ll \rho_2, \tag{3.13b}$$

$$\widetilde{\dot{h}}(0^+) \sim 1 + \kappa\frac{K_n'(\kappa)}{K_n(\kappa)} \text{ if } A \to -1 \text{ , i.e., } \rho_1 \gg \rho_2. \tag{3.13c}$$

The growth when $A \to 0$ is purely kinematic produced by the converging geometry, also observed in spherical geometries. To verify this consider a fluid element at radius $R(t)+h(t)$ whose base velocity is $\mu(t)/(R(t) + h(t))$, and a fluid element at radius $R(t)$ with velocity $\mu(t)/R(t)$. Growth naturally appears due to this difference in velocities and produces a dimensionless growth rate equal to unity.

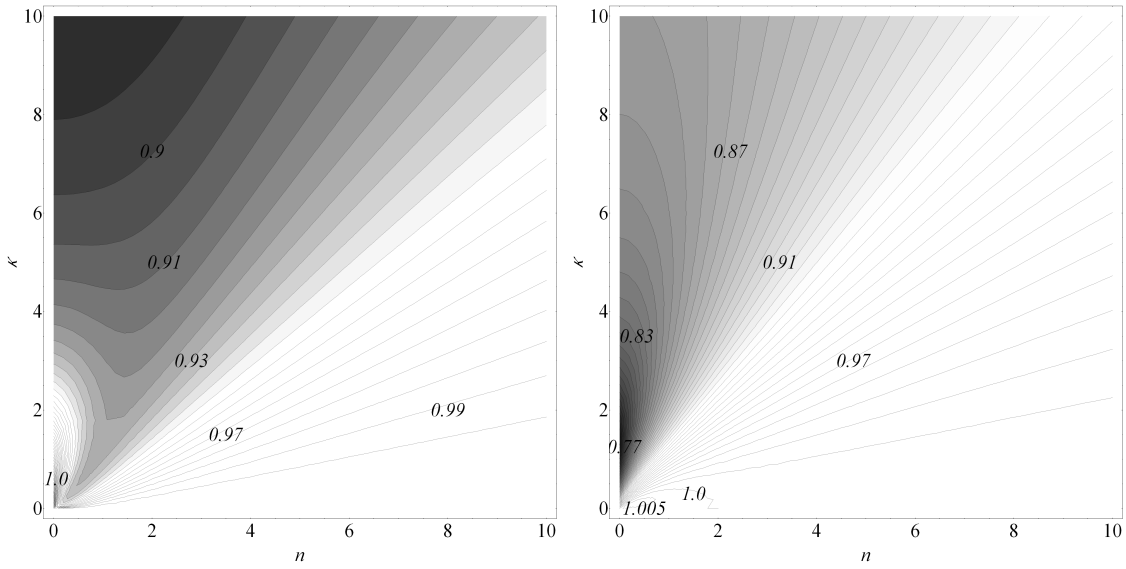

(a) $A = -0.5$ (b) $A = 0.5$

Figure 3.1: Iso-contours of the difference between the (dimensionless) cylindrical growth rate and the plane one $(1 + \kappa A F(n, \kappa, A)) - \sqrt{n^2 + \kappa^2} A$, in the wavenumber space (n, κ), with $\kappa \equiv kR_0$.

More interesting are the limit cases obtained when varying κ and n

$$\widetilde{\dot{h}}(0^+) \sim 1 + nA \text{ if } \kappa \ll n \text{ and } n \geq 1, \tag{3.14a}$$

$$\widetilde{\dot{h}}(0^+) \sim 1 + n\frac{2A}{1+A} \text{ if } \kappa \ll 1 \text{ and } n \ll 1, \tag{3.14b}$$

$$\widetilde{\dot{h}}(0^+) \sim 1 + \kappa A \text{ if } \kappa \gg n \text{ and } \kappa \gg 1. \tag{3.14c}$$

Equation (3.14a) corresponds to purely azimuthal perturbations [81], the limit $\kappa \ll n$ being equivalent to $\lambda_\theta \ll \lambda_z$ (strictly polar flow). The third limit behavior presented in Equation (3.14c) corresponds to purely axial perturbations. The effect of the curvature is not seen, except through the kinematic growth term, and the linear behavior is similar to the plane linear growth with z-perturbations. In dimensional quantities, the linear growth, excluding the kinematic growth component, is $kh(0)A\Delta W$, with $\Delta W = -\dot{R}(0^+)$, similar to Richtmyer's plane linear growth where ΔW was the constant speed at which the interface is accelerated in the direction of the shock propagation.

3.2.2.2 Critical Perturbations

We discuss here critical perturbations that are stable for any implosion or explosion history. For any $\dot{R}(t)$ or $\mu(t)$, then if $\dot{h}(t < 0) = 0$, then $\dot{h}(t) = 0, t > 0$. These perturbations do not grow and the perturbation amplitude remains fixed at h_0. Re-writing both conditions (3.7, 3.8) at the interface

for these critical perturbations, and integrating the second condition between $t = 0^-$ and $t > 0$ gives

$$\frac{\dot{R}H}{R} h_0 = g_j f_j'(R), \quad \text{for } j = 1, 2 \ , \tag{3.15a}$$

$$2h_0 \int_{0^-}^{t} \left[\left(\frac{\dot{R}^2}{R} + \ddot{R} \right) H + \dot{R} \delta_D \right] \mathrm{d}t = \left(\tfrac{1}{A} - 1 \right) \int_{0^-}^{t} f_1(R) \dot{g}_1 \mathrm{d}t - \left(\tfrac{1}{A} + 1 \right) \int_{0^-}^{t} f_2(R) \dot{g}_2 \mathrm{d}t \tag{3.15b}$$

Integrating by parts both integrals on the right-hand side of Equation (3.15b) and using Equation (3.15a) to evaluate the two resulting integrals produced, all integral terms cancel and, using Equations (3.9a,b) and (3.12), we obtain for any t

$$\left(kR\, A + \frac{1}{F(n, kR, A)} \right) \dot{R} = 0. \tag{3.16}$$

We eliminate the trivial case $\dot{R} = 0$ corresponding to a stationary interface. For a given history $R(t)$, and given n and k, critical perturbations occur only for specific values of $A_c \in [-1, 1]$ given by

$$1 + kR\, AF(n, kR, A) = 0. \tag{3.17}$$

Equation (3.17) is equivalent to determining the particular Atwood ratio $A_c \in [-1, 1]$ such that

$$A_c(n, kR) = \left(\frac{K_n(kR)}{K_n'(kR)} - \frac{I_n(kR)}{I_n'(kR)} \right) \Big/ \left(\frac{K_n(kR)}{K_n'(kR)} + \frac{I_n(kR)}{I_n'(kR)} + 2kR \right)^{-1}. \tag{3.18}$$

Iso-contours of A_c are plotted in Figure 3.2. It is observed that critical perturbations only appear for negative A which corresponds in general to a heavy-to-light shock interaction. The absolute value $|A_c|$ reaches its maximal value unity for a particular combination of small wavenumbers, while $|A_c| \to 0$ as the wavenumbers n or kR increase. Note also that Equation (3.17) is consistent with the expression (3.11a) in the limit $t \to 0, t > 0$, since $kR \to kR_0 \equiv \kappa$. We also recall that this phenomenon does not occur in plane geometry where the condition for critical perturbations derived from Richtmyer's impulsive growth rate is trivially $kA = 0$. In the limit of purely azimuthal perturbations $kR \ll n$ with $n \geq 1$, the condition $1 + nA = 0$ derived by Mikaelian in the case of one interface separating two cylindrical concentric shells ($N = 2$ in [81]) is recovered.

3.2.2.3 Assumption of Constant Interface Velocity

We now obtain an explicit expression for the growth amplitude as a function of time. For simplicity we consider the limit of purely azimuthal perturbations. Eliminating g_j from (3.8) using (3.7), a single second-order ODE for the perturbation amplitude h is obtained. This can be simplified in the azimuthal limit given (3.9a,b) for $k = 0$. The result has a form similar to that obtained by Bell [2]

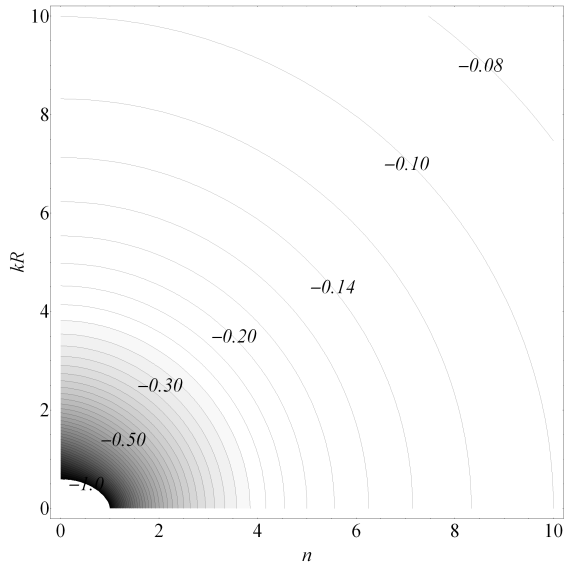

Figure 3.2: Contour levels of the Atwood ratio A_c corresponding to critical perturbations, in the wavenumber space (n, kR), for a given history $R(t)$.

for $A = \pm 1$ and for general Atwood ratios by Mikaelian (Equation (16) of [81])

$$\frac{\mathrm{d}}{\frac{d}{t}}\left(R^2\dot{h}\right) + (nA+1)[R\ddot{R}Hh + R\dot{R}(\delta_D h + (H-1)\dot{h})] = 0. \tag{3.19}$$

Our form is a result of defining the problem through the strength $m(t)$. Integrating the previous equation between $t = 0^-$ and t, t being sufficiently small enough that can assume that the imploding or exploding interface velocity remained almost unchanged), we integrate Equation (3.19) in t and recover Equation (3b) of [81] obtained assuming that the interface moves at a constant velocity ΔW related to the constant impulsive acceleration $\Delta W \delta_D(t)$. The dimensionless perturbation amplitude is:

$$\widetilde{h}(\widetilde{t}) = 1 - (nA+1)\left(1 - \frac{1}{\widetilde{R}(\widetilde{t})}\right), \tag{3.20}$$

where $\widetilde{R} \equiv R/R_0$ is the dimensionless position of the interface. Since the interface is assumed to move at a constant speed, $\widetilde{R}(\widetilde{t}) = 1 - \widetilde{t}$, and Equation (3.20) suggests that in the case $\widetilde{t} \ll 1$ (i.e., for large radii $R_0 \gg \Delta W\, t$ in the linear regime time considered), the dimensional perturbation amplitude reduces to $h(0)(1 + (nA+1)\Delta W t/R_0)$, which corresponds to the plane perturbation amplitude derived by Richtmyer $h(0)(1 + KA\Delta W t)$ if we replace K by n/R_0 (initial wavelength $2\pi R_0/n$) and ignore the geometrical component of the growth.

3.2.2.4 Effect of the Interface Acceleration

Unlike the planar case, the present unperturbed, or base flow, has no analytical solution. Further, we have so far ignored the acceleration of the interface for $t > 0$ produced by the nonuniform flow behind the converging shock. A detailed analysis presented in Appendix A utilizes the solution of Chisnell [15] for the flow behind the shock to approximate the post-shocked interface position right after the shock interaction ($t > 0$). We refer to Subsection 3.3.3 for a precise description of Chisnell's solution. This takes into account the post-shock acceleration of the interface $\ddot{R}(0^+)$. In dimensionless variables, this result can be expressed as

$$\widetilde{R}(\widetilde{t}) = 1 - \widetilde{t} - \frac{\left(\dfrac{\alpha_2}{V_{0_2}} - 1\right)\left[(2\alpha_2\gamma_2 - \gamma_2 - 1)\dfrac{\alpha_2}{V_{0_2}} - \alpha_2(\gamma_2 - 1)\right]}{2\alpha_2\left(2\dfrac{\alpha_2}{V_{0_2}} + \gamma_2 - 3\right)\dfrac{\alpha_2}{V_{0_2}}}\,\widetilde{t}^{\,2} + \mathcal{O}\left(\widetilde{t}^{\,3}\right), \tag{3.21}$$

where γ_2 is the adiabatic exponent in the fluid $j = 2$. For a given space index s (equal to 2 in cylindrical geometry), Guderley's exponent α_2 and the coefficient α_2/V_{0_2} (see Equation (3.10) of [15]) depend only on γ_2. For the case of SF_6, $\gamma_2 = 1.09$, $\widetilde{R} \simeq 1 - \widetilde{t} - 0.011\widetilde{t}^{\,2}$. This model predicts that, when the interface has traveled half-way to the origin, the trajectory correction due to the acceleration is of about 0.6%. By comparison, simulations in the same fluids using the same initialization showed a departure of about 2% for a wide range of incident Mach number. At this time of the instability growth, the interface has shown substantial radial convergence and the amplitude grown sufficiently that we can conclude that the interface acceleration effect is small compared with more important effects such as pure geometrical convergence, non-linearities, or shock proximity, as discussed in the following paragraph.

3.2.3 Effect of Shock Proximity

Until now the analysis has focused on the growth rate attained by small three-dimensional cylindrical perturbations assuming that reflected and transmitted waves produced by the shock refraction were instantaneously at infinity immediately following shock-interface impact. This asymptotic growth rate, written $\dot{h}(0^+)$ and defined in dimensionless variables by Equation (3.11a), is hereinafter denoted $\dot{h}_\infty$. To evaluate $\dot{h}_\infty$, A is now taken as the post-shock Atwood ratio A^+ and $h(0)$ the post-shock amplitude $h(0^+)$.

One effect to consider here is well described in Chapter 2 in the case when the reflected wave is a shock, in general characterizing light-to-heavy-type shock interactions. As both transmitted and reflected shocks recede, they limit the early small perturbation growth rate, which ultimately reaches the asymptotic level $\dot{h}_\infty$ in a characteristic time τ (see Equations (2.16, 2.19)). A typical case for which the model proves useful is large A; in this situation τ becomes very large and shock

proximity effects cannot be neglected (see for example Equation (2.37). Applying this model with the present conventions for the regions $j = 1$ and 2:

$$\dot{h}(t) \quad = \quad \frac{2\,\dot{h}_\infty}{(1-A^+)\coth(KS_1(t)) + (1+A^+)\coth(K(-S_2(t)))}, \tag{3.22}$$

where $S_1(t)$ (respectively $S_2(t)$) is the shock position of the reflected (respectively transmitted) shock evaluated in the frame of the moving interface and K is the wavenumber of the perturbation. Derived in plane geometry, the model allows for the choice of the shock positions. For simplicity, we assume, as in the plane case, that the shocks are moving at a constant speed U_{S_j} determined by solving the locally normal one-dimensional Riemann problem of an incident cylindrical shock impacting a cylindrical density interface. This assumption is justified in the plane case but ignores the non-uniform nature of the flow behind the traveling shock waves in the converging case. Because the modeling of the time-dependency of the shock speeds is not a trivial problem, we leave it for future work. For axial perturbations, $K \equiv k$. For azimuthal perturbations, the wavelength $\lambda_\theta(t) = 2\pi R(t)/n$ is time-dependent, and the corresponding wavenumber should be taken equal to $n/R(t)$. For simplicity, K will presently be identified with the initial azimuthal wavenumber $K \equiv n/R_0$.

3.3 Numerical Simulations of the Converging Cylindrical Linear RMI

3.3.1 Numerical Method

The simulations, run on the Lawrence Livermore National Laboratory (LLNL) machine *unclassified Purple* (uP), were conducted within the AMROC framework of Deiterding [21], based on the SAMR algorithm by Berger and Oliger [4]. The numerical method, applied to each Cartesian subgrid of the mesh hierarchy, consists of a hybrid method written for the multi-component Euler equations of gas dynamics assuming calorically perfect gas. A WENO scheme is used to capture discontinuities (such as shock waves, contact wave, or fine/coarse mesh interfaces) but switches to a low-numerical dissipation, explicit, center-difference scheme, TCD, in the smooth regions [44, 83].

Assume first purely azimuthal perturbations (no dependence on the axis coordinate z). The density interface, is nominally defined by a scalar field $\psi(r, \theta, t)$, interpolated from Cartesian data onto cylindrical coordinates, that asymptotic to $\psi(r, \theta, t) = 0$ on the air side and $\psi(r, \theta, t) = 1$ on SF_6. This is initially setup using a tanh profile with intrinsic thickness δ_0^C taken as about one fifth of the pre-shock perturbation amplitude h_0. When the shock impacts the smeared interface, it is compressed down to a thickness δ^C until the end of the shock refraction where both reflected and

transmitted shock travel away from the interface. It is important to ensure that during the whole simulation, in particular during the shock interaction, δ^C is fully resolved. The resolution, controlled by the number of refinement levels, is chosen such that at least 10 points are used to resolve the interface thickness.

At $t > 0$, we define the centerline of the smeared density interface by

$$r_c(\theta, t) \equiv \frac{\int_0^\infty r(1-\psi)\psi \mathrm{d}r}{\int_0^\infty (1-\psi)\psi \mathrm{d}r}. \tag{3.23}$$

At given t, for a fixed polar orientation θ, the scalar profile is well approximated by a tanh centered at $r_c(\theta, t)$ and with thickness $\delta^C(t)$:

$$\psi(\theta, t) = \frac{1}{2}\left[1 + \tanh\left(\frac{2(r - r_c(\theta, t))}{\delta^C(t)}\right)\right]. \tag{3.24}$$

It is easily verified that $r_c(\theta, t)$ is recovered when (3.24) is used in (3.23). The spike and the bubble positions and the flow velocity at these locations allow determination of the perturbation amplitude and growth rate as

$$h(t) = |\frac{r_{c_{spike}} - r_{c_{bubble}}}{2}|, \tag{3.25a}$$

$$\dot{h}(t) = |\frac{u_r|_{r_{c_{spike}}} - u_r|_{r_{c_{bubble}}}}{2}|. \tag{3.25b}$$

In order to compute the growth amplitude and rate of the spikes and bubbles, a simulation of the unperturbed system is run independently so that the position of the base interface centerline $r_{c_{unpert}}(t)$ can be calculated. We then define

$$h_S(t) = |\frac{r_{c_{spike}} - r_{c_{unpert}}}{2}|, \qquad h_B(t) = |\frac{r_{c_{bubble}} - r_{c_{unpert}}}{2}|, \tag{3.26a}$$

$$\dot{h}_S(t) = |\frac{u_r|_{r_{c_{spike}}} - u_r|_{r_{c_{unpert}}}}{2}|, \qquad \dot{h}_B(t) = |\frac{u_r|_{r_{c_{bubble}}} - u_r|_{r_{c_{unpert}}}}{2}|. \tag{3.26b}$$

The same process can be followed for purely axial perturbations (no dependence in θ) where, for a given z and t, the position of the interface centerline $r_c(z, t)$ is computed.

We choose $1/(a_0 K)$ as the reference time scale for data representation, where a_0 is the speed of sound in the region $j = 1$ ahead of the incident shock and K is the perturbation wavenumber ($K = k$ for purely axial modes and $K = n/R_0$ for purely azimuthal modes). The reference scale for the interface, spike, and bubble amplitudes is the pre-shock amplitude h_0, and the asymptotic growth rate $\dot{h}_\infty$ is the reference scale for the different growth rates represented. Note that the model for $\dot{h}/\dot{h}_\infty$ given by Equation (3.22) and plotted as a function of the dimensionless time $a_0 kt$ depends only on the incident Mach number through the values of A^+ and the shock velocities.

3.3.2 Parameters

Air $\rightarrow$ SF_6 is the combination of gases chosen. The ratios of specific heats are $\gamma_1 \equiv \gamma_{\text{air}} = 1.40$ and $\gamma_2 \equiv \gamma_{SF_6} = 1.09$. The pre-shock Atwood ratio is chosen such that the temperature is continuous across the initial interface, which is consistent with experimental conditions. Consequently A is a function only of the molecular weights of both species. For the gas combination chosen, the Atwood ratio $A = 0.67$ is large enough that the effects of shock proximity are important. The pre-shock perturbation amplitude h_0 is taken sufficiently small in order to remain in the linear regime as long as possible. We choose $h_0/R_0 = 0.005$. Post-shock amplitude and Atwood ratio h_0^+ and A^+ are evaluated from the simulation right after the shock interaction and depend on the incident shock strength. The varying parameters involved are the incident shock Mach number M_I immediately before impact onto the interface, and the perturbation wavenumbers n and k. To a given combination of parameters corresponds a numerical simulation from which amplitude and growth rate of the interface, spikes and bubbles are obtained. For what follows, we will refer to the plane case as the one commonly described in the literature, presented in Chapter 2 (for air$\rightarrow$ SF_6) and eventually in Subsection 3.3.6.

3.3.3 Converging Shock

We consider here ideal gases of different densities through which propagates an imploding shock wave. In order to describe correctly the converging character of the flow behind a shock front traveling down to the origin from infinity, the computation is initialized with solution of Chisnell [15]. Chisnell obtained an explicit approximate analytical solution for the full gas-dynamics flow behind a radially symmetric, imploding shock. Self-similar solutions are sought in terms of the variable $\xi = r/R_S(t)$ where the distance $R_S(t)$ of the shock from the origin at time t is given by

$$R_S(t) = R_{S_0}\left(\frac{t_S - t}{t_S}\right)^{\alpha}, \tag{3.27}$$

The Mach number M_S of the shock at $t = 0$ when the shock is at $r = R_{S_0}$ is related to the implosion time t_S through

$$t_S = \frac{\alpha R_{S_0}}{M_S a_0}. \tag{3.28}$$

Apart from this particular subsection, the imploding shock is referred to as the incident shock and its Mach number M_S at $t = 0$ is noted M_I, and the implosion t_S will be noted t_I. A study of the singular points of the set of the three ODE in ξ obtained for the density, radial velocity and pressure leads the determination of the similarity exponent α for different values of the specific heat ratio γ and for cylindrical ($s = 2$) and spherical ($s = 3$) geometries. The system of equations may be

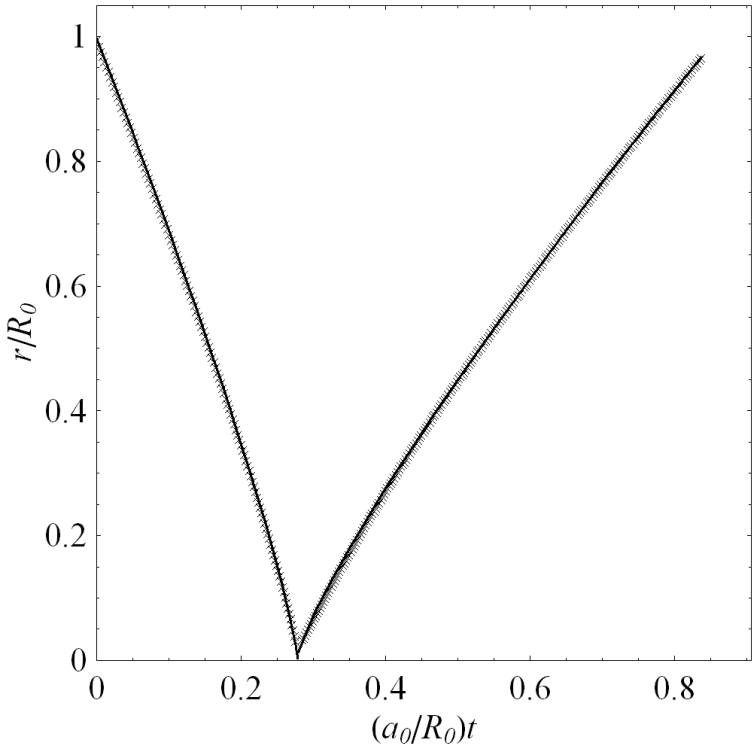

Figure 3.3: Imploding and exploding shock front average radial positions r/R_0 vs. $(a_0/R_0)t$. Superposition of two-dimensional simulation results of cylindrical shock initialized by Chisnell's solution (crosses) and a power-law least-square fit for both imploding and exploding shocks (solid line).

decoupled to provide a single ODE (Equation (2.11) in [15]) to integrate approximately and two supplementary equations to solve subsequently from the first one. Non-dimensional forms of the density ρ, radial velocity u_r and pressure p at time t and radial position r behind the shock, when this is located at $R_S(t)$, are obtained as a function of the similarity variable ξ:

$$\frac{\rho}{\rho_S} = \left(\frac{\alpha - \mathrm{V}(\xi)}{\alpha - \mathrm{V}_S}\right)^{\eta} \left(\frac{\mathrm{V}(\xi) + \mathrm{q}}{\mathrm{V}_S + \mathrm{q}}\right)^{\mathrm{D}}, \tag{3.29a}$$

$$\frac{u_r}{u_S} = \left(\frac{\mathrm{V}(\xi)}{\mathrm{V}_S}\right)^{1-\alpha} \left(\frac{\mathrm{V}(\xi) + \mathrm{q}}{\mathrm{V}_S + \mathrm{q}}\right)^{\mathrm{F}}, \tag{3.29b}$$

$$\frac{p}{p_S} = \left(\frac{\mathrm{V}(\xi)}{\mathrm{V}_S}\right)^{2(1-\alpha)} \left(\frac{\mathrm{V}(\xi) + \mathrm{q}}{\mathrm{V}_S + \mathrm{q}}\right)^{\mathrm{H}}, \tag{3.29c}$$

where, for each ξ, $\mathrm{V}(\xi)$ is found by solving

$$\xi = \left(\frac{\mathrm{V}_S}{\mathrm{V}}\right)^{\alpha} \left(\frac{\mathrm{V} + \mathrm{q}}{\mathrm{V}_S + \mathrm{q}}\right)^{\mathrm{F}}, \tag{3.30}$$

and in which (ρ_S, u_S, p_S) correspond to the flow just behind the shock (therefore depending on t), and are determined using Rankine-Hugoniot jump conditions normal to the shock. In Equation (3.29)

and (3.30), $(\mathrm{V}_S, \mathrm{q}, \eta, \mathrm{D}, \mathrm{F}, \mathrm{H})$ only depend on s and γ, directly or through α and α/V_0, which are determined by iteration in Section 3 of [15]. Approximate values for this couple are provided in Table 1 of [15] for various γ. Explicit expressions for the constants $(\mathrm{V}_S, \mathrm{q}, \eta, \mathrm{D}, \mathrm{F}, \mathrm{H})$ are

$$\mathrm{V}_S = \frac{2\alpha}{\gamma-1}, \tag{3.31a}$$

$$\mathrm{q} = -\frac{\alpha}{V_0}\frac{1}{1-s(\alpha/V_0-1)^2}, \tag{3.31b}$$

$$\eta = \left(\frac{s\gamma\alpha}{2(1-\alpha)}-1\right)^{-1}, \tag{3.31c}$$

$$\mathrm{D} = \frac{s-1}{1-s(\alpha/V_0-1)^2} - \left(\frac{s\gamma\alpha}{2(1-\alpha)}-1\right)^{-1}, \tag{3.31d}$$

$$\mathrm{F} = \alpha - \frac{1-(\alpha/V_0-1)^2}{1-s(\alpha/V_0-1)^2}, \tag{3.31e}$$

$$\mathrm{H} = \gamma\frac{s-1}{1-s(\alpha/V_0-1)^2} - 2(1-\alpha). \tag{3.31f}$$

The advantage of utilizing Chisnell's converging shock solution to initialize our RMI simulations is that, besides being easy to implement, it completely avoids spurious waves, such as those that would be produced using a standard initial Riemann problem-type initialization. It also leaves only the shock thickness as intrinsic length scale, since the shock has no memory of when it was produced.

As a preliminary test that the structure of the flow behind the converging shock, the shape, strength, and position of its front are correctly computed, we set up the simulation of a single self-similar converging shock traveling in air (assuming a constant $\gamma \simeq 1.40$). At $t = 0$, the shock has a Mach number $M_S = 3.0$ and stands at $R_{S_0} = R_0 = 1.0$, which represents $300\Delta x$, where the grid size Δx is the only length scale in the problem. Since the numerical method is written for Cartesian meshes, the circularity of the shock needs to be checked as it travels down to the center and reflects off as an exploding shock. The eccentricity of both imploding and exploding remains less than 0.002 which proves negligible the effects of the grid on the axisymmetry of the numerical solution. The self-similar structure of the flow behind the shock has also been observed down to very small radial positions of the shock front. Figure 3.3 shows good agreement between Guderley's solution and numerical simulations initialized using Chisnell's solution for the evolution of the shock front radial position. Results of a 3-parameter least-square fit of the form $R_{S_0}(1-t/t_S)^\alpha$ for the imploding shock and $R_S^E(t/t_S-1)^{\alpha^E}$ for the exploding shock are displayed on Table 3.1. The exact dimensionless implosion time is given by $(a_0/R_0)t_S = \alpha/M_S$ on Equation (3.28). The theoretical value $\alpha = 0.83532$ for $\gamma = 1.40$ can be found from various studies. First, Guderley's similarity solution assuming strong shock, the shock radius is given by the time relative to the time at which it reaches the center raised to some power smaller than unity [40]. Chester [13], Chisnell [14], and Whitham [114, 115] used geometrical shock dynamics to find approximate solutions, in which their approximate result for

the spherical case differs from the exact Guderley exponent by less than one percent. Hafner also found very precise values of the exponent using power series to solve the equations describing the imploding flow in Lagrangian coordinates [41]. Chisnell's recent description [15] provides us with approximate values of the exponent for cylindrical and spherical geometries and various γ, including the limits $\gamma \to 1^+$ and $\gamma \to \infty$. Good agreement is found between best fit and simulation data, and it is interesting to notice that the exploding shock has the same Guderley's exponent as the imploding shock, which has been observed in [40, 87].

Imploding shock	R_{S_0}/R_0	$(a_0/R_0)t_S$	α
exact	1.00	0.27844	0.83532
best fit	0.995	0.278	0.8354
Exploding shock	R_S^E/R_0	$(a_0/R_0)t_S$	α^E
exact	...	0.27844	0.83532
best fit	0.533	0.278	0.8355

Table 3.1: 3-parameter least-square fit for imploding and exploding shocks.

3.3.4 Axial Perturbations

This configuration is axisymmetric, as shown in Figure 3.4, since no azimuthal perturbation is applied. Highly refined two-dimensional simulations are performed in a plane (r, z) with azimuthal orientation θ. Geometric source terms are added to the right-hand side of the Euler equations to take into account the axisymmetry of the flow. The influence of the axial wavenumber and the incident Mach number are investigated. In this configuration, the main effect of the geometry on the axial perturbations is due to the acceleration of the flow towards the center.

3.3.4.1 Influence of the Axial Wavenumber k

Figure 3.5 shows the amplitude and growth rate of the interface perturbation, spikes (heavy fluid penetrating into light fluid), and bubbles (light fluid penetrating into heavy fluid), as a function of time, when a $M_I = 1.2$ incident shock impacts the air$\rightarrow$ SF_6 contact. Plots of the growth

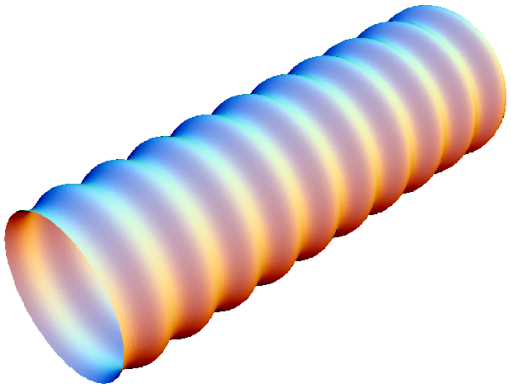

Figure 3.4: Purely axial perturbations for a cylindrical interface.

rates suggest that the higher frequency oscillations, a compressible-flow effect produced by the reverberation of waves traveling between the interface and the shocks, scale like the wavenumber k of the perturbation (we insist that M_I is fixed). The interface growth rate reaches an asymptotic value well predicted by the theoretical model described in Paragraph 3.2.2 and is well captured by the model extension using the reflected and transmitted shocks as walls moving at constant speeds in the frame of an interface moving also at a constant velocity, even though both shocks and interface accelerate when converging toward the origin. At late times, in particular for the highest wavenumber for which the asymptotic growth rate is the largest, the growth of the amplitude slows down, suggesting the appearance of non-linear effects as the amplitude becomes larger. The plots describing the spike and bubble behavior show that, first, a change of k mostly affects the bubble growth, and second, the late time slow-down is principally due to the slow-down in the bubble growth.

3.3.4.2 Influence of the Incident Shock Mach Number M_I

As we increase the incident Mach number for a fixed wavenumber, we first observe from Figure 3.6 that the oscillation frequencies do not only scale like the perturbation wavenumber but also on some unknown function of M_I. The interface amplitude and growth rate plots Figure 3.6a,b show that, for strong shock interaction, as the transmitted shock and interface converge faster toward the axis, the growth accelerates and fails to reach an asymptotic value as observed in the plane case for a wide range of M_I, or the axial case at low M_I. It should be noticed that, as M_I increases, the early linear regime is reduced as the perturbation amplitude does not remain small and, the interface and the transmitted shock converges faster towards the axis. As a consequence, the results were reported for a more limited time window. Since we observed earlier (see Paragraph 3.2.2.4) that the

acceleration of the interface has small effect, and noting that, for strong shocks, the interface tends to follow closely the transmitted shock, we suggest that the shock proximity is the main effect for the acceleration of the growth. This is not captured by the moving-wall model because, first, the transmitted shock speed is not constant (although when not too close to the origin its acceleration is not that large, as for the interface). Second, accelerating shocks should be used in our moving-wall model instead of walls moving at constant speed as it is the case in the plane geometry.

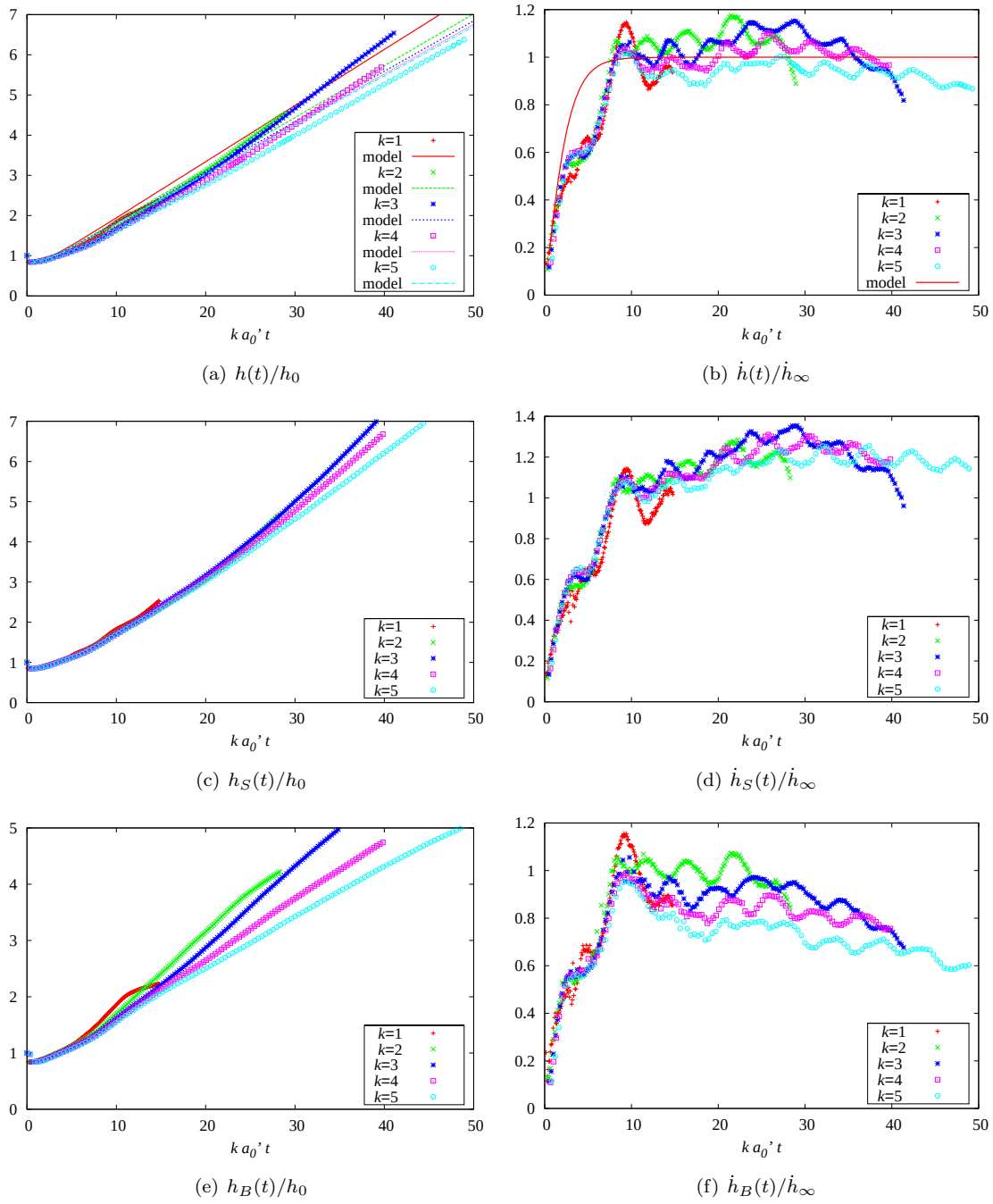

Figure 3.5: Axial perturbations: Dimensionless amplitude (left) and growth rate (right) vs. a_0kt of the interface perturbation (top), spike front (middle), and bubble front (bottom), plotted for different axial wavenumbers k; case air $\rightarrow$ SF_6, $h_0/R_0 = 0.005$, $M_I = 1.2$.

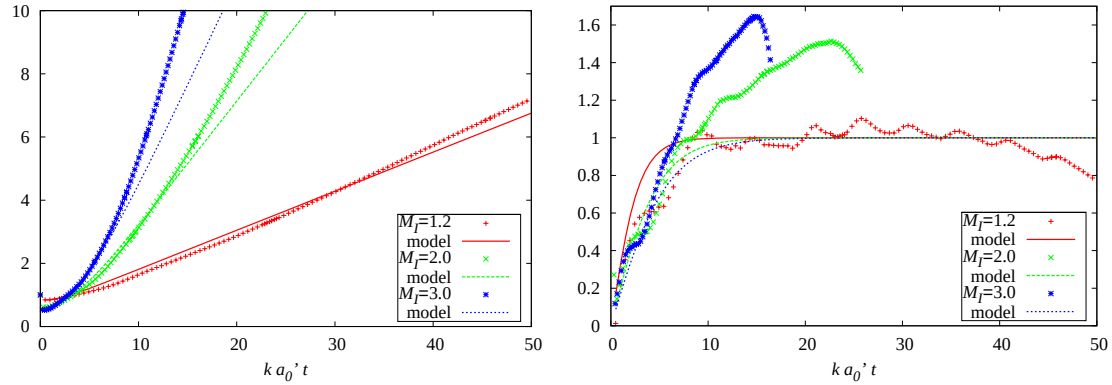

(a) $h(t)/h_0$ (b) $\dot{h}(t)/\dot{h}_\infty$

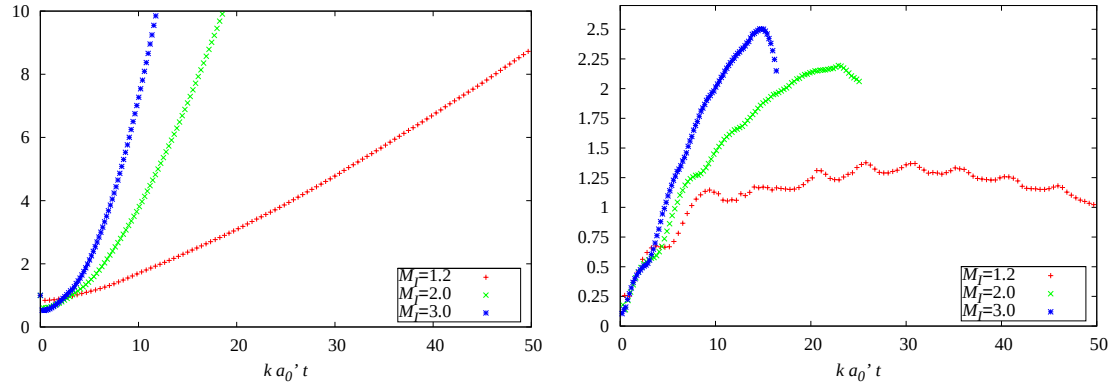

(c) $h_S(t)/h_0$ (d) $\dot{h}_S(t)/\dot{h}_\infty$

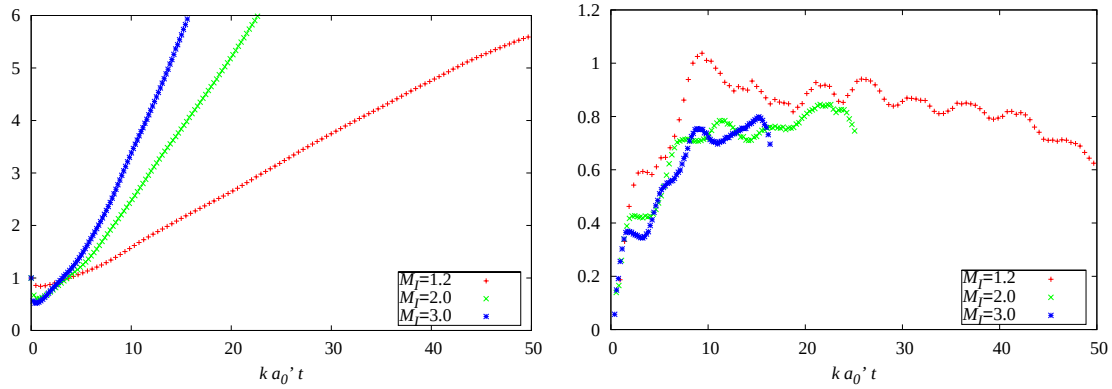

(e) $h_B(t)/h_0$ (f) $\dot{h}_B(t)/\dot{h}_\infty$

Figure 3.6: Axial perturbations: Dimensionless amplitude (left) and growth rate (right) vs. a_0kt of the interface perturbation (top), spike front (middle), and bubble front (bottom), plotted for three different incident Mach numbers M_I; case air $\rightarrow$ SF_6, $h_0/R_0 = 0.005$, $k = 4$.

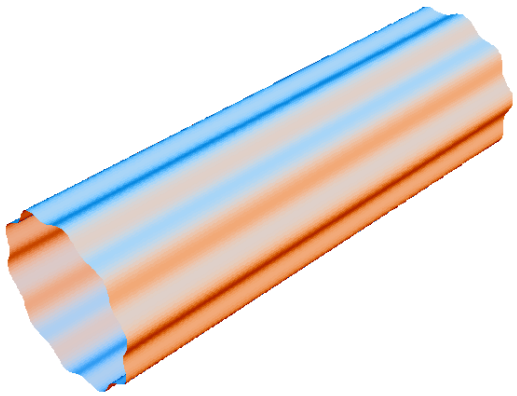

Figure 3.7: Purely azimuthal perturbations for a cylindrical interface.

3.3.5 Azimuthal Perturbations

We consider zero axial perturbation, as shown in Figure 3.7. Highly refined, two-dimensional simulations are performed in a polar plane (r, θ) with axial co-ordinate z, and the influence of the azimuthal wavenumber as well as M_I are considered. Two geometrical effects are present in this case: the acceleration of the flow towards the origin, like in the axial case, and the convergence effect as the azimuthal wavelength decreases during the implosion (the mode number n being invariant).

3.3.5.1 Influence of the Azimuthal Wavenumber n

As shown in Figures 3.8a,b obtained for M_I fixed, the model tends to predict well the characteristic time scale for the growth to reach a plateau. However, the value of the asymptotic growth rate is not well predicted for small n. For the highest value, the perturbation seems less sensitive to the effect of the curvature of the base interface; infinite values would correspond to the plane case. Indeed, similar to the plane case or the axial case, our best prediction of the asymptotic growth rate occurs for the case of highest n. Some high frequency oscillations are present for early times but tend to slowly disappear at later times, which was not the case in the axial or plane case. We conclude that the geometrical effect produced by converging geometry and predominant for low n is the main factor affecting the growth of the azimuthal instability, more so than the acceleration of both the interface and the transmitted shock. From Figures 3.8c–f, the behavior of the bubble structures, more than the spikes, shows the influence of curvature on the global growth of the interface.

3.3.5.2 Influence of the Incident Shock Mach Number M_I

The wavenumber is fixed to a quite high value, $n = 36$, so that the effect of the curvature discussed in the last paragraph is more de-correlated from the effects that the variation of M_I would produce.

The early time behavior observed in Figure 3.9b exhibits a plateau after the first initial acceleration of the growth. The duration of this plateau decreases as M_I increases. Ultimately, an acceleration of the growth is observed, while in the axial case shown in Figure 3.6 the growth acceleration for high M_I immediately follows the initial acceleration (for a dimensionless wavelength $kR_0 = 32$ comparable to $n = 36$). This is due to the fact that, as the interface is intensely accelerated towards the center by stronger incident shocks, the azimuthal wavenumber $n/R(t)$ increases accordingly and so does the growth.

3.3.6 Comparison Between Plane and Cylindrical Geometries

Both axial and azimuthal perturbations are compared to the plane growth, choosing the same wavelength $K = 3$ and amplitude $Kh_0 = 0.12$ just before the shock interaction occurs. We choose $M_I = 1.2$. Our earlier discussion is well summarized in Figure 3.10. It shows that the particularities in the growth increase as we go from plane to axial to azimuthal geometries, as the acceleration, shock proximity, and curvature effects impose their influences.

3.4 Summary

We have studied the linear stability of an interface between two compressible fluids following the passage of an imploding or exploding shock wave. Assuming incompressible flow between the transmitted and reflected shocks following shock impact, we have derived an expression for the asymptotic growth rate for a three-dimensional combination of single-mode azimuthal and axial perturbations as a function of the Atwood ratio A, the axial wavenumber k, the azimuthal wavenumber n, the initial radial position of the interface R_0, the perturbation amplitude $h(0)$ during the shock passage and ΔW the interface velocity right after the shock interaction:

$$\dot{h}_\infty = \frac{h(0)}{R_0}\Delta W\left[1 + 2kR_0A\Big/\left((1+A)\frac{I_n(kR_0)}{I_n'(kR_0)} - (1-A)\frac{K_n(kR_0)}{K_n'(kR_0)}\right)^{-1}\right]. \qquad (3.32)$$

Several different limit cases have been investigated, allowing recovery of Mikaelian's azimuthal theory [81] and Richtmyer's plane model [94]. We have discussed the existence of perturbations with zero growth, typical of curvilinear geometries and obtained for particular Atwood ratios given axial and azimuthal wavenumbers. The effect of shock proximity on the interface growth rate has been studied in the case of a reflected shock, which corresponds in general to a light-to-heavy shock interaction. Analytical predictions of the effect of parameters such as the incident shock strength, A, and both k and n have been compared with results obtained from highly resolved numerical simulations of cylindrically perturbed interfaces separating two perfect gases and impacted by self-similar converging shocks. It has been observed that the growth of the instability is mainly affected

by the incident shock strength and the curvature of the geometry. A parallel is finally made with simulations of the plane RMI. Future comparisons with the spherical geometry are planned.

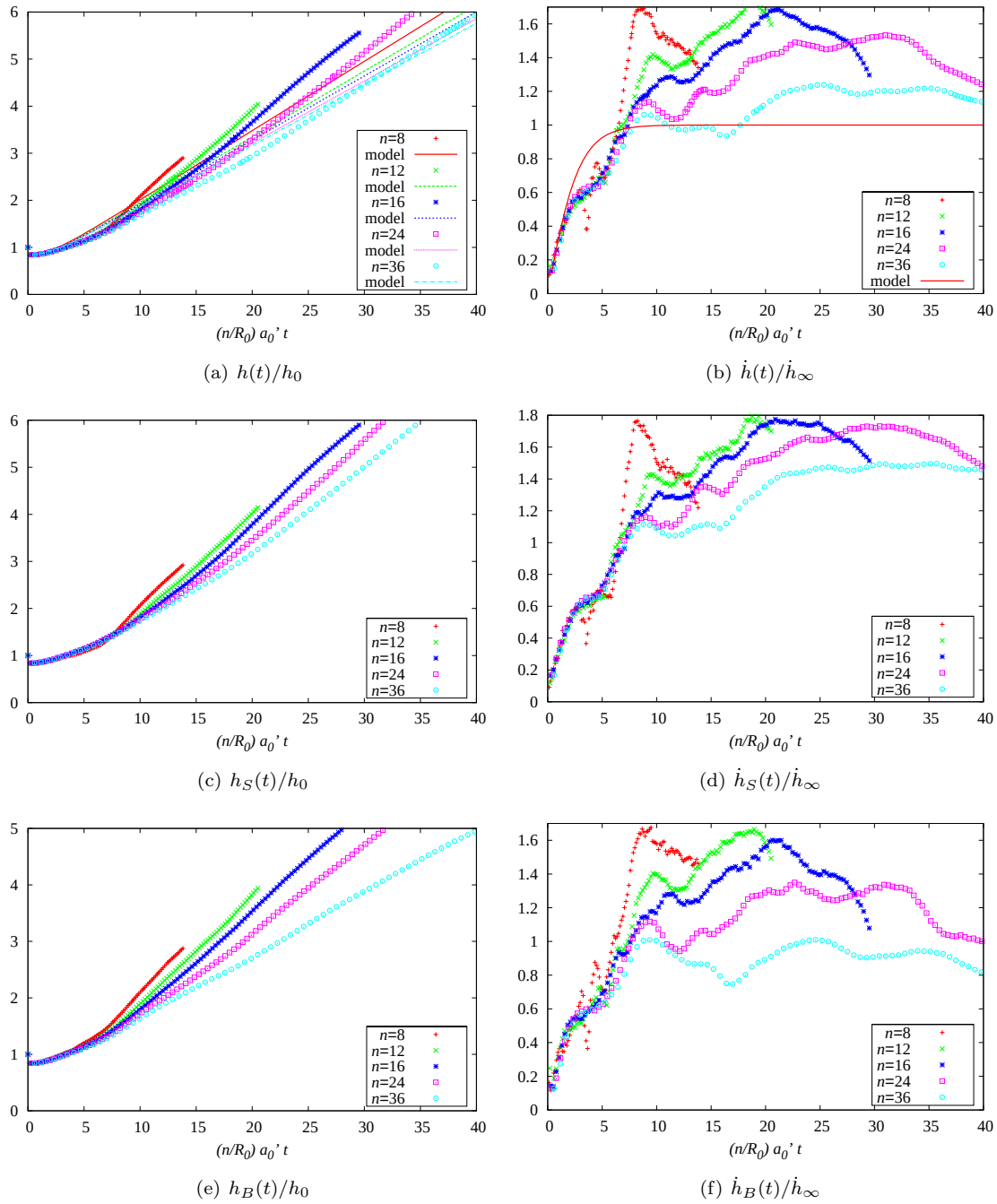

(a) $h(t)/h_0$ (b) $\dot{h}(t)/\dot{h}_\infty$

(c) $h_S(t)/h_0$ (d) $\dot{h}_S(t)/\dot{h}_\infty$

(e) $h_B(t)/h_0$ (f) $\dot{h}_B(t)/\dot{h}_\infty$

Figure 3.8: Azimuthal perturbations: Dimensionless amplitude (left) and growth rate (right) vs. $a_0(n/R_0)t$ of the interface perturbation (top), spike front (middle), and bubble front (bottom), plotted for different azimuthal wavenumbers n; case air $\rightarrow$ SF_6, $h_0/R_0 = 0.005$, $M_I = 1.2$.

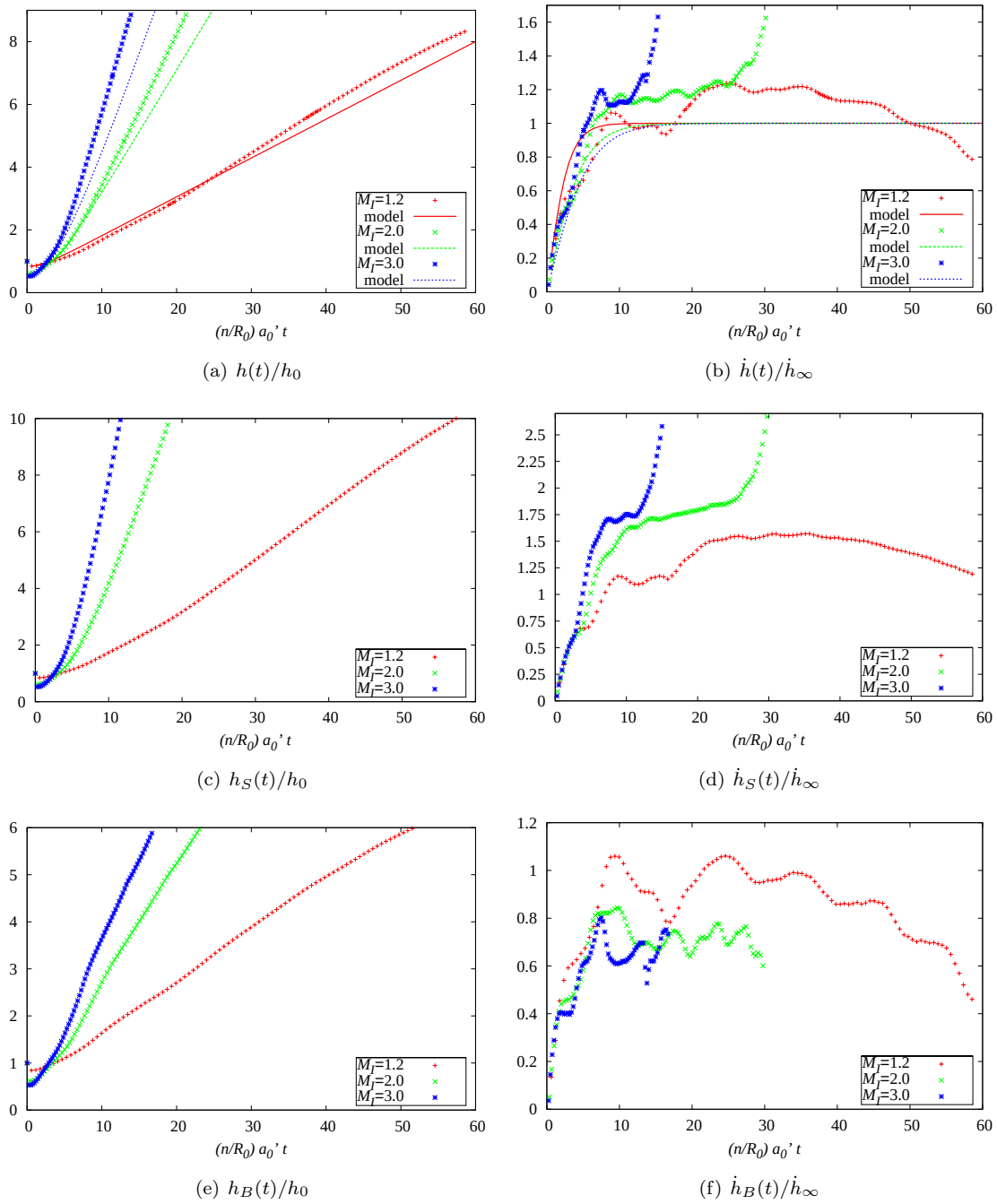

(a) $h(t)/h_0$ (b) $\dot{h}(t)/\dot{h}_\infty$

(c) $h_S(t)/h_0$ (d) $\dot{h}_S(t)/\dot{h}_\infty$

(e) $h_B(t)/h_0$ (f) $\dot{h}_B(t)/\dot{h}_\infty$

Figure 3.9: Azimuthal perturbations: Dimensionless amplitude (left) and growth rate (right) vs. $a_0(n/R_0)t$ of the interface perturbation (top), spike front (middle), and bubble front (bottom), plotted for three different incident Mach numbers M_I; case air $\rightarrow$ SF_6, $h_0/R_0 = 0.005$, $n = 36$.

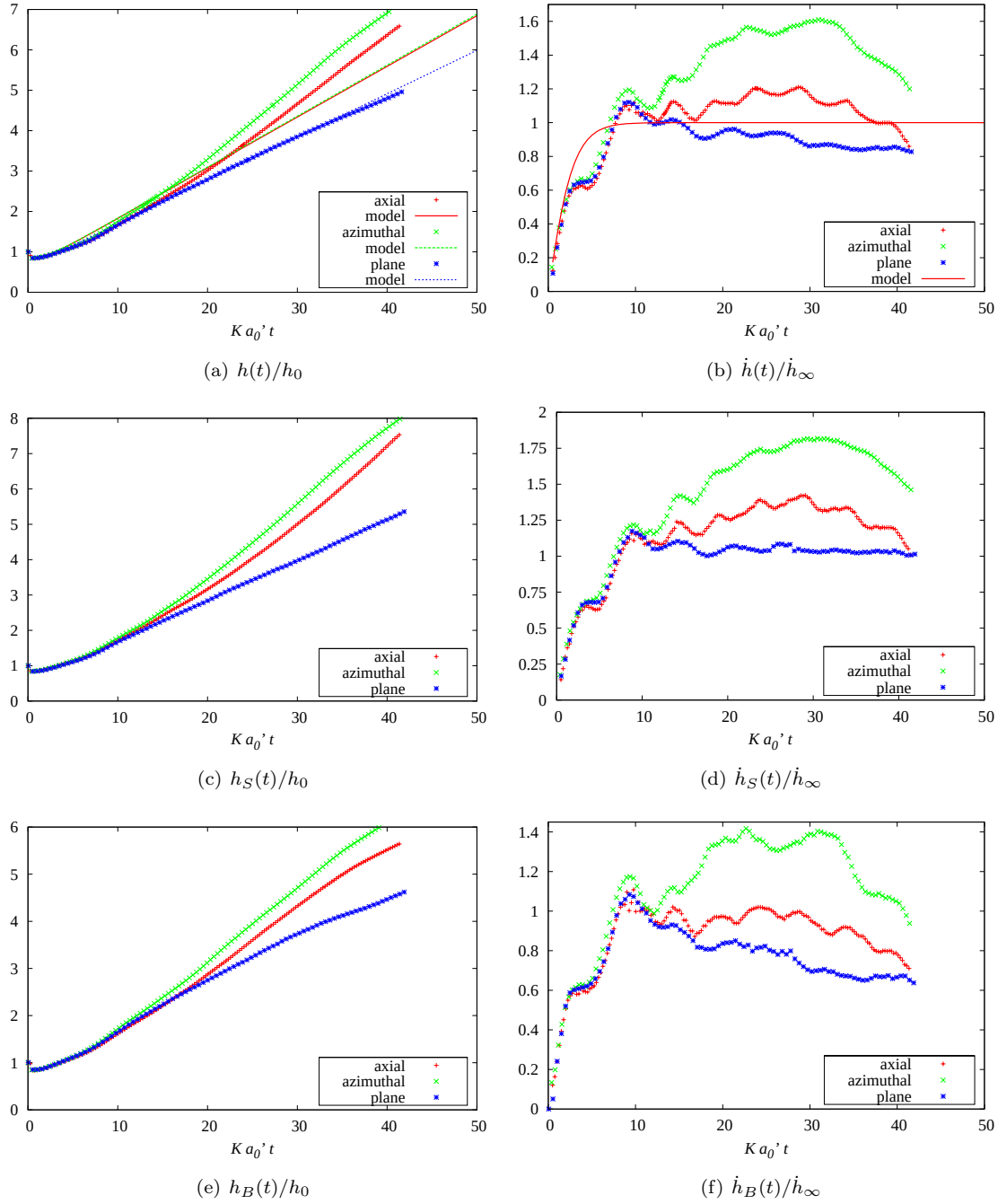

(a) $h(t)/h_0$ (b) $\dot{h}(t)/\dot{h}_\infty$

(c) $h_S(t)/h_0$ (d) $\dot{h}_S(t)/\dot{h}_\infty$

(e) $h_B(t)/h_0$ (f) $\dot{h}_B(t)/\dot{h}_\infty$

Figure 3.10: Dimensionless amplitude (left) and growth rate (right) vs. a_0Kt of the interface perturbation (top), spike front (middle), and bubble front (bottom), plotted for the azimuthal, axial, and plane perturbations; case air $\rightarrow$ SF_6, $M_I = 1.2$, $Kh_0 = 0.12$; for the azimuthal geometry $h_0/R_0 = 0.005$ and $K \equiv n/R_0 = 3$, for the axial geometry $h_0/R_0 = 0.005$ and $K \equiv k = 3$, for the plane geometry $K \equiv k = 3$.

Chapter 4

Wave Diagrams for Shock- and Reshock-Contact Interactions

4.1 Introduction

This work is a part of an on-going computational research on shock-generated mixing in Richtmyer-Meshkov (RM) flows with reshock in various geometries: plane, converging cylindrical, and converging spherical. An incident shock initially impacts a perturbed interface separating two fluids of different densities. The transmitted shock produced reflects off a wall/axis/origin and reshocks the distorted interface, initiating a strong turbulent mixing. In what follows, we use the generic term of 'inner boundary' to refer to the end wall, the axis, and the origin for the plane, cylindrical and spherical geometries respectively.

4.1.1 Previous Work

The experiments of Vetter and Sturtevant [109] and the simulations of Hill et al. [43] showed, for the light-air-to-heavy-SF_6 plane RMI mixing initiated at relatively low incident shock Mach numbers M_I, the importance of the reshock on the growth of the mixing zone in plane geometry. The stages in the life of the post-reshock turbulent mixing zone (TMZ) can be seen clearly in the turbulent kinetic energy of the flow. Figure 11 of [43] shows the total amount of energy deposited by the first reshock event, at 3.5 ms. Following a steep decay in energy forming the first stage in the post-reshock mixing zones life, a subsequent interaction with the expansion fan, shown in the wave diagram (sketch Figure 2 of [43]), deposits a large amount of energy over the duration of approximately 1 ms, peaking near 6 ms. This last deposition of baroclinic vorticity deposition corresponds to the second period of post-reshock growth. Examination of energy spectrum (Figure 12 of [43]) indicates that the expansion wave re-accelerating the mixing zone plays a major role, comparable to that of the reshock, in driving the growth of the mixing layer: an inertial subrange fully develops after the passage of this expansion wave.

Reshock in plane geometry occurred in the shock-tube experiments of Collins and Jacobs [17] and Jacobs and Krivets [54] where a single-mode air(acetone)/SF_6 interface is impacted by a $M_I = 1.21$ shock. These experiments serve as a reference for the two-dimensional simulations of Latini et al. [63] and Schilling et al. [100] using a ninth-order WENO method and investigating local and global mixing properties. In their simulations, the boundary condition at the end of the computational domain is changed from reflecting to outflow to allow the reflected expansion wave (following the reshock) to exit the domain. It is demonstrated that the reflected rarefaction has an important role in breaking symmetry and achieving late-time statistical isotropy of the velocity field.

Similarly, other experiments in plane geometry describe the reshock effect on the mixing. Figures 9–10 of [28] show the correlation between reshock and mixing growth using $x - t$ wave diagrams, for experiments of air→air and air→SF_6 interaction at $M_I = 1.25$. In his thesis work [9], in addition to studying light-to-heavy interactions (see, e.g., Figures 5.4 and 5.17 of [9] for air→SF_6 interaction at $M_I = 1.32$), Brouillette showed different growth profile for the heavy-to-light case clearly due to the different nature of the reshock process (see, e.g., Figures 5.5 and 5.19 of [9] for air→He ($A = -0.76$) interaction at $M_I = 1.30$).

Experimental research on the cylindrical geometry essentially reduces to the experiments by Hosseini and Takayama [50] and the simulations by Zhang and Graham [123]. Hosseini's experiments show the imploding RMI with reshock at the center for air→SF_6, air→Kr ($A = 0.46$), and air→He discontinuous interfaces (bubbles) accelerated by $M_I = 1.21$ shock waves. We recall from previous chapters that M_I is the incident shock Mach number as the shock front arrives at the interface. Radius-time $r - t$ wave diagrams presented in Figures 10, 11, and 12 of [50] (respectively, for SF_6, Kr, and He bubbles) analyze the first reshock event only, and successful comparisons for the transmitted shock Mach number evolution are made with Whitham's ray shock theory based on Chester-Chisnell-Whitham (CCW) method (p. 263 of [115]) assuming Duong and Milton's approximation [25] of the ray tube integral [49] (e.g., see Figure 7 of [50]). However, late-time evolution of the interface thickness in Figures 17, 18, and 19 of [50] draws attention to the importance of the second reshock stage, well described in [43] for the plane geometry. In Zhang's simulations [123], a study of the reshock using wave diagrams is present but lacks precision on the nature of the successive reshock events, except for the Class 4, i.e., heavy-to-light imploding interaction, where the simulations were run for sufficient time. Moreover, turbulent mixing cannot be achieved since the flow is computed in two dimensions, employs a shock-capturing method, and does not resolve or model the viscous dissipation scales. Therefore, it is difficult to draw conclusions concerning the precise role of the reshock on the computed interpenetration of the two fluids.

In spherical geometry, Kumar et al. investigated the effect of convergence on the growth of light-to-heavy and heavy-to-light interface thickness accelerated in conical geometry for M_I ranging between 1.39 and 1.60 [59]. However, the reshock influence was not studied since the focus was put

on the imploding phase (see $r-t$ wave diagrams in Figures 13 and 16 of [59], and mixing layer thickness evolution in Figures 24 and 25 of [59]).

On a general note, the research efforts just presented above do not tackle the effects of strong incident shocks, probably because of the inherent practical difficulties in studying such flows: the higher M_I, the closer to the wall/axis/center the mixing zone ends up stabilizing, and issues such as experimental design due to very high pressures at the center, precision of the measurements, or wall effects need to be solved. Turbulence generated by strong shocks is also a difficult problem to compute numerically (see Section 5.3).

4.1.2 Description of the Problem

The reshock process contains complex physics that is studied in this chapter by looking at the 'mean flow' when the interface is initially unperturbed. By symmetry of the initial unperturbed problem, the flow remains symmetrical and no RMI will occur. The plane geometry consists of the following one-dimensional problem: a plane shock interacts with a plane interface parallel to it, the transmitted shock reflecting off a wall parallel to the initial shock and interface. On the other hand, the converging geometry is described by the following radially symmetric one-dimensional problem: a converging, Guderley-type similarity shock defined in [15] (see Subsection 3.3.3) impacts a interface concentric to it, the transmitted shock converges down to the center and reflects off to reshock the interface. These problems are useful in elucidating the character of the one-dimensional shock impact and reshock physics that form the background of the three-dimensional turbulent mixing events covered in the next chapters.

4.2 On the One-Dimensional Simulations

4.2.1 Governing Equations

Ignoring in this chapter the effects of the viscosity of the fluids involved, the problem is best described by the Euler equations. The Euler equations are nonlinear hyperbolic equations that can be written in the following conservative form:

$$\frac{\partial \boldsymbol{q}}{\partial t} + \nabla \cdot \boldsymbol{F} = 0, \tag{4.1}$$

in particular, in Cartesian coordinates,

$$\frac{\partial \boldsymbol{q}}{\partial t} + \frac{\partial \boldsymbol{F}_k}{\partial x_k} = 0, \tag{4.2}$$

where repeated indices denote summation. In Equation (4.2) $\boldsymbol{q} = (\rho, \rho u_1, \rho u_2, \rho u_3, E, \rho\psi)^{\mathrm{T}}$ and the directional flux vector is given by

$$\boldsymbol{F}_k = \begin{pmatrix} \rho u_k \\ \rho u_1 u_k + \delta_{1k} p \\ \rho u_2 u_k + \delta_{2k} p \\ \rho u_3 u_k + \delta_{3k} p \\ (E+p)u_k \\ \rho\psi u_k \end{pmatrix}, \tag{4.3}$$

where ρ is the density, p the pressure, u_k the velocity components, and ψ a scalar field representing the mixture fraction of air and SF_6. The total energy E is related to the internal energy per unit mass, e, and the velocities by

$$E = \rho e + \frac{1}{2}\rho(u_k u_k). \tag{4.4}$$

For all the simulations reported, the ideal equation of state $p = \rho \mathrm{R} T/m$ is assumed, and the internal energy is given by $e = c_v T = p/(\rho(\gamma - 1))$.

The one-dimensional problem of the plane shock-contact interaction described in the previous subsection consists of solving the reduced system:

$$\frac{\partial \boldsymbol{q}}{\partial t} + \frac{\partial \boldsymbol{F}_x}{\partial x} = 0, \quad \text{with} \quad \boldsymbol{q} = \begin{pmatrix} \rho \\ \rho u_x \\ E \\ \rho\psi \end{pmatrix}, \quad \boldsymbol{F}_x = \begin{pmatrix} \rho u_x \\ \rho u_x^2 + p \\ (E+p)u_x \\ \rho\psi u_x \end{pmatrix}, \tag{4.5}$$

where x is the direction of the flow. The main advantage of a reduced system is simply that it allows the use of very high resolution compared to the equivalent three-dimensional computation of the same one-dimensional flow. On a more general note – this is not the goal of this chapter – even if the real problems of interest must be studied multi-dimensionally, reduced-order solutions are very valuable in validating numerical methods. A highly accurate solution to the one-dimensional problem can be computed on a very fine grid and used to test solutions computed with the multidimensional method. This is useful in checking that the code gives essentially the correct answer. It also allows one to determine how the numerical method suffers from grid-orientation effects which lead the flow to be better resolved in some directions than in others.

For the converging cylindrical and spherical shock-contact interactions, the flow studied is radially symmetric, the velocity being only radial and the flow depending only on the radial distance to the axis/origin r and the time t. We can rewrite the system of equations (4.1) in polar or spherical

coordinates, obtaining a system that reduces to a problem in r and t:

$$\frac{\partial \rho}{\partial t} + \frac{1}{r^{s-1}} \frac{\partial \left(r^{s-1} \rho u_r \right)}{\partial r} = 0, \tag{4.6a}$$

$$\frac{\partial \rho u_r}{\partial t} + \frac{1}{r^{s-1}} \frac{\partial \left(r^{s-1} \rho u_r^2 \right)}{\partial r} + \frac{\partial p}{\partial r} = 0, \tag{4.6b}$$

$$\frac{\partial E}{\partial t} + \frac{1}{r^{s-1}} \frac{\partial \left(r^{s-1} (E+p) u_r \right)}{\partial r} = 0, \tag{4.6c}$$

$$\frac{\partial \rho \psi}{\partial t} + \frac{1}{r^{s-1}} \frac{\partial \left(r^{s-1} \rho \psi u_r \right)}{\partial r} = 0, \tag{4.6d}$$

where the velocity vector reduces to the radial component u_r, and the space index s is 2 for cylindrical flow and 3 for spherical flow. This system can be rewritten in a form similar to (4.5) with a geometric source term:

$$\frac{\partial \boldsymbol{q}}{\partial t} + \frac{\partial \boldsymbol{F}_r}{\partial r} = \boldsymbol{S}, \text{ with } \boldsymbol{q} = \begin{pmatrix} \rho \\ \rho u_r \\ E \\ \rho \psi \end{pmatrix}, \ \boldsymbol{F}_r = \begin{pmatrix} \rho u_r \\ \rho u_r^2 + p \\ (E+p) u_r \\ \rho \psi u_r \end{pmatrix}, \ \boldsymbol{S} = -\frac{1}{r^{s-1}} \begin{pmatrix} \rho u_r \\ \rho u_r^2 \\ (E+p) u_r \\ \rho \psi u_r \end{pmatrix}. \tag{4.7}$$

4.2.2 Numerical Method

The hybrid scheme WENO-TCD by Hill and Pullin [44] is employed to solve the one-dimensional Euler equations (4.5) or (4.7): it is shock capturing but reverts to a centered stencil with low numerical viscosity in regions of smoother flow, which is of first importance for later performing accurate three-dimensional simulations of the turbulent mixing between the two fluids. A better description is provided in Section 5.3.

The practical advantage of solving the radially symmetric problem as a purely one-dimensional problem with a geometric source term is that the existing numerical solver for the Cartesian grid can be used directly without modification. However there is a drawback to solving (4.7) directly. The original multidimensional conservation law is not preserved, i.e., the numerical scheme may not be conservative in the multidimensional sense. Discrete conservation is a very important requirement in many numerical schemes to produce physical solution, especially for problems involving shock waves. Lax and Wendroff [64] have proved that the numerical solution of a conservative and consistent numerical scheme converges to the weak solution if it converges as the mesh is refined. A whole field of research (e.g., see [67, 96]) addresses this issue since it concerns many applications other than quasi one-dimensional problems (e.g., reacting flows, flows with external forces such as gravity, radiative heat transfer, bottom topography in shallow water).

Since it is not our purpose, we just need a preliminary test showing that strength and position of shocks are correct as the flow converges. We perform a one-dimensional simulation of Chisnell's

axisymmetric cylindrical converging shock traveling. The results are very similar to these obtained for the two-dimensional simulations in Figure 3.3 and Table 3.1, so we do not report them. A similar test could be done for the case of a single spherical converging shock. The geometric source terms become large as r tends to zero since they are proportional to $1/r^{s-1}$ (with $s = 2, 3$) and to increasingly high density, velocity, and pressure as the flow converges. Therefore, a small inner cylindrical or spherical reflective boundary $r = r_{in}$ has been set to avoid the singularity at $r = 0$.

For each of the three geometries, the initial plane, cylindrical, or spherical shock impacts the interface at a position R_0 with Mach number $M_I = 1.2$ or 3.0. As mentioned in Chapter 2 and 3, the temperature is set continuous across the initial interface, so that the Atwood ratio is fixed by the ratio of molecular weights of the species chosen: we test $A = 0.67$ for air$\rightarrow$$SF_6$ and $A = -0.67$ for SF_6 $\rightarrow$air. The resolution is uniform with grid size $R_0/20000$. The interface initial thickness (tanh) is $R_0/1000$. Zero-gradient outflow boundary conditions are used and the outer boundary is located at a distance $3R_0$ from the inner reflective boundary (wall, cylinder, or sphere) located at $r_{in} = R_0/1000$.

4.2.3 Visualization

The density Schlieren fields vs. position are output at regular and small-time intervals so that a two-dimensional position-time diagram with the density Schlieren in the third direction can be constructed. An example for the $M_I = 3.2$ cylindrical shock interaction with an air$\rightarrow$$SF_6$ interface is shown in Figure 4.1. The magnitude of the density gradient field $|\nabla\rho|$, or Schlieren, allows us to locate the interface and the shock across which the gradients are the highest. To locate other features, such that expansion fans, the Schlieren field is displayed in a log scale, the drawback being that some very small variations of the density due to the discrete nature of the signal can appear but have no physical meaning. To eliminate this 'noise' from our conclusions and to better understand the physics of the reshock, the characteristics curves are superposed onto the Schlieren fields, as displayed in the close-ups on the first and second stages of the reshock history Figure 4.2. The characteristics tangent to the field u (trajectories) should be parallel (on the wave diagram) to the interface position, and deflected by both incoming and outgoing (with respect to the inner boundary) shock waves, as seen on Figure 4.2b. The characteristics $u - a$ (a being the sound speed) should focus on incoming shocks, expand away from each other as they follow the head and tail trajectories of expansion fans traveling inwards, and are simply deflected by the interface and outgoing shocks. In particular, this family helps in determining the nature of the waves reflected from the various reshock interactions. Finally, the characteristics $u + a$ focus on outgoing shocks, expand away from each other as they follow the head and tail trajectories of expansion fans traveling outwards, and are simply deflected by the interface and incoming shocks. In particular, this family helps determine the nature of the waves reflecting off the inner boundary. We insist that in the radially symmetric

geometry the Riemann invariants, i.e., the quantities that remain constant along the characteristic directions of the flow, are different from the well-known Riemann invariants of the one-dimensional plane flow (e.g., see [62]).

The $M_I = 1.2$ cases usually show less contrast than $M_I = 3.0$, and weak reflected shocks can be sometimes hard to distinguish, so density plots vs. position must be viewed at the times of interest. For each geometry, M_I, and A, plots of the density profile vs. position are shown initially just before the incident shock-contact interaction, in between the first and second reverberation events, and at late time when the flow has stabilized. Finally, note that position is made dimensionless by R_0, time by R_0/a_0, and density by ρ_0 (see previous chapters and Table 5.5 in Chapter 5).

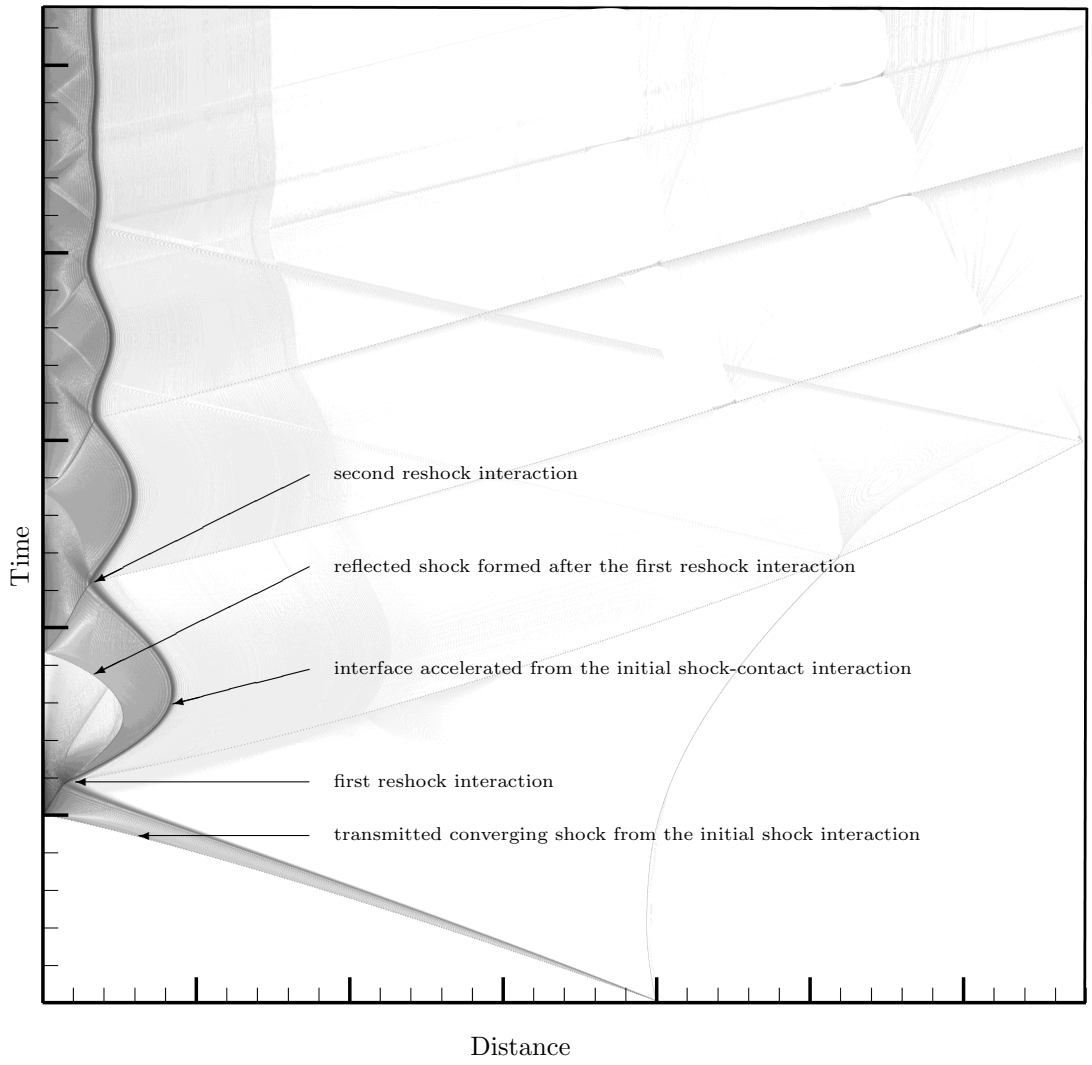

Figure 4.1: $r - t$ wave diagram: example of the $M_I = 3.2$ cylindrical shock interaction with an air→SF_6 interface. Density Schlieren levels (log scale) displayed.

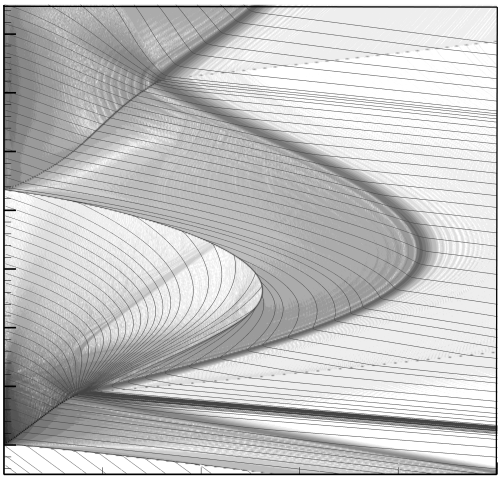

(a) $u - a$

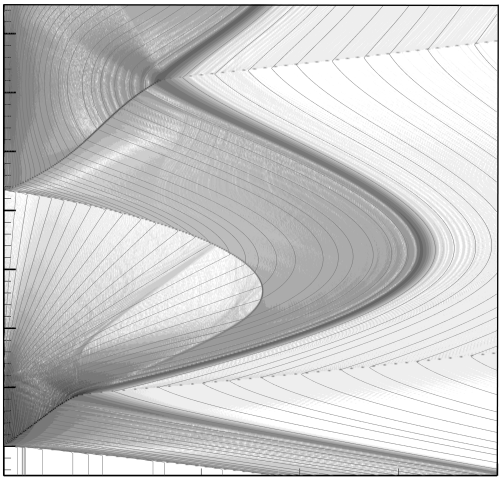

(b) u

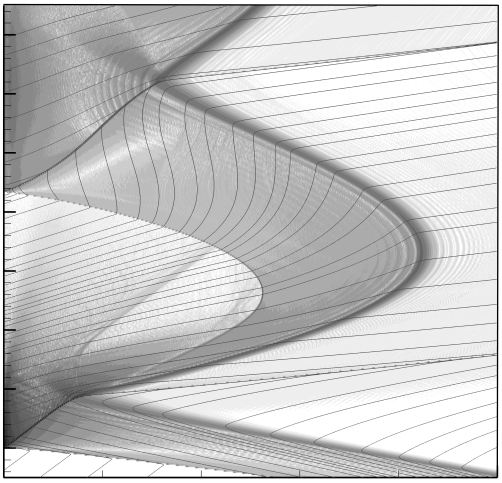

(c) $u + a$

Figure 4.2: Close-up on the first and second reverberations: example of the $M_I = 3.2$ cylindrical shock interaction with an air→SF_6 interface. Density Schlieren levels (log scale) displayed on a wave diagram and superposed to the three different families of characteristics, $u - a$ (top), u (middle), and $u + a$ (bottom).

4.3 Light-to-Heavy Interaction: Air $\rightarrow$ SF_6

In this section, we present comparisons of the one-dimensional wave diagrams for plane, cylindrical, and spherical geometries for the light-to-heavy interaction air$\rightarrow$ SF_6 corresponding to $A = 0.67$. SF_6 is contained in the region $r_{in} < r < R_0$, while air is contained in the region $r > R_0$. For all cases, we consider two incident Mach numbers $M_I = 1.2$ and $M_I = 3.0$.

4.3.1 Incident Mach Number $M_I = 1.2$

For such a low M_I, the Schlieren signal can appear weak on the log scale, thus density profiles at successive times shown on Figures 4.3 and 4.4 provide support to the analysis of the wave interactions.

4.3.1.1 Plane Geometry

In Figures 4.5a and 4.6a, note first the straight trajectories of the interface, shocks, expansion tails and heads, typical of the plane interaction (e.g., see Figure 2 of [43]). The transmitted shock produced from the initial shock-contact interaction and traveling into the heavy fluid reflects off the wall as a shock and reshocks the material interface at time 3.3. This heavy-to-light interaction produces an expansion inwards (Figures 4.6a and 4.3b) and gives a big enough increment of outward velocity to sharply reverse the interface motion outwards. The expansion wave reflects off the wall as an expansion wave that interacts with the interface at time 5.2 and gives a sufficiently large increment of inward velocity to smoothly reverse the interface motion inwards. From this expansion-interface interaction, a reflected expansion wave travels inward, reflects off the wall as an expansion, and interacts with the interface for a third reverberation. These reverberations alternately change the trajectory of the interface with weaker and weaker intensity, so that the interface stabilizes at around time 12, less than 4 times the first reshock time. The compression ratio $\mathfrak{Cr}$, defined as the ratio of the final position of the interface to its initial position and representing the degree of compression of the inner fluid, is $\mathfrak{Cr} \simeq 0.48$. Comparison made to Figure 5.4 of Brouillette's shock-tube experiments of the same gas combination accelerated at $M_I = 1.32$ [9] shows the effect of the wave reverberation into SF_6 as bringing the interface at rest, in less than 3 times the first reshock time.

4.3.1.2 Cylindrical Geometry

Figures 4.5b and 4.6b show curved trajectories owing to acceleration/deceleration effects due to the convergence of the geometry. The transmitted shock reflects off the center as a shock and reshocks the interface at time 3.2. A much earlier reshock than in the plane case was expected but the interface ends up decelerating on its way inwards just before the reshock. This is because ahead of the interface (in SF_6), the flow compressed between the transmitted shock and the interface is non-uniform. When the first reshock occurs, the interface has almost zero velocity. The reshock,

locally a plane heavy-to-light shock-contact interaction, produces an expansion propagating radially inwards (visible in Figure 4.3b), as occurs in the plane geometry. The increment of outward velocity is sufficiently large to reverse the interface motion. By tracking the density in between the first and second reverberations as shown on Figure 4.4a, as the expansion head starts reflecting off the wall, the density, pressure, and velocity fields following the expansion tail steepen to form a shock traveling inwards and reflecting off the center as a shock. Paragraph 21.7.1 of [68] confirms this observation by looking at the radial dam-break problem. Indeed, the reshock observed presently can be seen as a Riemann problem in cylindrical geometry, producing a reflected expansion traveling inward, a contact, and a transmitted shock outwards, just like the initial conditions of Subsection 21.7.1 of [68]. In this converging geometry, a shock forms (see Figure 21.4 of [68] at t=0.5 and 0.75) and reflects off the center as a shock (Figure 21.4 of [68] at t=1).

Meanwhile the interface slowly reverts its outward motion, reaches zero velocity at time 4.6, and starts moving inwards. A second reshock occurs at around 7.2 (see Figure 4.6b) which suddenly reverses the interface motion outwards. The following reverberations are self-similar reshocks of decreasing intensity that stabilize the interface at about time 18, less than 5 times the first reshock time, with $\mathfrak{Cr} \simeq 0.7$. Very similar experiments documented in [50] (cylindrical geometry, same gas combination, $M_I = 1.21$) show on a similar wave diagram (Figure 10 of [50]) how the interface decelerates before the first reshock, reverses its motion outwards from the first reshock and starts reversing it before the second reverberation. Unfortunately data stop right when the expansion wave traveling inwards into SF_6 reflects off the wall. Figure 6b of [123] does not show more than the first reshock.

4.3.1.3 Spherical Geometry

The wavy aspect of the interface trajectory is even more pronounced in this geometry as shows Figure 4.5c. The reverberation process is similar to the cylindrical geometry but more complex. The transmitted shock reflects as a shock and reshocks the interface earlier than in the plane and cylindrical cases since the transmitted shock converges faster. We would have expected, however, an even earlier reshock if the interface had not decelerated on its way inwards and started moving outwards before the first reshock occurs at time 2.75 and radius 0.685 (observe the deflected $u - a$ characteristics across the shock that reflected from the center, the sharp 'angular' change in interface motion, and how it is accelerated on Figure 4.6c). The reshock produces locally an expansion wave inwards, as seen in Figure 4.3b. In Figure 4.4b, showing density profiles between the first and second reverberations, the region following the tail of the expansion steepens to a shock as the flow converges toward the center. Moreover, the region ahead of the expansion head also steepens to a shock as it converges (visible in Figure 4.3b), which reflects off the center and interacts with the shock standing behind the expansion tail. As a result of this shock-shock interaction, a strong shock reflects towards

the center and a weaker one travels outwards. Meanwhile the interface slowly reverses its motion (around time 3.7), and moves inwards when it is reshocked at t=5.9 by the first (weak) shock. The interface inverts its motion again suddenly. There follows a stronger reshock at time 6.2 from the other shock. Therefore, what appears to be a unique reshock is actually two successive reshocks close to each other. Self-similar reshocks follow with decreasing intensity. The interface stabilizes at around time 29, less than 14 times the first reshock time, at $\mathfrak{Cr} \simeq 0.7$.

4.3.2 Summary

Expansion-contact interactions induce a smooth change in the interface motion, shock-contact interactions (or reshocks) have a sharp effect. As the geometries goes from plane to cylindrical to spherical, the interface oscillates with higher frequency and amplitude, and stabilizes in a longer time. As shown in Figure 4.3c, since energy needs to be conserved, when going from plane to spherical, $\mathfrak{Cr}$ decreases but the final level of inner density increases. The self-similar sequence for the interface motion to change inwards-outwards-inwards-outwards appears to be: (a) for the plane interaction a first reshock and two expansion wave interactions, (b) for the cylindrical case a first, a deceleration and a second reshock, (c) for the spherical case a first reshock, a deceleration and a second double-reshock.

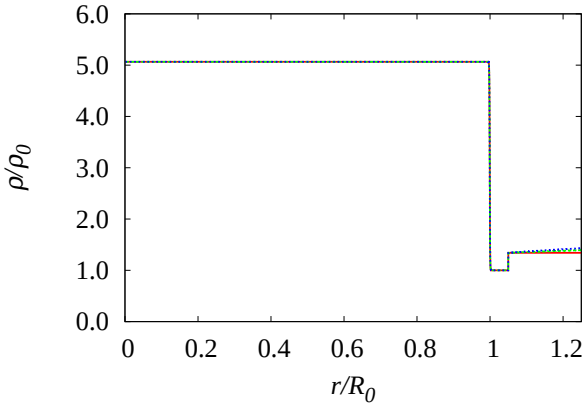

(a) $(a_0/R_0)t < 0$

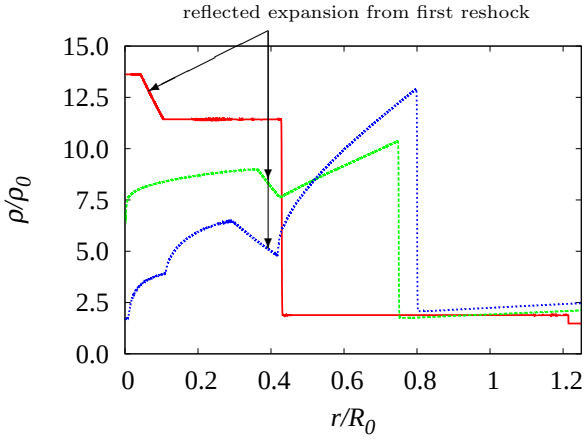

(b) $(a_0/R_0)t = 4.00$

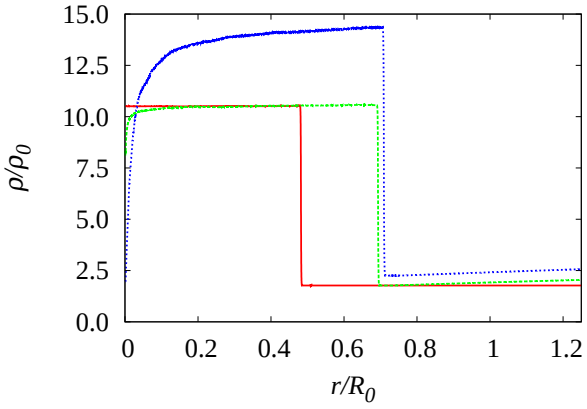

(c) $(a_0/R_0)t = 27.6$

Figure 4.3: Density ρ/ρ_0 vs. position r/R_0 for the air$\rightarrow$ SF_6 plane (red solid line), cylindrical (green long-dashed line), and spherical (blue small-dashed line) shock interactions for a $M_I = 1.2$ incident shock. Density profiles initially (top), after the first reshock event (middle), and at a late time (bottom). After the first reshock, a shock will form behind the expansion tail in the cylindrical and spherical geometries, and another shock will form ahead of the expansion head in the spherical geometry. The interface is initially located at $r/R_0 = 1$; at $r/R_0 \simeq 0.4$ for the plane geometry and $r/R_0 \simeq 0.8$ for the cylindrical/spherical cases after the first reshock; at $r/R_0 \simeq 0.5$ for the plane geometry and $r/R_0 \simeq 0.7$ for the cylindrical/spherical cases at late times.

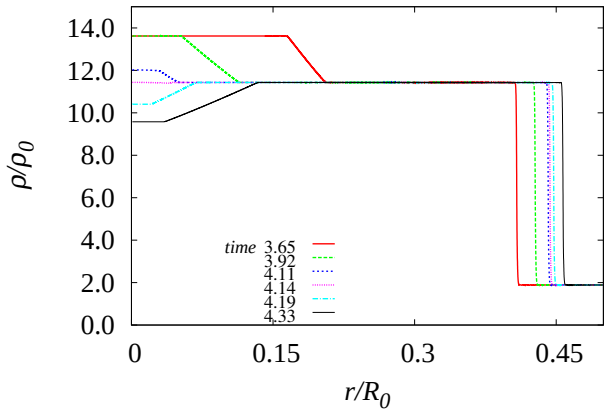

(a) Plane

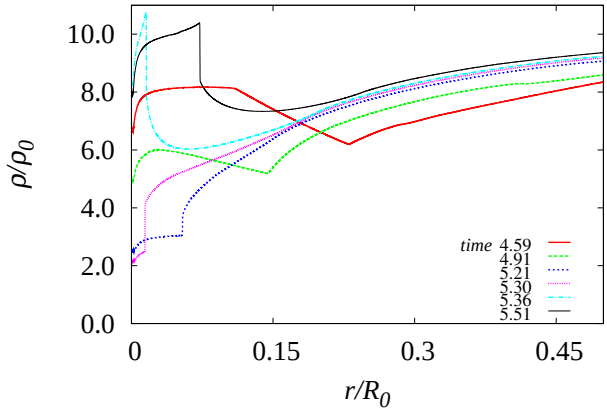

(b) Cylindrical

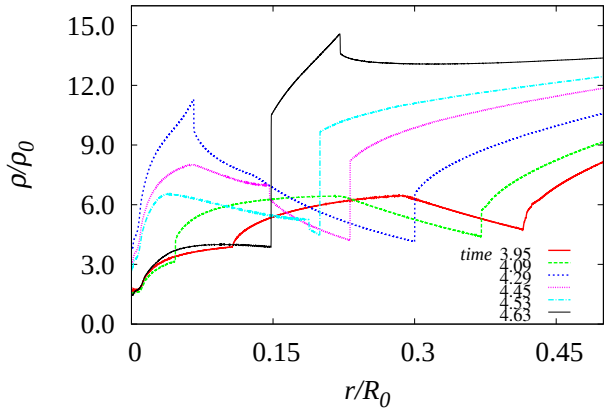

(c) Spherical

Figure 4.4: Density ρ/ρ_0 vs. radius r/R_0 for the air$\rightarrow$ SF_6 interactions at $M_I = 1.2$. Close-up at the center at different times between the first and second reshocks. (a) Plane case: the reflected expansion produced from the first reshock reflects off the wall as an expansion. (b) Cylindrical case: a shock forms behind the reflected expansion tail that was produced from the first reshock interaction, and reflects off the axis. (c) Spherical case: two shocks form behind the reflected expansion tail and ahead of its head; the inner shock reflects off the center and interacts with the outer one; the shock-shock interaction produces a weak shock traveling outwards to reshock the interface a second time, and a stronger and faster shock traveling inwards, reflecting off the center and reshocking the interface soon after the second reshock.

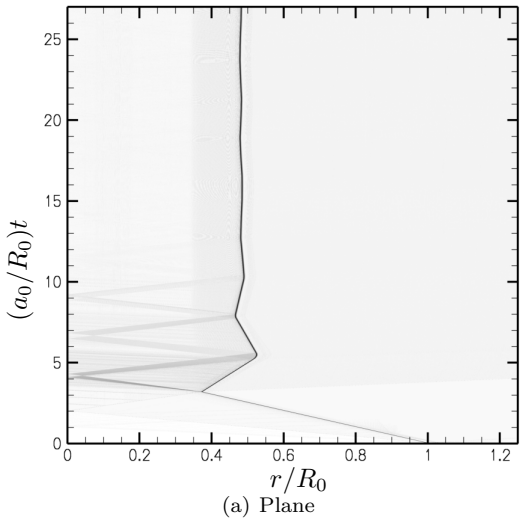

(a) Plane

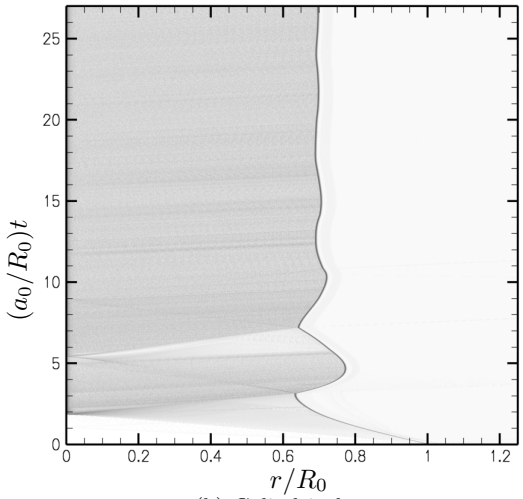

(b) Cylindrical

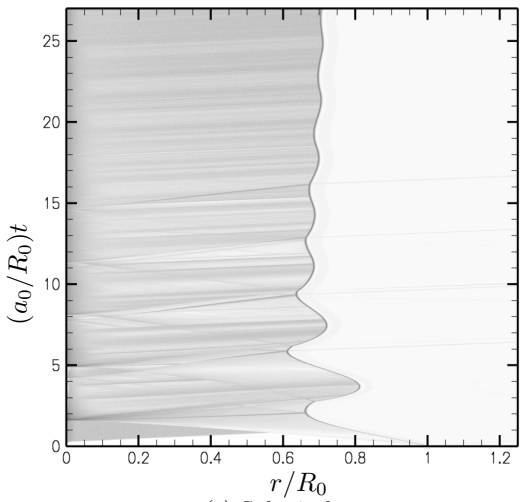

(c) Spherical

Figure 4.5: Wave diagrams for the air$\rightarrow$ SF_6 shock interaction for a $M_I = 1.2$ incident shock. Density Schlieren levels for the plane (top), cylindrical (middle), and spherical (bottom) shock interactions.

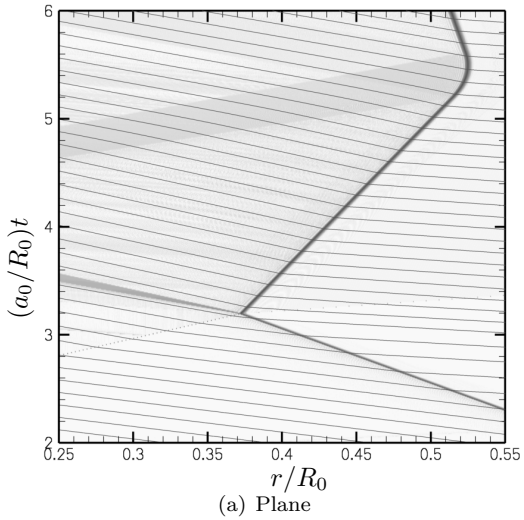

(a) Plane

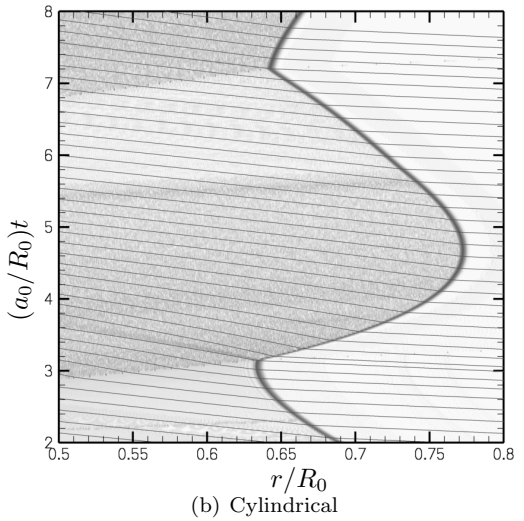

(b) Cylindrical

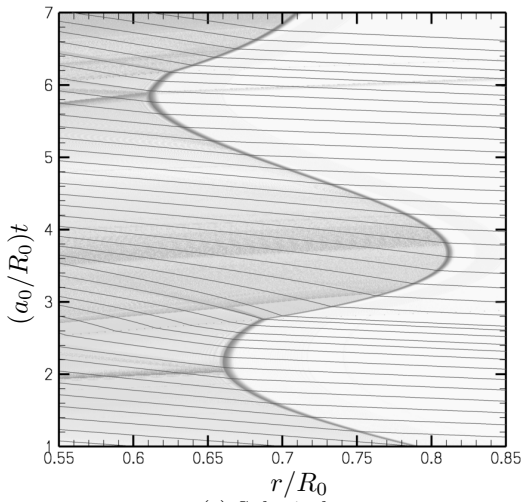

(c) Spherical

Figure 4.6: Wave diagrams for the air→ SF_6 shock interaction for a $M_I = 1.2$ incident shock. Close-up on the first and second reverberations, with characteristics $u - a$ superposed to density Schlieren levels for the plane (top), cylindrical (middle), and spherical (bottom) shock interactions.

4.3.3 Incident Mach Number $M_I = 3.0$

Similarly to the $M_I = 1.2$ case, various profiles of density shown in Figure 4.7 help support the observations made from the wave diagrams.

4.3.3.1 Plane Geometry

Note again the straight trajectories typical of the plane interaction in Figure 4.8a. The transmitted shock reflects off the center and reshocks the interface at time 0.68 (see Figure 4.9a), earlier than in the lower Mach case because both transmitted shock and interface travel faster (see Chapter 2). A reflected expansion is produced during the reshock and reverses the interface motion sharply. The expansion reflects off the wall and interacts with the interface at about time 0.82. The expansion produced reflects off the wall and reverberates again with the interface at time 0.97, etc., similarly with weaker intensity. The interface stabilizes at about time 1.5, less than 2 times the first reshock time, with $\mathfrak{Cr} \simeq 0.05$.

4.3.3.2 Cylindrical (Respectively Spherical) Geometry

Sharper wave reverberations traveling in the heavy fluid indicate sharper reshocks, as seen in Figure 4.8b (respectively 4.8c). The first reshock occurs at time 0.63 (respectively 0.54). The reshock is very early compared to the lower Mach case, and equivalent to the plane case at the same Mach number because the interface accelerated by the initial shock interaction follows closely the transmitted shock. When the first reshock occurs, the interface motion sharply reverses outwards with almost opposite velocity. As usual, the first reshock produces a reflected expansion fan inwards. While the expansion travels inwards and reflects off the center, a front steepens right on the tail of the expansion as for lower Mach case but much faster. The shock is stronger for $M_I = 3.0$ than for $M_I = 1.2$ and can be clearly seen on Figure 4.9b (respectively 4.9c): the characteristics $u - a$ coming from outside are deflected by the interface and focus on a single shock facing inwards. In the frame of the interface, this shock quickly detaches from the interface. The shock is visible in Figure 4.7b at a radius of 0.15 (respectively 0.31). The shock reverses its motion inwards and reflects off the center as a shock at time 1.04 (respectively 1.03). It reshocks the interface at time 1.32 (respectively 1.3). Successive reshock events of decreasing strengths follow self-similarly, as shown very distinctly in the spherical case in Figure 4.9c. The shocks forming from each reshock bifurcation detach faster and faster from the interface so that the third and following reshock events each appear to be heavy-to-light shock-contact interactions producing a reflected shock instead of an expansion wave. The interface finally stabilizes at around time 5 (respectively 7), less than 8 (respectively 13) times the first reshock time, with $\mathfrak{Cr} \simeq 0.1$ (respectively 0.15).

4.3.3.3 Summary

Similar observations to the $M_I = 1.2$ can be made, with lower $\mathfrak{Cr}$ and faster stabilization. The self-similar sequence for the interface motion to change inwards-outwards-inwards-outwards appears to be: (a) for the plane interaction a first reshock and two expansion wave interactions, (b) (respectively (c)) for the cylindrical (respectively spherical) case a first, a deceleration and a second reshock.

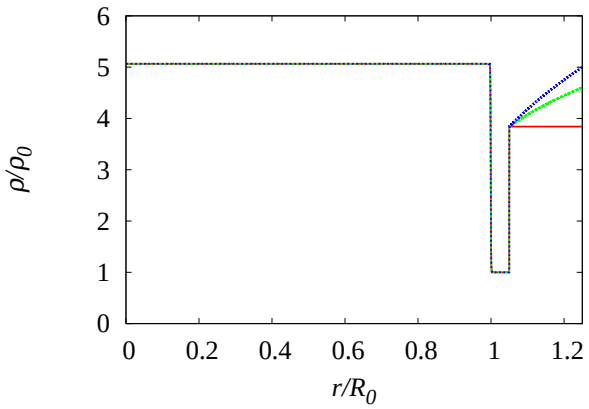

(a) $(a_0/R_0)t < 0$

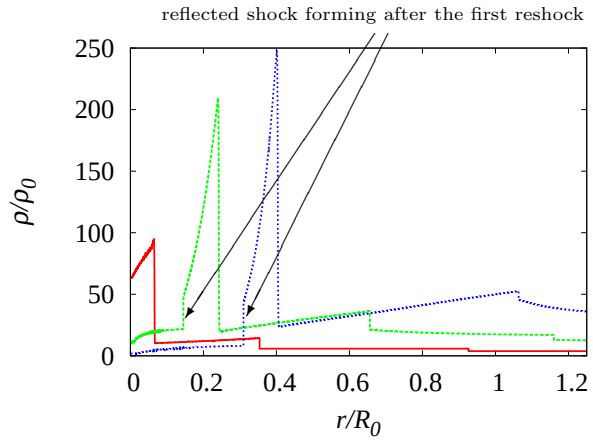

(b) $(a_0/R_0)t = 0.86$

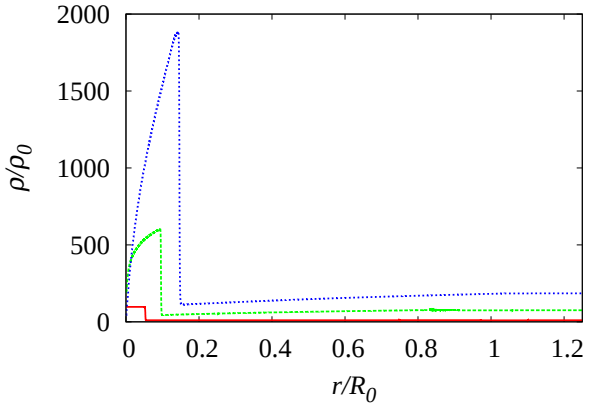

(c) $(a_0/R_0)t = 6.90$

Figure 4.7: Density ρ/ρ_0 vs. position r/R_0 for the air$\rightarrow$ SF_6 plane (red solid line), cylindrical (green long-dashed line), and spherical (blue small-dashed line) shock interactions for a $M_I = 3.0$ incident shock. Density profiles initially (top), after the first reshock event (middle), and at a late time (bottom). Shocks form behind the reflected expansion tail (see lower Mach case), and will reflect to reshock the interface a second time. The interface is initially located at $r/R_0 = 1$; at $r/R_0 \simeq 0.1$ for the plane geometry, $r/R_0 \simeq 0.3$ for the cylindrical case, and $r/R_0 \simeq 0.4$ for the spherical case after the first reshock; at $r/R_0 \simeq 0.05$ for the plane geometry, $r/R_0 \simeq 0.1$ for the cylindrical case, and $r/R_0 \simeq 0.2$ for the spherical case at late times.

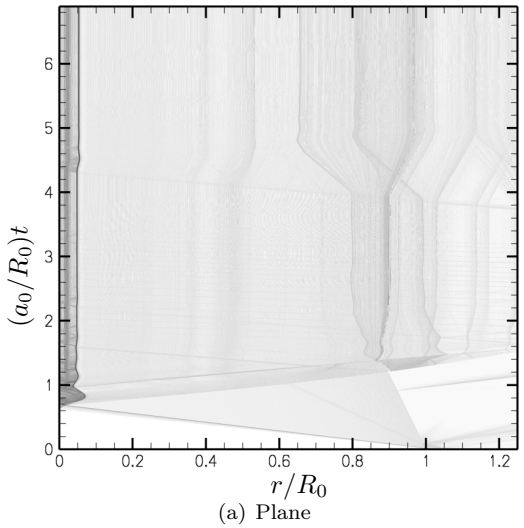

(a) Plane

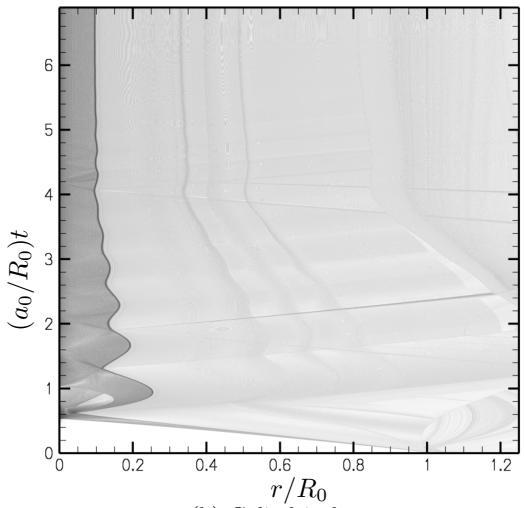

(b) Cylindrical

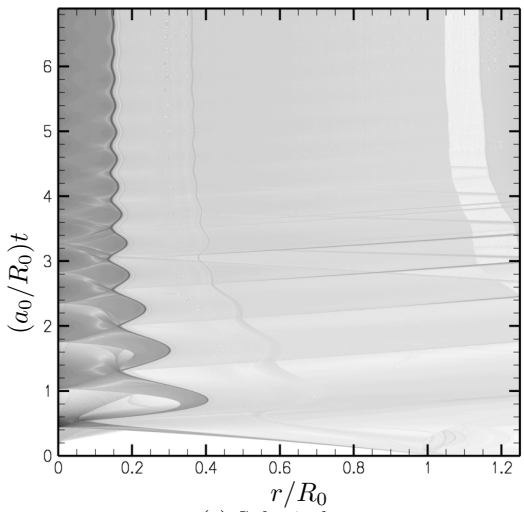

(c) Spherical

Figure 4.8: Wave diagrams for the air→ SF_6 shock interaction for a $M_I = 3.0$ incident shock. Density Schlieren levels for the plane (top), cylindrical (middle), and spherical (bottom) shock interactions.

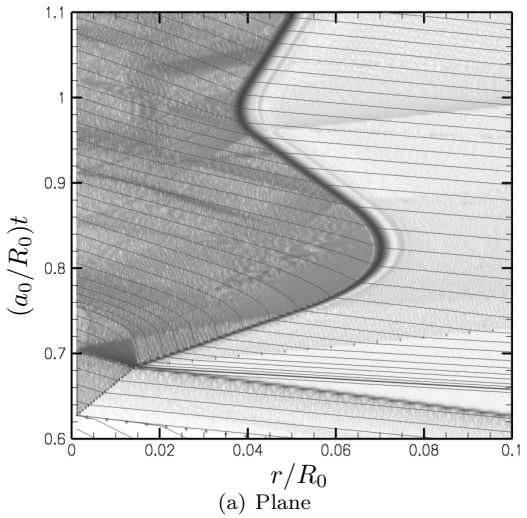

(a) Plane

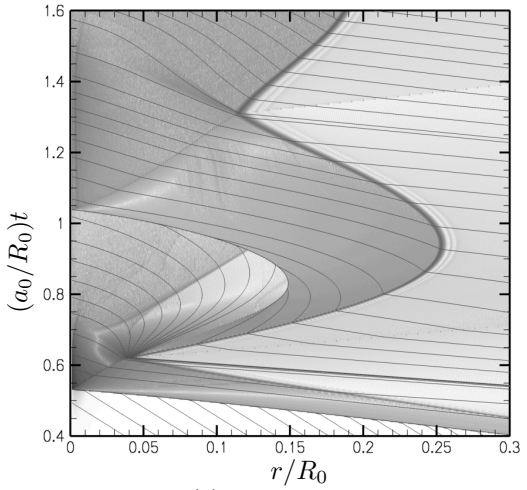

(b) Cylindrical

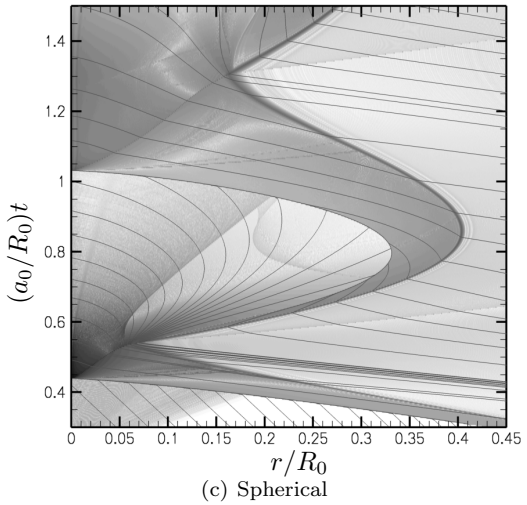

(c) Spherical

Figure 4.9: Wave diagrams for the air→ SF_6 shock interaction for a $M_I = 3.0$ incident shock. Close-up on the first and second reverberations, with characteristics $u - a$ superposed to density Schlieren levels for the plane (top), cylindrical (middle), and spherical (bottom) shock interactions.

4.4 Heavy-to-Light Interaction: $SF_6 \rightarrow$ Air

The heavy-to-light interaction exhibits quite different behavior to the light-to-heavy interaction and so is discussed separately. We consider the the combination SF_6 →air, that is $A = -0.67$, at two different incident shock Mach numbers, $M_I = 1.2$ and 3.0. SF_6 is now contained in the region $r > R_0$, while air is contained in the region $r_{in} < r < R_0$. Note that in the present section, the time is dimensionalized with the speed of sound of the outer fluid, SF_6.

4.4.1 Incident Mach Number $M_I = 1.2$

In the three geometries, after the transmitted shock reflects off the inner boundary, reshock of the interface occurs at time 0.65 for the plane case, 0.6 for the cylindrical, and 0.65 for the spherical geometries respectively. These light-to-heavy interactions each produce a reflected wave that travels inwards, reflects off the inner boundary, and then reshocks the interface a second time. Figures 4.11 and 4.12 show that all the reverberations are shock waves of decreasing intensity with time, such that the interface never reverses its motion and is gradually slowed down to stabilize in comparable dimensionless time of 2, which is more than 3 times the first reshock time. It is a relatively fast time with respect to first reshock time when comparing to the $A = 0.67$ case. The first reason is that all waves reflected from the reshock interactions are shocks that travel directly inwards. Second, the reshock history is also faster because the waves traveling between the boundary and the interface reverberate in a lighter fluid. We observe that $\mathfrak{Cr} \simeq 0.6$ for the plane, 0.65 for the cylindrical, and 0.6 for the spherical geometries; and the levels of final heavy fluid (outside) are of the same order (Figure 4.10). The plane case qualitatively agrees with the heavy-to-light air→He experiments at M=1.30 shown in Figure 5.5 of [9]. The cylindrical geometry compares to the Class 4 solution of Zhang's computations [123] (same incident Mach and gas combination): multiple reshocks are apparent at similar times, and a quick stabilization of the interface occurs at $\mathfrak{Cr} \simeq 0.68$. Similar features for the first and second reshocks are observed in Figure 12 [50] obtained from cylindrical air→He experiments at $M_I = 1.2$.

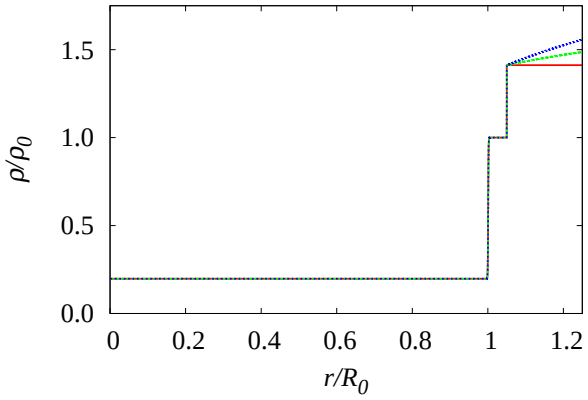

(a) $(a_0/R_0)t < 0$

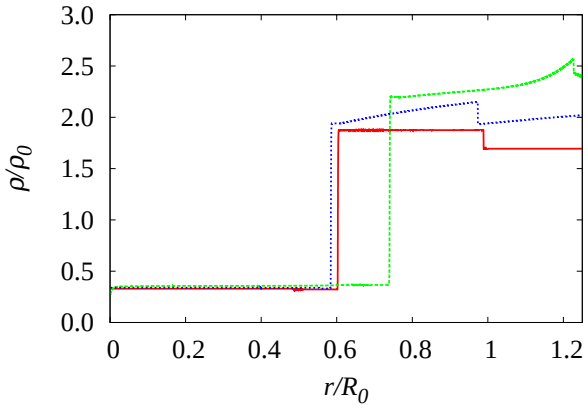

(b) $(a_0/R_0)t = 1.55$

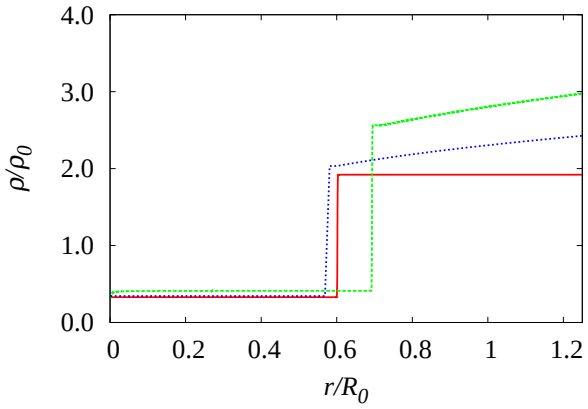

(c) $(a_0/R_0)t = 10.7$

Figure 4.10: Density ρ/ρ_0 vs. position r/R_0 for the SF_6 →air plane (red solid line), cylindrical (green long-dashed line), and spherical (blue small-dashed line) shock interactions for a $M_I = 1.2$ incident shock. Density profiles initially (top), after the first reshock event (middle), and at a late time (bottom). The interface is initially located at $r/R_0 = 1$; at $r/R_0 \simeq 0.6$ for the plane geometry, $r/R_0 \simeq 0.7$ for the cylindrical case, and $r/R_0 \simeq 0.6$ for the spherical case after the first reshock; at $r/R_0 \simeq 0.6$ for the plane geometry, $r/R_0 \simeq 0.7$ for the cylindrical case, and $r/R_0 \simeq 0.6$ for the spherical case at late times.

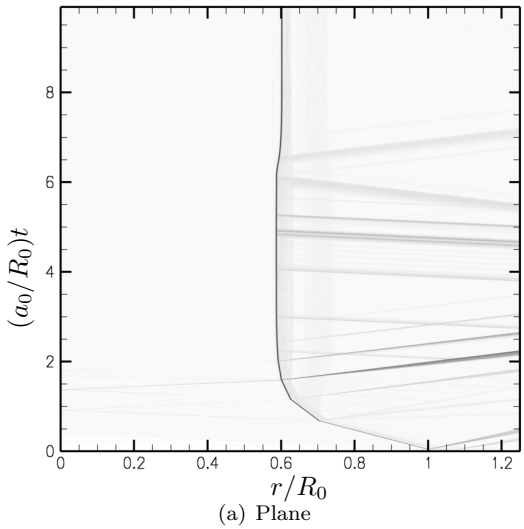

(a) Plane

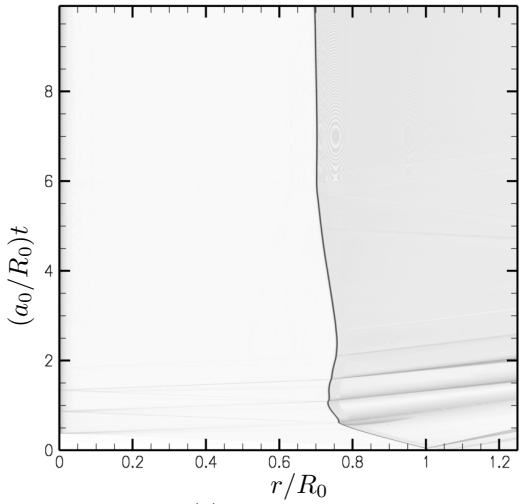

(b) Cylindrical

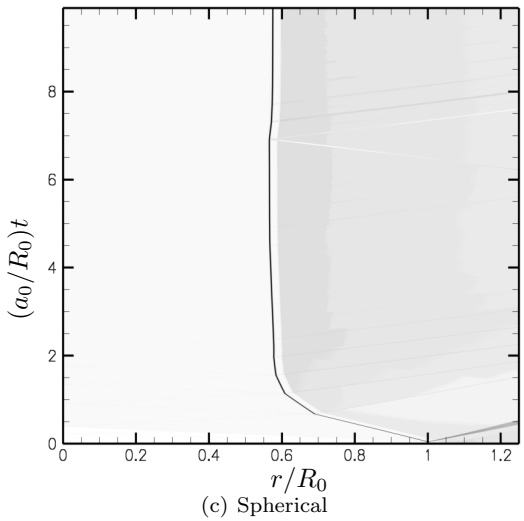

(c) Spherical

Figure 4.11: Wave diagrams for the SF_6 →air shock interaction for a $M_I = 1.2$ incident shock. Density Schlieren levels for the plane (top), cylindrical (middle), and spherical (bottom) shock interactions.

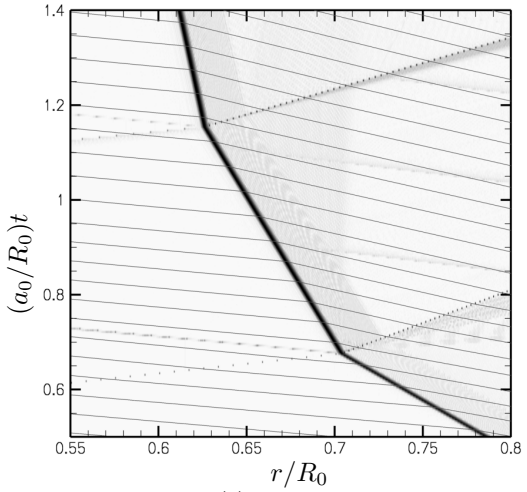

(a) Plane

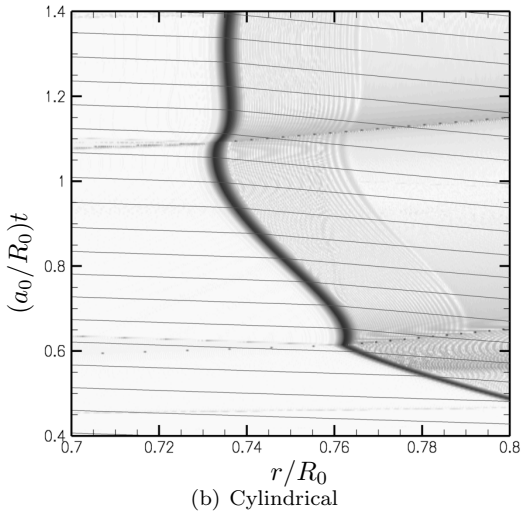

(b) Cylindrical

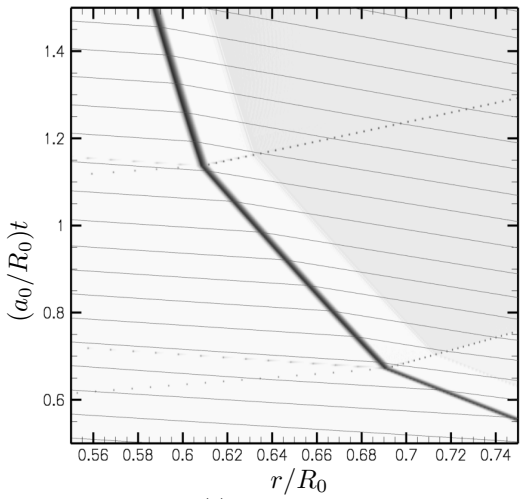

(c) Spherical

Figure 4.12: Wave diagrams for the SF_6 →air shock interaction for a $M_I = 1.2$ incident shock. Close-up on the first and second reverberations, with characteristics $u - a$ superposed to density Schlieren levels for the plane (top), cylindrical (middle), and spherical (bottom) shock interactions.

4.4.2 Incident Mach Number $M_I = 3.0$

Again, the three geometries are very similar. The transmitted shock produced during the initial interaction reflects off the center and reshocks the interface at time 0.275 for the plane case, 0.27 for the cylindrical one, and 0.265 for the spherical one). This light-to-heavy interaction produces a reflected wave that travels inwards, reflects off the center and reshocks the interface, etc. As seen in Figure 4.14 and particularly in Figure 4.15), all the reverberations are shock waves of decreasing intensity. The interface almost does not reverse its motion and is gradually slowed down to stabilize in a comparable dimensionless time of 0.6 (more than 2 times the first reshock time). This is relatively fast in terms of the first reshock time when comparing to the $A = 0.67$ case for the same incident shock strength. The $M_I = 3.0$ case differs from the $M_I = 1.2$ case on the transmitted shock produced from the first reshock interaction and traveling in SF_6 away from the interface: for $M_I = 1.2$, the reshock of relatively low strength is such that the transmitted shock produced from the reshock travels outwards (in the lab frame) and exits the domain quickly (see Figure 4.12). In the $M_I = 3.0$ case, the interface is accelerated more rapidly from the initial shock interaction so that, during the reshock, the transmitted shock actually travels inwards in the frame of the lab as shown Figure 4.15. This shock is actually strong. The second reshock, being weaker than the first, coupled with a decelerating interface, produces a new transmitted shock that travels outwards (in the lab frame) and interacts with the transmitted shock moving inwards from the first reshock interaction. Successive secondary interactions occur during the following reshock events. As a result, a strong shock exits the domain at an angle of about 45° angle as seen in the wave diagram Figure 4.14. Figure 4.13c shows its position at a late time. On the heavy side, the quite weak waves produced from the interactions between the successive transmitted shocks are traveling inwards to impact the interface, whose effect on average is this slight change in the interface position at $(a_0/R_0)t \simeq 0.5$ for all geometries. We find $\mathfrak{Cr} \simeq 0.06$ for the plane case, $\mathfrak{Cr} \simeq 0.05$ for the cylindrical, and $\mathfrak{Cr} \simeq 0.025$ for the spherical geometries, respectively. The final levels of heavy fluid density for the spherical geometry are twice that of the cylindrical geometry which is twice that of the plane geometry.

4.5 Summary

We have considered the one-dimensional shock-interface impact for three different geometries and two different incident Mach numbers, for both light-to-heavy and heavy-to-light initial configurations.

In the light-to-heavy case, it has been shown that the nature of the wave reverberation (specially the second wave reverberation) depends on the geometry. As mentioned in [43] for the plane geometry, the influence of the second reverberation on the turbulent mixing is as important as the first reshock. In the plane case, an expansion wave traveling away from the wall will deposit baroclinic vorticity over a finite period of time, and this secondary interaction is somewhat like the contin-

uous acceleration of the RTI. In contrast, in curved geometries, after the interface is accelerated by the first reshock, a period of deceleration follows, and then a second reshock occurs, operating an impulsive deposition of vorticity. All three geometries show oscillatory profiles of the interface unperturbed position resulting from the reverberation process, which, in the perturbed situation, is expected to influence the growth of spike and bubble structures coexisting within the TMZ. The heavy-to-light interaction exhibits successive reshocks independently of the geometry. The interface stabilizes quasi monotonically, without alternative inward/outward velocity increments. Both features will certainly influence the turbulent mixing differently than in the light-to-heavy RMI with reshock. While we described the physics of the flow if the interface were initially unperturbed, when a perturbation is initially superposed, spike and bubble structures will be differently affected by the various reverberating waves. It should also be added that the light-to-heavy and heavy-to-light RMI differ from one another in the sense that the heavy-to-light RMI is Rayleigh-Taylor (RT) unstable during the implosion (accelerating phase) while the light-to-heavy one is RT unstable during the explosion (decelerating phase).

Increasing the incident shock strength results in accelerating the time of the first reshock and focus the base interface closer to the wall/center. This is expected to affect the entrainment of inner fluid into the mixing region. The entrainment is also influenced by the geometry, since the volume of fluid trapped between the inner boundary and the TMZ differs as we move from plane to spherical geometry: it is of the order of $\mathfrak{Cr}L_yL_z$ for the plane case (with (y,z) transverse to the direction x of the flow), $\pi\mathfrak{Cr}^2L_z$ for the cylindrical one (with z direction of the cylindrical axis), and $4\pi\mathfrak{Cr}^3/3$ for the spherical one.

Future work will consist of testing different gas combinations, such as air/He (commonly used in experiments) or even lower Atwood combinations such air/CO_2.

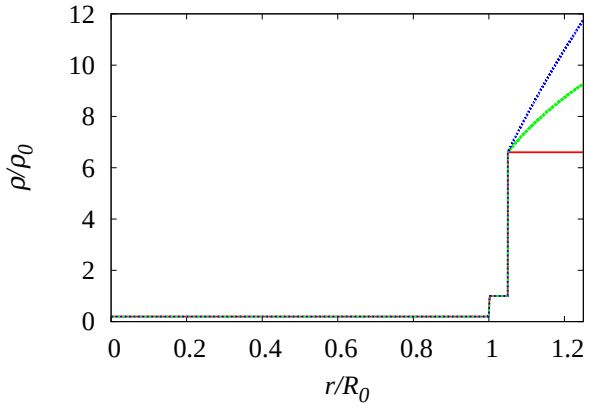

(a) $(a_0/R_0)t < 0$

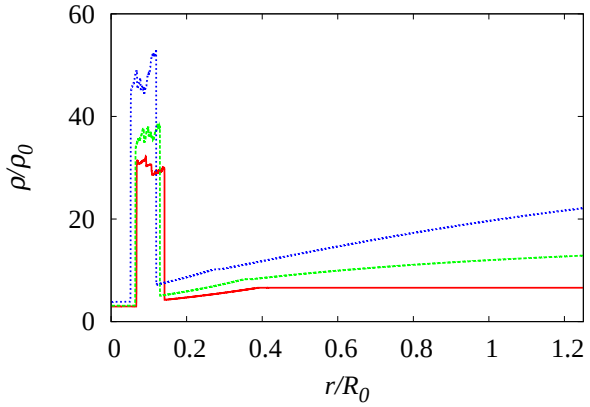

(b) $(a_0/R_0)t = 0.47$

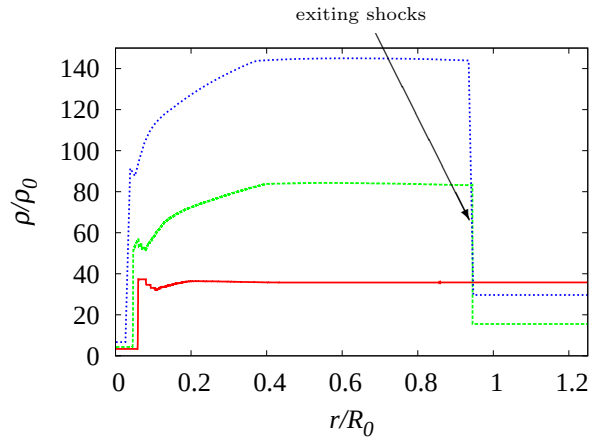

(c) $(a_0/R_0)t = 2.53$

Figure 4.13: Density ρ/ρ_0 vs. position r/R_0 for the SF_6 →air plane (red solid line), cylindrical (green long-dashed line), and spherical (blue small-dashed line) shock interactions for a $M_I = 3.0$ incident shock. Density profiles initially (top), after the first reshock event (middle), and at a late time (bottom). A strong shock resulting from the interactions of the transmitted shocks produced during the successive reshocks traveling outwards can be seen exiting the physical domain for late times. The interface is initially located at $r/R_0 = 1$; at $r/R_0 \simeq 0.05$ after the first reshock and at late times.

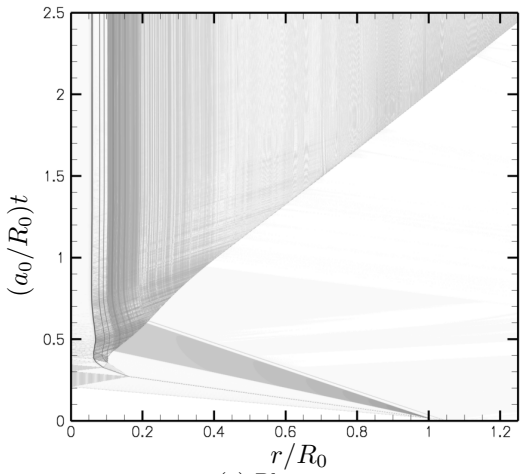

(a) Plane

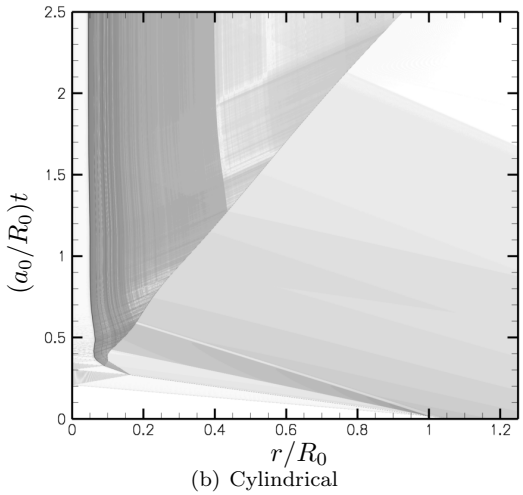

(b) Cylindrical

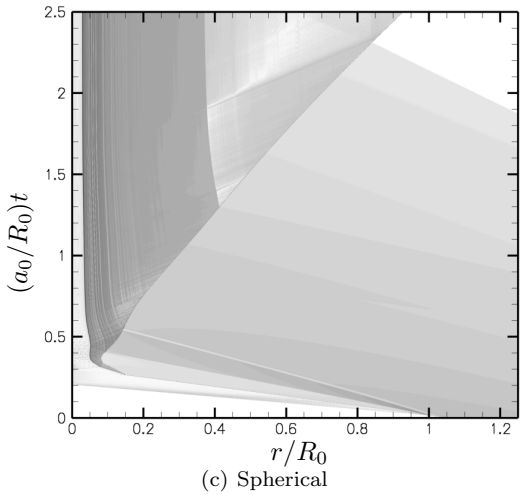

(c) Spherical

Figure 4.14: Wave diagrams for the SF_6 →air shock interaction for a $M_I = 3.0$ incident shock. Density Schlieren levels for the plane (top), cylindrical (middle), and spherical (bottom) shock interactions.

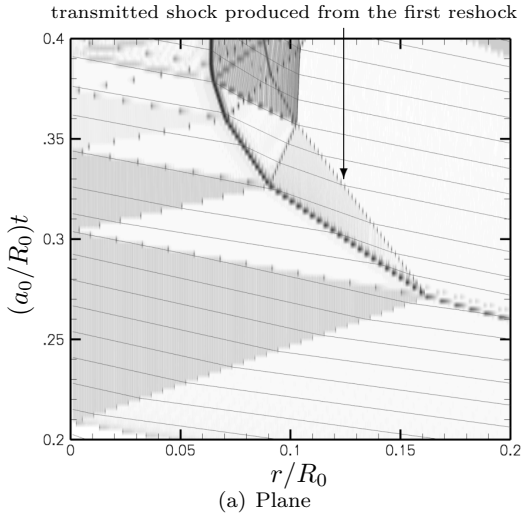

(a) Plane

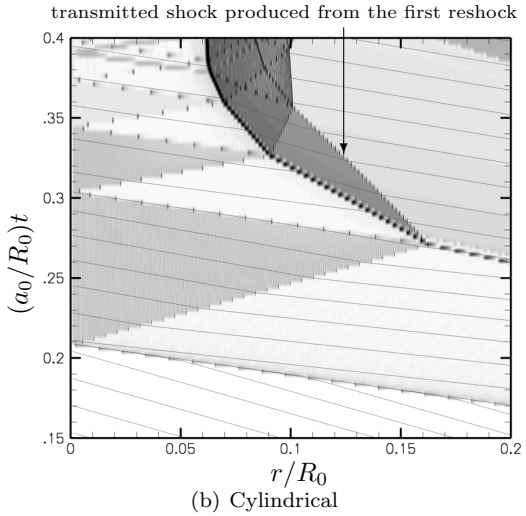

(b) Cylindrical

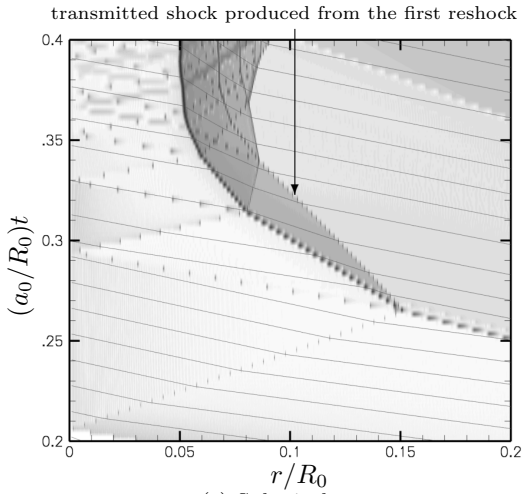

(c) Spherical

Figure 4.15: Wave diagrams for the SF_6 →air shock interaction for a $M_I = 3.0$ incident shock. Close-up on the first and second reverberations, with characteristics $u - a$ superposed to density Schlieren levels for the plane (top), cylindrical (middle), and spherical (bottom) shock interactions.

Chapter 5

Large-Eddy Simulations of Shock-Generated Mixing in a Cylindrical Geometry

5.1 Introduction

5.1.1 Flow Description

A two-dimensional schematic of the initial configuration is presented in Figure 5.1a: a converging cylindrical shock impacts at a Mach number M_I a perturbed, cylindrically shaped density interface that separates light air from heavy SF_6 (see Figure 5.1b), both at rest initially. The physical properties of these two gases are presented on Table 5.1. As described in Chapter 4, the present initial shock refraction produces a transmitted shock traveling and a reflected shock traveling inwards and outwards respectively, apart from the accelerated interface. The transmitted shock converges towards the axis, reflects off the apex, and reshocks the highly distorted interface, initiating strong turbulent mixing. Multiple reshock events follow self-similar way with decreasing intensity, eventually concentrating the heavy fluid inside. Strong initial incident shocks trap the heavy fluid closer to the apex than weaker incident shocks.

5.1.2 Domain Geometry and Boundary Conditions

The present simulation is conducted in a wedge-like geometry. The wedge angle is $\pi/2$. The computational domain, in cylindrical coordinates (r, θ, z) is:

$$r_{in} < r < \beta_r R_0, \quad 0 < \theta < \pi/2, \quad 0 < z < \beta_z \pi/2 \tag{5.1}$$

The inner cylindrical reflecting wall of radius r_{in} and the outer radial distance $\beta_r R_0$, with $\beta_r > 1$ is theoretically taken proportional to the wedge angle. β_z is a rational number that specifies the

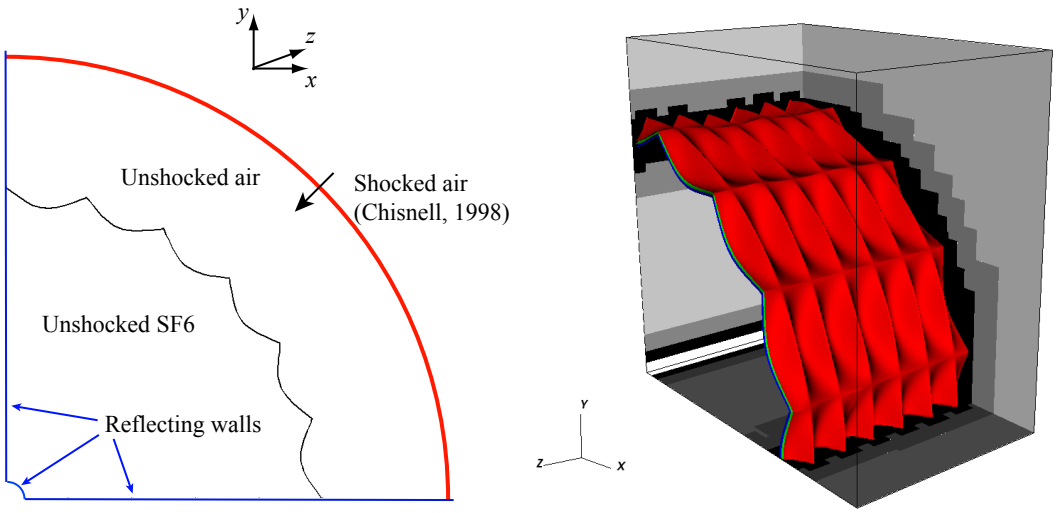

(a) (b)

Figure 5.1: (*a*) Initial flow description. Time $t = 0$ actually corresponds to the incident shock standing just behind the interface with Mach number M_I. (*b*) Scalar isosurfaces representing the initial perturbed interface (data from run 11 and run 12).

extension of the domain in the axial direction. See Tables 5.2, 5.3 and 5.4 for exact values of β_r and β_z.

It is assumed that shock-wave/boundary-layer interaction does not play a dominant role in the growth of the TMZ and slip boundary conditions are applied at the reflected walls $\theta = 0$ and $\theta = \pi/2$. In practice, experiments in shock-tubes [9, 109] have shown that the interaction of viscous boundary layers on the side walls of the test section can cause the formation of wall bubbles and interface contaminating jets. Brouillette demonstrated the generation of baroclinic vortical structures within the boundary layer from the interaction of waves reflected from the side walls and the distorted interface [9]. The strain induced by these vortical wall structures tends to make the TMZ thinner.

Property	air	SF_6
Molecular mass (kg kmol^{-1})	29.04	146.07
Atwood ratio with air A	0.0	0.67
Ratio of specific heats γ	1.40	1.09
Density (kg m^{-3})	1.18	5.97
Kinematic viscosity (10^{-6} m^{-2}s^{-1})	15.7	2.47
Prandtl number	0.71	0.90
Diffusion coefficient in air (10^{-6} m^{-2}s^{-1})	20.4	9.7

Table 5.1: Gas properties of air and SF_6 at 25°C and 1 atm.

The inner cylindrical reflecting wall of radius r_{in} is used to regularize the apex (see Figure 5.1a), as it is done in VTF experiments in a wedge. The measured location and extent of the TMZ suggest that the turbulent region does not reach the inner cylindrical wall as long as the incident shock Mach number is not too high. On the outer side of the domain, inflow boundary conditions are prescribed (see next subsection) for time t prior to the exit of the initial reflected shock from the computational domain. After that event, zero-gradient boundary conditions are prescribed. Periodic boundary conditions are used in the z-direction of the cylinder axis.

5.1.3 Initial Conditions

There are many ways to generate, in principle, a converging cylindrical shock. Hosseini and Takayama [50] use a device like a curved annular shock tube. Dimotakis and Samtaney [24] have proposed a method where a planar shock, incident on a shaped interface positioned at the entrance of a convergent wedge, produces a transmitted shock that is accurately cylindrical. The interface shape is tailored precisely so as to avoid Mach reflection at the wedge walls. Using geometrical shock dynamics, Hornung et al. [48] argue that, once formed, cylindrically (and spherically) symmetric converging shocks have an almost universal implosion profile that is essentially independent of the detailed means of shock generation. This almost universal form is that calculated by Ponchaut et al. [87]: it becomes asymptotic to Guderley power-law shock implosion in the strong-shock approximation.

Presently, the flow behind the cylindrical converging shock is initialized using the post-shock flow field of Chisnell [15]. We have confirmed the structure of this solution by simulation of a single converging shock, and the Guderley exponent, characterizing the shock position history, has been confidently computed before and after apex reflection (see Subsection 3.3.3 for more details). We recall that this choice of initial conditions completely avoids spurious waves and leaves only the shock thickness as intrinsic length scale. Simulations have been performed for the incident shock strength $M_I = 1.3$ and 2.0. The Chisnell solution is presently used both as an initial condition for the flow behind the shock as far as the outer boundary of the domain, and also to provide inflow boundary conditions on the outer boundary before the reflected shock exits the computational domain. The front of the incident converging shock is initially placed just behind the interface at radius $r = R_{S_0}$. At this position, the shock Mach number is M_I.

The interface is initially located around the mean radial position $r = R_0 < R_{S_0}$. Along any ray of azimuthal orientation θ and height z, the mixture ratio of air and SF_6 is mathematically initialized as $\tanh(2(r - r_I(\theta, z))/\delta_0^C)$. In this expression, r_I is the centerline position of the perturbed interface at (θ, z), and δ_0^C is the initial intrinsic thickness of the interface and is chosen small enough to be fully resolved, specially during the incident shock refraction where the interface is compressed to a thickness inferior to δ_0^C during the shock passage. To model the initial contact discontinuity

deformation, we choose a centerline surface radial displacement of the interface of the form

$$r_I(\theta, z) = R_0 - (h_0|\cos(n\theta)\cos(kz)| + h_1 f(\theta, z))\,. \tag{5.2}$$

The first term models the result of pushing the membrane through a wire mesh (find equivalent definition in the plane geometry in [109, 16, 43]), and represents small modes of amplitude h_0, about 5% of R_0, and with initial azimuthal wavelength $\lambda_{\theta_0} = \pi R_0/n$ and axial wavelength $\lambda_z = \pi/k$. The choice of k is a compromise between having a ratio of scale lengths comparable to the previously cited plane experiments and having adequate numerical resolution. Similar considerations are taken for the choice of n but for azimuthal wavelengths around the reshock time. At such time in the simulation, the azimuthal wavelength can be reduced by a factor of 10 for incident shock Mach numbers greater than 2.0. From the first perturbation term in Equation (5.2), it is expected that angular regions of the interface where the cosine argument is equal to $\pi/2$ will be subjected to strong baroclinic torque. The second term in Equation (5.2) is a symmetry-breaking perturbation with smaller amplitude h_1, about 10% of h_0. $f(\theta, z)$ has a random phase but a prescribed power spectrum of the form $\mathrm{K}^4 \exp(-(\mathrm{K}/\mathrm{K}_0)^2)$ with parameter $\mathrm{K}_0 = 1$ chosen such that the peak wavelength is $\pi\sqrt{2}R_0$ (long wavelength symmetry breaking). It represents the distortion of the wire mesh on the scale of the wedge in the azimuthal and axial directions. We refer to Tables 5.2, 5.3 and 5.4 for more details.

In choosing such clean initial conditions, the goal is to set up a canonical simulation that could be used as a reference simulation in cylindrical geometry. However, care has to be taken when analyzing late-time behavior in such unsteady flows. How the initial interface dominant shape (first term of Equation (5.2)) affects the late growth of the mixing layer is still a current research question. In [109], it is observed that a change in the disposition of the horizontal and vertical wire meshes can modify the mixing-layer growth before the reshock by a an order of magnitude. Strong influence of the initial conditions on the nonlinear stages of the mixing-zone growth has been also demonstrated by Greenough and Burke [38] who studied computations of the multimode RMI in the plane geometry. Therefore, flows generated from different initial conditions are not expected to compare well, in particular prior to the first reshock. To study the sensitivity of the flow to variations in the random part of the initial interface shape (second term of Equation (5.2)), simulations should be performed for an ensemble of initial conditions covering the spectrum of realizations of the random nature of the second term of Equation (5.2). Due to limited resources, we leave the study of the influence of initial conditions (e.g., interface shape and amplitude) on the flow statistics for future research.

On another note, there is a consensus in the belief that turbulent flows are, in some sense, ergodic. However, there seems to exist no direct evidence regarding the validity of the ergodicity hypothesis in turbulent flows, though some mathematical results regarding the ergodicity for the NavierStokes equations were reported recently (see for example [20]). Ergodicity is usually related to turbulent

flows being statistically stationary in time and homogeneous in space, which is not the case in the present flow. In theory, if the ergodic hypothesis were correct, it would not be necessary to perform a large number of time consuming "brutal force" experiments with different initial conditions in order to compare the temporal/spatial statistical value of a given observable against the ensemble-averaged value at a given time/location.

5.2 Governing Equations

5.2.1 Two-Component Favre-Filtered Navier-Stokes Equations

The reshock process produces a large dynamical range of turbulent scales, necessitating the use of LES. If the overbar denotes the filtering operation

$$\overline{f}(\boldsymbol{x}) = G_{\Delta_c} * f(\boldsymbol{x}) = \int G_{\Delta_c}(\boldsymbol{x} - \boldsymbol{x}')f(\boldsymbol{x}')\mathrm{d}\boldsymbol{x}', \tag{5.3}$$

with convolution kernel G_{Δ_c} with externally specified spatial width Δ_c, any Favre-filtered, or density weighted, quantities is defined by

$$\widetilde{f} = \overline{\rho f}/\overline{\rho}. \tag{5.4}$$

The filtering procedure described in Equation (5.3) is purely formal. It corresponds to a low-pass spatially uniform filter and allows one to locally distinguish flow features with a length-scale larger than Δ_c with length-scale smaller than Δ_c. In the LES context, the former are referred as 'resolved' while the latter class of flow structures is identified as 'sub-filter' or 'subgrid'. In practice, the filtering operation can only be performed explicitly from well-resolved fields obtained from experiments or DNS. However, by Favre-filtering of the Navier-Stokes equations [124], the LES transport equations of motion in a conservative form are formally obtained for the filtered density $\overline{\rho}$, momentum $\overline{\rho}\widetilde{u}_i$, total energy $\overline{E}$, and $\overline{\rho}\widetilde{\psi}$, where $\widetilde{\psi}$ is a filtered scalar field representing local mixture composition (mass fraction) between air ($\tilde{\psi} = 0$) and SF_6 ($\tilde{\psi} = 1$). In this procedure, the large scales to be simulated are separated from the small scales to be modeled at the subgrid level:

$$\frac{\partial\overline{\rho}}{\partial t} + \frac{\partial\overline{\rho}\widetilde{u}_j}{\partial x_j} = 0, \tag{5.5a}$$

$$\frac{\partial\overline{\rho}\widetilde{u}_i}{\partial t} + \frac{\partial(\overline{\rho}\widetilde{u}_i\widetilde{u}_j + \overline{p}\delta_{ij})}{\partial x_j} = \frac{\partial\overline{d}_{ij}}{\partial x_j} - \frac{\partial\tau_{ij}}{\partial x_j}, \tag{5.5b}$$

$$\frac{\partial\overline{E}}{\partial t} + \frac{\partial(\overline{E} + \overline{p})\widetilde{u}_j}{\partial x_j} = \frac{\partial}{\partial x_j}\left(\overline{\kappa}\frac{\partial\widetilde{T}}{\partial x_j}\right) + \frac{\partial\overline{d}_{ji}\widetilde{u}_i}{\partial x_j} - \frac{\partial q_j^T}{\partial x_j}, \tag{5.5c}$$

$$\frac{\partial\overline{\rho}\widetilde{\psi}}{\partial t} + \frac{\partial\overline{\rho}\widetilde{\psi}\widetilde{u}_j}{\partial x_j} = \frac{\partial}{\partial x_j}\left(\overline{\rho}\widetilde{D}\frac{\partial\widetilde{\psi}}{\partial x_j}\right) - \frac{\partial q_j^{\psi}}{\partial x_j}, \tag{5.5d}$$

where the subgrid stress tensor, and the heat and scalar transport fluxes are given by

$$\tau_{ij} = \overline{\rho}(\widetilde{u_i u_j} - \tilde{u}_i \tilde{u}_j), \tag{5.6a}$$

$$q_j^T = \overline{\rho}(\widetilde{c_p T u_j} - \tilde{c_p} \tilde{T} \tilde{u_j}), \tag{5.6b}$$

$$q_j^{\psi} = \overline{\rho}(\widetilde{\psi u_j} - \tilde{\psi} \tilde{u_j}), \tag{5.6c}$$

and where the filtered total energy $\overline{E}$, pressure $\overline{p}$, and deviatoric Newtonian stress tensor $\overline{d}_{ij}$ of the mixture are given by

$$\overline{E} = \frac{\overline{p}}{\widetilde{\gamma} - 1} + \frac{1}{2}\overline{\rho}(\widetilde{u}_k \widetilde{u}_k) + \frac{1}{2}\tau_{kk}, \tag{5.7a}$$

$$\overline{p} = \frac{\overline{\rho} \mathrm{R} \widetilde{T}}{\widetilde{m}}, \tag{5.7b}$$

$$\overline{d}_{ij} = \overline{\mu}\left(\left(\frac{\partial \widetilde{u}_i}{\partial x_j} + \frac{\partial \widetilde{u}_j}{\partial x_i}\right) - \frac{2}{3}\frac{\partial \widetilde{u}_k}{\partial x_k}\delta_{ij}\right). \tag{5.7c}$$

Note that, whilst Reynolds-averaged Navier-Stokes (RANS) approaches to modeling the Navier-Stokes equations decompose the velocity into mean and fluctuating components, the typical reorganization in LES is based upon the filter length scale Δ_c, often taken to be equal to the grid size employed.

In Equation (5.7b), R is the ideal gas constant, and the mean molecular weight $\widetilde{m}$ is defined as a function of the respective molecular weight of air and SF_6 by

$$\frac{1}{\widetilde{m}} = \frac{1 - \widetilde{\psi}}{m_{\mathrm{air}}} + \frac{\widetilde{\psi}}{m_{\mathrm{SF_6}}}. \tag{5.8}$$

From $\widetilde{m}$, the average specific heat ratio present in Equation (5.7a) and defined as

$$\widetilde{\gamma} = \frac{\widetilde{c}_p}{\widetilde{c}_p - \mathrm{R}/\widetilde{m}}, \tag{5.9}$$

can be determined since the average specific heat capacity at constant pressure is given by the following combination of element heat capacities for air and SF_6 (assumed to be temperature-independent)

$$\widetilde{c}_p = (1 - \widetilde{\psi}) c_{p,\mathrm{air}} + \widetilde{\psi} c_{p,\mathrm{SF_6}}. \tag{5.10}$$

Values of $\widetilde{\gamma}$ for pure air ($\tilde{\psi} = 0$) and pure SF_6 ($\tilde{\psi} = 1$) are listed in Table 5.1. Temperature-dependent transport properties of the mixture, i.e., viscosity $\overline{\mu}$, heat conduction $\overline{\kappa}$, and diffusivity $\widetilde{D}$, obey usual binary mixing rules and pure component mixing properties [93].

5.2.2 The Stretched-Vortex Subgrid Model

The stretched-vortex subgrid-scale (SGS) model [82] extended to compressible flows [58] and subgrid scalar transport for a constant-density fluid [88] is based on an explicit structural modeling of small-scale dynamics. The essential subgrid element is modeled by a distribution of stretching vortices that are approximate solutions of the Navier-Stokes equations [71]. The closure of Favre-filtered Navier-Stokes equations is achieved by providing the subgrid stress tensor τ_{ij}, the turbulent temperature flux q_i^T, and the mixture fraction flux q_i^ψ, formally defined in Equation (5.6) and modeled as

$$\tau_{ij} = \overline{\rho}\tilde{k}(\delta_{ij} - e_i^v e_j^v), \tag{5.11a}$$

$$q_i^T = -\overline{\rho}\frac{\Delta_c}{2}\tilde{k}^{1/2}(\delta_{ij} - e_i^v e_j^v)\frac{\partial(\tilde{c}_p\tilde{T})}{\partial x_j}, \tag{5.11b}$$

$$q_i^\psi = -\overline{\rho}\frac{\Delta_c}{2}\tilde{k}^{1/2}(\delta_{ij} - e_i^v e_j^v)\frac{\partial\tilde{\psi}}{\partial x_j}. \tag{5.11c}$$

Note that the SGS temperature flux is treated as a passive scalar. In Equation (5.11), e_i^v are the direction cosines of the subgrid vortex axis and Δ_c the cutoff length scale. The subgrid kinetic energy, $\tilde{k}$, is given by

$$\tilde{k} = \int_{\pi/\Delta_c}^{\infty} E(k)\mathrm{d}k = \int_{\pi/\Delta_c}^{\infty} \mathsf{K}_0\varepsilon^{2/3}k^{-5/3}\exp\left(-\frac{2k^2\overline{\mu}}{3|\tilde{a}|\overline{\rho}}\right)\mathrm{d}k. \tag{5.12}$$

The energy spectrum of the subgrid motion $E(k)$ is a function of K_0, Kolmogorov pre-factor, ε, the local cell-averaged dissipation, and $\tilde{a} = \tilde{S}_{ij}e_i^v e_j^v$, the axial strain along the subgrid vortex axis provided by the locally resolved rate-of-strain tensor

$$\tilde{S}_{ij} = \frac{1}{2}\left(\frac{\partial\tilde{u}_i}{\partial x_j} + \frac{\partial\tilde{u}_j}{\partial x_i}\right). \tag{5.13}$$

The implementation of the subgrid vortex model relies on the assumption of the alignment of $\boldsymbol{e^v}$ with extensional eigenvectors of $\tilde{S}_{ij}$ and with the resolved-scale vorticity [58]. Moreover, the parameter $\mathsf{K}_0\varepsilon^{2/3}$ is calculated for each cell using resolved-scale, second-order velocity structure function matching [110, 88]. For example, when averaging the structure function $\mathcal{F}_2(\boldsymbol{r})$ over a spherical surface of radius Δ and using the expression of $E(k)$,

$$\mathsf{K}_0\varepsilon^{2/3} = \frac{\overline{\mathcal{F}_2}(\Delta)}{\Delta^{2/3}\mathrm{A}}, \tag{5.14}$$

where A $\approx$ 1.90695. Typically, $\Delta = \Delta_c = \Delta x$, with Δx the finest grid spacing, and $\overline{\mathcal{F}_2}$ is evaluated from averaging the local resolved-scale velocity components

$$\overline{\mathcal{F}_2}(\triangle) = \frac{1}{6}\sum_{j=1}^{3}\left(\delta\tilde{u}_1^{+^2} + \delta\tilde{u}_2^{+^2} + \delta\tilde{u}_3^{+^2} + \delta\tilde{u}_1^{-^2} + \delta\tilde{u}_2^{-^2} + \delta\tilde{u}_3^{-^2}\right)_j, \tag{5.15}$$

where we defined $\delta\tilde{u}_i^{\pm}$, velocity component difference in the unitary direction $\boldsymbol{e}_j$ at the location $\boldsymbol{x}_o$, by

$$\delta\tilde{u}_i^{\pm} = \tilde{u}_i(\boldsymbol{x}_o \pm \boldsymbol{e}_j\Delta) - \tilde{u}_i(\boldsymbol{x}_o). \tag{5.16}$$

The stretched-vortex subgrid model has been used to compute the two-fluid mixing driven by the RTI, as presented [76]. The structural nature of this model has also facilitated the mathematical development of a multiscale treatment of the activity beyond the resolution cut-off and predictions of subgrid mixing properties [43]. For what follows, the presently defined Favre-filtered quantities are identified with resolved-scale quantities computed in the LES, so that overbars and tildes will be omitted in Section 5.4 and the sections following.

5.3 Computational Approach

5.3.1 AMROC Framework

The resolution requirements imposed by the physics of the flow vary greatly both spatially and temporally for this simulation. In particular, around discontinuities in the flow (e.g., shock waves) any high-order scheme drops to first-order accuracy and refining the mesh is an efficient way to reduce the numerical error around these sharp features. Therefore, the parallel framework AMROC developed by Deiterding [21], and based on the SAMR of Berger and Oliger [3, 3], proves to be decisive for the converging RMI, where refinement is needed around the multiple imploding and exploding shocks and the interface traveling down towards the inner apex, while coarse resolution is sufficient for the outer region. SAMR method provided large computational savings in the particular case of the converging RMI but also in other applications listed in [83].

5.3.1.1 On the Use of SAMR Cartesian Grid for Converging Flows

As shown in Figure 5.2, successful comparisons have been made between experiments of focusing of plane shocks in cylindrical geometry and solvers using Cartesian and body-fitted grids. Another validation test, similar to VTF Phase 0 experiments in spherical geometry, has shown good agreement between SAMR simulations on Cartesian grid and the experiments of conical shock-tube by Setchell et al. [102]. An initial plane shock of Mach 6 travels in Argon into a 10° half-angle cone. Conclusive

results are plotted in Figure 5.3a which shows the successive jumps in shock speed (measured on the centerline of the tube) corresponding to Mach stem collisions on the axis of symmetry. In the present work, as in the simulations presented in Figures 5.2a and 5.3, the ghost fluid method (GFM) [30] is utilized to numerically incorporate the non-Cartesian reflective wall boundary conditions arising at the small cylinder regularizing the apex (see Subsection 5.1.2).

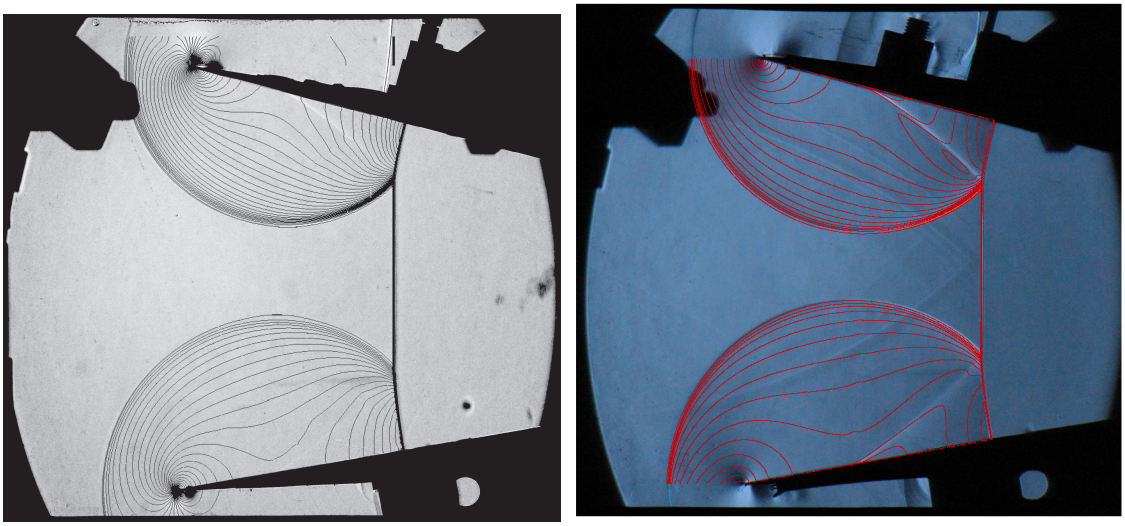

(a) Cartesian grid (b) Body-fitted grid

Figure 5.2: Converging shock focusing in a wedge. Overlay of experimental results from VTF Phase 0 and two-dimensional simulation data from the WENO-TCD patch solver formulated on a Cartesian grid (a) and a shock-capturing method formulated on a body-fitted grid (b). Courtesy of C. L. Bond, D. J. Hill, and G. Matheou.

5.3.2 Hybrid Numerical Method

The numerical method is formulated for uniform Cartesian grids and is effectively applied to each subgrid of the mesh hierarchy. The overall approach is an extension of the hybrid scheme by Hill and Pullin [44] to SAMR meshes with non-Cartesian embedded boundaries. We recall that a WENO scheme is used to capture discontinuities such as shock waves or fine/coarse mesh interfaces, but switches to a low-numerical dissipation, explicit, center-difference scheme, TCD, in the smooth or turbulent regions, optimal for the functioning of explicit LES such as the SGS stretched-vortex method.

Figure 5.4 shows the decay of the turbulent kinetic energy (TKE) obtained from LES of decaying compressible turbulence using the stretched-vortex SGS model and the 5-point TCD scheme. Good agreement with a 256^3 DNS is achieved. A similar simulation using WENO-5 shows poor results owing to the excessive numerical dissipation that overwhelms that of the SGS model. The dissipation in WENO is due to the fact that the method rarely achieves its optimal stencil and therefore exhibits

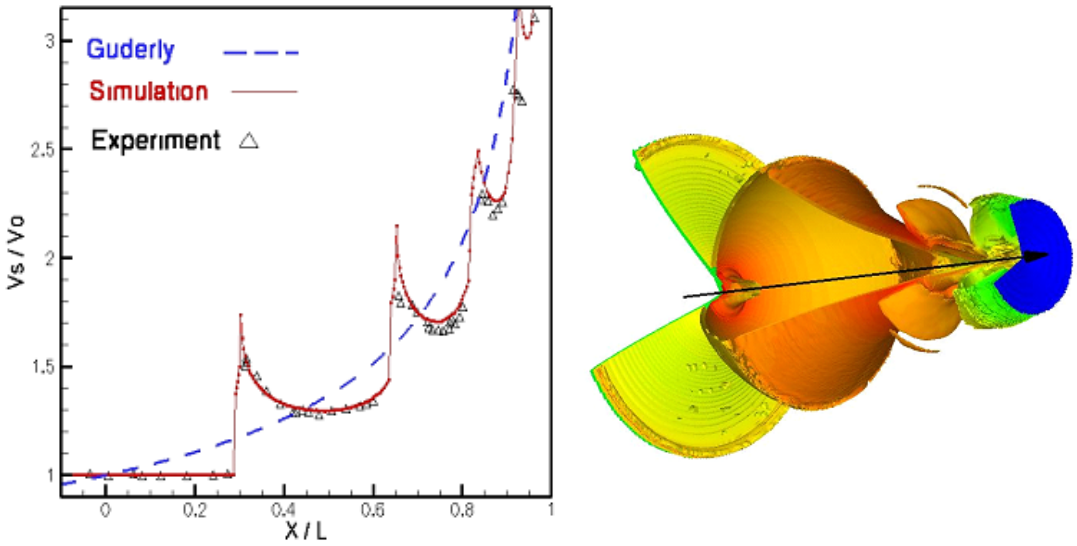

(a) Speed on the centerline

(b) Density Schlieren isosurfaces

Figure 5.3: Conical shock-tube experiments and two-dimensional axisymmetric simulations. (a) Radial speed (normalized by initial shock speed) on the centerline vs. distance to the center; (b) isosurfaces of the three-dimensional magnitude of the density gradient (Schlieren) colored by the density. Speeds over Mach 18 at last measurement. Courtesy of D. J. Hill.

the updwinding bias of its candidate stencils. Moreover, even recent higher-order implementations of WENO fail in creating a consistent stencil, since the convex combination of candidate stencils is based on local smoothness indicators. As a consequence, the dispersion relation is not predictable for such approaches and makes them not suited for accurate LES calculations. Similar conclusions can be drawn from other higher-order shock-capturing methods, e.g. using elaborate limiters. These considerations justify the use of hybrid schemes instead of pure shock-capturing methods or other implicit LES methods that introduce too much numerical dissipation in the flow and alter the decay of TKE.

5.3.2.1 TCD Stencil

In one dimension, the derivative of a function $f(x)$ can be discretely approximated on a uniform grid, at the location $x = i\Delta x$, by the following 5-point at least 2nd-order accurate stencil

$$\mathcal{D}_x f = \frac{1}{\triangle x} \left(\alpha(f_{i+2} - f_{i-2}) + (1/2 - 2\alpha)(f_{i+1} - f_{i-1})\right), \tag{5.17}$$

where the parameter $\alpha = 0$ corresponds to the exact 2nd-order explicit stencil and $\alpha = -1/12$ to the 4th-order stencil. As a tradeoff against accuracy, this parameter can be chosen to minimize truncation errors in LES in the sense of Ghosal [34, 35]. The value $\alpha = -0.197$ has been found in [44] and forms the TCD stencil.

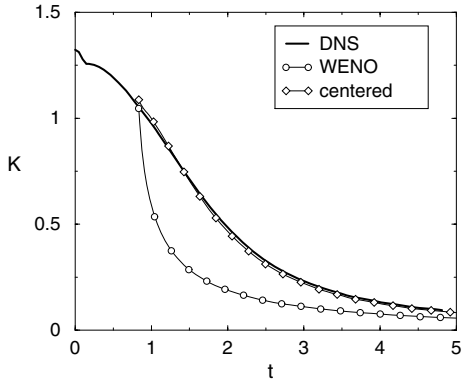

Figure 5.4: Comparison of decay of turbulence kinetic energy in a homogeneous decaying compressible LES computed on a grid of 32^3 points using standard WENO-5 vs. 5-point TCD scheme. DNS computed with a 256^3 grid and a Padé method, Case D9 of Samtaney et al. [98] with microscale Reynolds number of 175 and turbulent Mach number of 0.488.

5.3.2.2 Stable TCD Formulation

LES at very high Reynolds numbers using low-numerical dissipation centered discretizations raise the issue of numerical stability, since resolved and subgrid viscous dissipation sometimes provide negligible stabilization. For that reason, the momentum and scalar convective terms must be written in the following skew-symmetric form adapted to compressible flows [6], as follows:

$$\frac{\partial(\overline{\rho}\tilde{u}_i\tilde{u}_j)}{\partial x_j} \quad \mapsto \quad \frac{1}{2}\frac{\partial(\overline{\rho}\tilde{u}_i\tilde{u}_j)}{\partial x_j} + \frac{\overline{\rho}\tilde{u}_j}{2}\frac{\partial(\tilde{u}_i)}{\partial x_j} + \frac{\tilde{u}_i}{2}\frac{\partial(\overline{\rho}\tilde{u}_j)}{\partial x_j}, \tag{5.18a}$$

$$\frac{\partial(\overline{\rho}\tilde{\psi}\tilde{u}_j)}{\partial x_j} \quad \mapsto \quad \frac{1}{2}\frac{\partial(\overline{\rho}\tilde{\psi}\tilde{u}_j)}{\partial x_j} + \frac{\overline{\rho}\tilde{u}_j}{2}\frac{\partial(\tilde{\psi})}{\partial x_j} + \frac{\tilde{\psi}}{2}\frac{\partial(\overline{\rho}\tilde{u}_j)}{\partial x_j}. \tag{5.18b}$$

In compressible flows, robustness can be improved by rewriting the convective term in the energy equation in a skew-symmetric form as well. Honein and Moin [47] found that the most stable formulation is the one that conserve the variance in total internal energy $\tilde{e} = \overline{E}/\overline{\rho} - (\tilde{u}_k\tilde{u}_k)/2$:

$$\begin{aligned}\frac{\partial((\overline{E}+\overline{p})\tilde{u}_j)}{\partial x_j} \quad &\mapsto \quad \frac{1}{2}\frac{\partial(\overline{\rho}\tilde{e}\tilde{u}_j)}{\partial x_j} + \frac{1}{2}\overline{\rho}\tilde{u}_j\frac{\partial\tilde{e}}{\partial x_j} + \frac{1}{2}\tilde{e}\frac{\partial(\overline{\rho}\tilde{u}_j)}{\partial x_j} \\ &+ \quad \frac{1}{2}\tilde{u}_i\frac{\partial(\overline{\rho}\tilde{u}_i\tilde{u}_j)}{\partial x_j} + \frac{1}{2}\overline{\rho}\tilde{u}_i\tilde{u}_j\frac{\partial\tilde{u}_i}{\partial x_j} + \overline{p}\frac{\partial u_j}{\partial x_j} + \tilde{u}_j\frac{\partial\overline{p}}{\partial x_j}.\end{aligned} \tag{5.19a}$$

5.3.2.3 Flux-Based Formulation

The SAMR approach is based on flux discretizations. While WENO is naturally a flux-based formulation, the TCD scheme must be expressed in a flux form as well. First derivatives approximated by the difference operator $\mathcal{D}_x$ in Equation (5.17) can be written in a divergence-like flux difference

at the cell center i

$$\mathcal{D}_x f = \frac{F_{i+1/2} - F_{i-1/2}}{\Delta x}, \tag{5.20}$$

where the flux $F_{i+1/2}$ at the right-hand sidewall of the cell i is given by

$$F_{i+1/2} = \alpha\left(f_{i+2} + f_{i+1}\right) + (1/2 - \alpha)\left(f_{i+1} + f_i\right). \tag{5.21}$$

The derivation of the flux corresponding to the derivative of products in a skew-symmetric form is described in [83]. As a result:

$$\frac{\partial(fg)}{\partial x} \simeq \frac{1}{2}\Big(\mathcal{D}_x(fg) + f\mathcal{D}_x g + g\mathcal{D}_x f\Big) = \frac{F^{skew}_{i+1/2} - F^{skew}_{i-1/2}}{\Delta x}, \tag{5.22}$$

where

$$\begin{aligned} F^{skew}_{i+1/2} &= \frac{1}{2}\Big\{\alpha\big[(g_{i+1} + g_{i-1})(f_{i+1} + f_{i-1}) + (g_{i+2} + g_i)(f_{i+2} + f_i)\big] \qquad (5.23a)\\ &+ (1/2 - 2\alpha)\big[(f_{i+1} + f_i)(g_{i+1} + g_i)\big]\Big\}. \end{aligned}$$

In Equation (5.22), the functions f and g correspond to $\overline{\rho}\tilde{u}_k$ and $\tilde{u}_k$ for the convective term of the momentum transport equation given by (5.18a), and to $\overline{\rho}\tilde{u}_k$ and $\tilde{\psi}$ for the convective term of the scalar transport equation given by (5.18b). The energy convective contribution Equation (5.19) is separated in divergence-like terms whose fluxes are rewritten like Equation (5.21), and product-like terms whose fluxes are rewritten like Equation (5.23).

5.3.2.4 WENO-TCD Flux-Switching Technique

The WENO-TCD scheme requires an explicit 'switch' to change from WENO in regions of extremely high gradients, such as shocks, to the TCD scheme in smooth flow regions. Around discontinuities, the WENO scheme computes fluxes at cell walls based on a weighted convex combination of candidate stencils that minimizes interpolation across shocks. For the subgrid activity to be correctly computed, thereby assuring the quality of the LES, the use of WENO is restrained to regions containing shock waves only. The formulation of robust detection criteria of physical discontinuities problems remains an open research area, and work has essentially concentrated on geometrical criteria based, for instance, on normalized curvature of pressure and/or density (as in [44, 83] and other hybrid methods cited within). Instead, a new WENO/TCD switching method has been developed to better extract the physical nature of the compressible flow, therefore optimizing the use of WENO.

To illustrate the technique, consider the local one-dimensional Riemann problem at every cell wall

of the computation domain. An approximate solution, denoted by a subscript $\star$, can be computed using Roe-averaged quantities from the given left state (cell face i, subscript L) and right state (cell face $i+1$, subscript R). Lax entropy conditions allow for characterizing the type of the waves $\widetilde{u}-\overline{a}$ and $\widetilde{u}+\overline{a}$ (shock or rarefaction wave) connecting the right or left state from the central state $\star$, with $\overline{a}$ the filtered sound speed of the mixture. A shock is produced for the wave $\widetilde{u}\pm\overline{a}$ if

$$\widetilde{u}_R \pm \overline{a}_R < \widetilde{u}_\star \pm \overline{a}_\star < \widetilde{u}_L \pm \overline{a}_L. \tag{5.24}$$

In this set of inequalities, $\overline{a}_{L,R}$ is computed by evaluating $\sqrt{\widetilde{\gamma}\overline{p}/\overline{\rho}}$ at the left or right cell faces, and the central state $(\widetilde{u}_\star, \overline{a}_\star)$ corresponds to the Roe's averages [95]

$$\widetilde{u}_\star = \frac{\sqrt{\overline{\rho}_L}\widetilde{u}_L + \sqrt{\overline{\rho}_R}\widetilde{u}_R}{\sqrt{\overline{\rho}_L}+\sqrt{\overline{\rho}_R}}, \tag{5.25a}$$

$$\overline{a}_\star = \sqrt{(\widetilde{\gamma}_\star - 1)(\overline{H}_\star - \frac{1}{2}\widetilde{u}_\star^2)}, \tag{5.25b}$$

where the Roe-averaged filtered enthalpy $\overline{H}_\star$ and specific heat ratio $\widetilde{\gamma}_\star$ are given by

$$\overline{H}_\star = \frac{\sqrt{\overline{\rho}_L}\overline{H}_L + \sqrt{\overline{\rho}_R}\overline{H}_R}{\sqrt{\overline{\rho}_L}+\sqrt{\overline{\rho}_R}}, \tag{5.26a}$$

$$\widetilde{\gamma}_\star = \frac{\widetilde{c}_{p,\star}}{\widetilde{c}_{p,\star} - \widetilde{r}_{m,\star}}, \tag{5.26b}$$

$$\widetilde{c}_{p,\star} = \frac{\sqrt{\overline{\rho}_L}\widetilde{c}_{p,L} + \sqrt{\overline{\rho}_R}\widetilde{c}_{p,R}}{\sqrt{\overline{\rho}_L}+\sqrt{\overline{\rho}_R}}, \tag{5.26c}$$

$$\widetilde{r}_{m,\star} = \frac{\sqrt{\overline{\rho}_L}\widetilde{r}_{m,L} + \sqrt{\overline{\rho}_R}\widetilde{r}_{m,R}}{\sqrt{\overline{\rho}_L}+\sqrt{\overline{\rho}_R}}. \tag{5.26d}$$

In Equation (5.26), $(\overline{H}, \widetilde{c}_p, \widetilde{r}_m)_{L,R}$ are computed by evaluating $((\overline{p}+\overline{E})/\overline{\rho}, \widetilde{c}_p, \mathrm{R}/\widetilde{m})$ for the mixture at the left or right cell faces. The departure of the inequalities (5.24) is evaluated within a threshold value $\alpha_{\mathrm{Lax}}/a_\star$ in order to eliminate weak acoustic waves that could be easily handled by the TCD scheme. For better efficiency and flexibility, this criterion is combined with a geometrical test based on the mapping

$$\varphi(\vartheta) = \frac{2\vartheta}{(1+\vartheta)^2} \tag{5.27}$$

of the normalized pressure gradient ϑ_i at the cell face i

$$\vartheta_i = \frac{|\overline{p}_{i+1} - \overline{p}_i|}{|\overline{p}_{i+1} + \overline{p}_i|} \tag{5.28}$$

inspired from slope-limiting techniques. A threshold for the latter geometrical criterion is defined by α_{Map}. Algorithm 1 applied to the filtered vector of state q_i at the cell wall i summarizes the technique

for one-dimensional switching. Cell faces are actually marked in a tight area around regions where WENO is needed according to the criterion

$$\mathcal{C}_i = \{(x_{i-1/2}, x_{i+1/2}) \in \mathbb{R} : \ q_i \text{ satisfies Alg. 1}\}. \tag{5.29}$$

All cell faces in a neighborhood of size $m\Delta x$ (m given) of cell faces belonging to $\mathcal{C}_i$ are also flagged and WENO stencils will be constructed over the sets of cell faces $\mathcal{C}_i^m = \bigcup_{s=-m,m} C_{i+m}$.

Algorithm 1 Physical discontinuity detection algorithm.

```
if q_i verifies inequalities Equation (5.24) to some departure α_Lax then
  if φ(ϑ_i) > α_Map then
    Mark cell wall i
  end if
end if
```

If $F_{i+1/2}^{\text{WENO}}$ denotes the WENO fluxes and the inviscid fluxes are represented on a skew-symmetric form as $F_{i+1/2}^{\text{TCD}}$, the hybrid flux takes the form

$$F_{i+1/2} = \begin{cases} F_{i+1/2}^{\text{WENO}}, & \text{in } \mathcal{C}_i^m \\ F_{i+1/2}^{\text{TCD}}, & \text{in } \overline{\mathcal{C}_i^m}, \end{cases} \tag{5.30}$$

where $\overline{\mathcal{C}_i^m}$ denotes the complement of $\mathcal{C}_i^m$. Equation (5.30) assumes that no smoothness requirements are needed for the switch from one flux form to the other, while smooth transition should be enforced if the switch was made on the derivative itself. Moreover, by construction, the dispersion relation is preserved across schemes [44].

Comparing at different times the results of a one-dimensional simulation of a converging shock impacting a concentric density interface using either curvature detection or the present switching technique, it is observed that the curvature criterion cannot capture easily shocks of variable strengths unless the curvature threshold is set to a too low value, therefore increasing the amount of WENO in other regions of the computational domain. For example, the curvature criterion fails at capturing the shock formation described in Subsection 4.3.1, unless the curvature thresholds are manually changed as the flow evolves. Two- and three-dimensional versions of this new switching algorithm have been developed to treat complex configurations such as oblique waves, curved shocks, and more general shock waves not aligned with the computational grid. It is based on the construction of local Lax criteria(5.24) not only for the Cartesian velocity components but also for velocity projections in all diagonal directions $x-y$, $x-z$, and $y-z$. Comparisons with sensors relying on pressure fluctuations alone were performed as verification tests on complex one-dimensional examples

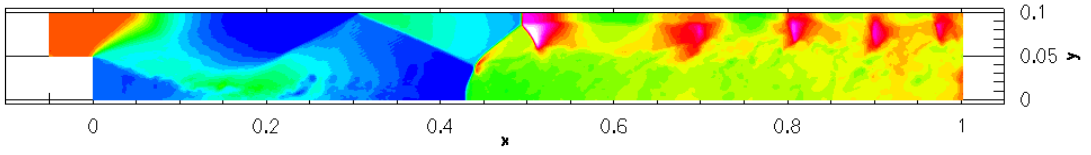

(a) Density

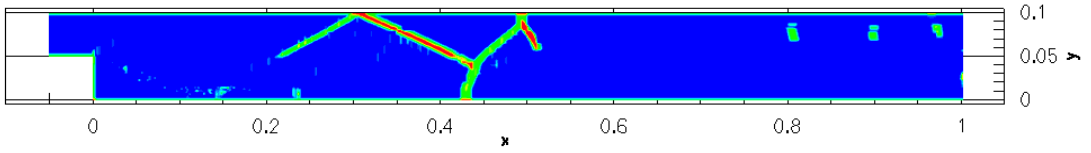

(b) WENO-TCD Flagging

Figure 5.5: Three-dimensional supersonic shear layer (periodic in the spanwise direction z). (x, y)-plane cut across the center of the jet of the density (top) and WENO-TCD flagging (bottom). WENO is turned on in the directions x and y (green) and x, y, and z (red) where shock waves are present. Courtesy of G. Matheou.

such as plane shock-contact interaction with reshock, radially symmetric cylindrical and spherical converging shock-contact interaction with reshock, shock-entropy wave interaction, colliding blast waves, vacuum test, etc.; and multi-dimensional examples as well, such as plane RMI, cylindrical converging RMI, supersonic shear layer (see Figure 5.5), supersonic inclined jet (see Figure 5.6), etc. The robustness of this technique is in the universality of the threshold values. The values of α_{Lax} and α_{Map} giving superior results to former criteria are both around 1% (see Tables 5.2, 5.3 and 5.4).

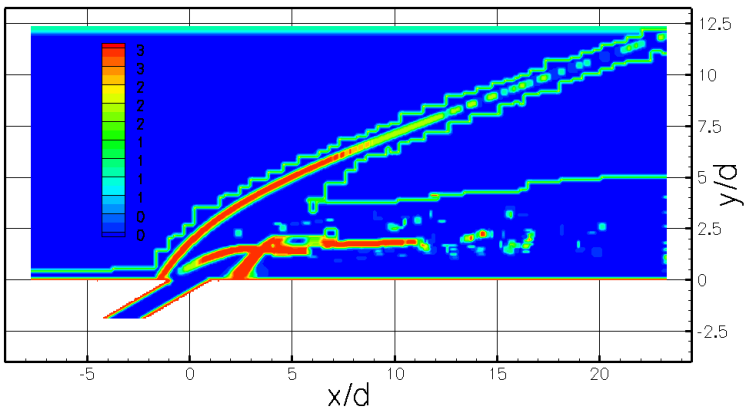

Figure 5.6: Three-dimensional supersonic inclined jet using SAMR (no periodicity in the z direction). (x, y)-plane cut of the WENO-TCD flagging. WENO is turned on in the directions x and y (green) and x, y, and z (red) where shock waves are present, in particular around the bow shock forming ahead of the jet. Courtesy of A. Ferrante.

5.3.3 Time-Marching Method for SAMR

The use of low-numerical dissipation centered schemes suitable for purely convective problems, as it is the case for high Reynolds number flows, requires particular temporal stability requirements. Explicit multi-stage schemes can be easily implemented within SAMR. Lower-order RungeKutta (RK) methods are not stable, so third or fourth-order RK time-marching methods are considered. RK substages can also be unstable when using upwinding in WENO: all RK coefficients must be positive in order to avoid undesirable oscillations around shocks where WENO is used. As a result, the optimal third-order strong stability preserving (SSP) RK scheme of [37] is chosen. Details are provided in Subsection 2.1 of [83].

5.3.4 Description of the Large-Eddy Simulations

Seven LES were performed on both the LLNL machine uP and the Center for Advanced Computing Research (CACR) shared heterogeneous cluster (SHC) at Caltech, and are listed in Tables 5.2, 5.3 and 5.4. The light-to-heavy air$\rightarrow$$SF_6$ interaction correspond to runs 12, A1/A1b for a $M_I = 1.2$ incident shock interaction, and run 11 and B1 for $M_I = 2.0$. Runs 12 and 11 are lower resolution simulations that respectively ran until a time of about four and seven times the first reshock time with reasonable computational cost. These simulations allowed us to follow the evolution of various properties of the mixing zone for the very long time. Runs A1 and B1 are twice refined in the three directions compared to runs 12 and 11 respectively. These simulations also contain more detailed statistics than the lower resolution runs. Run A1b is a full cylinder version of run A1 that has not been analyzed yet. It will be used for visualization purposes.

The heavy-to-light SF_6 $\rightarrow$air shock interaction is studied in the runs A2 and B2 at incident Mach numbers $M_I = 1.3$ and 2.0 respectively. They have the same resolution as the runs A1/A1b and B1. The runs are completed but are currently being post-processed.

Results on the air$\rightarrow$$SF_6$ interaction are presented in a fashion that puts in parallel the two incident Mach numbers. When possible, comparisons are made at similar times in the history of the flow (initial state, first reshock, first deceleration, etc.). We also compare this geometry to the plane configuration. Details on the post-processing methodology are listed in Appendices B and C.

The grid refinement criterion, based on the local density gradient, allows to refine both regions in the vicinity of the various shocks and the mixing layer. Owing to the geometry of the flow, at early times, finest grids are needed in less than 20% of the domain as the mixing layer spatial extension is still limited. The finest grids still represent a small fraction of the computational domain as the mixing layer is compressed during the reshock. However, after the first reshock, the finest grids can represent more than 70% of the domain as the mixing layer radially expands. At late times, the total number of cells for run A1 or B1 peaks around 220 million, to compare with the almost 300

million cells required if the grid is uniform and corresponds to the finest resolution. Therefore, for this particular flow SAMR proves to be useful mainly in the first half of the life of the mixing layer. At all times the largest portion of the computational cost corresponds to the numerical integration within the WENO-TCD scheme. While the TCD scheme is computationally very efficient, the expensive WENO method is in part responsible for that cost even though it is only used in the vicinity of shock. Since the multistage RK time-marching method requires a spatial synchronization at every substep, it is more communication-intensive than single-step methods.

	Parameters	run 12	run 11
Initial Conditions	Gas combination	**air→ SF_6**	**air→ SF_6**
	Pre-shock Atwood number A	0.66	0.66
	Incident Mach number M_I	**1.3**	**2.0**
	Unshocked outer fluid density ρ_0	0.27885	0.27885
	Unshocked outer fluid sound speed a_0	340	340
	Initial shock position R_{S_0}	1.05	1.05
	Initial interface position R_0	1.00	1.00
	Main pert. amplitude h_0	0.08	0.08
	Symmetry-breaking pert. amplitude h_1	0.01	0.01
	Symmetry-breaking pert. parameter K_0	1	1
	Azimuthal wavenumber n in $\lvert\cos(n\theta)\rvert$	8	8
	Axial wavenumber k in $\lvert\cos(kz)\rvert$	24	24
	Initial interface thickness δ_0^C	0.01	0.01
Geometry	Topology	1/4 **cylinder**	1/4 **cylinder**
	Approx. box dimensions (L_x, L_y, L_z)	$(1.3, 1.3, 0.785)$	$(1.3, 1.3, 0.785)$
	Exact (β_r, β_z)	$(83\pi/204, 1/2)$	$(83\pi/204, 1/2)$
	Base resolution $N_x \times N_y \times N_z$	$83 \times 83 \times 51$	$83 \times 83 \times 51$
	Additional levels of refinement	$(2, 2)$	$(2, 2)$
	Equivalent finest resolution	$332 \times 332 \times 204$	$332 \times 332 \times 204$
	Finest grid resolution $(\Delta x = \Delta y)$	$\Delta x = \Delta z \simeq 0.0039$	$\Delta x = \Delta z \simeq 0.0039$
	Inner cylindrical radius r_{in}	0.04	0.04
Numerics	Ghost cells	3	3
	LES cutoff scale Δ_c	Δx	Δx
	SGS vortex alignment on $S\&\Omega$	yes	yes
	SAMR Flagging on scaled $\lvert\nabla\overline{\rho}\rvert$ thresh.	0.15	0.15
	WENO-TCD thresh. $(\alpha_{\text{Lax}}, \alpha_{\text{Map}})$	$(0.01, 0.01)$	$(0.01, 0.01)$
Computations	Simulation time	0.030	0.020
	Nodes × CPUs/node	16 × 4 (shc)	16 × 4 (shc)
	CPU hours	49152	48384
	Number of cylindrical shells for stats	95	95

Table 5.2: Parameters used in the lower-resolution air→ SF_6 three-dimensional simulations of shock-driven mixing in a converging cylindrical geometry. MKS units. Note that $0.785 \simeq \pi/4$.

	Parameters	run A1	run A1b	run B1
Initial Conditions	Gas combination	**air→ SF_6**	**air→ SF_6**	**air→ SF_6**
	Pre-shock Atwood number A	0.66	0.66	0.66
	Incident Mach number M_I	**1.3**	**1.3**	**2.0**
	Unshocked outer fluid density ρ_0	0.27885	0.27885	0.27885
	Unshocked outer fluid sound speed a_0	340	340	340
	Initial shock position R_{S_0}	1.05	1.05	1.05
	Initial interface position R_0	1.00	1.00	1.00
	Main pert. amplitude h_0	0.03	0.03	0.03
	Symmetry-breaking pert. amplitude h_1	0.005	0.005	0.005
	Symmetry-breaking pert. parameter K_0	1	1	1
	Azimuthal wavenumber n in $\lvert\cos(n\theta)\rvert$	12	12	12
	Axial wavenumber k in $\lvert\cos(kz)\rvert$	22	22	22
	Initial interface thickness δ_0^C	0.005	0.005	0.005
Geometry	Topology	1/4 **cylinder**	**full cylinder**	1/4 **cylinder**
	Approx. box dimensions (L_x, L_y, L_z)	$(1.48, 1.48, 1.00)$	$(1.48, 1.48, 1.00)$	$(1.48, 1.48, 1.00)$
	Exact (β_r, β_z)	$(665\pi/1408, 7/11)$	$(665\pi/1408, 7/11)$	$(665\pi/1408, 7/11)$
	Base resolution $N_x \times N_y \times N_z$	$95 \times 95 \times 64$	$95 \times 95 \times 64$	$95 \times 95 \times 64$
	Additional levels of refinement	$(2, 2, 2)$	$(2, 2, 2)$	$(2, 2, 2)$
	Equivalent finest resolution	$760 \times 760 \times 512$	$760 \times 760 \times 512$	$760 \times 760 \times 512$
	Finest grid resolution ($\Delta x = \Delta y$)	$\Delta x = \Delta z \simeq 0.0019$	$\Delta x = 2\Delta z \simeq 0.0039$	$\Delta x = \Delta z \simeq 0.0019$
	Inner cylindrical radius r_{in}	0.04	0.04	0.04
Numerics	Ghost cells	3	3	3
	LES cutoff scale Δ_c	Δx	Δx	Δx
	SGS vortex alignment on $S\&\Omega$	yes	yes	yes
	SAMR Flagging on scaled $\lvert\nabla\overline{\rho}\rvert$ thresh.	0.15	0.15	0.15
	WENO-TCD thresh. $(\alpha_{\mathrm{Lax}}, \alpha_{\mathrm{Map}})$	$(0.01, 0.05)$	$(0.01, 0.05)$	$(0.01, 0.05)$
Computations	Simulation time	0.025	0.025	0.015
	Nodes × CPUs/node	32×4 (shc)	16×8 (uP)	32×4 (shc)
	CPU hours	89088	107520	99840
	Number of cylindrical shells for stats	280	280	280

Table 5.3: Parameters used in the higher-resolution air→ SF_6 three-dimensional simulations of shock-driven mixing in a converging cylindrical geometry. MKS units. Note that $1.000 \simeq 7\pi/22$.

	Parameters	run A2	run B2
Initial Conditions	Gas combination	**SF_6 →air**	**SF_6 →air**
	Pre-shock Atwood number A	-0.66	-0.66
	Incident Mach number M_I	**1.3**	**2.0**
	Unshocked outer fluid density ρ_0	0.27885	0.27885
	Unshocked outer fluid sound speed a_0	300	300
	Initial shock position R_{S_0}	1.05	1.05
	Initial interface position R_0	1.00	1.00
	Main pert. amplitude h_0	0.03	0.03
	Symmetry-breaking pert. amplitude h_1	0.005	0.005
	Symmetry-breaking pert. parameter K_0	1	1
	Azimuthal wavenumber n in $\lvert\cos(n\theta)\rvert$	12	12
	Axial wavenumber k in $\lvert\cos(kz)\rvert$	22	22
	Initial interface thickness δ_0^C	0.005	0.005
Geometry	Topology	1/4 **cylinder**	1/4 **cylinder**
	Approx. box dimensions (L_x, L_y, L_z)	$(1.48, 1.48, 1.00)$	$(1.48, 1.48, 1.00)$
	Exact (β_r, β_z)	$(665\pi/1408, 7/11)$	$(665\pi/1408, 7/11)$
	Base resolution $N_x \times N_y \times N_z$	$95 \times 95 \times 64$	$95 \times 95 \times 64$
	Additional levels of refinement	$(2, 2, 2)$	$(2, 2, 2)$
	Equivalent finest resolution	$760 \times 760 \times 512$	$760 \times 760 \times 512$
	Finest grid resolution ($\Delta x = \Delta y$)	$\Delta x = \Delta z \simeq 0.0019$	$\Delta x = \Delta z \simeq 0.0019$
	Inner cylindrical radius r_{in}	0.04	0.04
Numerics	Ghost cells	3	3
	LES cutoff scale Δ_c	Δx	Δx
	SGS vortex alignment on $S\&\Omega$	yes	yes
	SAMR Flagging on scaled $\lvert\nabla\overline{\rho}\rvert$ thresh.	0.15	0.15
	WENO-TCD thresh. $(\alpha_{\mathrm{Lax}}, \alpha_{\mathrm{Map}})$	$(0.01, 0.05)$	$(0.01, 0.05)$
Computations	Simulation time	running	running
	Nodes × CPUs/node	16 × 8 (uP)	16 × 8 (uP)
	CPU hours	...	...
	Number of cylindrical shells for stats	280	280

Table 5.4: Parameters used in the currently running higher-resolution SF_6 →air three-dimensional simulations of shock-driven mixing in a converging cylindrical geometry. MKS units. Note that $1.000 \simeq 7\pi/22$.

5.4 Cylindrical-Shell Statistics: Definitions

The natural symmetry of the problem results in defining as 'shell' a two-dimensional cylindrical surface of radius r extending in both θ and z directions. We define the instantaneous average for an arbitrary field Q over a shell of radius r at time t as

$$\langle Q\rangle(r,t) = \frac{1}{\mathcal{A}_r}\int\int f(r,\theta,z,t) r \mathrm{d}\theta \mathrm{d}z, \tag{5.31}$$

where $\mathcal{A}_r$ is the surface area of the shell of radius r ($\mathcal{A}_r = \pi L_z r/2$ for a $\pi/2$ wedge). The instantaneous volume-average of the quantity Q is simply obtained by integrating $\langle Q\rangle$ in the radial direction. Q can then be formally decomposed as

$$Q(\boldsymbol{x},t) = \langle Q\rangle(r,t) + Q'(r,\theta,z,t) = \widetilde{Q}(r,t) + Q''(r,\theta,z,t), \tag{5.32}$$

where the tilde now represents the instantaneous Favre-like, shell-average

$$\widetilde{Q}(r,t) = \frac{\langle \rho\, Q\rangle}{\langle\rho\rangle}, \tag{5.33}$$

Note that a shell-average computation involves first the interpolation of Cartesian fields over the shell that can possibly cross different SAMR patches being handled by different processors, then averaging the sampled fields. The sampling in z and θ is performed according to the smallest grid spacing, so that fields will be sample in both direction every Δx. Data comprised in wedge-like volumes $0 < \theta < \theta_{min} = \pi/30$ close to the horizontal wall, and $\theta_{max} = (\pi/2 - \pi/30) < \theta < \pi/2$ close to the vertical wall, are arbitrarily discarded to avoid wall-effects. From Equations (5.32) and (5.33), we can define the following instantaneous variances:

$$\mathrm{Var}(Q) \quad = \langle Q'^2\rangle = \langle Q^2\rangle - \langle Q\rangle^2, \tag{5.34a}$$

$$\mathrm{Var}_\rho(Q) \quad = \widetilde{Q''^2} = \widetilde{Q^2} - \tilde{Q}^2 = \frac{\langle \rho Q^2\rangle}{\langle\rho\rangle} - \frac{\langle \rho Q\rangle^2}{\langle\rho\rangle^2}. \tag{5.34b}$$

For each M_I, shell-averages are used to gain a better understanding of the different stages of the growth of the mixing layer. In what follows, we investigate for example the evolution of the mixing-layer center position and width. Shell-averages on both the resolved- and the subgrid-scale flow quantities can illustrate the importance of the subgrid kinetic energy and dissipation in the mixing. Various spectra are also computed late in the mixing evolution on cylindrical shells taken across the center of the mixing zone. The effect of the anisotropy of the flow on the various dynamic scales of the turbulence is quantified using directionally dependent Taylor and Kolmogorov microscales. The

Quantity of interest	Length	Density	Speed	Time	TKE per unit mass	turbulent dissipation
Characteristic quantity	R_0	ρ_0	$a_0 = \sqrt{\gamma_{\text{air}} \frac{p_0}{\rho_0}}$	$\frac{R_0}{a_0}$	a_0^2	$\varepsilon_0 \equiv \mu_0 \frac{a_0^2}{\rho_0 R_0^2}$
Evaluation (MKS units)	1.0	0.27885	340	0.0029	115000	0.5796

Table 5.5: Basic characteristic quantities for dimensionless data representation. The index 0 denotes the fluid standing initially on the side where the incident shock comes from.

mixing properties are finally analyzed by investigating probability density functions (p.d.f.s) taken at different shell radii across the width of the layer.

The above shell-averaged quantities are made dimensionless, by a similar choice of parameters made in Chapters 3 and 4. We summarize these definitions in Table 5.5. The characteristic turbulent TKE per unit mass and turbulent dissipation are also listed. Note that these definitions depend only on the nature of the outer unshocked fluid properties (here unshocked air).

5.5 The Different Stages in the Growth of the Mixing Layer

5.5.1 Visualization

Figures 5.7 and 5.8 show the evolution of the mixing layer at different stages of its growth, by looking at the scalar isosurfaces corresponding to a mass fraction of 50% (center), for 75% air (or spike, the portion of heavy fluid penetrating into light fluid), and for 75% SF_6 (or bubble, the portion of light fluid penetrating into heavy fluid). The first snapshot corresponds to the interface accelerated towards the apex as the spikes and bubbles are stretched away from each other. The second picture shows the compressed state of the mixing layer during the first reshock and the phase inversion. The late turbulent mixing displays a wide range of dynamic scales as shown on the bottom subfigure, for each Mach number. Notice the SAMR levels displayed on the background that the mesh is refined in the region of the mixing zone and around shocks. For example, the reflected shock produced from the initial shock refraction is seen slowly exiting the domain on Figures 5.8a,b. The transmitted shock produced from the first reshock interaction exits the domain on Figure 5.8c.

5.5.2 Mixing-Zone Growth

To measure mixing-zone growth, the mixture fraction $\langle\psi\rangle$ is shell-averaged in the azimuthal and axial directions and the width of the mixing region δ at time t is defined according to

$$\delta(t) = 4 \int_{r_{in}}^{r_{out}} (1 - \langle\psi\rangle)\langle\psi\rangle \mathrm{d}r. \tag{5.35}$$

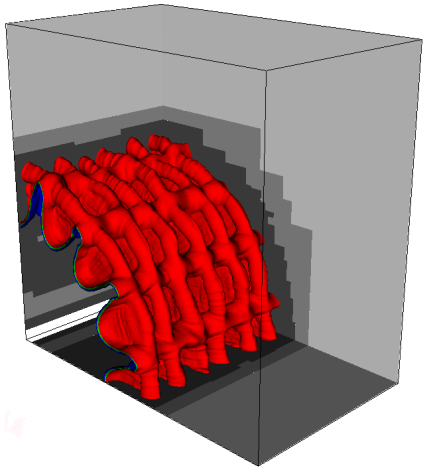

(a)

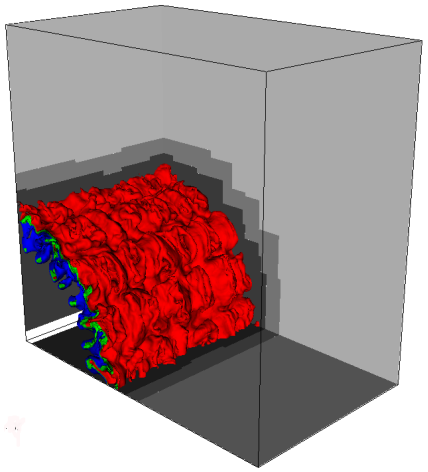

(b)

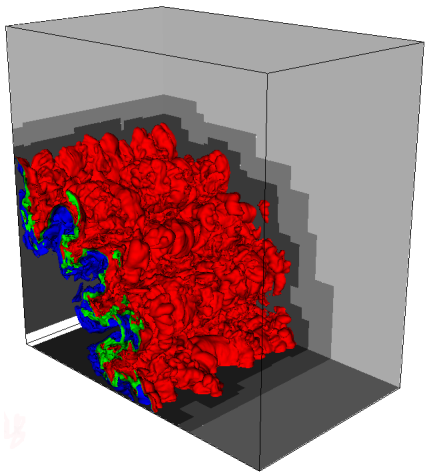

(c)

Figure 5.7: Differently colored iso-surfaces for mass fractions $\psi = 73.1\%$, 50%, and 26.9% visualize the evolution of the mixing zone: (a) the interface converges towards the axis; (b) the interface is reshocked a first time; (c) late-time turbulent mixing is observed. The gray levels on the background planes represent the domains of different mesh refinement. Case air$\rightarrow$SF$_6$, $M_0 = 1.3$.

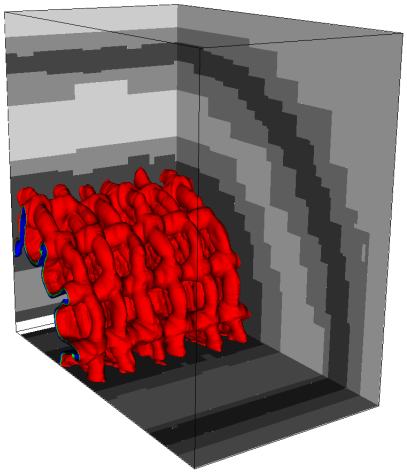

(a)

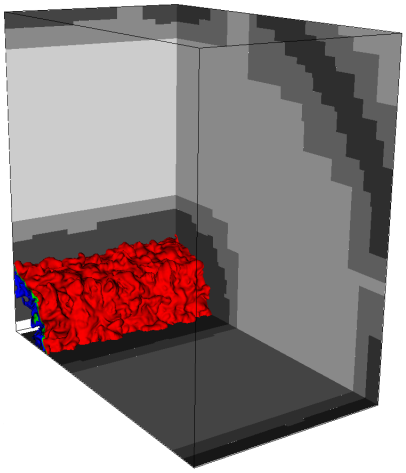

(b)

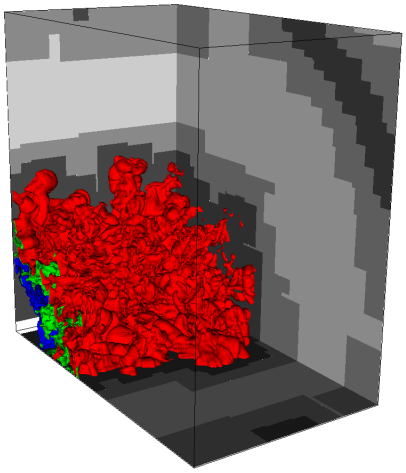

(c)

Figure 5.8: Differently colored iso-surfaces for mass fractions $\psi = 73.1\%$, 50%, and 26.9% visualize the evolution of the mixing zone: (a) the interface converges towards the axis; (b) the interface is reshocked a first time; (c) late-time turbulent mixing is observed. The gray levels on the background planes represent the domains of different mesh refinement. Case air$\rightarrow$SF$_6$, $M_0 = 2.0$.

To understand this definition, one can think of a smooth radial profile $\langle\psi\rangle$ of the mixture fraction from air outside ($\langle\psi\rangle = 0$) to SF_6 inside ($\langle\psi\rangle = 0$) in the form of a tanh function of intrinsic thickness δ and centered on the mixing-zone center $r = r_c$. In this case it is easy to show that δ verifies Equation (5.35), providing that the boundaries $r = r_{in}$ and $r = r_{out}$ are sufficiently far from r_c, i.e. $\delta \ll r_c - r_{in}$ and $\delta \ll r_{out} - r_c$. Another interpretation is mentioned later in Subsection 5.8.1. Figure 5.9 shows the evolution of the width δ and its growth $\dot{delta}$ for both Mach numbers. We also define the mixing-zone center r_c as

$$r_c(t) = 4 \int_{r_{in}}^{r_{out}} \frac{r}{\delta(t)} (1 - \langle\psi\rangle)\langle\psi\rangle \mathrm{d}r, \tag{5.36}$$

which is plotted in Figure 5.10.

To confirm what is observed in figures 5.9 and 5.10, and following the approach of Chapter 4, the different stages in the acceleration of an air→SF_6 interface initially impacted by a shock of incident Mach number $M_I = 1.3$ or 2.0 are summarized in Table 5.6. All the quantities displayed in this table are obtained from the simulations and compared to simulations and experiments performed in plane geometry. In Table 5.6, the different characteristic times describing the evolution of the mixing layer, the interface velocities and the Atwood ratios agree well with the one-dimensional radially symmetric simulations described in Chapter 4. The initial shock refraction produces a transmitted shock that reflects off the axis to reshock the interface. As seen in Chapter 4 for the cylindrical air→SF_6, the reshock interaction is followed by the formation of a shock in the heavy fluid that will reflect off the apex to reshock the interface a second time but with lower intensity (negative peak in the growth rate plot Figure 5.9). Meanwhile, the interface, which was accelerated outwards by the first reshock, decelerates to move radially inwards when it is reshocked a second time. There follows a late-time slower growth, that stabilizes earlier for $M_I = 1.3$ while the mixing layer keeps growing and expanding radially from its radial position at the first reshock for $M_I = 2.0$.

Close-ups of the growth around the first and second shock interactions are displayed in Figures 5.11 and 5.12. The growth observed is strongly non-linear and consists of highly distorted, non-single-mode initial perturbations. For the first shock interaction, the growth rates are different from the plane case because they are not defined the same way. In the plane case, the interface growth rate saturates before the interface is reshocked and the saturation growth rate is the one reported in the previous table. It is low compared to the cylindrical growth rates because there is no geometrical effect that forces the perturbations to grow (see Chapter 3 for similar observations on the linear growth). After the first reshock (second shock interaction), the growth is linear with time, for both Mach numbers, as observed in the plane case and noticed in Hosseini's experiments on cylindrical RMI [50]. Comparisons with Hosseini's experiments remain difficult as these experiments correspond to different initial conditions and have a visual definition of the mixing-layer

	$M_I = 1.3$ (or $M_I = 1.24$ for plane geom.)	$M_I = 2.0$ (or $M_I = 1.98$ for plane geom.)
Time of incident shock interaction	0.20	0.08
Post-shock amplitude $h(0^+)/R_0$	0.05	0.0382
Meas. plane $h(0^+)/L_{y,z}$	0.01	0.005
Post-shock Atwood ratio A^+	0.712	0.766
Shocked interface velocity difference $\Delta W/a_0$	0.292	0.829
Meas. plane $\Delta W/a_0$	0.212	0.827
Approx. shocked growth rate	0.10	0.354
Meas. plane shocked growth rate	0.006	0.022
Time of first reshock	2.4	1.1
Meas. plane time of first reshock	3.2	0.7
Post-reshock amplitude $h(0^+)_{rs}/R_0$	0.120	0.138
Meas. plane $h(0^+)_{rs}/L_{y,z}$	0.08	0.05
Post-reshock Atwood ratio A^+_{rs}	0.74	0.83
Reshocked interface velocity difference $\Delta W_{rs}/a_0$	85.6	1.26
Approx. reshocked growth rate	0.188	0.293
Meas. plane reshocked growth rate	0.05	0.214
Time of first deceleration	4.0	1.6
Time of second reshock	4.6	2.2
Time of second deceleration	7.3	2.8
Final time achieved for lower resolution runs	$\simeq 11$ for run 12	$\simeq 8$ for run 11
Final time achieved for higher resolution runs	$\simeq 9$ for run A1	$\simeq 5$ for run B1

Table 5.6: Key approximate dimensionless times $(a_0/R_0)t$, growth rates $(1/a_0)d\delta/dt$, interface velocity differences $\Delta W/a_0$ created by the shock acceleration, post-shock perturbation amplitudes $h(0^+)/R_0$ and Atwood ratios A^+, characterizing the important stages of a cylindrical air→SF_6 interface accelerated by a cylindrical converging shock of incident Mach number $M_I = 1.3$ and 2.0. Comparisons with Vetter and Sturtevant's plane experiments at $M_I = 1.24$ and $M_I = 1.98$ [109, 43]. In these experiments, the sound speed is $a_0 \simeq 339$ m.s^{-1} for the case $M_I = 1.24$ and $a_0 \simeq 347$ m.s^{-1} for $M_I = 1.98$.

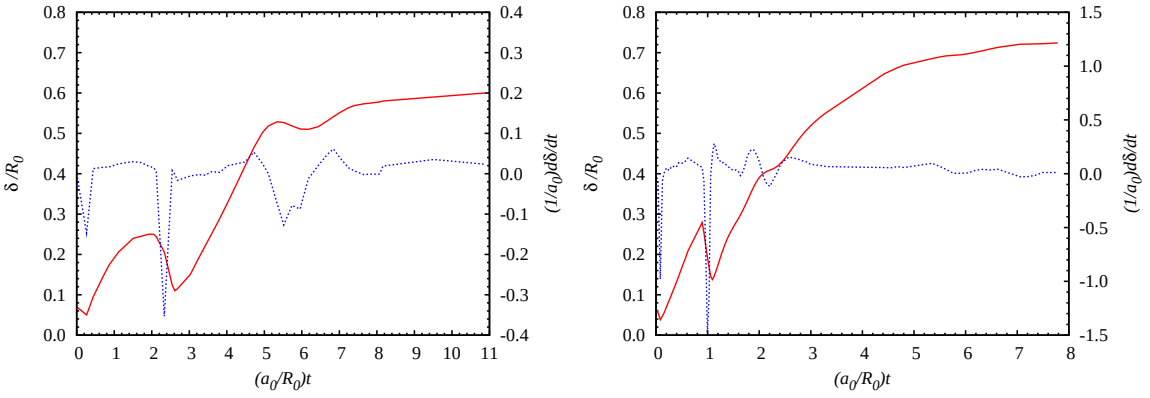

(a) $M_I = 1.3$

Figure 5.9: Evolution of the mixing-layer width δ (red solid line) and growth rate $d\delta/dt$ (blue small-dashed line). Case $M_I = 1.3$ (left) and 2.0 (right).

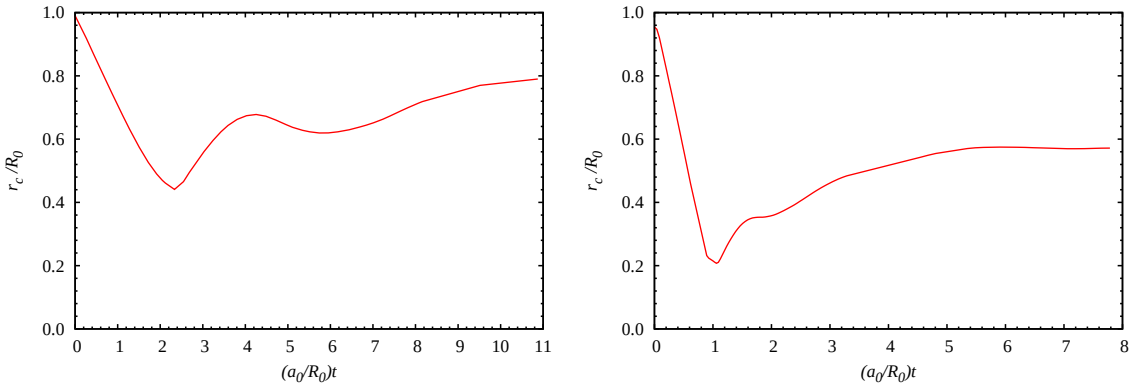

(a) $M_I = 1.3$ (a)' $M_I = 2.0$

Figure 5.10: Evolution of the mixing-layer center r_c. Case $M_I = 1.3$ (left) and 2.0 (right).

width. The post-reshock growth should be compared to the classic experimental observations of the plane post-reshock growth $\simeq 0.28 A_{rs}^{+} \Delta W_{rs} t$. We display finally the evolution of spike and bubble shell-averaged radial velocities $\langle u_r \rangle_s$ and $\langle u_r \rangle_b$ in Figure 5.13 and volume V per unit axial length of the mixing zone in Figure 5.14.

A scalar function is defined by $Y = 2\psi - 1$ such that $Y \in [-1, 1]$. As depicted in Figure 5.15, the scalar profile evolves to shapes different from the initial tanh-like profile, and exhibits irregular features as a consequence of complex large-scale dynamics. After the initial shock interaction, organized spikes and bubbles segregate distinctly until the first reshock where the interface is compressed then re-expanded. The post-reshock dynamics induces a more chaotic flow that, on average, is represented by wider profiles of the scalar shell-averages. For $M_I = 2.0$, the entrainment of inner heavy fluid captured in between the apex and the mixing zone is illustrated by a slow decrease in the amount of pure heavy fluid on the very left side of the mixing zone.

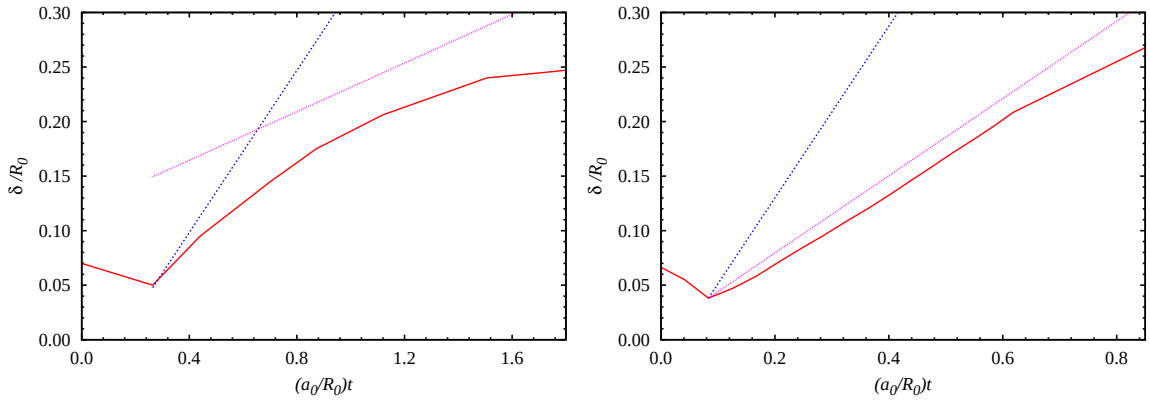

(a) $M_I = 1.3$ (a)' $M_I = 2.0$

Figure 5.11: Evolution of the mixing-layer width δ following the initial shock interaction. Simulation (red solid line), three-dimensional linear impulsive model $\dot{h}_\infty/a_0$ (blue small-dashed line), and $\beta\dot{h}_\infty/a_0$ (pink dotted line), with $\beta = 0.3$ for $M_I = 1.3$ and $\beta = 0.45$ for $M_I = 2.0$. $\dot{h}_\infty$ given by Equation (3.32). Case $M_I = 1.3$ (left) and 2.0 (right).

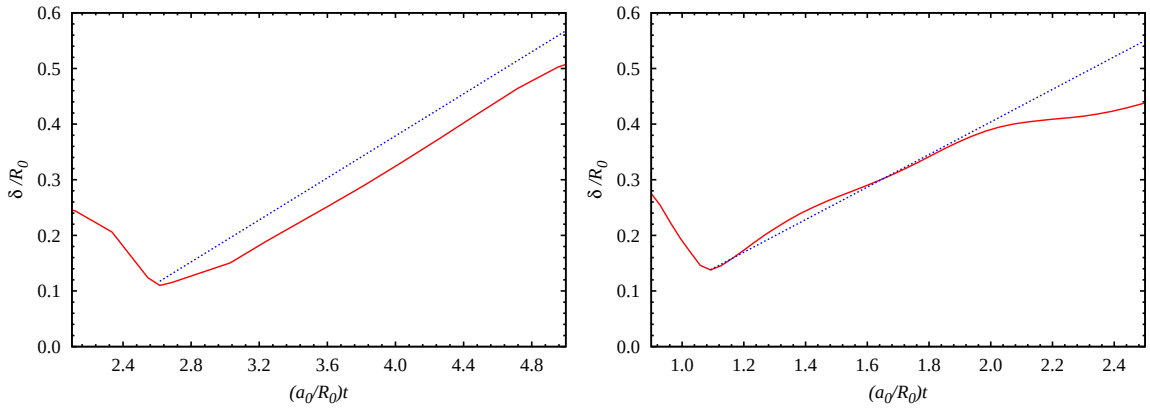

(a) $M_I = 1.3$ (a)' $M_I = 2.0$

Figure 5.12: Evolution of the mixing-layer width δ following the first reshock. Simulation (red solid line) and $\beta_{rs}A^+_{rs}\Delta W_{rs}$ (blue small-dashed line), with A^+_{rs} and ΔW_{rs} determined at the reshock interaction and $\beta_{rs} = 0.75$ for $M_I = 1.3$ and $\beta_{rs} = 0.28$ for $M_I = 2.0$. Case $M_I = 1.3$ (left) and 2.0 (right).

5.5.3 Turbulence Statistics

5.5.3.1 Shell-Averaged Statistics vs. Radius At Different Stages

Favre-like shell-averaged statistics of the turbulent activity such as resolved-scale TKE $\langle K \rangle$, subgrid-scale TKE $\langle k \rangle$ (per unit mass), resolved-scale dissipation $\langle \varepsilon_{res} \rangle$, and subgrid energy transfer $\langle \varepsilon_{sgs} \rangle$

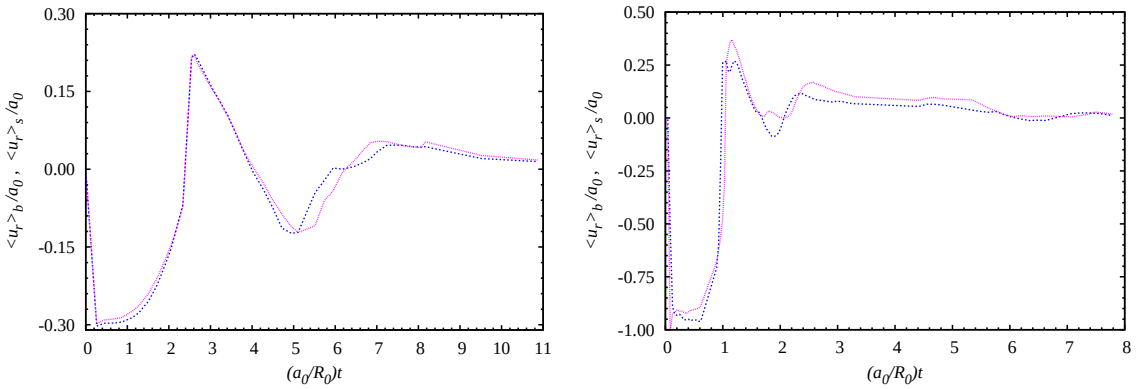

(a) $M_I = 1.3$ (a)' $M_I = 2.0$

Figure 5.13: Evolution of the bubble and spike shell-averaged radial velocities $\langle u_r \rangle_b$ (blue small-dashed line) and $\langle u_r \rangle_s$ (pink dotted line). Case $M_I = 1.3$ (left) and 2.0 (right).

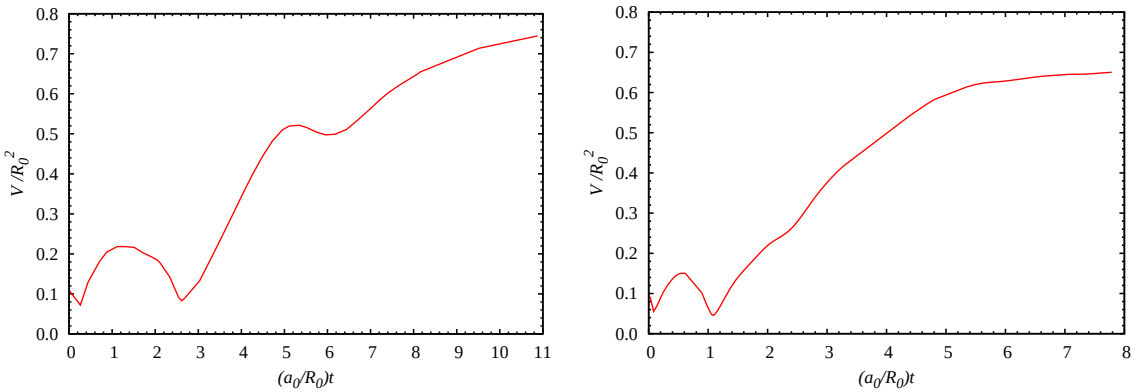

(a) $M_I = 1.3$ (a)' $M_I = 2.0$

Figure 5.14: Evolution of the mixing-layer volume per unit $z-$length V. Case $M_I = 1.3$ (left) and 2.0 (right).

read as follows:

$$\langle K \rangle = \frac{1}{2}\mathrm{Var}_\rho(u_i u_i), \tag{5.37a}$$

$$\langle k \rangle = \frac{\langle \tau_{ii} \rangle}{2\langle \rho \rangle}, \tag{5.37b}$$

$$\langle \varepsilon_{res} \rangle = \frac{\langle d'_{ij} S'_{ij} \rangle}{\langle \rho \rangle}, \tag{5.37c}$$

$$\langle \varepsilon_{sgs} \rangle = -\frac{\langle \tau'_{ij} S'_{ij} \rangle}{\langle \rho \rangle}. \tag{5.37d}$$

$\langle \varepsilon \rangle - \langle \varepsilon_{res} \rangle \equiv \langle \varepsilon_{sgs} \rangle$, with $\langle \varepsilon \rangle$ the total dissipation, represents the transfer of kinetic energy through the wave mode π/Δ_c and is provided by the stretched-vortex SGS model using Equation (5.11a). The total dissipation $\langle \varepsilon \rangle$ is simply related to the the shell-average of $\sigma'_{ij} S'_{ij}$ where $\sigma_{ij} = d_{ij} - \tau_{ij}$ represents

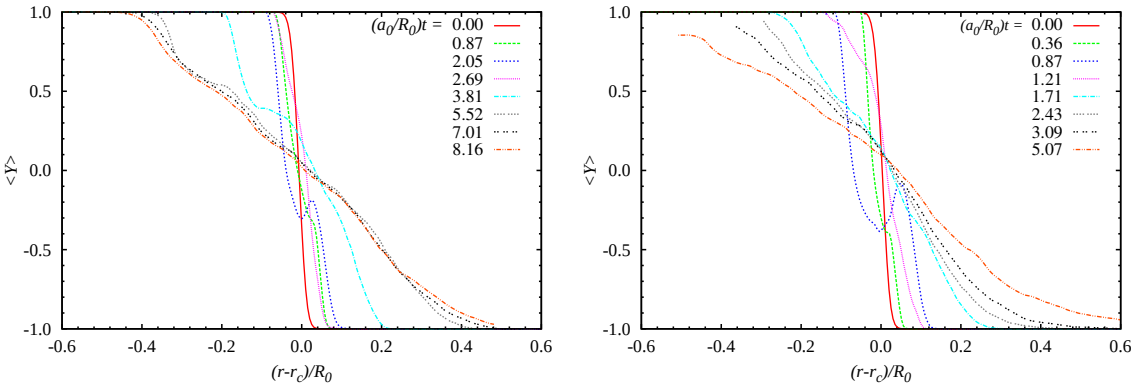

(a) $M_I = 1.3$ (a)' $M_I = 2.0$

Figure 5.15: Shell-averaged scalar $\langle Y \rangle$ centered on the mixing-layer center r_c vs. r, at different stages of the mixing-layer evolution. Case $M_I = 1.3$ (left) and 2.0 (right).

the total (resolved plus subgrid) stress tensor. Using Equation (5.37), we have the equalities

$$\begin{aligned} \langle \varepsilon \rangle &= \langle \varepsilon_{res} \rangle + \langle \varepsilon_{sgs} \rangle \\ &= \frac{1}{\langle \rho \rangle} \left(\langle d_{ij} S_{ij} \rangle - \langle d_{ij} \rangle \langle S_{ij} \rangle \right) - \frac{1}{\langle \rho \rangle} \left(\langle \tau_{ij} S_{ij} \rangle - \langle \tau_{ij} \rangle \langle S_{ij} \rangle \right) \\ &= \frac{1}{\langle \rho \rangle} \left(\langle \sigma_{ij} S_{ij} \rangle - \langle \sigma_{ij} \rangle \langle S_{ij} \rangle \right). \end{aligned} \tag{5.38}$$

The total TKE is used to define the turbulent intensity

$$u' = \sqrt{\frac{2(\langle K \rangle + \langle k \rangle)}{3}}, \tag{5.39}$$

and the turbulent Mach number

$$M_t = \frac{u'}{\langle a \rangle}, \tag{5.40}$$

where $a = \sqrt{\gamma p / \rho}$ is the sound speed.

The following figures confirm the history of the mixing-layer evolution by focusing on the post-shock flow, the post-reshock flow and the flow at very late time. Figure 5.16 shows the increasing variance in the scalar field as the turbulent mixing occurs, while Figure 5.17 indicates the highly-compressible character of the wave interactions with the mixing zone, in particular for $M_I = 2.0$. The initial density ratio of heavy fluid to light fluid is 5. For both $M_I = 1.3$ and $M_I = 2.0$, the final density ratio of heavy inner fluid and light outer fluid remains close to 5. To compare, in the plane RMI with reshock involving the same species, the final ratio is approximately 6.5 (see Figure 6b of [43]). In the future, it will be interesting to compare these ratios with the ratios obtained for the heavy-to-light interactions (run A2 and B2).

The stretched vortex subgrid model allows us to estimate directly the local subgrid kinetic energy and dissipation. Figure 5.18 shows that $\langle K \rangle$ is about 10 to 15 times larger than its subgrid counterpart, while Figure 5.19 indicates that the subgrid dissipation is about 20 (respectively 60) times the resolved dissipation before the reshock for $M_I = 1.3$ (respectively 2.0), and become 50 times the resolved dissipation (respectively 100) as unresolvable scales, producing dissipation, develop after reshock. The weakly compressible nature of the flow late after reshock is shown in Figure 5.20 representing the evolution of the shell-averaged Mach number $\langle M \rangle$, with $M = |\boldsymbol{u}|/c$, and turbulent Mach number M_t. The turbulent Mach number peaking around the center of the mixing zone at values ranging from 0.03 to 0.06. This is similarly observed in the plane case and generally in RMI-driven turbulent mixing. Finally, the strong radial anisotropy of the flow is displayed in shell-averaged velocity component profiles (see Figure 5.21): the radial component allows us to see the transmitted shocks from the initial and re-shock interactions. At $M_I = 1.3$, the late-time flow expands radially outwards while for $M_I = 2.0$ there exists a region of change in the radial velocity direction, around the center of the mixing zone.

The radial profiles of the scalar and density variances in Figures 5.15, 5.16, and 5.17, and the shell-averaged Mach number in Figure 5.20 show important differences in the flow structure between the $M_I = 1.3$ case and the $M_I = 2.0$ case. Before the first reshock, for $M_I = 2.0$, the spikes and bubbles evolve more distinctly than for $M_I = 1.3$. For $M_I = 2.0$, the reshock occurs closer to the axis and the post-reshock mixing layer expands radially from a location close to the axis to a radius of the order of the initial radial position of the mixing layer. For $M_I = 1.3$, the reshock occurring further away from the axis, the final extent of the mixing layer is reduced.

5.5.3.2 On the Decaying Turbulence

A global measure of turbulence is obtained by looking at the volume-averaged total TKE, TKE_{vol}, that recalls the various stages and wave interactions in the mixing-zone growth (Figure 5.22). Bumps indicate the various shock interactions. Ultimately, the reverberations become weaker and the energy deposited by baroclinic means during the first wave interactions, decays.

From u' (see Equation (5.40)) and the total turbulent dissipation (see Equation (5.37)), an integral length scale, or technically the distance after which the self correlation of the velocity components vanishes, and a turbulent Reynolds number can also be computed as

$$\ell = \frac{u'^3}{\langle \varepsilon_{res} \rangle + \langle \varepsilon_{sgs} \rangle}, \tag{5.41a}$$

$$Re_\ell = \frac{u'\ell}{\langle \nu \rangle}, \tag{5.41b}$$

where the kinematic viscosity is $\nu = \mu/\rho$. The late-time decay of TKE is also observed on plots of the integral length scale and turbulent Reynolds number evaluated at the center of the mixing layer

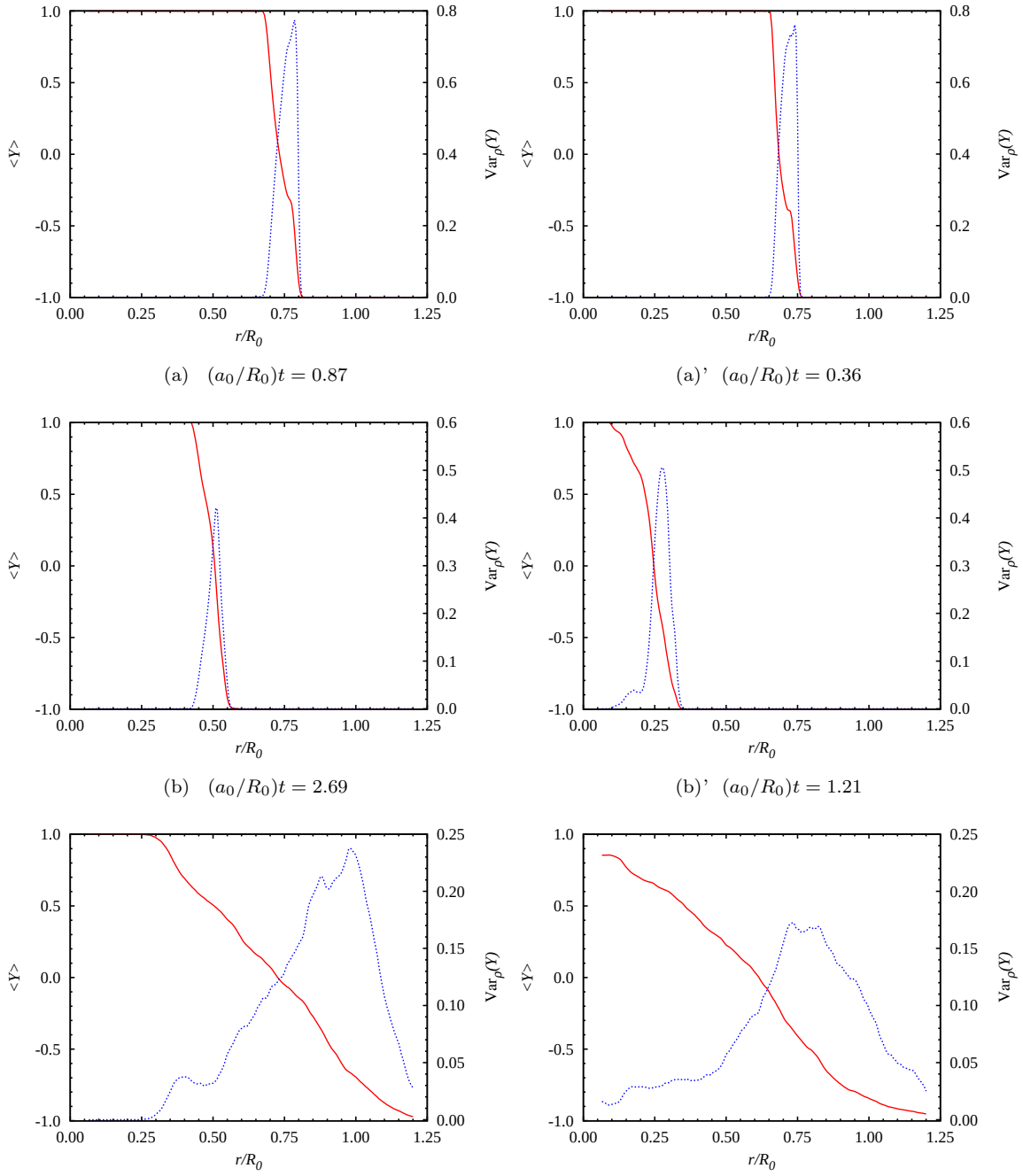

(a) $(a_0/R_0)t = 0.87$ (a)' $(a_0/R_0)t = 0.36$

(b) $(a_0/R_0)t = 2.69$ (b)' $(a_0/R_0)t = 1.21$

(c) $(a_0/R_0)t = 8.16$ (c)' $(a_0/R_0)t = 5.07$

Figure 5.16: Shell-averaged scalar $\langle Y \rangle$ (red solid line) and scalar variance $\mathrm{Var}_\rho(Y)$ (blue small-dashed line) vs. r, after the incident shock interaction (top), right after the first reshock (middle), and at late time (bottom). Case $M_I = 1.3$ (left) and 2.0 (right).

and presented in Figures 5.23 and 5.24.

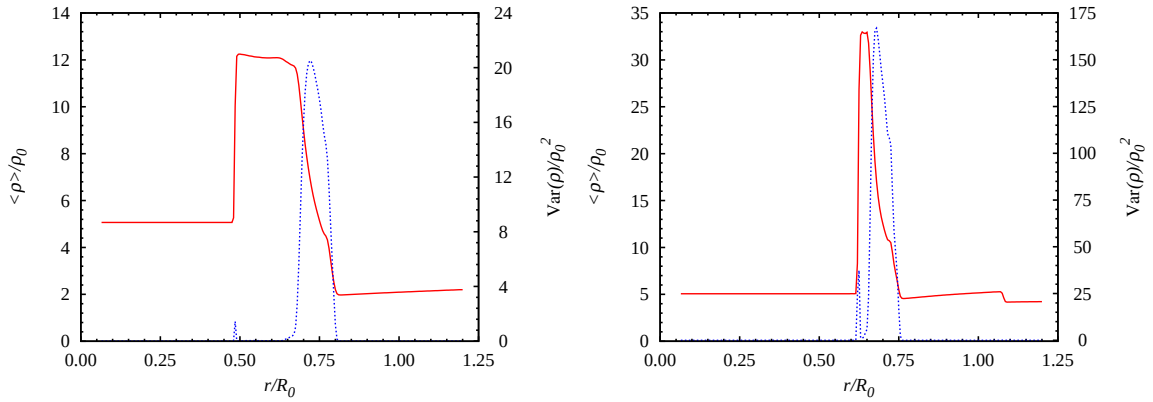

(a) $(a_0/R_0)t = 0.87$ (a)' $(a_0/R_0)t = 0.36$

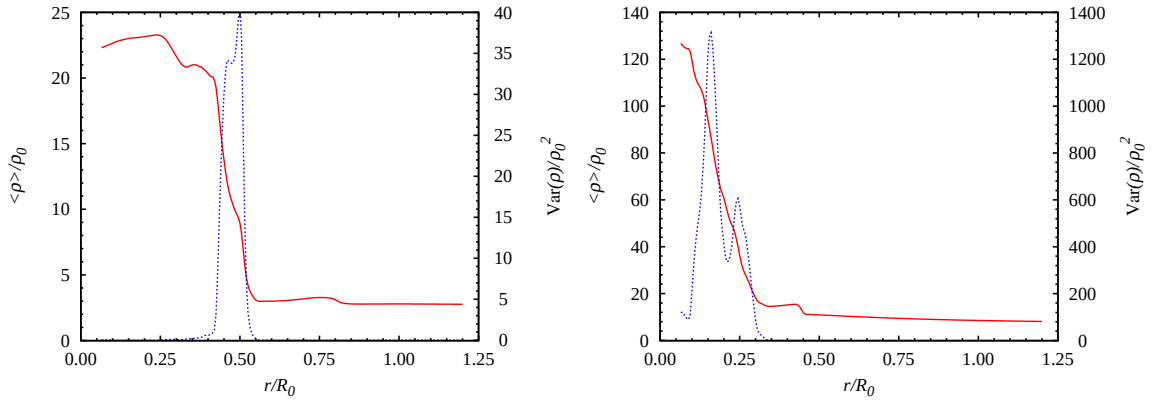

(b) $(a_0/R_0)t = 2.69$ (b)' $(a_0/R_0)t = 1.21$

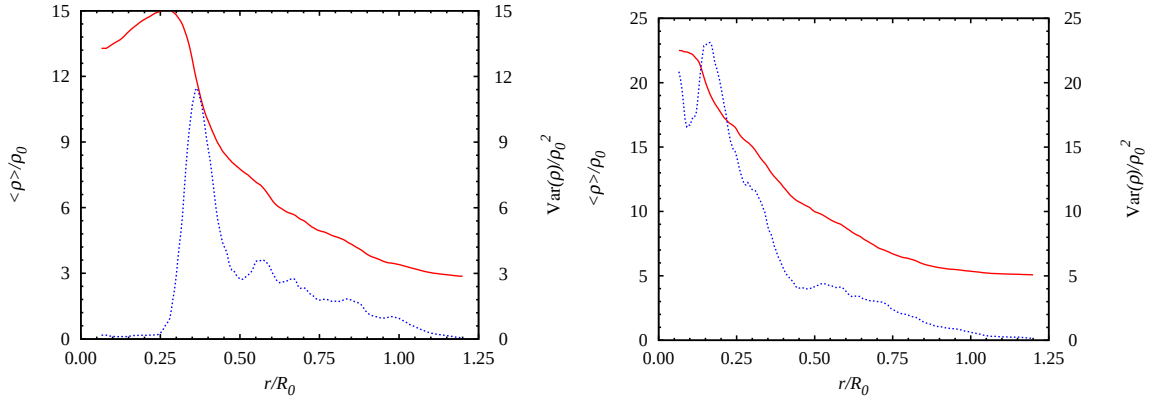

(c) $(a_0/R_0)t = 8.16$ (c)' $(a_0/R_0)t = 5.07$

Figure 5.17: Shell-averaged density $\langle\rho\rangle$ (red solid line) and density variance Var(ρ) (blue small-dashed line) vs. r, after the incident shock interaction (top), right after the first reshock (middle), and at late time (bottom). Case $M_I = 1.3$ (left) and 2.0 (right).

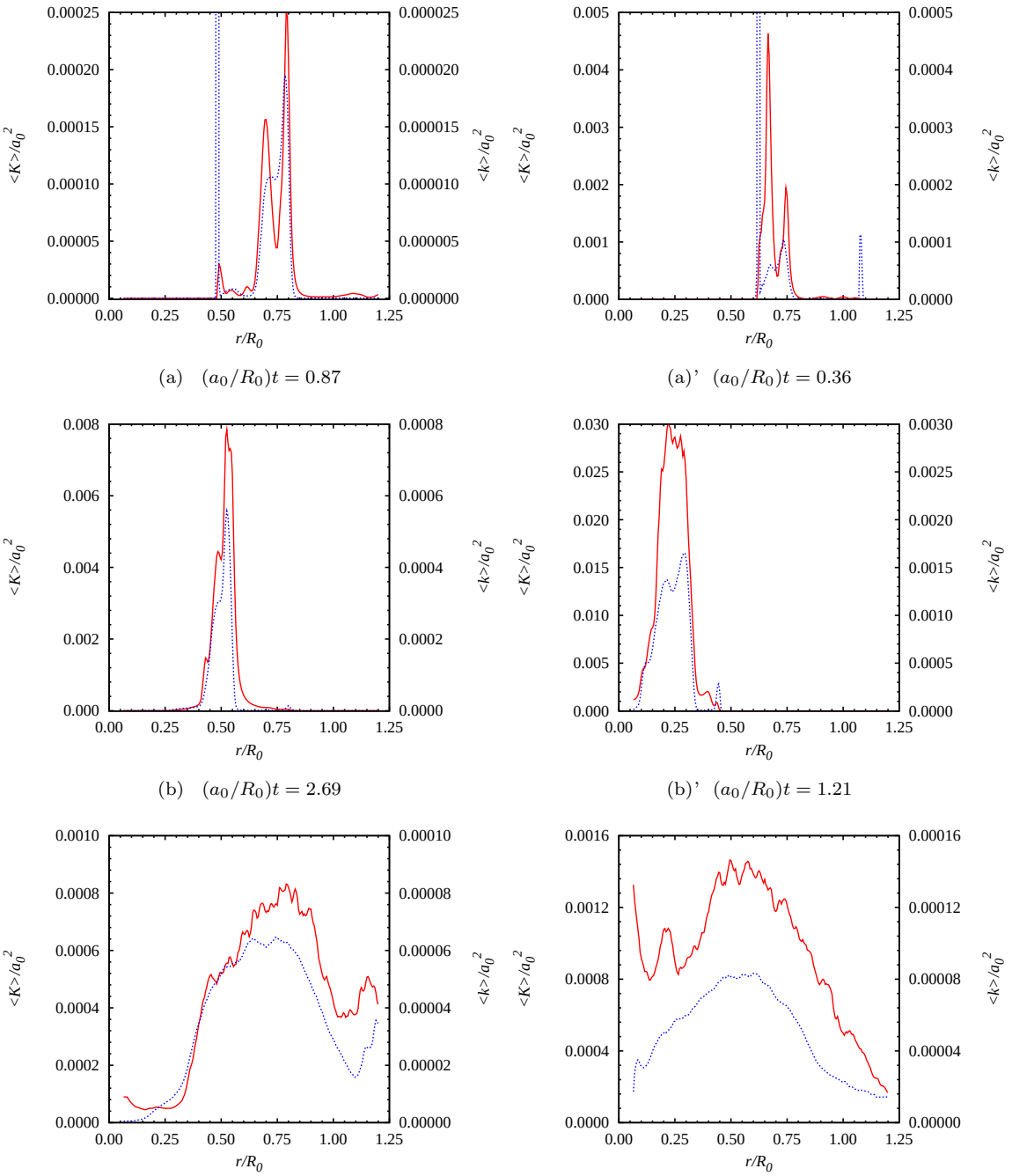

(a) $(a_0/R_0)t = 0.87$ (a)' $(a_0/R_0)t = 0.36$

(b) $(a_0/R_0)t = 2.69$ (b)' $(a_0/R_0)t = 1.21$

(c) $(a_0/R_0)t = 8.16$ (c)' $(a_0/R_0)t = 5.07$

Figure 5.18: Shell-averaged resolved scale turbulent kinetic energy $\langle K \rangle$ (red solid line) and subgrid turbulent kinetic energy $\langle k \rangle$ (blue small-dashed line) vs. r, after the incident shock interaction (top), right after the first reshock (middle), and at late time (bottom). Note the order of magnitude difference in the scale of the plots: $\langle K \rangle \sim 10\langle k \rangle$ for the case $M_I = 1.3$ and $\langle K \rangle \sim 20\langle k \rangle$ for the case $M_I = 2.0$. Case $M_I = 1.3$ (left) and 2.0 (right).

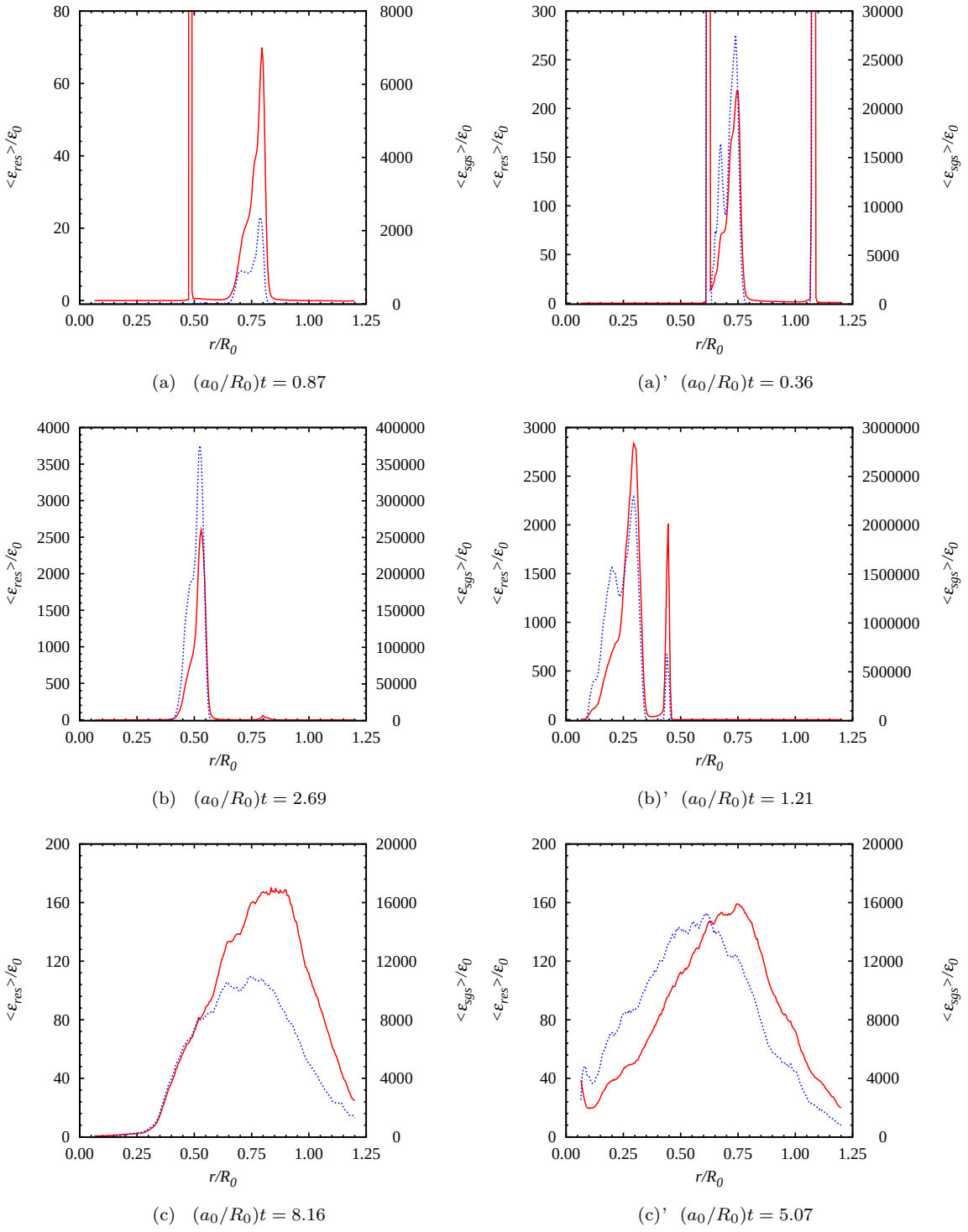

(a) $(a_0/R_0)t = 0.87$ (a)' $(a_0/R_0)t = 0.36$

(b) $(a_0/R_0)t = 2.69$ (b)' $(a_0/R_0)t = 1.21$

(c) $(a_0/R_0)t = 8.16$ (c)' $(a_0/R_0)t = 5.07$

Figure 5.19: Shell-averaged resolved scale dissipation rate $\langle \varepsilon_{res} \rangle$ (red solid line) and subgrid dissipation $\langle \varepsilon_{sgs} \rangle$ (blue small-dashed line) vs. r, after the incident shock interaction (top), right after the first reshock (middle), and at late time (bottom). Note the order of magnitude difference in the scale of the plots: for the case $M_I = 1.3$ (respectively 2.0) $\langle \varepsilon_{sgs} \rangle \sim 30 \langle \varepsilon_{res} \rangle$ (respectively 100) prior to the first reshock, $\langle \varepsilon_{sgs} \rangle \sim 200 \langle \varepsilon_{res} \rangle$ (respectively 1000) after the first reshock, and $\langle \varepsilon_{sgs} \rangle \sim 100 \langle \varepsilon_{res} \rangle$ (respectively 100) at late time. Case $M_I = 1.3$ (left) and 2.0 (right).

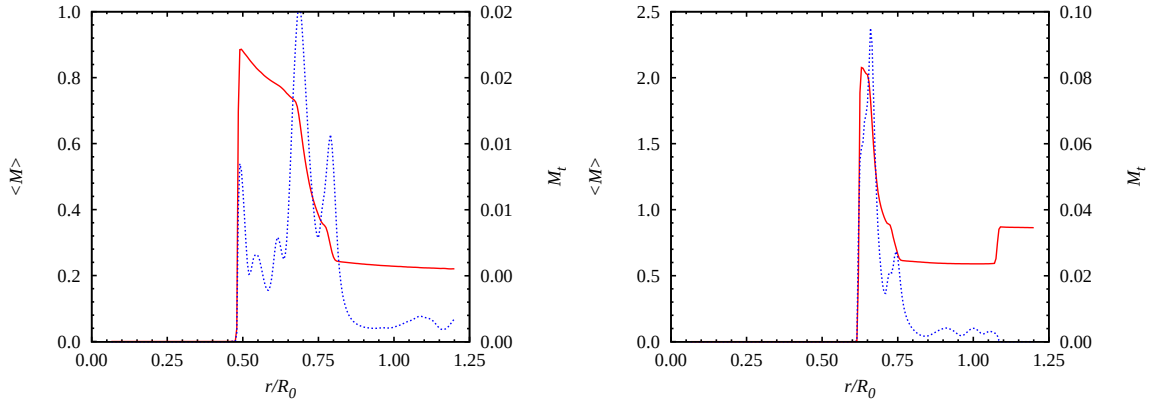

(a) $(a_0/R_0)t = 0.87$ (a)' $(a_0/R_0)t = 0.36$

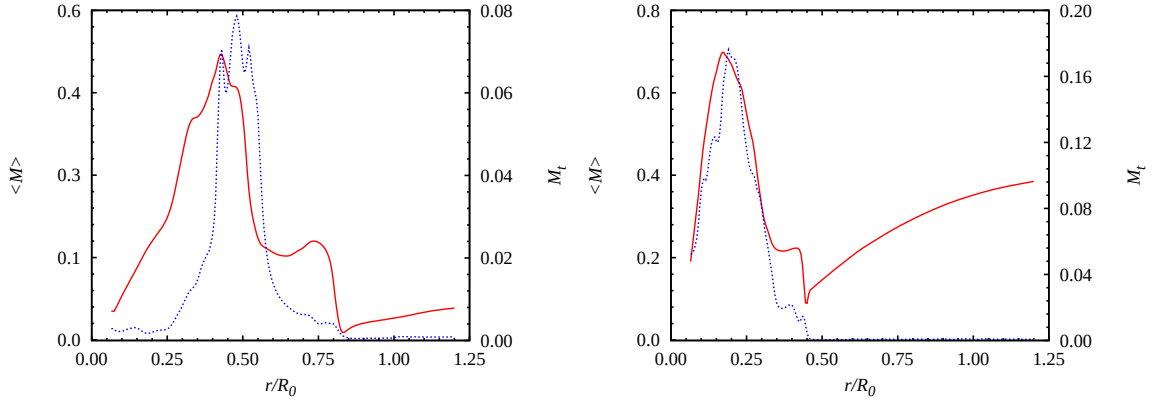

(b) $(a_0/R_0)t = 2.69$ (b)' $(a_0/R_0)t = 1.21$

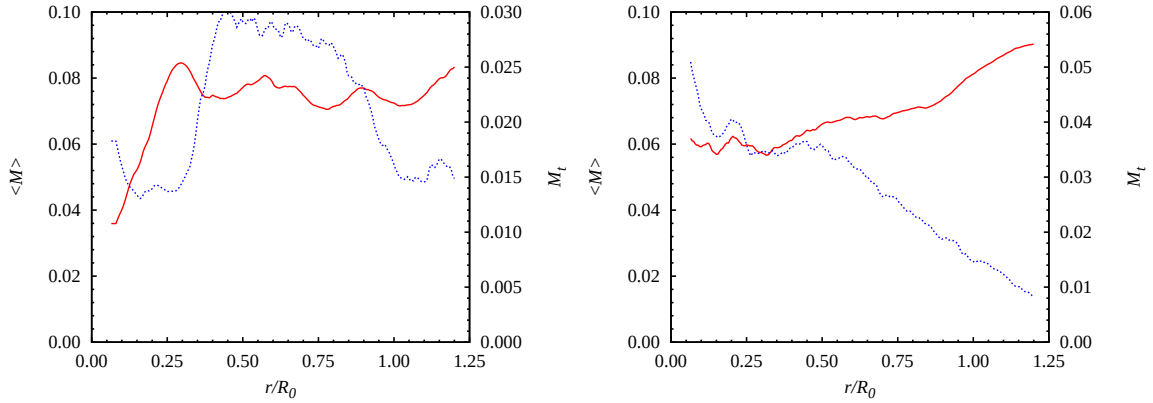

(c) $(a_0/R_0)t = 8.16$ (c)' $(a_0/R_0)t = 5.07$

Figure 5.20: Shell-averaged Mach number $\langle M \rangle$ (red solid line) and turbulent Mach number M_t (blue small-dashed line) vs. r, after the incident shock interaction (top), right after the first reshock (middle), and at late time (bottom). Note the order of magnitude difference in the scale of the plots. Case $M_I = 1.3$ (left) and 2.0 (right).

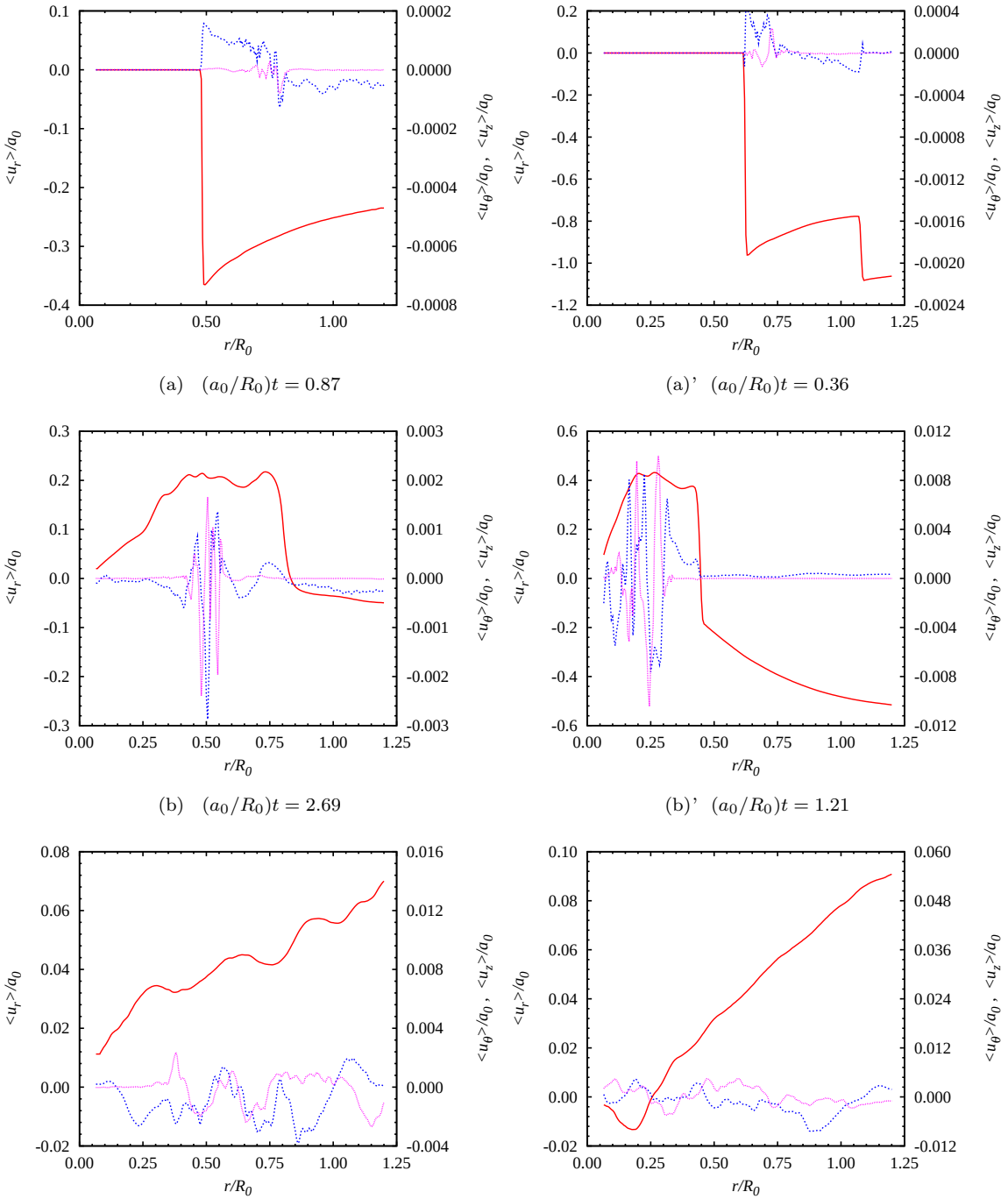

(a) $(a_0/R_0)t = 0.87$

(a)' $(a_0/R_0)t = 0.36$

(b) $(a_0/R_0)t = 2.69$

(b)' $(a_0/R_0)t = 1.21$

(c) $(a_0/R_0)t = 8.16$

(c)' $(a_0/R_0)t = 5.07$

Figure 5.21: Shell-averaged radial velocity component $\langle u_r \rangle$ (red solid line), azimuthal velocity component $\langle u_\theta \rangle$ (blue small-dashed line) and axial velocity component $\langle u_z \rangle$ vs. r, after the incident shock interaction (top), right after the first reshock (middle), and at late time (bottom). Note the order of magnitude difference in the scale of the plots. Case $M_I = 1.3$ (left) and 2.0 (right).

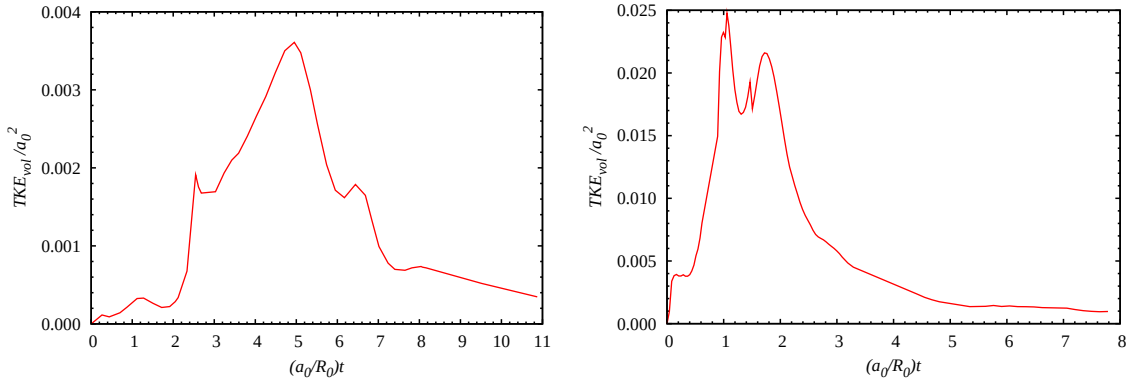

(a) $M_I = 1.3$ (a)' $M_I = 2.0$

Figure 5.22: Volume-averaged total turbulent kinetic energy TKE_{vol} as a function of time. Case $M_I = 1.3$ (left) and 2.0 (right).

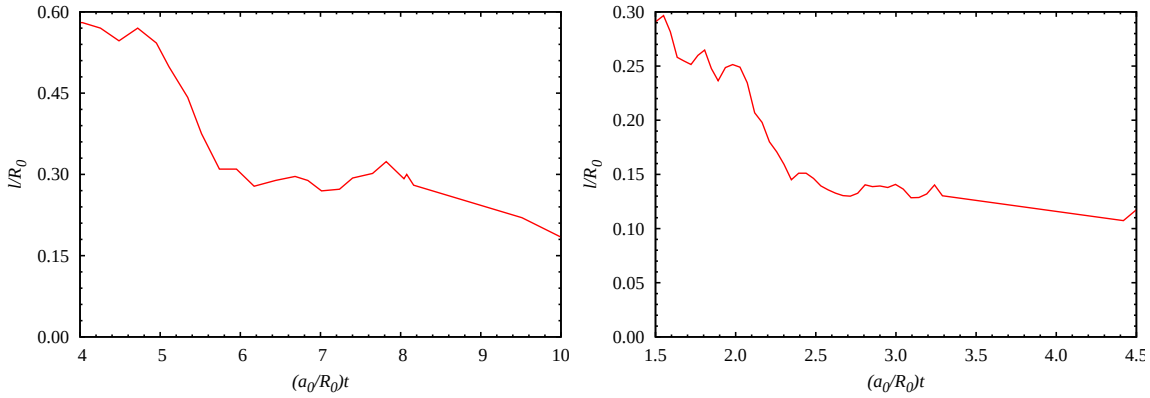

(a) $M_I = 1.3$ (a)' $M_I = 2.0$

Figure 5.23: Shell-averaged integral length scale ℓ computed in the center of the mixing zone $r = r_c$ as a function of time, during the decay of turbulent kinetic energy. Case $M_I = 1.3$ (left) and 2.0 (right).

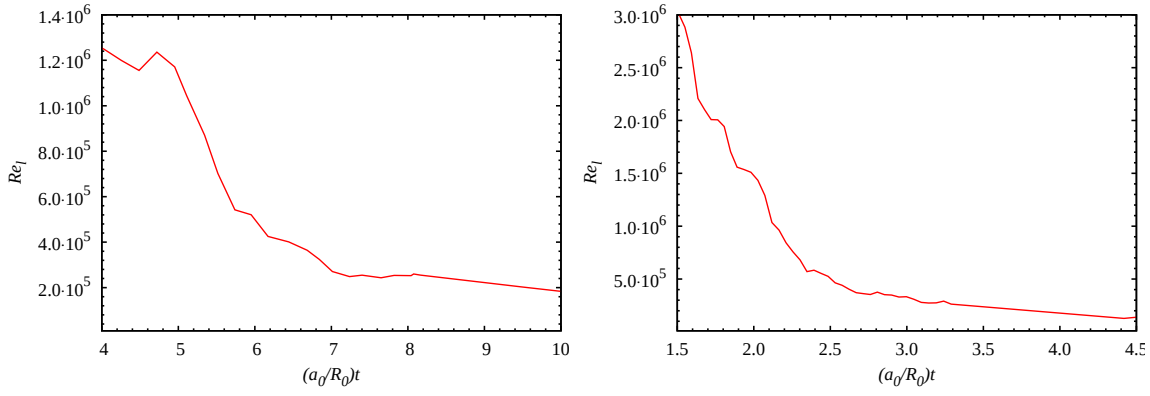

(a) $M_I = 1.3$ (a)' $M_I = 2.0$

Figure 5.24: Shell-averaged turbulent Reynolds number Re_ℓ computed in the center of the mixing zone $r = r_c$ as a function of time, during the decay of turbulent kinetic energy. Case $M_I = 1.3$ (left) and 2.0 (right).

5.6 Instantaneous Velocity, Density and Scalar Spectra

5.6.1 Time Evolution

Density, scalar and velocity fields can be sampled over the shell located at the center of the mixing zone, in the θ and z directions. For a given sampled field $f(r, \theta, z, t)$, applying the Fourier transform of f in the periodic z-direction and averaging the power spectrum coefficients over the θ-direction, an instantaneous one-dimensional spectrum E_f is defined as a function of the axial wavenumber k_z and evaluated at $r = r_c$ as

$$E_f(k_z)(r_c, t) = \frac{1}{\theta_{max} - \theta_{min}} \int_{\theta_{min}}^{\theta_{max}} |\widehat{F}(r_c, \theta, k_z, t)|^2 \mathrm{d}\theta, \tag{5.42}$$

where $\widehat{F}$ is the Fourier transform of f in the z-direction. Figure 5.25 shows radial velocity spectra at different times: right after the first reshock, right after the second reshock, later after the second reshock, and at very late time. As time progresses, the peak of each spectrum moves to lower wavenumber and an inertial range forms, approaching the universal Kolmogorov $k_z^{-5/3}$ scaling, as observed by Hill et al. [43] in the plane geometry.

5.6.2 Late-Time Spectra

Figure 5.26 confirms the Kolmogorov-like energy spectrum for the three components of the velocity. Except for u_z, minimal aliasing errors are observed at the highest wavenumbers, and we recall that no explicit filtering of any kind was performed, and WENO is not active across the mixing zone. However, the use of bandwidth-optimized centered stencils, such as TCD, combined with skew-symmetric discretization partly helps minimize the accumulation of energy owing to high-wavenumber aliasing errors.

We performed various tests for homogeneous decaying turbulence in a three-dimensional box that confirmed that aliasing is only seen for the any one-dimensional power spectra of the u_k velocity components taken in the kth direction only. Two-dimensional, or radial, spectra will minimize the aliased aspect of the one-dimensional spectra for high wavenumbers, since aliased one-dimensional spectrum of a given component u_k in the kth direction is combined with non-aliased one-dimensional spectrum of u_k in a jth direction orthogonal to the kth. This leads to the following comment: the general issue with compressible solvers for Navier-Stokes or LES is that the discretized equations do not converge to the incompressible equations in the limit of zero Mach number. As a result, the discrete equations support unphysical modes that make simulations unstable. Spectral methods are special in the sense that the pressure equation does converge to the incompressible version. This problem, also well known in the finite element community, is the cause of aliasing errors in collocated method and is generally referred to as “weak momentum” coupling. Consider for example

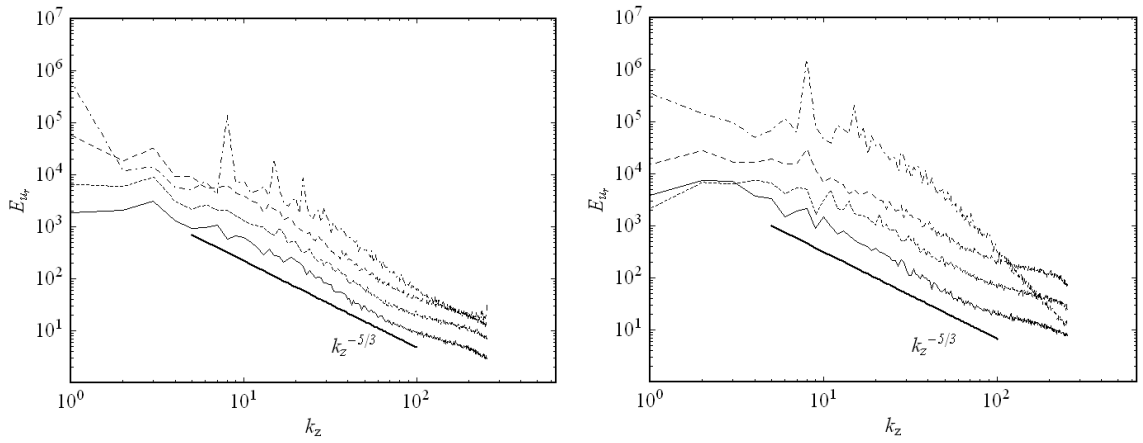

(a) $M_I = 1.3$ (a)' $M_I = 2.0$

Figure 5.25: k_z-power spectra of velocity $E_{u_r}(k_z)$ computed in the center shell of the mixing zone at four different times: For $M_I = 1.3$ (left), $(a_0/R_0)t = 2.69$ (dashed-dot line), $(a_0/R_0)t = 5.52$ (long dashed-line), $(a_0/R_0)t = 6.44$ (small-dashed line), and $(a_0/R_0)t = 8.16$ (solid line). For $M_I = 2.0$ (right), $(a_0/R_0)t = 1.21$ (dashed-dot line), $(a_0/R_0)t = 2.43$ (long-dashed line), $(a_0/R_0)t = 3.09$ (small-dashed line), and $(a_0/R_0)t = 5.07$ (solid line). All computed wavenumbers shown and $k_{max} = 256$.

the momentum in the x-direction at node i, the pressure gradient will be computed from nodes $i+1$ and $i-1$, but not from node i. This larger stencil produces a more or less large scale decoupling of the momentum and mass conservation/energy equations that leads to the generation of waves at the finest resolution ($2\Delta x$ mode) that grows. In addition, the first derivative centered operator (see Equation (5.17)) used to compute resolved or subgrid viscous dissipation terms has, by construction, no contribution at the highest wave numbers and cannot stabilize the growth of the $2\Delta x$ mode. As expected, the momentum spectrum in the direction of the pressure gradient will show aliasing at high wavenumbers. In the context of collocated methods, Rhie-Chow-like interpolations partially solve the problem as they are equivalent to adding numerical viscosity in a significant way. The best approach is to improve the representation of discrete, second derivatives (involved in the viscous dissipation terms) at high wavenumbers in order to make them more dissipative at these wavenumbers. For the resolved part, the operator $\mathcal{D}_x\mathcal{D}_x$ has actually been rewritten in a narrow stencil form that can see the mode $2\Delta x$. In LES however, the resolved viscous dissipation term is negligible and the subgrid fluxes would have to be decomposed and discretized in a narrow stencil as well. The issue is still to be resolved.

While they are governed by different equations, density and scalar exhibit spectra that correlate well as shown in Figure 5.27. Figure 5.28 indicates that the spectrum $E_{u_r}(k_z)$, corresponding to the direction of anisotropy, contains more than a third of the total kinetic energy.

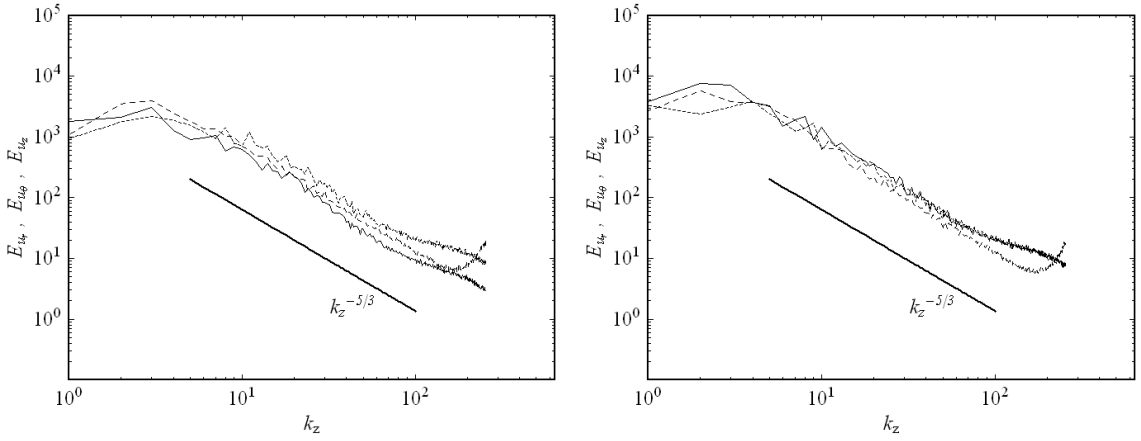

(a) $M_I = 1.3$ (a)' $M_I = 2.0$

Figure 5.26: k_z-power spectra of velocity components $E_{u_r}(k_z)$ (solid line), $E_{u_\theta}(k_z)$ (small-dashed line), and $E_{u_z}(k_z)$ (long-dashed line) computed in the center shell of the mixing zone at late time $(a_0/R_0)t = 8.16$ for $M_I = 1.3$ (left) and $(a_0/R_0)t = 5.07$ for $M_I = 2.0$ (right). All computed wavenumbers shown and $k_{max} = 256$.

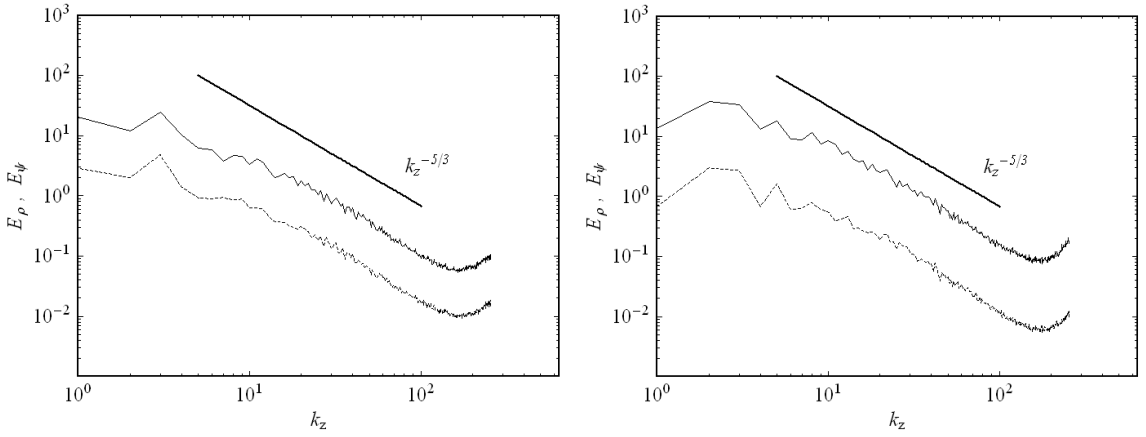

(a) $M_I = 1.3$ (a)' $M_I = 2.0$

Figure 5.27: k_z-power spectra of density $E_\rho(k_z)$ (solid line) and $E_\psi(k_z)$ (dashed line) computed in the center shell of the mixing zone at late time $(a_0/R_0)t = 8.16$ for $M_I = 1.3$ (left) and $(a_0/R_0)t = 5.07$ for $M_I = 2.0$ (right). All computed wavenumbers shown and $k_{max} = 256$.

5.7 Kolmogorov and Taylor Statistics

The anisotropy of the flow is further investigated in this section by looking at the evolution of various characteristic scales of the flow at the center of the mixing zone $r = r_c(t)$. We are first interested in the Kolmogorov microscales, the smallest turbulence length scale, associated with viscous dissipation of kinetic energy. From the classic definition of the Kolmogorov microscale for isotropic turbulence, we define η at r_c

$$\eta(t) = \left(\frac{\langle \nu \rangle^3 (r_c, t)}{\langle \varepsilon \rangle (r_c, t)} \right)^{1/4}, \tag{5.43}$$

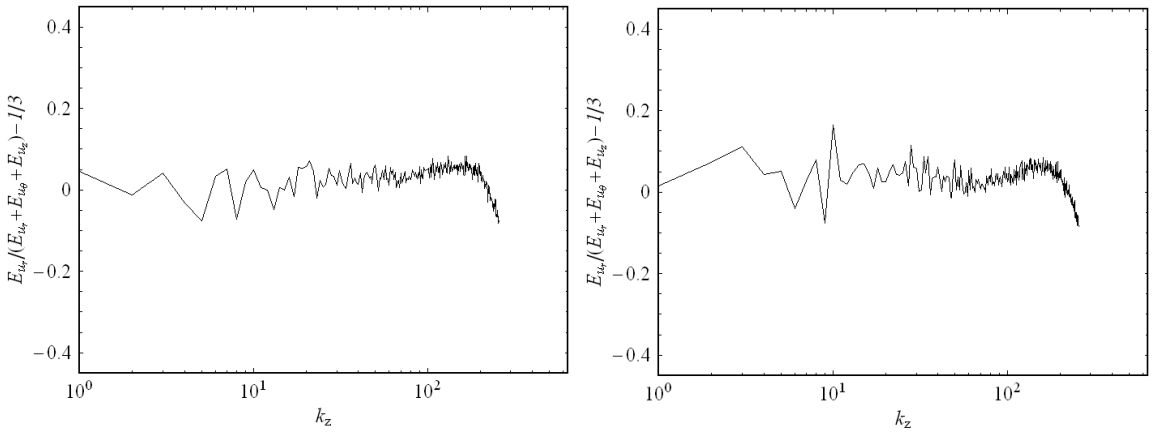

(a) $M_I = 1.3$ (a)' $M_I = 2.0$

Figure 5.28: Measure of anisotropy displayed on the k_z-power spectra $E_{u_r}(k_z)/(E_{u_r}(k_z)+E_{u_\theta}(k_z)+E_{u_z}(k_z)) - 1/3$ computed in the center shell of the mixing zone at late time $(a_0/R_0)t = 8.16$ for $M_I = 1.3$ (left) and $(a_0/R_0)t = 5.07$ for $M_I = 2.0$ (right). All computed wavenumbers shown and $k_{max} = 256$.

where $\langle\varepsilon\rangle$ is given by Equation (5.38). In the runs A1 (respectively B1), we observe in Figure 5.29a (respectively 5.29a') that $\eta \simeq \Delta x/70$ (respectively $\Delta x/100$) at late times, which justifies the use of subgrid modeling to model the viscous dissipation produced at scales smaller than the finest grid spacing Δx. To study the isotropy of the viscous dissipation scales, Kolmogorov microscales in the r-, θ-, and z-direction can be defined by

$$\eta_r(t) = \left(\frac{\langle\nu\rangle^3(r_c,t)}{\langle\varepsilon_r\rangle(r_c,t)}\right)^{1/4}, \tag{5.44a}$$

$$\eta_\theta(t) = \left(\frac{\langle\nu\rangle^3(r_c,t)}{\langle\varepsilon_\theta\rangle(r_c,t)}\right)^{1/4}, \tag{5.44b}$$

$$\eta_z(t) = \left(\frac{\langle\nu\rangle^3(r_c,t)}{\langle\varepsilon_z\rangle(r_c,t)}\right)^{1/4}, \tag{5.44c}$$

where the total dissipation rates in the r-, θ-, and z-direction are given by

$$\langle\varepsilon_r\rangle = \frac{1}{\langle\rho\rangle^2}\left(\langle\rho\sigma_{rr}S_{rr}\rangle - \langle\sigma_{rr}\rangle\langle\rho S_{rr}\rangle\right), \tag{5.45a}$$

$$\langle\varepsilon_\theta\rangle = \frac{1}{\langle\rho\rangle^2}\left(\langle\rho\sigma_{\theta\theta}S_{\theta\theta}\rangle - \langle\sigma_{\theta\theta}\rangle\langle\rho S_{\theta\theta}\rangle\right), \tag{5.45b}$$

$$\langle\varepsilon_z\rangle = \frac{1}{\langle\rho\rangle^2}\left(\langle\rho\sigma_{zz}S_{zz}\rangle - \langle\sigma_{zz}\rangle\langle\rho S_{zz}\rangle\right). \tag{5.45c}$$

In Appendix C, the above diagonal components of the stress tensor $\boldsymbol{\sigma}$ and the strain-rate tensor $\boldsymbol{S}$ in the cylindrical basis are given as a function of their respective components in Cartesian coordinates (see definitions in Equations (5.7c), (5.11a) and (5.13). It is observed (not shown) that after the first reshock, η_θ and η_z are almost the same at the center of the mixing layer. Because of such shell

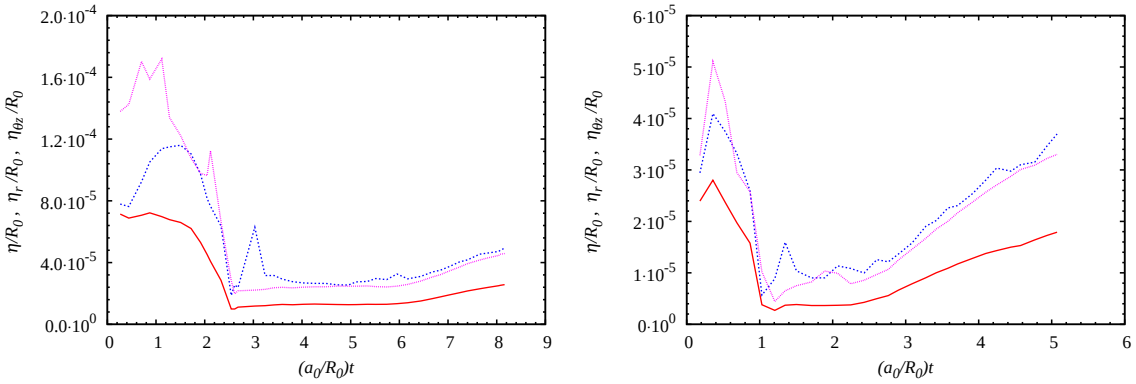

(a) $M_I = 1.3$ (a)' $M_I = 2.0$

Figure 5.29: Shell-averaged Kolmogorov microscales η (red solid line), η_r (blue small-dashed line), and $\eta_{\theta z}$ (pink dotted line) computed in the center of the mixing $r = r_c$ zone as a function of time. Case $M_I = 1.3$ (left) and 2.0 (right).

isotropy, it is convenient to combine θ and z components, namely,

$$\eta_{\theta z} = \frac{1}{2}(\eta_\theta + \eta_z), \tag{5.46}$$

and to compare this to η_r defined in the direction of inhomogeneity of the mean flow. Figure 5.29 confirms that the first reshock is responsible for the creation of a wide range of scales, in particular smaller and smaller scales at which the dissipation occurs. Following the reshock, the radial expansion of the mixing zone is associated with increase of Kolmogorov scales in the radial direction. These results also indicate late-time isotropy in the radial and transverse scales. For isotropic turbulence, we would also expect similar dissipation rates in any direction of the flow, and therefore same Kolmogorov microscales.

We are also interested in the Taylor microscales, the 'smallest large scale' in the turbulent flow, i.e. the scale for which viscous dissipation begins to affect the eddies. It marks the transition from the inertial subrange to the dissipation range. The isotropic Taylor microscale λ_T at r_c is classically given by

$$\lambda_T(t) = \sqrt{\frac{15\langle\nu\rangle(r_c,t)}{\langle\varepsilon\rangle(r_c,t)}}u'(r_c,t). \tag{5.47}$$

Similarly, Taylor microscales in the r-, θ- and z-direction can be defined by

$$\lambda_r(t) = \sqrt{\frac{\mathrm{Var}_\rho(u_r)(r_c,t)}{\mathrm{Var}_\rho(S_{rr})(r_c,t)}}, \tag{5.48a}$$

$$\lambda_\theta(t) = \sqrt{\frac{\mathrm{Var}_\rho(u_\theta)(r_c,t)}{\mathrm{Var}_\rho(S_{\theta\theta})(r_c,t)}}, \tag{5.48b}$$

$$\lambda_z(t) = \sqrt{\frac{\mathrm{Var}_\rho(u_z)(r_c,t)}{\mathrm{Var}_\rho(S_{zz})(r_c,t)}}. \tag{5.48c}$$

Note that if the mean flow had zero velocity and constant density (e.g. in RT flow starting with two fluids at rest), and considering for simplicity Cartesian coordinates, i being 1, 2 or 3, $\mathrm{Var}_\rho(u_i) = \langle u_i^2 \rangle$ and $\mathrm{Var}_\rho(S_{ii}) = \langle (\partial u_i/\partial x_i)^2 \rangle$ (no sum on i). As for the Kolmogorov microscales, it is observed (not shown) that after the first reshock, λ_θ and λ_z are almost the same at the center of the mixing layer. Because of such isotropy transversally to the radial flow, it is again convenient to combine θ and z components, namely,

$$\lambda_{\theta z} = \frac{1}{2}(\lambda_\theta + \lambda_z), \tag{5.49}$$

and to compare this to λ_r defined in the direction of inhomogeneity of the mean flow. Figure 5.30 indicates again reshock, post-reshock events, and late-time evolution. The final Taylor microscales are about ten times the finest grid spacing. Anisotropy between radial and transverse directions remains strong until late time when λ_r and $\lambda_{\theta z}$ approach each other for $M_I = 2.0$, and even converge for $M_I = 1.3$. This can be compared to the plane RTI (e.g., see [19]) where an isotropic driving term (the gravity) sustains the anisotropy at the microscale level at late times. In our case, the driving terms, in other words the traveling waves, act impulsively or over a short period of time, confirming the late-time rather isotropic character of the microscales. For isotropic turbulence, we would expect similar Taylor microscales. Figure 5.31 depicts the temporal evolution of various Taylor Reynolds numbers in the center of the mixing layer $r = r_c(t)$. These are defined as

$$Re_{\lambda_T}(t) = \frac{u'(r_c,t)\lambda_T(t)}{\langle \nu \rangle(r_c,t)}, \tag{5.50a}$$

$$Re_{\lambda_r}(t) = \frac{\sqrt{\mathrm{Var}_\rho(u_r)(r_c,t)}\lambda_r(t)}{\langle \nu \rangle(r_c,t)}, \tag{5.50b}$$

$$Re_{\lambda_\theta}(t) = \frac{\sqrt{\mathrm{Var}_\rho(u_\theta)(r_c,t)}\lambda_\theta(t)}{\langle \nu \rangle(r_c,t)}, \tag{5.50c}$$

$$Re_{\lambda_z}(t) = \frac{\sqrt{\mathrm{Var}_\rho(u_z)(r_c,t)}\lambda_z(t)}{\langle \nu \rangle(r_c,t)}, \tag{5.50d}$$

$$Re_{\lambda_{\theta z}}(t) = \frac{1}{2}(Re_{\lambda_\theta}(t) + Re_{\lambda_z}(t)). \tag{5.50e}$$

The isotropy in the flow is also manifest in the Taylor Reynolds numbers evolution.

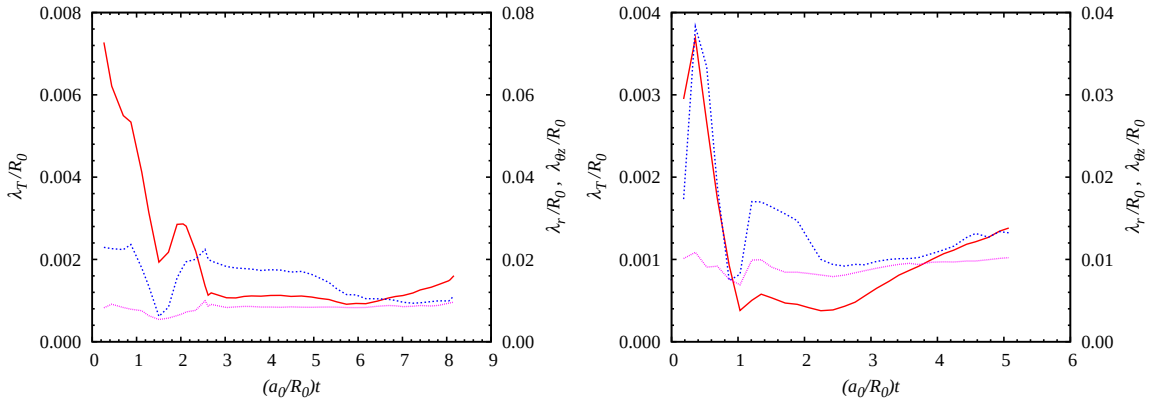

(a) $M_I = 1.3$ (a)' $M_I = 2.0$

Figure 5.30: Shell-averaged Taylor microscales λ_T (red solid line), λ_r (blue small-dashed line), and $\lambda_{\theta z}$ (pink dotted line) computed in the center of the mixing zone $r = r_c$ as a function of time. Note the order of magnitude difference in the scale of the plots. Case $M_I = 1.3$ (left) and 2.0 (right).

Profiles of the shell-averaged mixture fraction have shown that the mixing displays inhomogeneities (e.g., spike and bubbles), even at late times, associated with the anisotropic direction r. It is therefore of interest to investigate Taylor-like microscales related to variances in the scalar field

$$\lambda_{Y_r}(t) = \sqrt{\frac{\mathrm{Var}_\rho(Y)(r_c,t)}{\mathrm{Var}_\rho(\frac{\partial Y}{\partial r})(r_c,t)}}, \tag{5.51a}$$

$$\lambda_{Y_\theta}(t) = \sqrt{\frac{\mathrm{Var}_\rho(Y)(r_c,t)}{\mathrm{Var}_\rho(\frac{1}{r}\frac{\partial Y}{\partial \theta})(r_c,t)}}, \tag{5.51b}$$

$$\lambda_{Y_z}(t) = \sqrt{\frac{\mathrm{Var}_\rho(Y)(r_c,t)}{\mathrm{Var}_\rho(\frac{\partial Y}{\partial z})(r_c,t)}}, \tag{5.51c}$$

$$\lambda_{Y_{\theta z}}(t) = \frac{1}{2}(\lambda_{Y_\theta}(t) + \lambda_{Y_z}(t)). \tag{5.51d}$$

As for the Taylor microscale, isotropy is found in directions of extension of the shell crossing the mixing-zone center as λ_{Y_θ} and λ_{Y_z} are almost the same after the reshock (not shown). Late-time, near-perfect isotropy of the scalar Taylor microscales is observed for both incident Mach numbers as seen in Figure 5.32

5.8 Mixing Statistics

LES subgrid 'mixing' models generally consider only resolved-scale transport, and do not attempt to capture the small-scale mixing process between the two fluids. The present simulations model the subgrid flux of a passive scalar (see Equation (5.11c), but do not explicitly model the scalar mixing that occurs within the subgrid, at scales below the cutoff. In other words, the overall subgrid

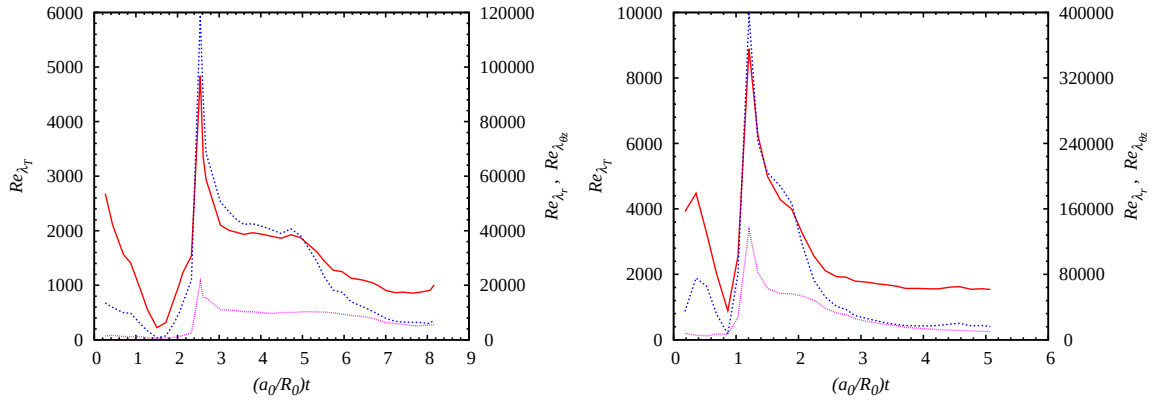

(a) $M_I = 1.3$ (a)' $M_I = 2.0$

Figure 5.31: Shell-averaged Taylor Reynolds numbers Re_{λ_T} (red solid line), Re_{λ_r} (blue small-dashed line), and $Re_{\lambda_{\theta z}}$ (pink dotted line) computed in the center of the mixing zone $r = r_c$ as a function of time. Note the order of magnitude difference in the scale of the plots. Case $M_I = 1.3$ (left) and 2.0 (right).

model does not use or model information concerning the real diffusivity of the fluids involved. We note that this is not true of the subgrid momentum flux, which incorporates direct knowledge of the viscosity μ within the exponential cutoff for the SGS energy spectrum. This then appears, in turn, in the SGS momentum flux terms. Hill et al. [43] actually use an extension of the stretched-vortex model to predict the contribution of certain mixing statistics below the cutoff scale. This work is also described by the term 'subgrid continuation'. In particular, Pullin and Lundgren's model of the mixing of a passive scalar inside a stretched-spiral vortex [89] has been used to study the effect of the Schmidt number on continued scalar spectra and p.d.f.s (see [74]). The present LES does not focus on subgrid continuation and therefore is only computing the 'stirring' of the scalar at the level of the resolved scales, even though, somewhat inaccurately, we use the term 'mixing' to qualify the turbulent evolution of the scalar field after the reshock. As a final remark, this work does not look into the mixing transition [23] and this subject is left for possible future investigations.

5.8.1 Local-Composition Evolution

The width of the mixing region δ defined in Equation (5.35) can be rewritten

$$\delta(t) = \int_{r_{in}}^{r_{out}} \psi_m(\langle\psi\rangle)\mathrm{d}r, \tag{5.52}$$

with

$$\psi_m(\psi) = 4\psi(1-\psi). \tag{5.53}$$

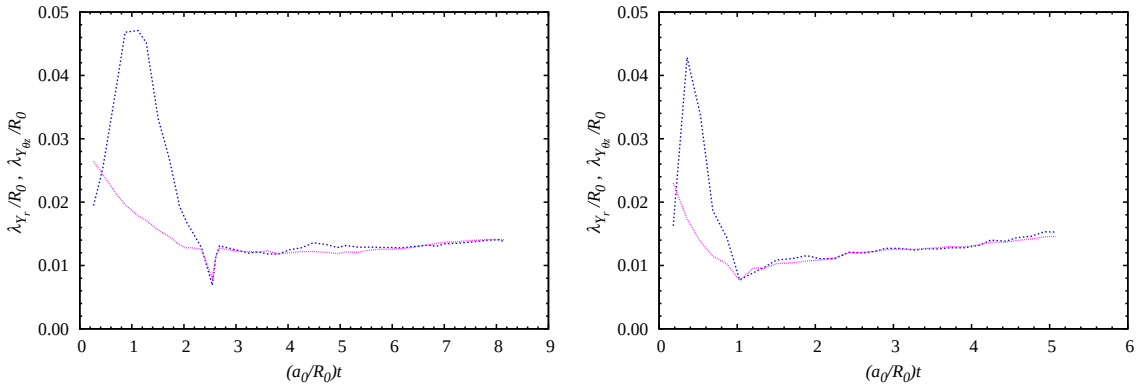

(a) $M_I = 1.3$ (a)' $M_I = 2.0$

Figure 5.32: Shell-averaged scalar Taylor microscales λ_{Y_r} (blue small-dashed line) and $\lambda_{Y_{\theta z}}$ (pink dotted line) computed in the center of the mixing zone $r = r_c$ as a function of time. Case $M_I = 1.3$ (left) and 2.0 (right).

ψ_m has a very similar profile to the fraction of mixed fluid defined in [19] by the amount of product produced by a fast-kinetic chemical reaction between the light and heavy fluid

$$\psi_m(\psi) = \begin{cases} \psi/\psi_s, & \text{if } \psi \leq \psi_s \\ (1-\psi)/(1-\psi_s), & \text{if } \psi > \psi_s, \end{cases} \tag{5.54}$$

where ψ_s is the mixture fraction for a stoichiometric mixture. $\psi_s = 1/2$ would indicate that the product of the mixing is equally composed of each reactant. The chemical product is of course limited by the amount of lean reactant. If all fluid on a particular cylindrical surface were mixed, its composition would be $\psi(r,\theta,z) = \langle\psi\rangle(r)$. Therefore, δ can be interpreted as the thickness of mixed fluid that would result if the entrained volumes of pure fluids were entering the turbulent mixing layer to become perfectly homogenized in the directions θ and z of extension of each cylindrical shell across the mixing zone. For that reason, δ can be also called an "entrainment length" or "maximum chemical product thickness", and is referred to as P_m. On the other hand, we define the "total chemical product thickness" or "mixing length" as

$$P_t(t) = \int_{r_{in}}^{r_{out}} \langle\psi_m(\psi)\rangle \mathrm{d}r = 4\int_{r_{in}}^{r_{out}} \langle\psi(1-\psi)\rangle \mathrm{d}r. \tag{5.55}$$

To quantify the state of the mixing within the layer, a mixing parameter is defined as the ratio of the two product thicknesses

$$\Xi = \frac{P_t}{P_m} = \left(\int_{r_{in}}^{r_{out}} (\langle\psi\rangle - \langle\psi^2\rangle)\mathrm{d}r\right) \Big/ \left(\int_{r_{in}}^{r_{out}} (\langle\psi\rangle - \langle\psi\rangle^2)\mathrm{d}r\right), \tag{5.56}$$

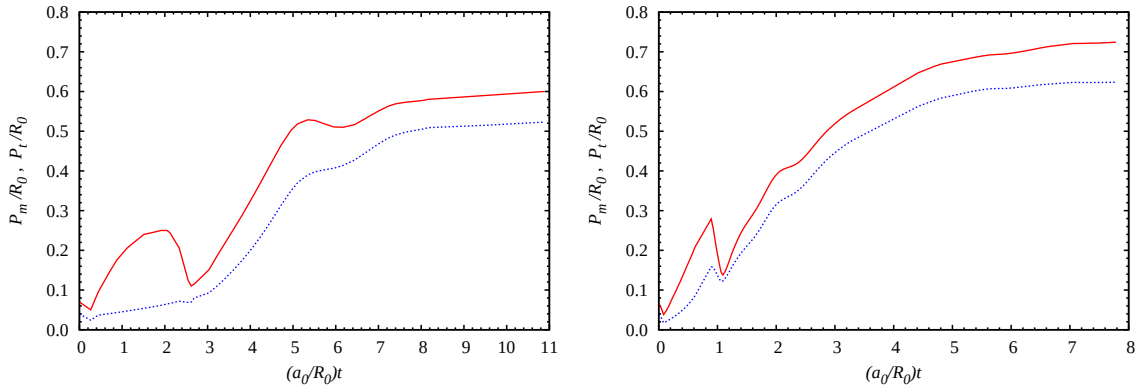

(a) $M_I = 1.3$ (a)' $M_I = 2.0$

Figure 5.33: Evolution of the entrainment length P_m (red solid line) and the mixing length P_t (blue small-dashed line). Case $M_I = 1.3$ (left) and 2.0 (right).

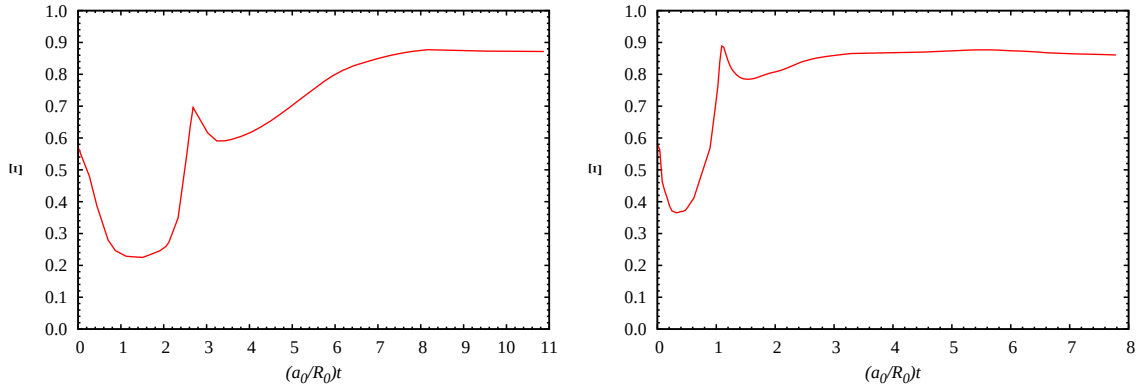

(a) $M_I = 1.3$ (a)' $M_I = 2.0$

Figure 5.34: Evolution of the mixing parameter Ξ. Case $M_I = 1.3$ (left) and 2.0 (right).

and measures the total product formed relative to the product that would be created if all entrained fluid were perfectly mixed within each shell. In general $\Xi < 1$. The time evolution of the global quantities P_m and P_t, and Ξ are shown in Figure 5.33 and Figure 5.34 respectively. During reshock, the mixing layer is compressed, as shown by the profile of P_m. Following the reshock, P_t increases rapidly, indicating significantly increased mixing. This is also indicated by the sharply peaked values of Ξ. Well-mixed fluid observed after the reshock is achieved faster for $M_I = 2.0$ than for $M_I = 1.3$, right after the reshock, suggesting that the strength of the reshock immediately affects the mixing.

5.8.2 Joint Density-Mixture Fraction Probability Density Functions

In order to study the inhomogeneity of the turbulent mixing due to the different structures (spikes and bubbles), that act differently on either side of the mixing zone, we sample the mixture fraction and density fields interpolated over cylindrical shells of given radius to create the Reynolds joint

density-mixture fraction p.d.f. as follows:

$$\tilde{\mathrm{P}}(\psi;\boldsymbol{x},t) \equiv \frac{1}{\langle\rho\rangle}\int \rho \mathrm{P}(\rho,\psi;\boldsymbol{x},t)\mathrm{d}\rho. \tag{5.57}$$

The shells of interest are those crossing the mixing zone in its center ($\langle\psi\rangle = 0.50$, $r = r_c$), the one corresponding to the region dominated by spike structures ($\langle\psi\rangle = 0.25$, $r = r_s$), and the one corresponding to the region dominated by bubble structures ($\langle\psi\rangle = 0.75$, $r = r_b$). Before reshock, the two fluids are mostly unmixed, and the p.d.f. shows two peaks for values of the mixture fraction of 0 and 1. After the first reshock, the p.d.f. at the shell cutting through the mixing-zone center r_c exhibits a strong central mode, while for the shells r_b and r_s, the two peaks have moved towards the mixing-zone center, away from the pure fluid values 0 and 1, indicating mixing progress. It is observed that the strength of these two regions of the mixing zone with high density gradients is sustained by the successive wave reverberation carrying pressure gradients in the radial direction. For both incident Mach numbers, the bimodal nature of the mixing at the center of the mixing zone is apparent at later times, as indicated in Figure 5.35. For $M_I = 2.0$, the mixing zone contains larger amount of SF_6 than for $M_I = 1.3$, as the p.d.f. is shifted towards $\psi = 1$. This is explained by the fact that at higher Mach numbers, the compression ratio is low enough and the density of inner fluid (here SF_6) sufficiently high that the entrainment of heavy fluid into the mixing layer is more efficient than for lower incident Mach numbers. Comparisons can be made with the plane geometry at late times when the mixing-layer growth started to stabilize (figure 15d of [43]): the bimodal nature of the p.d.f. is more pronounced and the p.d.f. at the center of the mixing layer is spread over a wider range of mixture fractions.

5.9 Summary

This work has presented on-going research on LES of shock-generated mixing in RM flow in a canonical cylindrical converging geometries. A hybrid numerical method has been used on each subgrid of the mesh hierarchy within the AMROC framework: it is a shock capturing method but reverts to a centered scheme with low numerical viscosity in regions of smoother flow. The stretched-vortex SGS model has allowed for the capturing of the small-scale mixing process between the a light fluid, outside, and a heavy fluid, inside, and vice-versa. Results have focused on the evolution of the mixing layer and its internal statistics including various spectra and p.d.f.s of mixed mass fractions. A detailed quantitative analysis has also been conducted including space-time histories of instantaneous cylindrical shell-averages of diverse quantities, taken concentrically to the main shocks. We have run simulations for the converging cylindrical air$\rightarrow SF_6$ and $SF_6\rightarrow$air, but the latter case is subject to current post-processing. Comparisons have been made with the plane RMI

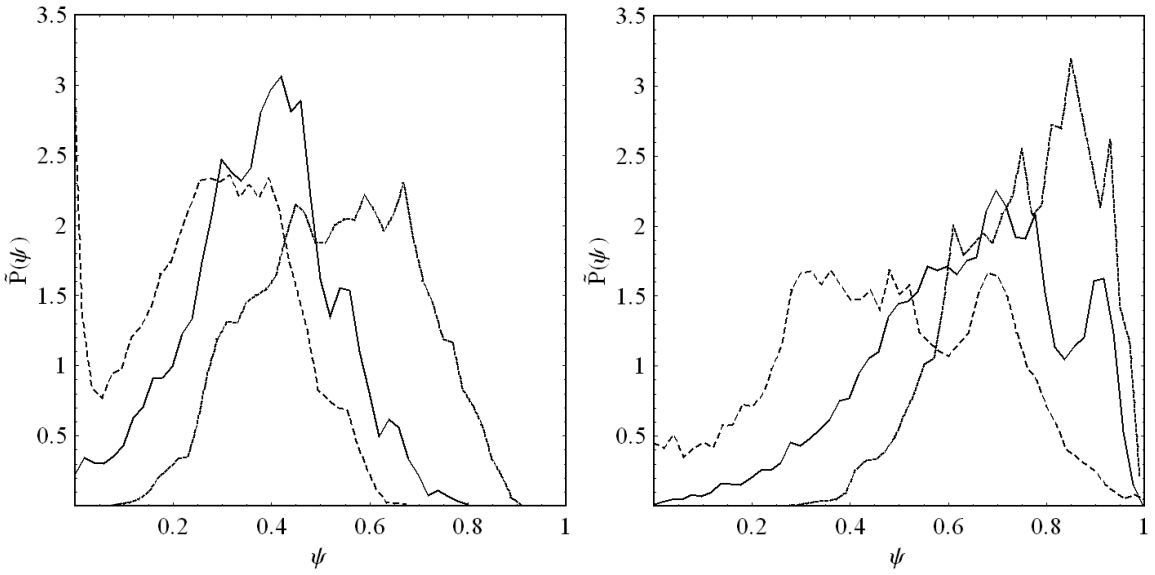

(a) $M_I = 1.3$ (a)' $M_I = 2.0$

Figure 5.35: Probability density function $\tilde{\mathrm{P}}(\psi)$ of the mixture fraction at different times calculated from the resolved scales, across three shells of the mixing zone: $r_b \equiv r_c - \delta/4$ (small-dashed line), r_c (solid line), and $r_s \equiv r_c + \delta/4$ (dashed line), at late time $(a_0/R_0)t = 8.16$ for $M_I = 1.3$ (left) and $(a_0/R_0)t = 5.07$ for $M_I = 2.0$ (right).

with reshock for an air→SF_6 interface studied by Vetter and Sturtevant [109] and Hill et al. [43].

The successive reverberation waves prove to be responsible for the intense growth of the mixing zone. After the second reshock event, a long decay of the turbulent energy is observed. At later times, the growth stabilizes and the TMZ remains weakly compressible. Various late-time energy spectra taken at the center of the mixing zone show an inertial subrange approaching the universal $k_z^{-5/3}$ scaling. The long-term mixing in the converging geometry exhibits a similar but somewhat less pronounced bimodal aspect than in the planar case. The local isotropic nature of the flow has been scrutinized through diverse statistics over cylindrical shells penetrating through the mixing layer.

Chapter 6

Conclusion

6.1 Summary

The interaction of a shock wave with a contact surface separating two fluids of different densities has been studied theoretically and computationally in converging geometries. The investigation was motivated by a desire to understand the effects of wave interactions on the RMI in plane and converging geometries. Chapter 2 focused on the early linear regime when reflected and transmitted waves created during the shock refraction at an initially slightly perturbed interface affect the reach of the terminal growth rate predicted by Richtmyer. A characteristic time scale was found to model this effect. The analysis considers receding shock waves as effective walls within the context of an incompressible flow. Simulations at various incident Mach numbers and gas combinations confirmed this model, in particular at high Mach numbers when the accelerated interface follows closely the transmitted shock. We also attempted to model in a simple manner the asymptotic growth rate, with promising results.

Chapter 3 presented first an incompressible model of the asymptotic growth rate for three-dimensional cylindrical perturbations. It explained in particular the existence of critical perturbations specific to curved geometries. In a second part, with the help of simulations of the Euler equations for ideal gas, it was showed that, in the cylindrical geometry, linear azimuthal perturbations grow to a higher final growth rate level than axial perturbations and plane perturbations of equivalent initial wavenumbers, due to geometric convergence, flow acceleration and shock proximity. Our simulations covered various Mach numbers and wavenumbers (for a fixed gas combination). Our compressible simulations differ from Mikaelian's incompressible computations of linear RMI for two-dimensional cylindrical perturbations [81] that aimed to simulate gelatin-ring experiments.

Chapter 4 focused on shock and reshock interactions in plane, cylindrical and spherical geometries, for various Mach numbers and in the light-to-heavy and heavy-to-light combinations. We considered and unperturbed interface and built wave diagrams to analyze the reverberation process when the interface is processed by waves reflecting from the wall/axis/center after it has been

accelerated initially. We first noticed important differences between the light-to-heavy and heavy-to-light case. In the light-to-heavy interaction, the reshock process shows complex shock formation in curved geometries while expansion wave interactions follow the first reshock interaction in the plane geometry. As a result, the interface mean position is alternately accelerated and decelerated to finally reach a stable equilibrium. For high incident Mach numbers, the final position is much closer to the wall/axis/center than the initial position. The light-to-heavy interaction is characterized by successive reshocks of decreasing strengths. In all geometries, the interface monotonically reaches a final stable position.

In Chapter 5, we presented large-eddy simulations of the light-to-heavy cylindrical RMI and the turbulent mixing driven by the wave reverberation observed in the previous chapters. We confirmed differences from the plane geometry. In particular, the growth of the mixing layer lasts longer than the plane geometry (more than three times the first reshock time, depending on the incident Mach number). As in the plane case, a decay of turbulent kinetic energy was observed after the first reshock, approaching the $k^{-5/3}$ universal Kolmogorov scaling. During the late time mixing, the turbulence is weakly compressible, independent of the incident Mach number. Isotropy is found for the Kolmogorov directional microscales, and Taylor directional microscales converge at late time, which differs from the RTI-driven mixing [19]. Anisotropy was noticed for the velocity power spectra, suggesting the effect of the radial expansion on the dynamics of the turbulence. The mixing efficiency was found greater for the high incident Mach number case. Probability density functions of the mixture fraction across the mixing layer showed a somewhat less bimodal character than the plane case, suggesting in particular a different entrainment process of the inner heavy fluid into the mixing zone.

6.2 Future Work

The work presented here invites many possible directions for continued research.

Asymptotic Growth in the Plane Linear RMI

An attempt to model the asymptotic growth rate has been conducted with promising results and a simpler expression than Wouchuk's analysis. More effort is needed to complete this model.

Linear Perturbations in the Imploding Spherical RMI

To complete the work on the effects of the geometry on the linear regime of the RMI, the stability of spherical slightly perturbed contact surfaces could be studied as well. The difficulties lies in the fact that the problem cannot be reduced to two-dimensional simulations, therefore making highly refined

computations difficult to achieve. The only work achieved in this context is the linear incompressible model of Mikaelian exposed in [80].

Effect of the Atwood Ratio on the Linear Growth

In the heavy-to-light interaction, a reflected expansion fan is produced and, as shown in the literature for the plane case, is responsible for a different growth evolution than the light-to-heavy case (e.g., phase inversion). For imploding cylindrical and spherical linear perturbations, the interface is also RT unstable.

Effect of the Atwood Ratio on the Shock-Generated Mixing

Simulations of the mixing in the heavy-to-light cylindrical converging RMI are being post-processed and will be compared to the light-to-heavy simulations. Because the reverberation process is different and the stability of perturbations are reversed with the light-to-heavy case (RT unstable for the imploding phase, stable for the exploding one), a different turbulent mixing is expected.

Effect of the Initial Perturbation Shape on the Shock-Generated Mixing

In the three-dimensional simulations, a single mode-like perturbed surface was considered with a smaller symmetry-breaking perturbation superposed. However, in real flows the interface is random and contains perturbations of many modes. The interaction between different modes could lead to a complicated process of bubble merger in which the large bubbles are generated from the small bubbles. Therefore, geometric effects could play a more important role for multi-mode interface.

Validation Against VTF Phase 2 Experiments

These experiments aim to focus a plane shock on a cylindrical shock traveling down a wedge and interacting with a perturbed interface.

Shock-Generated Mixing in a Converging Spherical Geometry

Similarly to the cylindrical geometry, the mixing can be studied in the spherical geometry where the convergence is more pronounced. Azimuthal and polar modes should interact differently than orthogonal modes in the plane geometry or azimuthal and axial modes in the cylindrical case.

Appendix A

Interface Acceleration for Self-Similar Converging Shock-Contact Interactions

Chisnell [15] considers the collapse of cylindrical and spherical shock waves moving through an ideal gas with constant ratio of specific heats. Chisnell sought self-similar solutions of the Euler equations behind the shock with radial symmetry in terms of the variables r/R_I where the distance $R_I(t)$ of the incident converging shock from the origin at time $t < 0$ needs to be of the form

$$R_I(t) = R_0 \left(\frac{t_I - t}{t_I} \right)^{\alpha_1}, \tag{A.1}$$

where $t = 0$ would be the time of the shock-interface interaction if there was an interface, $t_I > 0$ the implosion time, and α_1 the similarity exponent corresponding to the shock propagating in region $j = 1$, sometimes called Guderley's exponent, characterizing the shock position history during the implosion. The Mach number M_I of the incident shock at $t = 0$ is related to t_I through

$$t_I = \frac{\alpha_1 R_0}{M_I a_0}. \tag{A.2}$$

At a given time t, the flow behind the shock ($r > R_I$) is fully determined by the knowledge of the flow just ahead of the shock front, the Mach number of the shock at t, and the adiabatic exponent γ_1. The similarity exponent found by Chisnell is in excellent agreement with exact values obtained in the literature.

Consider now the normal interaction of a converging shock with an unperturbed density interface. We assume that the transmitted shock produced behaves like the incident converging shock, except that it travels in region $j = 2$ with adiabatic exponent γ_2. First, the shock front position is assumed

to follow the self-similar implosion

$$R_T(t) = R_0 \left(\frac{t_T - t}{t_T} \right)^{\alpha_2} \tag{A.3}$$

where t_T is the implosion time. This is related to the transmitted shock Mach number M_T at $t = 0$ (obtained from the one-dimensional problem of the shock interaction) by

$$t_T = \frac{\alpha_2 R_0}{M_T a_0} \sqrt{\frac{\gamma_1}{\gamma_2} \frac{1 + A}{1 - A}}. \tag{A.4}$$

Second, we consider that the flow behind the transmitted shock and ahead of the accelerated interface, i.e., for $R_T(t) \leq r \leq R(t)$, has the self-similar properties described by Chisnell. Indeed, the only way that the self-similar nature of the flow can be disturbed is by the characteristics coming from the reflected waves produced during the shock interaction. The interface is treated passively, that is, it is the path of a particle that is at $r = R_0$ at $t = 0$ and has the position $r = R(t)$ at $t > 0$. Its speed $\dot{R}(t)$ is given by the self-similar radial velocity field $u_r(R(t), t)$ given by Chisnell's solution $u(r, t)$ applied behind the transmitted shock at $r = R(t)$.

We apply the following change of variables:

$$\xi = \frac{r}{R_T(t)}, \tag{A.5a}$$

$$t' = t. \tag{A.5b}$$

Partial derivatives in these two sets of variables are related by

$$\frac{\partial}{\partial r} = \frac{1}{R_T} \frac{\partial}{\partial \xi}, \tag{A.6a}$$

$$\frac{\partial}{\partial t} = \frac{\partial}{\partial t'} - \xi \frac{\dot{R}_T}{R_T} \frac{\partial}{\partial \xi}. \tag{A.6b}$$

In that set of variables, the velocity field given by Equation (2.14b) of [15] becomes:

$$u_r(\xi, t') = \frac{\dot{R}_T(t')}{\alpha_2} \xi \mathrm{V}(\xi), \tag{A.7}$$

where $\mathrm{V}(\xi)$ is given by Equation (4.4b) of [15]. To obtain the interface acceleration $\ddot{R}(t)$ given by du_r/dt evaluated at $r = R(t)$, we compute

$$\frac{Du_r}{Dt} = \frac{\partial u_r}{\partial t} + u_r \frac{\partial u_r}{\partial r} = \frac{\partial u_r}{\partial t'} + \left(\frac{u_r}{R_T} - \xi \frac{\dot{R}_T}{R_T} \frac{\partial u_r}{\partial \xi} \right). \tag{A.8}$$

For simplicity, $t' \to t$. Using Equation (A.7) and differentiating Equation (4.4b) of [15],

$$\frac{\mathrm{d}\xi}{\xi} = \left(\frac{\mathrm{F}_2}{\mathrm{V}+\mathrm{q}_2} - \frac{\alpha_2}{\mathrm{V}}\right)\mathrm{dV}, \tag{A.9}$$

with F_2 given by Equation (4.2c) using Equation (3.6) and q_2 given by Equation (3.9c) in [15], Equation (A.8) becomes

$$\frac{Du_r}{Dt} = -\frac{\xi R_T}{t_T^2}\left(1-\frac{t}{t_T}\right)^{-2}\mathrm{V}^2\,\frac{(\mathrm{F}_2-\alpha_2+1)\mathrm{V}+\mathrm{q}_2(1-\alpha_2)-\mathrm{F}_2}{(\mathrm{F}_2-\alpha_2)\mathrm{V}-\mathrm{q}_2\alpha_2}. \tag{A.10}$$

Taking successively the limit $\xi \to R/R_T$ (i.e., $r \to R$) and $t \to 0^+$ of Equation (A.10), and observing that in that limit $\mathrm{V} \to \mathrm{V}(1) \equiv \mathrm{V}_S$ given by Equation (2.15c) of [15] applied in region $j = 2$, the interface acceleration right after the shock interaction is

$$\ddot{R}(0^+) = -\frac{R_0}{t_T^2}\,\mathrm{V}_S^2\frac{(\mathrm{F}_2-\alpha_2+1)\mathrm{V}_S+\mathrm{q}_2(1-\alpha_2)-\mathrm{F}_2}{(\mathrm{F}_2-\alpha_2)\mathrm{V}_S-\mathrm{q}_2\alpha_2}. \tag{A.11}$$

Since $\mathrm{V}_S = 2\alpha_2/(\gamma_2+1)$ and from the expressions of F_2 and q_2 written in [15], Equation (A.11) becomes:

$$\ddot{R}(0^+) = -\frac{R_0}{t_T^2}\,\frac{4\alpha_2\left(\dfrac{\alpha_2}{V_{0_2}}-1\right)\left[(2\alpha_2\gamma_2-\gamma_2-1)\,\dfrac{\alpha_2}{V_{0_2}}-\alpha_2(\gamma_2-1)\right]}{(1+\gamma_2)^2\left(2\dfrac{\alpha_2}{V_{0_2}}+\gamma_2-3\right)\dfrac{\alpha_2}{V_{0_2}}}. \tag{A.12}$$

In the strong shock limit, which is that used by Chisnell, it can be easily shown, from the one-dimensional Riemann problem of the shock interaction that

$$\Delta W \simeq \frac{2}{\gamma_2+1}|\dot{R}_T(0^+)|. \tag{A.13}$$

Using Equation (A.3), we obtain an estimate for the implosion time t_T

$$t_T \simeq \frac{2\alpha_2}{\gamma_2+1}\frac{R_0}{\Delta W}, \tag{A.14}$$

and Equation (A.12) becomes

$$\ddot{R}(0^+) = -\frac{\Delta W^2}{R_0}\,\frac{\left(\dfrac{\alpha_2}{V_{0_2}}-1\right)\left[(2\alpha_2\gamma_2-\gamma_2-1)\,\dfrac{\alpha_2}{V_{0_2}}-\alpha_2(\gamma_2-1)\right]}{\alpha_2\left(2\dfrac{\alpha_2}{V_{0_2}}+\gamma_2-3\right)\dfrac{\alpha_2}{V_{0_2}}}, \tag{A.15}$$

which we plug into the dimensionless Taylor development of the interface radius to obtain Equa-

tion (3.21)

$$\widetilde{R}(\widetilde{t}) = 1 + \left(\frac{1}{\Delta W}\dot{R}(0^+)\right)\widetilde{t} + \frac{1}{2}\left(\frac{R_0}{\Delta W^2}\ddot{R}(0^+)\right)\widetilde{t}^2 + \mathcal{O}\left(\widetilde{t}^3\right). \tag{A.16}$$

Appendix B

Shell-Averaged Equations

B.1 Introduction

This appendix is an introduction to on-going research that aim to investigate the effect of uncertainties in the shape of the interface between the two fluids on the transition to turbulence and on profiles of turbulent transport properties within the mixing layer. Diagnostics will include detailed space-time histories of shell averages, parallel (in the plane geometry) or concentrically (in cylindrical geometry) to the shock, of base quantities, and of terms in the turbulent kinetic energy, the turbulent mass flux and the density self-correlation equations. The basic statistics are listed in Appendix C.

B.2 Plane Richtmyer-Meshkov Instability

The basic configuration will be air-SF_6 in a light-to-heavy configuration, with a planar incident shock at $M_I = 1.5$, 2.0, and 3.0. The simulation geometry will consist of a square tube configuration with periodic boundary conditions in two directions.

B.2.1 Basic Quantities

Using a bar to denote a plane-average in a $(y-z)$-plane (parallel to the incident shock) at position x, and at time t, define for quantity $X(x,y,z,t)$

$$X(x,y,z,t) \equiv \overline{X}(x,t) + X'(x,y,z,t), \tag{B.1a}$$

$$X(x,y,z,t) \equiv \widetilde{X}(x,t) + X''(x,y,z,t), \tag{B.1b}$$

$$\widetilde{X}(x,t) \equiv \frac{\overline{\rho X}}{\overline{\rho}}, \tag{B.1c}$$

where ρ is the total gas density. The base quantities will consist of

$$\overline{\rho}, \quad \overline{u_i}, \quad \overline{p}, \quad \overline{T}, \quad \widetilde{u_i}, \quad \overline{\rho'\,u_i'}, \quad \overline{\rho'\,u_i'\,u_j'}, \quad \overline{u_i'\,u_j'}, \quad \overline{\rho'\,\nu'}, \tag{B.2}$$

where u_i is velocity, p is pressure, T temperature, and $\nu = 1/\rho$. Also

$$R_{ij} \equiv \overline{\rho\,u_i''\,u_j''}, \quad \overline{K} \equiv \frac{R_{nn}}{2\overline{\rho}}. \tag{B.3}$$

will be calculated. For what follows, $x \equiv 1$, $y \equiv 2$, and $z \equiv 3$.

B.2.2 Un-Modeled Equations

In addition, the terms appearing in three important un-modeled equations will be calculated. These are terms comprising the turbulent kinetic energy, the turbulent mass flux, and the density self-correlation equations. These are, respectively

$$\begin{aligned}
\frac{\partial(\overline{\rho}\,\overline{K})}{\partial t} + \frac{\partial(\overline{\rho}\,\overline{K}\,\widetilde{u_x})}{\partial x} &= a_x\,\frac{\partial \overline{p}}{\partial x} - R_{ix}\frac{\partial \widetilde{u_i}}{\partial x} - a_i\,\frac{\partial \overline{\sigma}_{xi}}{\partial x} - \frac{1}{2}\frac{\partial(\overline{\rho\,u_i''\,u_i''\,u_x''})}{\partial x} - \frac{\partial(\overline{u_x'\,p'})}{\partial x} \\
&+ \frac{\partial \overline{u_i'\,\sigma_{xi}'}}{\partial x} + \overline{p'\frac{\partial u_i'}{\partial x_i}} - \overline{\sigma_{ji}'\frac{\partial u_i'}{\partial x_j}},
\end{aligned} \tag{B.4a}$$

$$\begin{aligned}
\frac{\partial(\overline{\rho}\,a_x)}{\partial t} + \frac{\partial(\overline{\rho}\,a_x\,\widetilde{u_x})}{\partial x} &= b\left(\frac{\partial \overline{p}}{\partial x} - \frac{\partial \overline{\sigma}_{xx}}{\partial x}\right) + \overline{\rho}\left(\overline{\nu'\,\frac{\partial p'}{\partial x}} - \overline{\nu'\,\frac{\partial \sigma_{jx}'}{\partial x_j}}\right) \\
&- \overline{\rho}\,a_x\,\frac{\partial(\widetilde{u_x} - a_x)}{\partial x} + \left(\frac{\overline{\rho'\,u_x'^{\,2}} - R_{xx}}{\overline{\rho}}\right)\frac{\partial \overline{\rho}}{\partial x} + \overline{\rho}\,\frac{\partial(a_x^2)}{\partial x} \\
&- \left(\frac{\partial(\overline{\rho'\,u_x'^{\,2}})}{\partial x} + \overline{\rho}\,\overline{u_x'\,\frac{\partial u_j'}{\partial x_j}}\right),
\end{aligned} \tag{B.4b}$$

$$\frac{\partial b}{\partial t} + \overline{u_x}\,\frac{\partial b}{\partial x} = -\frac{(1+b)}{\overline{\rho}}\frac{\partial(\overline{\rho}\,a_x)}{\partial x} - \overline{\rho}\,\frac{\partial(\overline{\nu'\,u_x'})}{\partial x} + 2\,\overline{\rho}\,\overline{\nu'\,\frac{\partial u_i'}{\partial x_i}}. \tag{B.4c}$$

Note that:

$$R_{ij} = \overline{\rho\,u_i'\,u_j'} - \overline{\rho}\,a_i\,a_j \tag{B.5}$$

where $a_i = \overline{\rho'\,u_i'}/\overline{\rho}$ is the turbulent mass flux and $b = -\overline{\rho'\,\nu'}$ is the density self-correlation. We note that all of the base quantities and the various terms appearing in the above equations are functions of x and t through the evolution of the simulation. Some terms of these equations (for example, averages of products of deviatoric stresses and velocity gradients) may have substantial subgrid contributions. Equations for a_y and a_z (in the plane of the mixing zone) should be statistically zero, so only the a_x equation has been written.

B.3 Cylindrical Richtmyer-Meshkov Instability

B.4 Basic Quantities

Using brackets to denote a shell-average in a (θ, z)-surface at position r, and at time t, define for quantity $Q(r, \theta, z, t)$

$$Q(r,\theta,z,t) \equiv \langle Q\rangle(r,t) + Q'(r,\theta,z,t), \tag{B.6a}$$

$$Q(r,\theta,z,t) \equiv \widetilde{Q}(r,t) + Q''(r,\theta,z,t), \tag{B.6b}$$

$$\widetilde{Q}(r,t) \equiv \frac{\langle \rho\, Q\rangle}{\langle\rho\rangle}, \tag{B.6c}$$

where ρ is the total gas density. Define

$$\nu_\rho \equiv \frac{1}{\rho}, \quad R_{pq} \equiv \langle \rho\, u_p''\, u_q''\rangle, \quad \langle K\rangle \equiv \frac{R_{nn}}{2\langle\rho\rangle}. \tag{B.7}$$

For what follows, (i, j) =1, 2, or 3 stands for x, y, or z. Cylindrical coordinates are (r, θ, z).

B.5 Un-Modeled Equations

In addition, the terms appearing in three important un-modeled equations will be calculated. These are terms comprising the turbulent kinetic energy, the turbulent mass flux, and the density self-correlation equations. These are, respectively

$$\begin{aligned}
\frac{\partial(\langle\rho\rangle\,\langle K\rangle)}{\partial t} &+ \frac{1}{r}\frac{\partial(r\langle\rho\rangle\,\langle K\rangle\,\widetilde{u_r})}{\partial r} = a_r\,\frac{\partial\langle p\rangle}{\partial r} - \left[R_{rr}\frac{\partial\widetilde{u_r}}{\partial r} + R_{\theta\theta}\frac{\widetilde{u}_r}{r} + R_{r\theta}\left(\frac{\partial\widetilde{u_\theta}}{\partial r} - \frac{\widetilde{u_\theta}}{r}\right) + R_{rz}\frac{\partial\widetilde{u_z}}{\partial r}\right] \\
&- \frac{1}{r}\left[a_r\left(\frac{\partial(r\langle\sigma_{rr}\rangle)}{\partial r} - \langle\sigma_{\theta\theta}\rangle\right) + a_\theta\left(\frac{\partial(r\langle\sigma_{r\theta}\rangle)}{\partial r} + \langle\sigma_{r\theta}\rangle\right) + a_z\frac{\partial(r\langle\sigma_{rz}\rangle)}{\partial r}\right] \\
&- \frac{1}{2r}\frac{\partial(r\langle\rho\,|\boldsymbol{u}''|^2u_r''\rangle)}{\partial r} - \frac{1}{r}\frac{\partial(r\langle u_r'\,p'\rangle)}{\partial r} \\
&+ \frac{1}{r}\frac{\partial\left[r(\langle\sigma_{rr}'\,u_r'\rangle + \langle\sigma_{r\theta}'\,u_\theta'\rangle + \langle\sigma_{rz}'\,u_z'\rangle)\right]}{\partial r} \\
&+ \langle p'\nabla\cdot\boldsymbol{u}'\rangle - \langle\boldsymbol{\sigma}':\nabla\boldsymbol{u}'\rangle, \qquad \text{(B.8a)}
\end{aligned}$$

$$\begin{aligned}
\frac{\partial(\langle\rho\rangle\,a_r)}{\partial t} &+ \frac{1}{r}\frac{\partial(r\langle\rho\rangle\,a_r\,\widetilde{u_r})}{\partial r} - \frac{\langle\rho\rangle a_\theta\widetilde{u_\theta}}{r} = b\left[\frac{\partial\langle p\rangle}{\partial r} - \frac{1}{r}\left(\frac{\partial(r\langle\sigma_{rr}\rangle)}{\partial r} - \langle\sigma_{\theta\theta}\rangle\right)\right] + \langle\rho\rangle\,\langle\nu_\rho'\,\frac{\partial p'}{\partial r}\rangle \\
&- \langle\rho\rangle\,\left[\frac{1}{r}\langle\nu_\rho'\,\frac{\partial(r\sigma_{rr}')}{\partial r}\rangle + \frac{1}{r}\langle\nu_\rho'\,\frac{\partial\sigma_{r\theta}'}{\partial\theta}\rangle + \langle\nu_\rho'\,\frac{\partial\sigma_{rz}'}{\partial z}\rangle - \frac{\langle\nu_\rho'\sigma_{\theta\theta}'\rangle}{r}\right] \\
&- \langle\rho\rangle\left(a_r\,\frac{\partial(\widetilde{u_r} - a_r)}{\partial r} - \frac{a_\theta(\widetilde{u_\theta} - a_\theta)}{r}\right) + \left(\frac{\langle\rho'\,u_r'^{\,2}\rangle - R_{rr}}{\langle\rho\rangle}\right)\frac{\partial\langle\rho\rangle}{\partial r} \\
&+ \frac{\langle\rho\rangle}{r}\left(\frac{\partial(ra_r^2)}{\partial r} - a_\theta^2\right) \\
&- \frac{1}{r}\left(\frac{\partial(r\langle\rho' u_r'^{\,2}\rangle)}{\partial r} - \langle\rho' u_\theta'^{\,2}\rangle\right) - \langle\rho\rangle\langle u_r'\nabla\cdot\boldsymbol{u}'\rangle, \qquad \text{(B.8b)}
\end{aligned}$$

$$\frac{\partial b}{\partial t} + \langle u_r\rangle\,\frac{\partial b}{\partial r} = -\frac{(1+b)}{r\langle\rho\rangle}\frac{\partial(r\langle\rho\rangle\,a_r)}{\partial r} - \frac{\langle\rho\rangle}{r}\frac{\partial(r\langle\nu_\rho'\,u_r'\rangle)}{\partial r} + 2\,\langle\rho\rangle\,\langle\nu_\rho'\,\nabla\cdot\boldsymbol{u}'\rangle, \qquad \text{(B.8c)}$$

where $a_q = \langle\rho'\,u_q'\rangle/\langle\rho\rangle$ ($q = r, \theta$ or z) is the turbulent mass flux and $b = -\langle\rho'\,\nu_\rho'\rangle$ is the density self-correlation. We note that all of the base quantities and the various terms appearing in the above equations are functions of r and t through the evolution of the simulation.

Appendix C

Shell-Averaged Statistics: Methodology

The following procedure has been applied to a combination of air and SF_6 but could be directly applied to any two-fluid combination.

C.1 The Statistics Class Within AMROC

A statistics class `WENOStatistics`, present in the directory `vtf/amroc/weno/`, allows to interpolate keys (e.g., the density) at any location of the computational domain as well as to take averages over one-dimensional streaks or two-dimensional surfaces (probes). The class is associated to a parser in `vtf/amroc/weno/StatParser/` that allows the user to define his keys and probes in his local application directory through an input file `Stats.def`. The file produced is `Stats?.dat` where `?` corresponds to the time steps at which the statistics are evaluated.

Since the interpolation was intended for the GFM method that currently is first-order by definition, the interpolation class available was only first-order. Even if one would construct a correct cut-cell method, a first-order interpolation should be sufficient to lead to an overall second-order scheme, since the results are used in the numerical flux approximation only. Also for constructing fluid-structure coupling values, first-order is more than enough, since our time splitting approach is first-order only, too. However, for statistics purposes, a second-order interpolation `vtf/amroc/clawpack/src/?d/interpolation/intpol?_quad.f` (where `?` stands for the dimensions 1, 2, or 3) was developed.

The original class allowed only keys (or basic mathematical functions of these keys) directly derived from the vector of state ($\rho, \rho u_1, \rho u_2, \rho u_3, E, \rho Y, T,$ `dcflag`, `sgske`). Therefore, any additional quantity, e.g., the subgrid stress components, had to be carried in an auxiliary output array in the vector of state, slowing down the computation significantly since the vector of state is manipulated every time step while the statistics are effectively used only at the desired time

steps. In order to enable the definition of customized output, the file `Output.f90`, which originally contains routines used to produce HDF data files for visualization purposes, handles the requests for new output. With this new generic interface, all auxiliary internal states of the LES module are computed as needed. Moreover, the user can now install in their local application directory `vtf/amroc/weno/applications/...` hooks inside the `Output.f90` with whatever they want. Since we had to initialize the patch array boundaries to do this interaction with the patch solver, we had to define a new class `F77FileOutput` and overload the parent function `Transpose` to first initialize the patch variables before the user could have access to the internal state of the solver.

C.2 Output of Basic Quantities

The couple (`nc`,`qo(i,j,k)`) coded in `Output.f90` and `Output_hook.f90` (`qout(nc)` in `Stats.def`) is listed. It concerns basic resolved and subgrid quantities.

1) ρ

2) u_1 (or u or u_x)

3) u_2 (or v or u_y)

4) u_3 (or w or u_z)

5) E

6) T

7) p

8) γ

9) Y , mass fraction (+1 for SF_6, -1 for Air)

10) `dcflag`

11) $\frac{\tau_{kk}}{2\rho}$, subgrid kinetic energy (where τ_{ij} is the subgrid stress given by Pullin's stretched-vortex subgrid model)

12) τ_{11}

13) τ_{22}

14) τ_{33}

15) τ_{12}

16) τ_{13}

17) τ_{23}

18) $-\tau_{ij}S_{ij}$, subgrid dissipation (where $S_{ij} = \frac{1}{2}\left(\frac{\partial u_i}{\partial x_j} + \frac{\partial u_j}{\partial x_i}\right)$ is the resolved strain tensor)

19) σ_Y^2 , subgrid scalar variance, without k^{-1} correction to the scalar spectrum (use `qout(54)` instead)

20) `fstruc`, structure function

21) `sstruc1`, scalar structure function

22) μ , viscosity coefficient

23) $\frac{\partial u_1}{\partial x_1}$

24) $\frac{\partial u_1}{\partial x_2}$

25) $\frac{\partial u_1}{\partial x_3}$

26) $\frac{\partial u_2}{\partial x_1}$

27) $\frac{\partial u_2}{\partial x_2}$

28) $\frac{\partial u_2}{\partial x_3}$

29) $\frac{\partial u_3}{\partial x_1}$

30) $\frac{\partial u_3}{\partial x_2}$

31) $\frac{\partial u_3}{\partial x_3}$

32) $d_{ij}S_{ij}$, resolved dissipation (where $d_{ij} = 2\mu\left(S_{ij} - \frac{1}{3}S_{kk}\delta_{ij}\right)$ is the resolved stress tensor)

33) $\frac{\partial Y}{\partial x_1}$

34) $\frac{\partial Y}{\partial x_2}$

35) $\frac{\partial Y}{\partial x_3}$

36) $\frac{\partial p}{\partial x_1}$

37) $\frac{\partial p}{\partial x_2}$

38) $\frac{\partial p}{\partial x_3}$

39) $\frac{\partial \sigma_{1i}}{\partial x_i}$, where $\sigma_{ij} = d_{ij} - \tau_{ij}$ is the total stress

40) $\frac{\partial \sigma_{2i}}{\partial x_i}$

41) $f_1^Y = -\frac{q_1^Y}{\rho}$, where q_i^Y is the subgrid scalar flux defined in Equation (3.11c) of [43]

42) f_2^Y

43) f_3^Y

44) $\widetilde{a}_S$, axial strain along the subgrid vortex axis using alignment with the resolved scale strain tensor S_{ij}

45) $e3_x$, first resolved strain eigenvector component

46) $e3_y$, second component

47) $e3_z$, third component

48) $\widetilde{a}_\omega$, the axial strain along the subgrid vortex axis using alignment with the resolved scale vorticity $\boldsymbol{\omega}$

49) o_x , first resolved vorticity component

50) o_y , second component

51) o_z , third component

52) λ , vorticity alignment weight ($0 \leq \lambda \leq 1$); the strain alignment weight is $1 - \lambda$

53) $\mathsf{K}_0\varepsilon^{2/3}$, group prefactor for the subgrid energy spectrum

54) K_Y , group prefactor for the subgrid scalar spectrum (including k^{-1} contribution to the scalar spectrum)

55) σ_Y^2 , subgrid scalar variance (including k^{-1} contribution to the scalar spectrum).

C.3 One-Dimensional Statistics

This section concerns quantities interpolated over shells of radii r (at given time t). We are therefore interested in the variation of these quantities when varying r, at time t.

C.3.1 Basic Shell-Averaged Quantities

From the previous basic output quantities can be computed basic shell-averaged quantities over cylindrical shells of given radii. The basic shell-averages and a listing of the cylindrical shells are enumerated in the local file `Stats.def`. The statistics class produces data files `Stats?.dat` at the desired time `?` step.

1) $\langle r \rangle$, radius $r = \sqrt{x^2 + y^2}$

2) $\langle \rho \rangle$

3) $\langle \rho^2 \rangle$

4) $\langle u_r \rangle$

5) $\langle u_r^2 \rangle$

6) $\langle \rho u_r \rangle$

7) $\langle \rho u_r^2 \rangle$

8) $\langle u_\theta \rangle$

9) $\langle u_\theta^2 \rangle$

10) $\langle \rho u_\theta \rangle$

11) $\langle \rho u_\theta^2 \rangle$

12) $\langle u_z \rangle$

13) $\langle u_z^2 \rangle$

14) $\langle \rho u_z \rangle$

15) $\langle \rho u_z^2 \rangle$

16) $\langle \frac{1}{2} \tau_{ii} \rangle$, subgrid turbulent kinetic energy

17) $\langle p \rangle$

18) $\langle p^2 \rangle$

19) $\langle T \rangle$

20) $\langle T^2 \rangle$

21) $\langle c \rangle$, speed of sound $c = \sqrt{\frac{\gamma p}{\rho}}$

22) $\langle c^2 \rangle$

23) $\langle M \rangle$, Mach number $M = \frac{|\boldsymbol{u}|}{c} = \sqrt{\frac{\rho u_i u_i}{\gamma p}}$

24) $\langle M^2 \rangle$

25) $\langle Y \rangle$, passive scalar. $Y = 1$ for SF_6 and -1 for Air, define also $\psi = \frac{1}{2}(1 + Y)$ representing the percentage of SF_6 (heavy-fluid mass fraction), therefore $\langle \psi \rangle = \frac{1}{2}(1 + \langle Y \rangle)$

26) $\langle Y^2 \rangle$, and $\langle \psi^2 \rangle = \frac{1}{4}(1 + 2\langle Y \rangle + \langle Y^2 \rangle)$

27) $\langle \rho Y \rangle$

28) $\langle \rho Y^2 \rangle$

29) $\langle X \rangle = \langle \frac{1-\alpha+(1+\alpha)Y}{1+\alpha+(1-\alpha)Y} \rangle$, mol fraction, where $\alpha = \frac{\mathrm{M}_{\mathrm{SF}_6}}{\mathrm{M}_{\mathrm{Air}}}$. $X = 1$ for SF_6 and -1 for Air. $\mathrm{M}_{\mathrm{Air}} = 26.8288$ g.mol^{-1} and $\mathrm{M}_{\mathrm{SF}_6} = 146.05$ g.mol^{-1}

30) $\langle X^2 \rangle$

31) $\langle \rho X \rangle$

32) $\langle \rho X^2 \rangle$

33) $\langle \tau_{11} \rangle$

34) $\langle \tau_{22} \rangle$

35) $\langle \tau_{33} \rangle$

36) $\langle \tau_{12} \rangle$

37) $\langle \tau_{13} \rangle$

38) $\langle \tau_{23} \rangle$

39) $\langle -\tau_{ij} S_{ij} \rangle$

40) $\langle \nu \rangle$, $\nu = \frac{\mu}{\rho}$ kinematic viscosity

41) $\langle S_{11} \rangle$

42) $\langle S_{22} \rangle$

43) $\langle S_{33} \rangle$

44) $\langle S_{12} \rangle$

45) $\langle S_{13} \rangle$

46) $\langle S_{23} \rangle$

47) $\langle d_{11} \rangle$

48) $\langle d_{22} \rangle$

49) $\langle d_{33} \rangle$

50) $\langle d_{12} \rangle$

51) $\langle d_{13} \rangle$

52) $\langle d_{23} \rangle$

53) $\langle d_{ij} S_{ij} \rangle$

54) $\langle \frac{\partial Y}{\partial x_1} \rangle$

55) $\langle \frac{\partial Y}{\partial x_2} \rangle$

56) $\langle \frac{\partial Y}{\partial x_3} \rangle$

57) $\langle \frac{\partial Y}{\partial x_j} \frac{\partial Y}{\partial x_j} \rangle$

58) $\langle f_1^Y \rangle$

59) $\langle f_2^Y \rangle$

60) $\langle f_3^Y \rangle$

61) $\langle f_i^Y \frac{\partial Y}{\partial x_i} \rangle$

62) $\langle \nu_\rho \rangle$, where $\nu_\rho = 1/\rho$

63) $\langle \nu_\rho u_r \rangle$

64) $\langle \nu_\rho S_{ii} \rangle$

65) $\langle u_r u_\theta \rangle$

66) $\langle u_r u_z \rangle$

67) $\langle u_\theta u_z \rangle$

68) $\langle \rho u_r u_\theta \rangle$

69) $\langle \rho u_r u_z \rangle$

70) $\langle \rho u_i u_i u_r \rangle$

71) $\langle p S_{ii} \rangle$

72) $\langle p u_r \rangle$

73) $\langle \sigma_{rr} \rangle = \langle \cos(\theta)^2 \sigma_{11} + \sin(\theta)^2 \sigma_{22} + \sin(2\theta)\sigma_{12} \rangle$, where recall $\sigma_{ij} = d_{ij} - \tau_{ij}$

74) $\langle \sigma_{r\theta} \rangle = \langle \frac{1}{2}\sin(2\theta)(\sigma_{22} - \sigma_{11}) + \cos(2\theta)\sigma_{12} \rangle$

75) $\langle \sigma_{rz} \rangle = \langle \cos(\theta)\sigma_{13} + \sin(\theta)\sigma_{23} \rangle$

76) $\langle u_r \sigma_{rr} \rangle = \langle u_r \left(\cos(\theta)^2 \sigma_{11} + \sin(\theta)^2 \sigma_{22} + \sin(2\theta)\sigma_{12} \right) \rangle$

77) $\langle u_\theta \sigma_{r\theta} \rangle = \langle u_\theta \left(\frac{1}{2}\sin(2\theta)(\sigma_{22} - \sigma_{11}) + \cos(2\theta)\sigma_{12} \right) \rangle$

78) $\langle u_z \sigma_{rz} \rangle = \langle u_z \left(\cos(\theta)\sigma_{13} + \sin(\theta)\sigma_{23} \right) \rangle$

79) $\langle \nu_\rho \frac{\partial p}{\partial r} \rangle = \langle \nu_\rho \left(\cos(\theta)\frac{\partial p}{\partial x_1} + \sin(\theta)\frac{\partial p}{\partial x_2} \right) \rangle$

80) $\langle u_r S_{ii} \rangle$

81) $\langle \nu_\rho \left(\cos(\theta)\frac{\partial \sigma_{1i}}{\partial x_i} + \sin(\theta)\frac{\partial \sigma_{2i}}{\partial x_i} \right) \rangle$

82) $\langle \rho S_{rr} \rangle = \langle \rho \frac{\partial u_r}{\partial r} \rangle = \langle \rho \left(\cos(\theta)^2 S_{11} + \sin(\theta)^2 S_{22} + \sin(2\theta) S_{12} \right) \rangle$

83) $\langle \rho S_{rr}^2 \rangle$

84) $\langle \rho S_{\theta\theta} \rangle = \langle \frac{\rho}{r} \left(\frac{\partial u_\theta}{\partial \theta} + u_r \right) \rangle = \langle \rho \left(\sin(\theta)^2 S_{11} + \cos(\theta)^2 S_{22} - \sin(2\theta) S_{12} \right) \rangle$

85) $\langle \rho S_{\theta\theta}^2 \rangle$

86) $\langle \rho S_{zz} \rangle = \langle \rho \frac{\partial u_z}{\partial z} \rangle$

87) $\langle \rho S_{zz}^2 \rangle$

88) $\langle \rho \sigma_{rr} S_{rr} \rangle = \langle \rho (\cos(\theta)^2 \sigma_{11} + \sin(\theta)^2 \sigma_{22} + \sin(2\theta)\sigma_{12})(\cos(\theta)^2 S_{11} + \sin(\theta)^2 S_{22} + \sin(2\theta) S_{12}) \rangle$

89) $\langle \rho \sigma_{\theta\theta} S_{\theta\theta} \rangle = \langle \rho (\sin(\theta)^2 \sigma_{11} + \cos(\theta)^2 \sigma_{22} - \sin(2\theta)\sigma_{12})(\sin(\theta)^2 S_{11} + \cos(\theta)^2 S_{22} - \sin(2\theta) S_{12}) \rangle$

90) $\langle \rho \sigma_{zz} S_{zz} \rangle$

91) $\langle \rho \frac{\partial Y}{\partial r} \rangle = \langle \rho \left(\cos(\theta)\frac{\partial Y}{\partial x_1} + \sin(\theta)\frac{\partial Y}{\partial x_2} \right) \rangle$

92) $\langle \rho \left(\frac{\partial Y}{\partial r} \right)^2 \rangle = \langle \rho \left[\cos(\theta)^2 \left(\frac{\partial Y}{\partial x_1} \right)^2 + \sin(\theta)^2 \left(\frac{\partial Y}{\partial x_2} \right)^2 + \sin(2\theta)\frac{\partial Y}{\partial x_1}\frac{\partial Y}{\partial x_2} \right] \rangle$

93) $\langle \frac{\rho}{r}\frac{\partial Y}{\partial \theta}\rangle = \langle \rho\left(-\sin(\theta)\frac{\partial Y}{\partial x_1}+\cos(\theta)\frac{\partial Y}{\partial x_2}\right)\rangle$

94) $\langle \rho\left(\frac{1}{r}\frac{\partial Y}{\partial \theta}\right)^2\rangle = \langle \rho\left[\sin(\theta)^2\left(\frac{\partial Y}{\partial x_1}\right)^2+\cos(\theta)^2\left(\frac{\partial Y}{\partial x_2}\right)^2-\sin(2\theta)\frac{\partial Y}{\partial x_1}\frac{\partial Y}{\partial x_2}\right]\rangle$

95) $\langle \rho\frac{\partial Y}{\partial z}\rangle$

96) $\langle \rho\left(\frac{\partial Y}{\partial z}\right)^2\rangle$.

C.3.2 Derived Quantities

C.3.2.1 Quantities Depending on (r,t)

From the basic shell-averaged derived previously contained in `Stats?.dat` at a time t corresponding to the iteration `?`, other interesting averages can be derived for each shell of radius r. The post-processing is achieved through the file `parseStats.cpp` In particular, two variances can be defined:

$$\mathrm{Var}(Q) \equiv \langle Q'^2\rangle = \langle Q^2\rangle - \langle Q\rangle^2, \tag{C.1a}$$

$$\mathrm{Var}_\rho(Q) \equiv \widetilde{Q''^2} = \widetilde{Q^2} - \tilde{Q}^2 = \frac{\langle \rho Q^2\rangle}{\langle\rho\rangle} - \frac{\langle \rho Q\rangle^2}{\langle\rho\rangle^2}. \tag{C.1b}$$

97) $\mathrm{Var}(\rho)$

98) $\mathrm{Var}(u_r)$

99) $\mathrm{Var}_\rho(u_r)$

100) $\mathrm{Var}(u_\theta)$

101) $\mathrm{Var}_\rho(u_\theta)$

102) $\mathrm{Var}(u_z)$

103) $\mathrm{Var}_\rho(u_z)$

104) $\mathrm{Var}(M)$

105) $\mathrm{Var}(p)$

106) $\mathrm{Var}(T)$

107) $\mathrm{Var}(c)$

108) $\mathrm{Var}(Y)$, note that $\mathrm{Var}(\psi) = \frac{1}{4}\mathrm{Var}(Y)$

109) $\mathrm{Var}_\rho(Y)$, similarly $\mathrm{Var}_\rho(\psi) = \frac{1}{4}\mathrm{Var}_\rho(Y)$

110) $1-\langle Y\rangle^2$, integrate over r to compute entrainment length

111) $1 - \langle Y^2 \rangle$, integrate over r to compute mixing length

112) $\mathrm{Var}(X)$

113) $\mathrm{Var}_\rho(X)$

114) $1 - \langle X \rangle^2$, integrate over r to compute entrainment length

115) $1 - \langle X^2 \rangle$, integrate over r to compute mixing length

116) $KE \equiv \frac{1}{2}\left(\langle \rho u_r^2 \rangle + \langle \rho u_\theta^2 \rangle + \langle \rho u_z^2 \rangle\right)$

117) $\langle K \rangle \equiv \frac{1}{2}\left(\mathrm{Var}_\rho(u_r) + \mathrm{Var}_\rho(u_\theta) + \mathrm{Var}_\rho(u_z)\right)$, resolved turbulent kinetic energy

118) $\langle k \rangle \equiv \frac{\langle \tau_{ii} \rangle}{2\langle \rho \rangle}$, subgrid turbulent kinetic energy (per unit mass)

119) $K \equiv \langle K \rangle + \langle k \rangle$, total turbulent kinetic energy

120) $u' = \sqrt{\frac{2K}{3}}$, turbulent intensity

121) $M_t = \frac{u'}{\langle c \rangle}$

122) $\langle \varepsilon_{res} \rangle \equiv \frac{1}{\langle \rho \rangle}\left(\langle d_{ij} S_{ij} \rangle - \langle d_{ij} \rangle \langle S_{ij} \rangle\right)$, resolved turbulent dissipation

123) $\langle \varepsilon_{sgs} \rangle \equiv -\frac{1}{\langle \rho \rangle}\left(\langle \tau_{ij} S_{ij} \rangle - \langle \tau_{ij} \rangle \langle S_{ij} \rangle\right)$, subgrid energy transfer

124) $\langle \varepsilon \rangle \equiv \langle \varepsilon_{res} \rangle + \langle \varepsilon_{sgs} \rangle$, turbulent dissipation

125) $\ell = \frac{u'^3}{\langle \varepsilon \rangle}$, turbulence integral scale

126) $Re_\ell = \frac{u' \ell}{\langle \nu \rangle}$, turbulent Reynolds number

127) $t_\ell = \frac{\ell}{u'}$

128) $\lambda_r = \sqrt{\frac{\mathrm{Var}_\rho(u_r)}{\mathrm{Var}_\rho(S_{rr})}}$, Taylor microscale in the r-direction

129) $Re_{\lambda_r} = \frac{\sqrt{\mathrm{Var}_\rho(u_r)}\lambda_r}{\langle \nu \rangle}$, Taylor-scale Reynolds number in the r-direction

130) $\lambda_\theta = \sqrt{\frac{\mathrm{Var}_\rho(u_\theta)}{\mathrm{Var}_\rho(S_{\theta\theta})}}$, Taylor microscale in the θ-direction

131) $Re_{\lambda_\theta} = \frac{\sqrt{\mathrm{Var}_\rho(u_\theta)}\lambda_\theta}{\langle \nu \rangle}$, Taylor-scale Reynolds number in the θ-direction

132) $\lambda_z = \sqrt{\frac{\mathrm{Var}_\rho(u_z)}{\mathrm{Var}_\rho(S_{zz})}}$, Taylor microscale in the z-direction

133) $Re_{\lambda_z} = \frac{\sqrt{\mathrm{Var}_\rho(u_z)}\lambda_z}{\langle \nu \rangle}$, Taylor-scale Reynolds number in the z-direction

134) $\lambda_{\theta z} = \frac{\lambda_\theta + \lambda_z}{2}$

135) $Re_{\lambda_{\theta z}} = \frac{Re_{\lambda_\theta} + Re_{\lambda_z}}{2}$

136) $\lambda_T = \sqrt{\frac{15\langle\nu\rangle}{\langle\varepsilon\rangle}}u'$, Taylor microscale

137) $Re_{\lambda_T} = \frac{u'\lambda_T}{\langle\nu\rangle}$, Taylor-scale Reynolds number

138) $\langle\varepsilon^Y_{res}\rangle = \langle D\rangle\left(\langle\frac{\partial Y}{\partial x_j}\frac{\partial Y}{\partial x_j}\rangle - \langle\frac{\partial Y}{\partial x_j}\rangle\langle\frac{\partial Y}{\partial x_j}\rangle\right)$, resolved scalar dissipation, where $D = \nu/Sc$

139) $\langle\varepsilon^Y_{sgs}\rangle = \langle f^Y_i\frac{\partial Y}{\partial x_i}\rangle - \langle f^Y_i\rangle\langle\frac{\partial Y}{\partial x_i}\rangle$, subgrid scalar dissipation

140) $\langle\varepsilon^Y\rangle \equiv \langle\varepsilon^Y_{res}\rangle + \langle\varepsilon^Y_{sgs}\rangle$, total turbulent scalar dissipation

141) $\lambda_{Y_r} = \sqrt{\frac{\mathrm{Var}_\rho(Y)}{\mathrm{Var}_\rho(\frac{\partial Y}{\partial r})}}$, scalar Taylor microscale in the r-direction

142) $\lambda_{Y_\theta} = \sqrt{\frac{\mathrm{Var}_\rho(Y)}{\mathrm{Var}_\rho(\frac{1}{r}\frac{\partial Y}{\partial\theta})}}$, scalar Taylor microscale in the θ-direction

143) $\lambda_{Y_z} = \sqrt{\frac{\mathrm{Var}_\rho(Y)}{\mathrm{Var}_\rho(\frac{\partial Y}{\partial z})}}$, scalar Taylor microscale in the z-direction

144) $\eta_r = \left(\frac{\langle\nu\rangle^3}{\angle\varepsilon_r\rangle}\right)^{1/4}$, Kolmogorov scale in the r-direction, where $\angle\varepsilon_r\rangle = \frac{1}{\langle\rho\rangle^2}\left(\langle\rho\sigma_{rr}S_{rr}\rangle - \langle\sigma_{rr}\rangle\langle\rho S_{rr}\rangle\right)$ is the (resolved+sgs) turbulent r-dissipation

145) $\eta_\theta = \left(\frac{\langle\nu\rangle^3}{\angle\varepsilon_\theta\rangle}\right)^{1/4}$, Kolmogorov scale in the θ-direction, where $\angle\varepsilon_\theta\rangle = \frac{1}{\langle\rho\rangle^2}\left(\langle\rho\sigma_{\theta\theta}S_{\theta\theta}\rangle - \langle\sigma_{\theta\theta}\rangle\langle\rho S_{\theta\theta}\rangle\right)$ is the (resolved+sgs) turbulent θ-dissipation

146) $\eta_z = \left(\frac{\langle\nu\rangle^3}{\angle\varepsilon_z\rangle}\right)^{1/4}$, Kolmogorov scale in the z-direction, where $\angle\varepsilon_z\rangle = \frac{1}{\langle\rho\rangle^2}\left(\langle\rho\sigma_{zz}S_{zz}\rangle - \langle\sigma_{zz}\rangle\langle\rho S_{zz}\rangle\right)$ is the (resolved+sgs) turbulent z-dissipation

147) $\eta_{\theta z} = \frac{\eta_\theta + \eta_z}{2}$

148) $\eta = \left(\frac{\langle\nu\rangle^3}{\langle\varepsilon\rangle}\right)^{1/4}$, Kolmogorov scale

149) $b = -\langle\rho'\nu'_\rho\rangle = -1 + \langle\rho\rangle\langle\nu_\rho\rangle$, density self-correlation

150) $\widetilde{u}_r$

151) $\widetilde{u}_\theta$

152) $\widetilde{u}_z$

153) $a_r = \frac{\langle\rho' u'_r\rangle}{\langle\rho\rangle} = \widetilde{u}_r - \langle u_r\rangle$, turbulent mass flux

154) $a_\theta = \frac{\langle\rho' u'_\theta\rangle}{\langle\rho\rangle} = \widetilde{u}_\theta - \langle u_\theta\rangle$

155) $a_z = \frac{\langle\rho' u'_z\rangle}{\langle\rho\rangle} = \widetilde{u}_z - \langle u_z\rangle$

156) $R_{rr} = \langle\rho\rangle\mathrm{Var}_\rho(u_r)$

157) $R_{\theta\theta} = \langle\rho\rangle\mathrm{Var}_\rho(u_\theta)$

158) $R_{r\theta} = \langle\rho u_r u_\theta\rangle - \frac{\langle\rho u_r\rangle\langle\rho u_\theta\rangle}{\langle\rho\rangle}$

159) $R_{rz} = \langle \rho u_r u_z \rangle - \frac{\langle \rho u_r \rangle \langle \rho u_z \rangle}{\langle \rho \rangle}$

160) $\langle \rho \, |\boldsymbol{u}''|^2 u_r'' \rangle = \langle \rho u_i u_i u_r \rangle + \langle \rho \rangle \widetilde{u}_i \widetilde{u}_i \widetilde{u}_r - 2\langle u_r u_i \rangle \widetilde{u}_i - 2\langle K \rangle \langle \rho \rangle \widetilde{u}_r$

161) $\langle \nu_\rho' u_r' \rangle = \langle \nu_\rho u_r \rangle - \langle \nu_\rho \rangle \langle u_r \rangle$

162) $\langle \nu_\rho' \nabla \cdot \boldsymbol{u}' \rangle = \langle \nu_\rho S_{ii} \rangle - \langle \nu_\rho \rangle \langle S_{ii} \rangle$

163) $\langle p' u_r' \rangle = \langle p u_r \rangle - \langle p \rangle \langle u_r \rangle$

164) $\langle p' \nabla \cdot \boldsymbol{u}' \rangle = \langle p S_{ii} \rangle - \langle p \rangle \langle S_{ii} \rangle$

165) $\langle \boldsymbol{\sigma}' : \nabla \boldsymbol{u}' \rangle = \langle \rho \rangle \langle \varepsilon \rangle$

166) $\langle \sigma_{rr}' u_r' \rangle = \langle \sigma_{rr} u_r \rangle - \langle \sigma_{rr} \rangle \langle u_r \rangle$

167) $\langle \sigma_{r\theta}' u_\theta' \rangle = \langle \sigma_{r\theta} u_\theta \rangle - \langle \sigma_{r\theta} \rangle \langle u_\theta \rangle$

168) $\langle \sigma_{rz}' u_z' \rangle = \langle \sigma_{rz} u_z \rangle - \langle \sigma_{rz} \rangle \langle u_z \rangle$

169) $\langle \sigma_{\theta\theta} \rangle = \langle \sigma_{11} \rangle + \langle \sigma_{22} \rangle - \langle \sigma_{rr} \rangle$

170) $\langle \nabla \cdot \boldsymbol{u} \rangle = \langle S_{ii} \rangle$

171) $\langle \nu_\rho' \frac{\partial p'}{\partial r} \rangle = \langle \nu_\rho \frac{\partial p}{\partial r} \rangle - \langle \nu_\rho \rangle \frac{\partial \langle p \rangle}{\partial r}$

172) $\langle u_r' \nabla \cdot \boldsymbol{u}' \rangle = \langle u_r S_{ii} \rangle - \langle u_r \rangle \langle S_{ii} \rangle$.

C.3.2.2 Quantities Depending on t Only and Based on the Mass Fraction Y

Quantities depending only on t and based on the mass fraction Y are computed:

1) t , time

2) $TKE_{vol}(t) = \frac{1}{rd - rdi} \int_{rdi}^{rd} K \mathrm{d}r$, volume-averaged total turbulent kinetic energy (actually this is not based on the mass fraction analysis but it was coded together with the following quantities)

3) $\delta(t) \equiv P_m(t) = \int_{rdi}^{rd} (1 - \langle Y \rangle^2) \mathrm{d}r$, mixing zone width (entrainment length)

4) $P_t(t) = \int_{rdi}^{rd} (1 - \langle Y^2 \rangle) \mathrm{d}r$, mixing length

5) $\Xi(t) = \frac{P_t}{P_m}$, mixing parameter (relative amount of molecularly mixed fluid within the TMZ)

6) $r_c(t) = \frac{1}{\delta_{mz}} \int_{rdi}^{rd} r(1 - \langle Y \rangle^2) \mathrm{d}r$, average radius of the center of the mixing zone

7) $r_b(t) = r_c - \frac{1}{4}\delta$, bubble average position ($\sim 73.1\%$ SF_6 in mass)

8) $r_s(t) = r_c + \frac{1}{4}\delta$, spike average position ($\sim 73.1\%$ Air in mass)

9) $V(t) = \alpha \delta r_c$, volume of the mixing zone (per unit z-length), where α is the angle of the wedge

10) $E(t) = \frac{r_c^2 - r_b^2}{r_s^2 - r_c^2}$, entrainment ratio

11) $Y_E(t) = \frac{E}{1+E}$, mean composition if all entrained fluid was homogeneously mixed

12) $\ell(t) = \ell(r_c(t), t)$

13) $Re_\ell(t) = Re_\ell(r_c(t), t)$

14) $\lambda_r(t) = \lambda_r(r_c(t), t)$

15) $Re_{\lambda_r}(t) = Re_{\lambda_r}(r_c(t), t)$

16) $\lambda_\theta(t) = \lambda_\theta(r_c(t), t)$

17) $Re_{\lambda_\theta}(t) = Re_{\lambda_\theta}(r_c(t), t)$

18) $\lambda_z(t) = \lambda_z(r_c(t), t)$

19) $Re_{\lambda_z}(t) = Re_{\lambda_z}(r_c(t), t)$

20) $\lambda_{\theta z}(t) = \lambda_{\theta z}(r_c(t), t)$

21) $Re_{\lambda_{\theta z}}(t) = Re_{\lambda_{\theta z}}(r_c(t), t)$

22) $\lambda_T(t) = \lambda_T(r_c(t), t)$

23) $Re_{\lambda_T}(t) = Re_{\lambda_T}(r_c(t), t)$

24) $\lambda_{Y_r}(t) = \lambda_{Y_r}(r_c(t), t)$

25) $\lambda_{Y_\theta}(t) = \lambda_{Y_\theta}(r_c(t), t)$

26) $\lambda_{Y_z}(t) = \lambda_{Y_z}(r_c(t), t)$

27) $\eta_r(t) = \eta_r(r_c(t), t)$

28) $\eta_\theta(t) = \eta_\theta(r_c(t), t)$

29) $\eta_z(t) = \eta_z(r_c(t), t)$

30) $\eta_{\theta z}(t) = \eta_{\theta z}(r_c(t), t)$

31) $\eta(t) = \eta(r_c(t), t)$

32) $\dot{\delta}(t) = 2(\langle u_r \rangle(r_s(t), t) - \langle u_r \rangle(r_b(t), t))$ growth rate (depends on the definition of r_b and r_s)

33) $Re_\delta(t) = \frac{\delta \dot{\delta}}{\nu_c}$, outer-scale Reynolds number, where $\nu_c = \langle \nu \rangle(r_c, t)$ is the shell-averaged viscosity at the center of the mixing zone

34) $r_c^{\%}(t) = \frac{1}{2}(r_b^{\%} + r_s^{\%})$, average radius of the center of the mixing zone

35) $r_b^{\%}(t) = \{r|\langle Y\rangle(r,t) = 1-\epsilon\}$, bubble average position ($(1-\epsilon)\%$ SF_6 in mass)

36) $r_s^{\%}(t) = \{r|\langle Y\rangle(r,t) = \epsilon\}$, spike average position ($(1-\epsilon)\%$ Air in mass)

37) $\delta^{\%}(t) = r_s^{\%} - r_b^{\%}$, mixing zone width

38) $V^{\%}(t) = \alpha\delta^{\%}r_c^{\%}$, volume of the mixing zone (per unit z-length), where α is the angle of the wedge

39) $E^{\%}(t) = \frac{r_c^{\%2} - r_b^{\%2}}{r_s^{\%2} - r_c^{\%2}}$, entrainment ratio

40) $Y_E^{\%}(t) = \frac{E^{\%}}{1+E^{\%}}$, mean composition if all entrained fluid was homogeneously mixed

41) $\dot{\delta}^{\%}(t) = \langle u_r\rangle(r_s^{\%}(t),t) - \langle u_r\rangle(r_b^{\%}(t),t)$ growth rate (depends on the definition of $r_b^{\%}$ and $r_s^{\%}$)

42) $Re_{\delta^{\%}}(t) = \frac{\delta^{\%}\dot{\delta}^{\%}}{\nu_c^{\%}}$, outer-scale Reynolds number, where $\nu_c^{\%} = \langle\nu\rangle(r_c^{\%},t)$ is the shell-averaged viscosity at the center of the mixing zone.

C.3.2.3 Quantities Depending on t Only and Based on the Mol Fraction X

A similar list of quantities based on the mol fraction X is:

1) t , time

2) $TKE_{vol}(t) = \frac{1}{rd-rdi}\int_{rdi}^{rd} K\mathrm{d}r$, volume-averaged total turbulent kinetic energy

3) $\delta(t) \equiv P_m(t) = \int_{rdi}^{rd}(1-\langle X\rangle^2)\mathrm{d}r$, mixing zone width (entrainment length)

4) $P_t(t) = \int_{rdi}^{rd}(1-\langle X^2\rangle)\mathrm{d}r$, mixing length

5) $\Xi(t) = \frac{P_t}{P_m}$, mixing parameter (relative amount of molecularly mixed fluid within the TMZ)

6) $r_c(t) = \frac{1}{\delta_{mz}}\int_{rdi}^{rd} r(1-\langle X\rangle^2)\mathrm{d}r$, average radius of the center of the mixing zone

7) $r_b(t) = r_c - \frac{1}{4}\delta$, bubble average position ($\sim 73.1\%$ SF_6 in mol)

8) $r_s(t) = r_c + \frac{1}{4}\delta$, spike average position ($\sim 73.1\%$ Air in mol)

9) $V(t) = \alpha\delta r_c$, volume of the mixing zone (per unit z-length), where α is the angle of the wedge

10) $E(t) = \frac{r_c^2 - r_b^2}{r_s^2 - r_c^2}$, entrainment ratio

11) $X_E(t) = \frac{E}{1+E}$, mean composition if all entrained fluid was homogeneously mixed

12) $\ell(t) = \ell(r_c(t),t)$

13) $Re_\ell(t) = Re_\ell(r_c(t),t)$

14) $\lambda_r(t) = \lambda_r(r_c(t),t)$

15) $Re_{\lambda_r}(t) = Re_{\lambda_r}(r_c(t), t)$

16) $\lambda_\theta(t) = \lambda_\theta(r_c(t), t)$

17) $Re_{\lambda_\theta}(t) = Re_{\lambda_\theta}(r_c(t), t)$

18) $\lambda_z(t) = \lambda_z(r_c(t), t)$

19) $Re_{\lambda_z}(t) = Re_{\lambda_z}(r_c(t), t)$

20) $\lambda_{\theta z}(t) = \lambda_{\theta z}(r_c(t), t)$

21) $Re_{\lambda_{\theta z}}(t) = Re_{\lambda_{\theta z}}(r_c(t), t)$

22) $\lambda_T(t) = \lambda_T(r_c(t), t)$

23) $Re_{\lambda_T}(t) = Re_{\lambda_T}(r_c(t), t)$

24) $\lambda_{Y_r}(t) = \lambda_{Y_r}(r_c(t), t)$

25) $\lambda_{Y_\theta}(t) = \lambda_{Y_\theta}(r_c(t), t)$

26) $\lambda_{Y_z}(t) = \lambda_{Y_z}(r_c(t), t)$

27) $\eta_r(t) = \eta_r(r_c(t), t)$

28) $\eta_\theta(t) = \eta_\theta(r_c(t), t)$

29) $\eta_z(t) = \eta_z(r_c(t), t)$

30) $\eta_{\theta z}(t) = \eta_{\theta z}(r_c(t), t)$

31) $\eta(t) = \eta(r_c(t), t)$

32) $\dot{\delta}(t) = 2(\langle u_r \rangle(r_s(t), t) - \langle u_r \rangle(r_b(t), t))$ growth rate (depends on the definition of r_b and r_s)

33) $Re_\delta(t) = \frac{\delta\dot{\delta}}{\nu_c}$, outer-scale Reynolds number, where $\nu_c = \langle \nu \rangle(r_c, t)$ is the shell-averaged viscosity at the center of the mixing zone

34) $r_c^{\%}(t) = \frac{1}{2}(r_b^{\%} + r_s^{\%})$, average radius of the center of the mixing zone

35) $r_b^{\%}(t) = \{r | \langle X \rangle(r, t) = 1 - \epsilon\}$, bubble average position ($(1-\epsilon)\%$ SF_6 in mol)

36) $r_s^{\%}(t) = \{r | \langle X \rangle(r, t) = \epsilon\}$, spike average position ($(1-\epsilon)\%$ Air in mol)

37) $\delta^{\%}(t) = r_s^{\%} - r_b^{\%}$, mixing zone width

38) $V^{\%}(t) = \alpha\delta^{\%}r_c^{\%}$, volume of the mixing zone (per unit z-length), where α is the angle of the wedge

39) $E^{\%}(t) = \frac{r_c^{\%2} - r_b^{\%2}}{r_s^{\%2} - r_c^{\%2}}$, entrainment ratio

40) $X_E^{\%}(t) = \frac{E^{\%}}{1+E^{\%}}$, mean composition if all entrained fluid was homogeneously mixed

41) $\dot{\delta}^{\%}(t) = \langle u_r \rangle(r_s^{\%}(t), t) - \langle u_r \rangle(r_b^{\%}(t), t)$ growth rate (depends on the definition of $r_b^{\%}$ and $r_s^{\%}$)

42) $Re_{\delta^{\%}}(t) = \frac{\delta^{\%}\dot{\delta}^{\%}}{\nu_c^{\%}}$, outer-scale Reynolds number, where $\nu_c^{\%} = \langle \nu \rangle(r_c^{\%}, t)$ is the shell-averaged viscosity at the center of the mixing zone.

C.4 Two-Dimensional Statistics For Spectrum, P.d.f., Subgrid Continuation...

This section concerns quantities interpolated (without averaging) over particular shells of radii r, at time t, therefore depending on (θ, z) only. The post-processing is done in the file `parseSpectrum.cpp`.

1) ρ

2) u_r

3) u_θ

4) u_z

5) Y (or ψ)

6) $\frac{\nu}{|\widetilde{a}_S|}$

7) $e3_x$

8) $e3_y$

9) $e3_z$

10) $\frac{\nu}{|\widetilde{a}_\omega|}$

11) o_x

12) o_y

13) o_z

14) λ

15) $\mathsf{K}_0 \varepsilon^{2/3}$

16) K_Y

17) σ_Y^2

18) $\boldsymbol{\omega} \cdot \boldsymbol{\omega}$, enstrophy.

We deduce from these (θ, z) two-dimensional data obtained on shell of given radius r:

1) Spectra at the center of the TMZ and at the spike and bubble average radii

2) P.d.f. of the joint-density mass fraction Y at the center of the TMZ and at the spike and bubble average radii

3) P.d.f. of the joint-density mol fraction X at the center of the TMZ and at the spike and bubble average radii

4) $Y_M(t) = \frac{\int_{rdi}^{rd} Y_m p_m \mathrm{d}r}{\int_{rdi}^{rd} p_m \mathrm{d}r}$, mixed-fluid composition averaged over the entire mixing zone, where $Y_m(r,t) = \frac{\int_{-1+2\epsilon}^{1-2\epsilon} Y p_Y \mathrm{d}Y}{p_m}$ is the mixed-fluid composition on the shell r, $p_m(r,t) = \int_{-1+2\epsilon}^{1-2\epsilon} p_Y \mathrm{d}Y$ probability of finding mixed fluid on the shell r, $p_Y(Y;r,t)$ p.d.f. of Y over the shell r. The threshold $\psi = \epsilon$ corresponds to ϵ percent SF_6 (in mass)

5) $X_M(t) = \frac{\int_{rdi}^{rd} X_m p_m \mathrm{d}r}{\int_{rdi}^{rd} p_m \mathrm{d}r}$, mixed-fluid composition averaged over the entire mixing zone, where $X_m(r,t) = \frac{\int_{-1+2\epsilon}^{1-2\epsilon} X p_X \mathrm{d}X}{p_m}$ is the mixed-fluid composition on the shell r, $p_m(r,t) = \int_{-1+2\epsilon}^{1-2\epsilon} p_X \mathrm{d}X$ probability of finding mixed fluid on the shell r, $p_X(X;r,t)$ p.d.f. of X over the shell r. Same definition of ϵ but in mol

6) P.d.f. of alignment angles at the center of the TMZ and at the spike and bubble average radius.

Bibliography

[1] Arnett, D., Bahcall, J. N., Kirshner, R. P., and Woosler, S. E. Supernova 1987A. *Annu. Rev. Astron. Astrophys. 27* (1989), 629–700.

[2] Bell, G. I. Taylor instability on cylinders and spheres in small amplitude approximation. *Los Alamos Scientific Laboratory Report LA-1321* (1951).

[3] Berger, M. J., and Colella, P. Local adaptive mesh refinement for shock hydrodynamics. *J. Comp. Phys. 82*, 1 (1989), 64–84.

[4] Berger, M. J., and Oliger, J. Adaptive mesh refinement for hyperbolic partial-differential equations. *J. Comp. Phys. 53*, 3 (1984), 484–512.

[5] Berthoud, G. Vapor explosions. *Annu. Rev. Fluid Mech. 32* (2000), 573–611.

[6] Blaisdell, G. A. *Numerical simulation of compressible homogeneous turbulence.* PhD thesis, Stanford University, 1991.

[7] Briscoe, M. G., and Kovitz, A. A. Experimental and theoretical study of the stability of plane shock waves reflected normally from a perturbed flat wall. *J. Fluid Mech. 31* (1968), 529–546.

[8] Brode, H. L. Numerical solutions of spherical blast waves. *J. Appl. Phys. 26* (1955), 766–775.

[9] Brouillette, M. *On the interaction of shock waves with contact surfaces between gases of different densities.* PhD thesis, California Institute of Technology, 1989.

[10] Brouillette, M. The Richtmyer–Meshkov instability. *Annu. Rev. Fluid Mech. 34* (2002), 445–468.

[11] Cabot, W. Comparison of two- and three-dimensional simulations of miscible Rayleigh–Taylor instability. *Phys. Fluids 18*, 4 (2006), 045101.

[12] Cabot, W. H., Cook, A. W., Miller, P. L., Laney, D., Miller, M. C., and Childs, H. Large-eddy simulation of Rayleigh–Taylor instability. *Phys. Fluids 17*, 9 (2005), 091106.

[13] Chester, W. The quasi-cylindrical shock tube. *Phil. Mag. 45* (1954), 1293–1301.

[14] Chisnell, R. F. The normal motion of a shock wave through a nonuniform one-dimensional medium. *Proc. R. Soc. Lond. 232* (1955), 350–370.

[15] Chisnell, R. F. An analytic description of converging shock waves. *J. Fluid Mech. 354* (1998), 357–375.

[16] Cohen, R. H., Dannevik, W. P., Dimits, A. M., Eliason, D. E., Mirin, A. A., Zhou, Y., Porter, D. H., and Woodward, P. R. Three-dimensional simulation of a Richtmyer–Meshkov instability with a two-scale initial perturbation. *Phys. Fluids 14*, 10 (2002), 3692–3709.

[17] Collins, B. D., and Jacobs, J. W. PLIF flow visualization and measurements of the Richtmyer-Meshkov instability of an air/SF_6 interface. *J. Fluid Mech. 464* (2002), 113–136.

[18] Cook, A. W., Cabot, W., and Miller, P. L. The mixing transition in Rayleigh–Taylor instability. *J. Fluid Mech. 511* (2004), 333–362.

[19] Cook, A. W., and Dimotakis, P. E. Transition stages of Rayleigh–Taylor instability between miscible fluids. *J. Fluid Mech. 443* (2001), 69–99.

[20] Da Prato, G., and Debussche, A. Ergodicity for the 3D stochastic NavierStokes equations. *J. Math. Pures Appl. 82* (2003), 877–947.

[21] Deiterding, R. Construction and application of an AMR algorithm for distributed memory computers. In *Adaptive Mesh Refinement – Theory and Applications* (2005), T. Plewa, T. Linde, and V. G. Weirs, Eds., vol. 41 of *Lecture Notes in Computational Science and Engineering*, Springer, pp. 361–372.

[22] Deiterding, R., Radovitzky, R., Mauch, S. P., Noels, L., Cummings, J. C., and Meiron, D. I. A Virtual Test Facility for the efficient simulation of solid material response under strong shock and detonation wave loading. *Engineering with Computers 22*, 3–4 (2006), 325–347.

[23] Dimotakis, P. E. The mixing transition in turbulent flows. *J. Fluid Mech. 409* (2000), 69–97.

[24] Dimotakis, P. E., and Samtaney, R. Planar shock cylindrical focusing by a perfect-gas lens. *Physics of Fluids 18*, 3 (2006), 031705.

[25] Duong, D. Q., and Milton, B. E. The Mach-reflection of shock waves in converging cylindrical channels. *Exp. Fluids 3*, 3 (1985), 161–168.

[26] Dýakov, S. P. The interaction of shock waves with small perturbations. *J. Exptl.-Theoret. Phys. (USSR). 33*, 4 (1957), 948–974.

[27] Eliasson, V., Apazidis, N., Tillmark, N., and Lesser, M. B. Focusing of strong shocks in an annular shock tube. *Shock Waves 15*, 3-4 (2006), 205–217.

[28] Erez, L., Sadot, O., Oron, D., Erez, G., Levin, L. A., Shvarts, D., and Ben-Dor, G. Study of the membrane effect on turbulent mixing measurements in shock tubes. *Shock Waves 10*, 4 (2000), 241–251.

[29] Evans, A. K. Instability of converging shock waves and sonoluminescence. *Phys. Rev. E 54*, 10 (1996), 5004–5011.

[30] Fedkiw, R. P., Aslam, T., Merriman, B., and Osher, S. A non-oscillatory Eulerian approach to interfaces in multimaterial flows (the ghost fluid method). *J. Comput. Phys. 152*, 2 (1999), 457–492.

[31] Fraley, G. Rayleigh–Taylor stability for a normal shock wave-density discontinuity interaction. *Phys. Fluids 29*, 2 (1986), 376–386.

[32] Frost, D. L. Dynamics of explosive boiling of a droplet. *Phys. Fluids 31*, 9 (1988), 2554–2561.

[33] Fryxell, B., Müller, E., and Arnett, D. Instabilities and clumping in SN 1987A. I. Early evolution in two dimensions. *Astrophys. J. 1991* (1984), 619–634.

[34] Ghosal, S. An analysis of numerical errors in large-eddy simulations of turbulence. *J. Comput. Phys. 125*, 1 (1996), 187–206.

[35] Ghosal, S. Mathematical and physical constraints on large-eddy simulation of turbulence. *AIAA J. 37*, 4 (1999), 425–433.

[36] Glendinning, S. G., Bolstad, J., Braun, D. G., Edwards, M. J., Hsing, W. W., Lasinski, B. F., Louis, H., Miles, A., Moreno, J., Peyser, T. A., Remington, B. A., Robey, H. F., Turano, E. J., Verdon, C. P., and Zhou, Y. Effect of shock proximity on Richtmyer–Meshkov growth. *Phys. Plasmas 10*, 5 (2003), 1931–1936.

[37] Gottlieb, S., Shu, C.-W., and Tadmor, E. Strong stability-preserving high-order time discretization methods. *SIAM Rev. 43*, 1 (2001), 89–112.

[38] Greenough, J. A., and Burke, E. The effect of initial conditions on late time asymptotics and mixing for multimode Richtmyer-Meshov instability. In *Proceedings of the Ninth International Workshop on the Physics of Compressible Turbulent Mixing* (2004), Cambridge Univ Press.

[39] Griffond, J. Linear interaction analysis for Richtmyer–Meshkov instability at low Atwood numbers. *Phys. Fluids 18*, 5 (2006), 054106.

[40] Guderley, G. Starke Kugelige und zylindrische Verdichtungsstösse in der Nähe des Kugelmittelpunktes bzw der Zylinderachse. *Luftfahrtforschung 19* (1942), 302–312.

[41] Hafner, P. Strong convergent shock waves near the center of convergence: a power series solution. *SIAM J. Appl. Maths 48*, 6 (1988), 1244–1261.

[42] Hecht, J., Alon, U., and Shvarts, D. Potential flow models of Rayleigh–Taylor and Richtmyer–Meshkov bubble fronts. *Phys. Fluids 6*, 12 (1994), 4019–4030.

[43] Hill, D. J., Pantano, C., and Pullin, D. I. Large-eddy simulation and multi-scale modeling of Richtmyer–Meshkov instability with reshock. *J. Fluid Mech. 557* (2006), 29–61.

[44] Hill, D. J., and Pullin, D. I. Hybrid tuned center-difference-WENO method for large eddy simulations in the presence of strong shocks. *J. Comput. Phys. 194*, 2 (2004), 435–450.

[45] Holder, D. A., Smith, A. V., Barton, C. J., and Youngs, D. L. Mix experiments using a two-dimensional convergent shock-tube. *Laser Part. Beams 21*, 3 (2003), 403–409.

[46] Holmes, R. L., Dimonte, G., Fryxell, B., Gittings, M. L., Grove, J. W., Schneider, M., Sharp, D. H., Velikovich, A. L., Weaver, R. P., and Zhang, Q. Richtmyer–Meshkov instability growth: experiment, simulation and theory. *J. Fluid Mech. 389* (1999), 55–79.

[47] Honein, A. E., and Moin, P. Higher entropy conservation and numerical stability of compressible turbulence simulations. *J. Comput. Phys. 201*, 2 (2004), 531–545.

[48] Hornung, H. G., Pullin, D. I., and Ponchaut, N. On the question of universality of imploding shock waves. *Accepted by Acta Mechanica* (In Press 2008).

[49] Hosseini, H. R., Onodera, O., and Takayama, K. Stability of converging cylindrical shock waves in a vertical annular co-axial diaphragmless shock tube. *Trans. Jpn. Soc. Aeronaut. Space Sci. 42*, 135 (1999), 19–26.

[50] Hosseini, S. H. R., and Takayama, K. Experimental study of Richtmyer–Meshkov instability induced by cylindrical shock waves. *Phys. Fluids 17*, 8 (2005), 084101.

[51] Howard, D., and Sturtevant, B. In vitro study of the mechanical effects of shock-wave lithotripsy. *Ultrasound Med. Biol. 23* (1997), 1107–1122.

[52] Hsing, W. W., and Hoffman, N. M. Measurement of feedthrough and instability growth in radiation-driven cylindrical implosions. *Phys. Rev. Lett. 78*, 20 (1997), 3876–3879.

[53] Hurricane, O. A., Burke, E., Maples, S., and Viswanathan, M. Saturation of Richtmyer's impulsive model. *Phys. Fluids 12*, 8 (2000), 2148–2151.

[54] Jacobs, J. W., and Krivets, V. V. Experiments on the late-time development of single-mode Richtmyer–Meshkov instability. *Phys. Fluids 17* (2005), 034105.

[55] Jones, M. A., and Jacobs, J. W. A membraneless experiment for the study of Richtmyer–Meshkov instability of a shock-accelerated gas interface. *Phys. Fluids 9*, 10 (1997), 3078–3085.

[56] Jun, B., Jones, T. W., and Norma, M. L. Interaction of Rayleigh–Taylor fingers and circumstellar cloudlets in young supernova remnants. *Astrophysical J. 468* (1996), 59–63.

[57] Khokhlov, A. M., Oran, E. S., and Thomas, G. O. Numerical simulation of deflagration-to-detonation transition: the role of shock-flame interactions in turbulent flames. *Combust. Flames 117* (1999), 323–339.

[58] Kosovic, B., Pullin, D. I., and Samtaney, R. Subgrid-scale modeling for large-eddy simulations of compressible turbulence. *Phys. Fluids 14*, 4 (2002), 1511–1522.

[59] Kumar, S., Hornung, H. G., and Sturtevant, B. Growth of shocked gaseous interfaces in a conical geometry. *Phys. Fluids 15*, 10 (2003), 3194–3208.

[60] Landau, L. D., and Lifshitz, E. M. *Fluid Mechanics*, 2nd ed. Pergamon, 1987.

[61] Lanier, N. E., Barnes, C. W., Batha, S. H., Day, R. D., Magelssen, G. R., Scott, J. M., Dunne, A. M., Parker, K. W., and Rothman, S. D. Multimode seeded Richtmyer–Meshkov mixing in a convergent, compressible, miscible plasma system. *Phys. Plasmas 10*, 5 (2003), 1816–1821.

[62] Lappas, T., Leonard, A., and Dimotakis, P. E. Riemann invariant manifolds for the multidimensional Euler equations. *SIAM J. Sci. Comput. 20*, 4 (1999), 1481–1512.

[63] Latini, M., Schilling, O., and Don, W. S. Effects of WENO flux reconstruction order and spatial resolution on reshocked two-dimensional Richtmyer–Meshkov instability. *J. Comput. Phys. 221*, 2 (2007), 805–836.

[64] Lax, P. D., and Wendroff, B. Systems of conservation laws. *Comm. Pure Appl. Math. 13* (1960), 217–237.

[65] Layzer, D. On the gravitational instability of two superposed fluids in a gravitational field. *Astrophys. J. 122* (1955), 1–12.

[66] Legrand, M., and Toque, N. Interface instabilities occurring during an explosive driven implosion. In *Proceedings of the Third International Workshop on the Physics of Compressible Turbulent Mixing* (1991), p. 9.

[67] LeVeque, R. J. Balancing source terms and flux gradients in high-resolution Godunov methods: the quasi-steady wave-propagation algorithm. *J. Comput. Phys. 146*, 1 (1998), 346–365.

[68] LeVeque, R. J. *Finite Volume Methods for Hyperbolic Problems*. Cambridge University Press, 2002.

[69] Lindl, J. D. *Inertial confinement fusion: the quest for ignition and energy gain using indirect drive*. Springer, 1998.

[70] Lindl, J. D., McCrory, R. L., and Campbell, E. M. Progress towards ignition and burn propagation in inertial confinement fusion. *Phys. Today 45* (1992), 32–40.

[71] Lundgren, T. S. Strained spiral vortex model for turbulence fine structure. *Phys. Fluids 25*, 12 (1982), 2193–2203.

[72] Maglieri, D. J., and Plotkin, K. J. *Aeroacoustics of Flight Vehicles*. Acoustical Society of America, 1995.

[73] Maran, S. P., Sonneburn, G., Pun, C. S. J., Lundqvist, P., Iping, R. C., and Gull, T. R. Physical conditions in circumstellar gas surrounding SN 1987A 12 years after outburst. *Astrophys. J. 545* (2000), 390–398.

[74] Matheou, G. *Large-eddy simulation of molecular mixing in a recirculating shear flow*. PhD thesis, Caltech, 2008.

[75] Matsui, N., Mima, K., Honda, M., and Nishiguchi, A. Analysis of rippled shock-wave propagation and ablation-front stability by theory and hydrodynamic simulation. *J. Plasma Phys. 61*, 1 (1999), 43–50.

[76] Mattner, T. W., Pullin, D. I., and Dimotakis, P. E. Large-eddy simulations of miscible Rayleigh-Taylor instability. In *Proceedings of the Ninth International Workshop on the Physics of Compressible Turbulent Mixing* (2004), Cambridge Univ Press, pp. 578–585.

[77] Meshkov, E. E. Instability of the interface of two gases accelerated by a shock wave. *Soviet Fluid Dyn. 4*, 5 (1969), 101–108.

[78] Meshkov, E. E., Nevmerzhitsky, N. V., Rogachev, V. G., and Zhidov, I. G. Turbulent mixing development investigation with converging jelly rings. In *Proceedings of the Fourth*

International Workshop on the Physics of Compressible Turbulent Mixing (1993), P. Linden, D. Youngs, and S. Daniel, Eds., Cambridge Univ Press, pp. 578–585.

[79] Meshkov, E. E., Nevmerzhitsky, N. V., and Zmushko, V. V. On possibilities of investigating hydrodynamic instabilities and turbulent mixing development in spherical geometry. In *The Physics of Compressible Turbulent Mixing* (1997), G. Jourdan and L. Houas, Eds., *Lecture Notes in Computational Science and Engineering*, Impr. Caractère, pp. 343–347.

[80] Mikaelian, K. O. Rayleigh–Taylor and Richtmyer–Meshkov instabilities and mixing in stratified spherical shells. *Phys. Rev. A 42* (1990), 3400–3420.

[81] Mikaelian, K. O. Rayleigh–Taylor and Richtmyer–Meshkov instabilities and mixing in stratified cylindrical shells. *Phys. Fluids 17*, 9 (2005), 094105.

[82] Misra, A., and Pullin, D. I. A vortex-based model for large-eddy simulation. *Phys. Fluids 9*, 8 (1997), 2443–2454.

[83] Pantano, C., Deiterding, R., Hill, D. J., and Pullin, D. I. A low numerical dissipation patch-based adaptive mesh refinement method for large-eddy simulation of compressible flows. *J. Comput. Phys. 221*, 1 (2007), 63–87.

[84] Payne, R. B. A numerical method for a converging cylindrical shock. *J. Fluid Mech. 2* (1957), 185–200.

[85] Peng, G., Zabusky, N. J., and Zhang, S. Vortex-accelerated secondary baroclinic vorticity deposition and late-intermediate time dynamics of a two-dimensional Richtmyer–Meshkov interface. *Phys. Fluids 15*, 12 (2003), 3730–3744.

[86] Plesset, M. S. On the stability of fluid flows with spherical symmetry. *J. Appl. Phys. 25* (1954), 96–98.

[87] Ponchaut, N., Hornung, H. G., Pullin, D. I., and Mouton, C. A. On imploding cylindrical and spherical shock waves in a perfect gas. *J. Fluid Mech. 560* (2006), 103–122.

[88] Pullin, D. I. A vortex-based model for the subgrid flux of a passive scalar. *Phys. Fluids 12*, 9 (2000), 2311–2319.

[89] Pullin, D. I., and Lundgren, T. S. Axial motion and scalar transport in stretched spiral vortices. *Phys. Fluids 13*, 9 (2001), 2553–2563.

[90] Putterman, S. J. Sonoluminescence-sound into light. *Sci. Am. 272* (1995), 32–37.

[91] Ramshaw, J. D. Simple model for linear and nonlinear mixing at unstable fluid interfaces in spherical geometry. *Phys. Rev. E 60*, 2 (1999), 1775–1780.

[92] Rayleigh, L. *Scientific Papers*, vol. 2. Dover, 1965.

[93] Reid, R. C., Prausnitz, J. M., and Polling, B. E. *The Properties of Gases and Liquids.* McGraw-Hill, 1987.

[94] Richtmyer, R. D. Taylor instability in shock acceleration of compressible fluids. *Commun. Pure Appl. Math. 13* (1960), 297–319.

[95] Roe, P. L. Approximate riemann solvers, parameter vectors, and difference schemes. *J. Comput. Phys. 43*, 2 (1981), 357–372.

[96] Rossmanith, J. A., Bale, D. S., and LeVeque, R. J. A wave propagation algorithm for hyperbolic systems on curved manifolds. *J. Comput. Phys. 199*, 2 (2004), 631–662.

[97] Saltz, D., Graham, M. J., Holmes, R. L., Zoldi, C. A., Weaver, R. P., and Gittings, M. L. Richtmyer-Meshov instability in cylindrical geometry. In *Proceedings of the Seventh International Workshop on the Physics of Compressible Turbulent Mixing* (1999), Cambridge Univ Press.

[98] Samtaney, R., Pullin, D. I., and Kosovic, B. Direct numerical simulation of decaying compressible turbulence and shocklet statistics. *Phys. Fluids 13*, 5 (2001), 1415–1430.

[99] Samtaney, R., and Zabusky, N. J. Circulation deposition on shock-accelerated planar and curved density-stratified interfaces: models and scaling laws. *J. Fluid Mech. 269* (1993), 45–78.

[100] Schilling, O., Latini, M., and Don, W. S. Physics of reshock and mixing in single-mode Richtmyer–Meshkov instability. *Phys. Rev. E 76* (2007), 026319.

[101] Schwendeman, D. W., and Whitham, G. B. On converging shock-waves. *Proc. R. Soc. London Ser. A–Math. Phys. Eng. Sci. 413* (1987), 297–311.

[102] Setchell, R. E., Storm, E., and Sturtevant, B. An investigation of shock strengthening in a conical convergent channel. *J. Fluid Mech. 56* (1972), 505–522.

[103] Smarr, L., Wilson, J. R., Barton, R. T., and Bowers, R. L. Rayleigh–Taylor overturn in supernova core collapse. *Astrophysical J. 246* (1981), 515–525.

[104] Srebro, Y., Elbaz, Y., Sadot, O., Arazi, L., and Shvarts, D. A general buoyancy-drag model for the evolution of the Rayleigh–Taylor and Richtmyer–Meshkov instabilities. *Laser Part. Beams 21* (2003), 347–353.

[105] Stone, J. M., Xu, J., and Mundy, L. G. Formation of 'bullets' by hydrodynamical instabilities in stellar outflows. *Nature 377* (1995), 315–317.

[106] Sweeney, M. A., and Perry, F. C. Investigation of shell stability in imploding cylindrical targets. *J. Appl. Phys. 52* (1981), 4487–4502.

[107] Taylor, G. I. The instability of liquid surfaces when accelerated in a direction perpendicular to their planes. *Proc. R. Soc. London, Sec. A 201* (1950), 192–196.

[108] Vandenboomgaerde, M., Mügler, C., and Gauthier, S. Impulsive model for the Richtmyer–Meshkov instability. *Phys. Rev. E 58*, 2 (1998), 1874–1882.

[109] Vetter, M., and Sturtevant, B. Experiments on the Richtmyer–Meshkov instability of an air/SF_6 interface. *Shock Waves 4* (1995), 247–252.

[110] Voelkl, T., and Pullin, D. I. A physical-space version of the stretched-vortex subgrid-stress model for large-eddy simulations. *Phys. Fluids 12*, 7 (2000), 1810–1825.

[111] Waddell, J. T., Niederhaus, C. E., and Jacobs, J. W. Experimental study of Rayleigh–Taylor instability: Low Atwood number liquid systems with single-mode initial perturbations. *Phys. of Fluids 13*, 5 (2001), 1263–1273.

[112] Watanabe, M., and Takayama, K. Stability of converging cylindrical shock-waves. *JSME Int. J. II–Fluid Eng. Heat 35* (1992), 218–227.

[113] Whitham, G. B. A new approach to problems of shock dynamics. Part I. Two-dimensional problems. *J. Fluid Mech. 2* (1957), 145–171.

[114] Whitham, G. B. On the propagation of shock waves through regions of non-uniform area or flow. *J. Fluid Mech. 4* (1958), 337–360.

[115] Whitham, G. B. *Linear and Nonlinear Waves.* Wiley-Interscience, 1973.

[116] Wouchuk, J. G. Growth rate of the linear Richtmyer–Meshkov instability when a shock is reflected. *Phys. Rev. E 63*, 5 (2001), 056303.

[117] Wouchuk, J. G. Growth rate of the Richtmyer–Meshkov instability when a rarefaction is reflected. *Phys. Plasmas 8*, 6 (2001), 2890–2907.

[118] Wouchuk, J. G., and Nishihara, K. Linear perturbation growth at a shocked interface. *Phys. Plasmas 3*, 10 (1996), 3761–3776.

[119] Yang, T., Kubota, T., and Zukoski, E. E. Applications of shock-induced mixing to supersonic combustion. *AIAA J. 31* (1993), 854–862.

[120] Yang, Y., Zhang, Q., and Sharp, D. H. Small amplitude theory of Richtmyer–Meshkov instability. *Phys. Fluids 6*, 5 (1994), 1856–1873.

[121] Zabusky, N. J. Vortex paradigm for accelerated inhomogeneous flows: visiometrics for the Rayleigh–Taylor and Richtmyer–Meshkov environments. *Annu. Rev. of Fluid Mech. 31* (1999), 495–536.

[122] Zhang, Q., and Graham, M. J. Scaling laws for unstable interfaces driven by strong shocks in cylindrical geometry. *Phys. Rev. Lett. 79* (1997), 2674–2677.

[123] Zhang, Q., and Graham, M. J. A numerical study of Richtmyer–Meshkov instability driven by cylindrical shocks. *Phys. Fluids 10*, 4 (1998), 974–992.

[124] Zhang, T. A., Dahlburg, R. B., and Dahlburg, J. P. Direct and large-eddy simulations of 3-dimensional compressible navier-stokes turbulence. *Phys. Fluids A-Fluid Dyn. 4* (1992), 127–140.